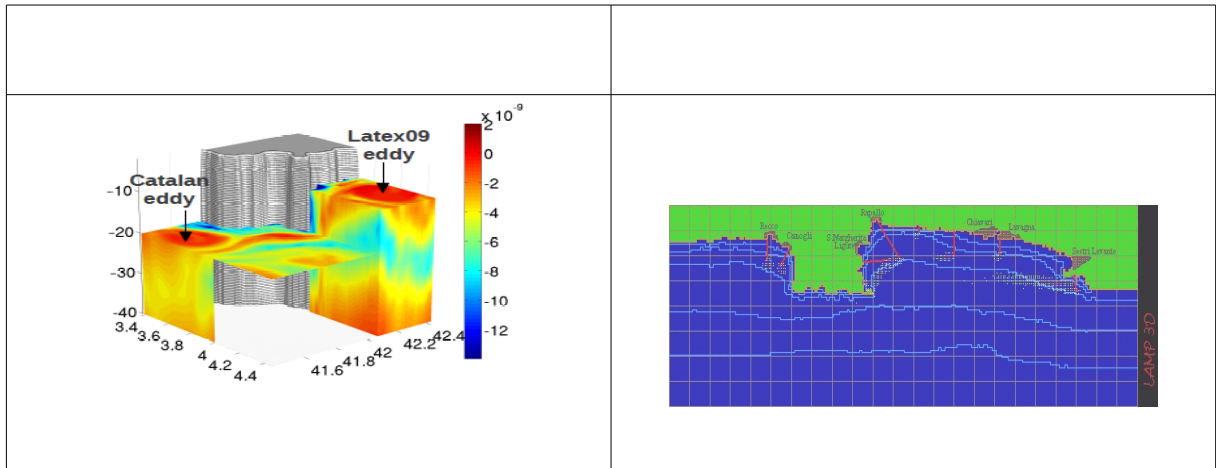


Andrea M. Doglioli

Course Notes and Tutorials

The Lagrangian Approach



VS DRAFT

last revision : 14 December 2022

Contributions

The text of this document has benefited from contributions by A. Petrenko and F. d'Ovidio who also contribute to the lectures.

Acknowledgements

I would like to thank all my students and colleagues for their comments, questions, corrections, and suggestions. In particular, these course notes benefited from contributions by A Allou, R Belon, N Daniault, JL DEVENON J Gatti, Z. Hu, Y José, M Kersalé, M Magaldi, E Martinez, F Mattioli, F Nencioli, and D Piga.

This English version was translated from the French original by XpertScientific editing and consulting services (<https://xpertsscientific.com>) using funding from Copernicus Academy.

Translated to English from:

Doglioli, A.M. (2019), *Notes de Cours et Travaux Dirigés de Approche Lagrangienne*, Université d'Aix-Marseille, Marseille, France.

www.mio.univ-amu.fr/~doglioli/Doglioli_ApprocheLagrangienne.pdf

This material is distributed under the Creative Commons license [<http://creativecommons.org/>]

You are free to:

- reproduce, distribute and communicate this creation to the public
- modify this creation

under the following conditions:

Attribution — You must give appropriate credit, provide a link to the license, and indicate if changes were made. You may do so in any reasonable manner, but not in any way that suggests the licensor endorses you or your use.

NonCommercial — You may not use the material for commercial purposes.

ShareAlike — If you remix, transform, or build upon the material, you must distribute your contributions under the same license as the original.

No additional restrictions — You may not apply legal terms or technological measures that legally restrict others from doing anything the license permits.



This work has been produced with the free software Open Office <http://www.openoffice.org>

Table of Contents

1. Introduction

- 1.1 Historical background
- 1.2 Temporal and spatial scales
- 1.3 Advection and dispersion

2. Fundamentals

- 2.1 Continuity equation
- 2.2 Momentum equations
- 2.3 The quasi-horizontal movement approximation
- 2.4 The hydrostatic and Boussinesq approximations
- 2.5 Surface and bottom friction
- 2.6 Turbulent viscosity
- 2.7 Linearisation of equations
- 2.8 The shallow-water equations
- 2.9 Examples of simple models: geostrophy and the Ekman layer
- 2.10 Inertial currents and oscillations (given by A.Petrenko)
- 2.11 The Omega equation for estimating vertical velocities (given by A.Petrenko)

3. Coastal eddies

- 5.1 Background
- 5.2 Boundary layers
- 5.3 Flow regimes
- 5.4 Shallow water vorticity equation
- 5.5 Flow separation at a cape or headland
- 5.6 Example : circulation near the Promontoir de Portofino
- 5.7 Example : eddies in the Gulf of Lion
- 5.8 Example : circulation around the Hawai'ian islands

4. Isolated eddies

- 4.1 Equations to describe the dynamics of isolated eddies
- 4.2 Vorticity
- 4.3 Example : Meddies (eddies of Mediterranean origin)
- 4.4 Example : Numerical study of the collision of a Meddy with an underwater mountain
- 4.5 Techniques for identifying and tracking eddies
- 4.6 Example : tracking eddies in the Cape Basin and in the Gulf of Lion

5. Advection and diffusion

- 7.1 Conservation theorem
- 7.2 Turbulence as a stochastic process
- 7.3 Eulerian and Lagrangian approaches
- 7.4 Lagrangian particle tracking models
- 7.5 Implementing a random walk model and an advection-diffusion model
- 7.6 Coupled physical-biogeochemical modelling
- 7.7 Example : dispersion of copepods and jellyfish in the North Western Mediterranean
- 7.8 Example : dispersion of waste products from an aquaculture site
- 7.9 Example : Lagrangian connectivity study in the Mediterranean
- 7.10 Lagrangian coherent structures and Lyapunov exponents
- 7.11 Example : in situ observation of a hyperbolic point in the Gulf of Lion (by A.Petrenko)
- 7.12 Example : study of FSLE in the Gulf of Trieste using radar measurements

Bibliography and useful links

- Csanady, G. (1982), *Circulation in the coastal ocean*. D.Reidel Publishing Company, Kluwer Group, Dordrech, Holland .
- Daniault, N. (2005), Océanographie Physique pour l'École Navale. Cours en ligne, Université de Bretagne Occidentale, Brest, France .http://stockage.univ-brest.fr/~daniault/oceano_physique.pdf
- Tomczak, M. (1998), *Shelf and Coastal Oceanography*. Cours en ligne, Flinders University of South Australia, Adelaide, Australia .<http://www.es.flinders.edu.au/~mattom/ShelfCoast/newstart.html>
- Pedloski, J (2003), *Waves in the Ocean and Atmosphere. Introduction to Wave Dynamics*. Springer, USA .
- Carton, X. (2001), *Hydrodynamical modeling of oceanic vortices*. Surv. Geophys., 22,179-263.
- Berta, M., Ursella, L., Nencioli, F., Doglioli, A.M., Petrenko, A.A., Cosoli, S. (submitted after minor revision). *Surface transport in the Northeastern Adriatic Sea from FSLE analysis of HF radar measurements*. Cont. Shelf Res. [see preprint](#)
- Bouffard, J., Nencioli, F., Escudier, R., Doglioli, A.M., Petrenko, A.A., Pascual, A.,Poulain, P.-M. (submitted after revision). *Lagrangian analysis of satellite-derived currents: Application to the North Western Mediterranean coastal dynamics*. Adv. Space Res. [see preprint](#)
- Doglioli, A.M., Nencioli, F., Petrenko, A.A., Fuda, J.-L., Rougier, G., Grima, N. (2013). *A software package and hardware tools for in situ experiments in a Lagrangian reference frame*. J. Atmos. Ocean. Tech., Vol.30, pp.1940-1950, [doi: 10.1175/JTECH-D-12-00183.1](https://doi.org/10.1175/JTECH-D-12-00183.1). [see preprint](#)
- Kersalé, M., Petrenko, A.A., Doglioli, A.M., Dekeyser, I., Nencioli, F. (2013). *Physical characteristics and dynamics of the coastal Latex09 Eddy derived from in situ data and numerical modeling*. J. Geophys. Res., Vol.118, pp.1-11, [doi:10.1029/2012JC008229](https://doi.org/10.1029/2012JC008229). [see preprint](#)
- Campbell, R., Diaz F., Hu, Z.Y., Doglioli, A.M., Petrenko, A.A., Dekeyser, I. (2013). *Nutrients and plankton spatial distributions induced by a coastal eddy in the Gulf of Lion. Insights from a numerical model*. Progr. Oceanogr., Vol.109, pp.47-69, [doi : 10.1016/j.pocean.2012.09.005](https://doi.org/10.1016/j.pocean.2012.09.005). [see preprint](#)
- Nencioli, F., d'Ovidio, F., Doglioli, A.M., Petrenko, A.A. (2011). *Surface coastal circulation patterns by in-situ detection of Lagrangian Coherent Structures*. Geophys. Res. Lett., Vol.38, L17604, [doi:10.1029/2011GL048815](https://doi.org/10.1029/2011GL048815). [see preprint](#)
- Hu, Z.H., Petrenko, A.A., Doglioli, A.M., Dekeyser, I. (2011). *Numerical study of eddy generation in the western part of the Gulf of Lion*. J. Geophys. Res., Vol.116, C12030, [doi:10.1029/2011JC007074](https://doi.org/10.1029/2011JC007074). [see preprint](#)
- Kersalé, M., Doglioli, A.M., Petrenko, A.A. (2011). *Sensitivity study of the generation of mesoscale eddies in a numerical model of Hawaii islands*. Ocean Sci., Vol.7, pp.277-291, [doi : 10.5194/os-7-277-2011](https://doi.org/10.5194/os-7-277-2011) . [see Open Access paper](#) or [see preprint](#)
- Hu, Z.H., Petrenko, A.A., Doglioli, A.M., Dekeyser, I. (2011). *Study of a mesoscale anticyclonic eddy in the western part of the Gulf of Lion*. J. Mar. Syst., Vol.88/1, pp.3-11, [doi: 10.1016/j.jmarsys.2011.02.008](https://doi.org/10.1016/j.jmarsys.2011.02.008) . [see preprint](#)
- De Gaetano, P., Vassallo, P., Bartoli, M., Nizzoli, D., Doglioli, A.M., Magaldi, M.G., Fabiano, M. (2011). *Impact of new measured Mediterranean mineralization rates on the fate of simulated aquaculture wastes*. Aquac. Res., Vol.42, pp.1359-1370, [doi: 10.1111/j.1365-2109.2010.02724.x](https://doi.org/10.1111/j.1365-2109.2010.02724.x). [see preprint](#)
- Qiu, Z.F., Doglioli, A.M., He, Y.J., Carlotti, F.(2011). *Lagrangian model of Zooplankton dispersion: numerical schemes comparisons and parameter sensitivity tests*. Chin. J. Oceanol. Limn., Vol. 29/2, pp.438-445, [doi: 10.1007/s00343-011-0015-9](https://doi.org/10.1007/s00343-011-0015-9) . [see preprint](#)
- Qiu, Z.F., Doglioli, A.M., Hu, Z.Y., Marsaleix, P., Carlotti, F. (2010). *The influence of hydrodynamic processes on zooplankton transport and distributions in the North Western Mediterranean: estimates from a Lagrangian model*. Ecol. Model., Vol.221/23, pp.2816-2827, [doi: 10.1016/j.ecolmodel.2010.07.025](https://doi.org/10.1016/j.ecolmodel.2010.07.025) . [see preprint](#)
- Hu, Z.H., Doglioli, A.M., Petrenko, A.A., Marsaleix, P., Dekeyser, I. (2009). *Numerical simulations of eddies in the Gulf of Lion*. Ocean Model., Vol.28/4, pp.203-208, [doi: 10.1016/j.ocemod.2009.02.004](https://doi.org/10.1016/j.ocemod.2009.02.004) . [see preprint](#)
- De Gaetano, P., Doglioli, A.M., Magaldi, M.G., Vassallo, P., Fabiano, M. (2008). *FOAM, a new simple benthic degradative module for the LAMP3D model: an application to a Mediterranean fish farm*. Aquac. Res., Vol.39/11, pp.1229-1242, [doi:10.1111/j.1365-2109.2008.01990.x](https://doi.org/10.1111/j.1365-2109.2008.01990.x) . [see preprint](#)
- Doglioli, A.M., Blanke, B., Speich, S., Lapeyre, G. (2007). *Tracking coherent structures in a regional ocean model with wavelet analysis: application to Cape Basin Eddies*. J. Geophys. Res., 112, C05043, [doi:10.1029/2006JC003952](https://doi.org/10.1029/2006JC003952) . [see preprint](#)

- Doglioli, A.M., Veneziani, M., Blanke, B., Speich, S., Griffa, A. (2006). *A Lagrangian analysis of the Indian-Atlantic interocean exchange in a regional model*. *Geophys. Res. Lett.*, 33, L14611, doi:10.1029/2006GL026498 . [see preprint](#)
- Vassallo, P., Doglioli, A.M., Rinaldi, F., Beiso, I. (2006). *Determination of physical behaviour of feed pellets in Mediterranean water*. *Aquac. Res.*, Vol.37/2, pp.119-126, doi: 10.1111/j.1365-2109.2005.01403.x . [see preprint](#)
- Doglioli, A. M., Griffa, A., Magaldi, M.G. (2004). *Numerical study of a coastal current on a steep slope in presence of a cape: The case of the Promontorio di Portofino*. *J. Geophys. Res.*, 109, C12033, doi:10.1029/2004JC002422 . [see preprint](#)
- Doglioli, A. M., Magaldi, M. G., Vezzulli, L., Tucci, S. (2004). *Development of a numerical model to study the dispersion of wastes coming from a marine fish farm in the Ligurian Sea (Western Mediterranean)*. *Aquaculture*. Vol.231/1-4, pp.215-235, doi:10.1016/j.aquaculture.2003.09.030 . [see preprint](#)
- Lévy, M. (2008). *The modulation of biological production by oceanic mesoscale turbulence*, *Lect. Notes Phys.*, 744, 219-261, DOI 10.1007/978-3-540-75215-8_9, Transport in Geophysical flow: Ten years after, J. B. Weiss and A. Provenzale (Eds), Springer ([pdf](#))
- Signell, R. e Geyer, W. (1991). *Transient eddy formation around headlands*. *J. Geophys. Res.*, 96(C2):2561–2575.
- Pizzigalli, C., V. Rupolo, E. Lombardi, and B. Blanke (2007), Seasonal probability dispersion maps in the Mediterranean Sea obtained from the Mediterranean Forecasting System Eulerian velocity fields, *J. Geophys. Res.*, 112, C05012, doi:10.1029/2006JC003870.
- Griffa gr12008**
- Griffa, A. 1996. Applications of stochastic particle models to oceanographic problems, *in Stochastic Modeling in Physical Oceanography*, P. M. R. Adler and B. Rozovskii, eds., Birkhäuser Verlag, 114–140.
- Gaspar, Grigoris, Lefevre, 1990, A Simple Eddy Kinetic Energy Model for Simulations of the Oceanic Vertical Mixing' Tests at Station Papa and Long-Term Upper Ocean Study Site, JGR
- Monin A S and Ozmidov R V 1981 *Ocean turbulence* (Leningrad:Gidrometeoizdat)
- Batchelder, H.P., Edwards, C.A., Powell T.M., 2002. Individualbased models of copepod populations in coastal upwelling regions: implications of physiologically and environmentally influenced diel vertical migration on demographic success and nearshore retention. *Progress in Oceanography*. 53, 307333
- Bennett, J.R., Clites, A.H., 1987. Accuracy of trajectory calculation in a finitedifference circulationmodel. *J. comp. Phys.* 68(2), 272282.
- Darmofal, D.L., Haimes, R., 1996. An analysis of 3D particle path integration algorithms. *Journal of computational physics*. 123, 182195.
- Garcia, R.M., Flores, H.T., 1999. Computer Modeling of Oil Spill Trajectories With a High Accuracy Method. *Spill Science and Technology bulletin*. 5(5/6), 323330
- Oliveira, L.A., Costa V.A.F., Baliga, B.R., 2002. A lagrangianEulerian model of particle dispersion ina turbulent plane mixing layer. *International Journal for numerical methods in fluids*. 40, 639653.
- Parada, C., Van der Lingen C.D., Mullon, C., Penven, P., 2003. Modelling the effect of buoyancy on the transport of anchovy (*Engraulis capensis*) eggs from spawning to nursery grounds in the southern Benguela: an IBM approach. *Fisheries Oceanography*. 12(3), 170184
- Tittensor, D.P., Deyoung, B., Tang, C.L., 2003. Modelling the distribution, sustainability and diapause emergence timing of the copepod *Calanus finmarchicus* in the Labrador Sea. *Fisheries Oceanography*. 12(4/5), 299316.
- Visser, A.W., 1997. Using random walk models to simulate the vertical distribution of particles in a turbulent water column. *Marine Ecology Progress Series*. 158, 275281.

1. Introduction

1.1 Historical background

Historically, the ocean has been rather poorly sampled, mainly due to the difficulties of organizing and successfully carrying out oceanographic campaigns. The latter also poses methodological challenges linked to the complexity of marine flows as well as technological (and thus financial) limitations to operate in an environment that is essentially hostile to man.

Systematic observations began in the 1880s with Nansen's pioneering campaigns, however, throughout the first half of the 20th century, observational and theoretical efforts were mainly focused on depicting large-scale circulation. %, considered stable.

The classic models of Sverdrup, Stommel, or Munk proposed a large-scale stationary circulation. This view has strongly influenced how physical oceanographers viewed the oceans for many decades, namely as being traversed by stable currents.

This overly simplified vision can be attributed to a lack of detailed *in situ* information, on the one hand, and to the difficulty, or even the impossibility, of analytically solving the Navier-Stokes equations without very strong simplifying assumptions, on the other hand.

It was only in the 1960s that technological advances made it possible to carry out the first measurements at a higher temporal (order 10 days) and spatial (order 10 km) resolutions.

The pioneering study by Swallow⁵⁹ off Portugal, on the eastern part of the subtropical North Atlantic gyre, demonstrated how currents could vary over periods of a few weeks and over distances of a few tens of nautical miles. In addition, they did not detect any uniform decrease in the intensity of the current which debunked the assumption of a fluid at rest (hydrostatic approximation), a common approach when assuming geostrophy.

Then, the advent of drifting buoys and satellite imagery of the sea surface temperature showed a spatio-temporal variability that transformed the oceanographic vision of the Gulf Stream (e.g., Richardson⁸⁰) from of a quiet flow to a swirling river.

The term “ring” became common in the 1970s to designate cyclonic or anticyclonic eddies that break away from a main current, trapping a body of water at their centre and transporting it over hundreds or even thousands of kilometres for periods ranging from months to years (Olson⁹¹).

The discovery of this high degree of variability in the ocean confronted oceanographers with “the immensity of their task” (Semtner⁹⁵). This led to the use supercomputers in order to numerically solve the equations that govern ocean dynamics. Numerical models have proven invaluable for helping to improve our understanding of the basic processes and their interdependence and assist with the interpretation of observations.

While the first circulation models developed in the 1960s had a rather low resolution, by the mid 1970s the rapid increase in computing power and the development of new numerical methods made it possible to construct models with resolutions of the same order as the first Rossby radius of deformation that were thus capable of resolving processes such as meanders in large ocean currents and their possible evolution into closed recirculations giving rise to the largest oceanic eddies.

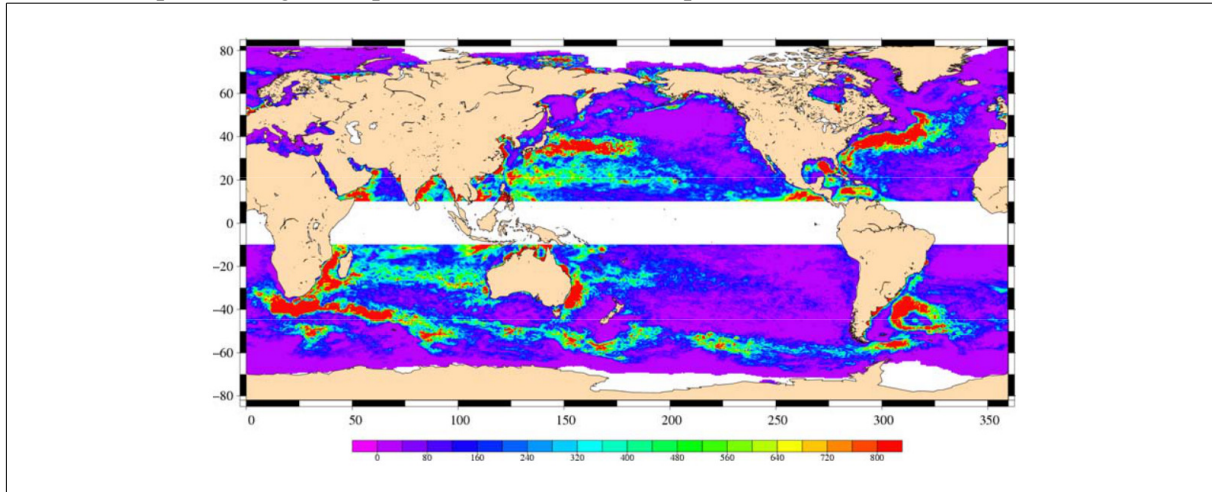
Only by integrating the three approaches of *in situ* observations, satellite remote sensing, and numerical modelling were we able to obtain the information necessary to create animations such as the *Perpetual Ocean* (<https://www.nasa.gov/topics/earth/features/perpetual-ocean.html>), a visually effective tool to highlight the highly dynamic and turbulent nature of oceanic circulation. While admiring these animations, one cannot help but feel fascinated by the hundreds of vortices and meanders that fill the world's seas and oceans to highlight the high level of so-called mesoscale variability.

When the circulation associated with these vortices is particularly intense, we begin to move away from geostrophic equilibrium as we also have to start taking into account the centrifugal force created by the rotation of the vortex; then we enter what is usually referred to as cyclo-geostrophic equilibrium (Carton, 2001).

In the 1980s, measurements using Lagrangian buoys revealed how a large part of the oceans' kinetic energy is associated with mesoscale eddies (Richardson⁸³).

The amount of this mesoscale eddy-related kinetic energy is generally about one order of magnitude greater than the energy contained in the mean flow (Wyrki et al., 1976; Richardson, 1983). \AD{Ferrari}

Maps of the *Eddy Kinetic Energy* (EKE) obtained from satellite altimetry measurements make it possible to identify areas where currents are subject to great instabilities and generate “rings” [for an example see fig {EKEpascual} taken from] [] {pascual06}.



Maps of the Eddy Kinetic Energy [cm^2s^{-2}] in the global ocean from satellite measurements. After \citep{pascual06}

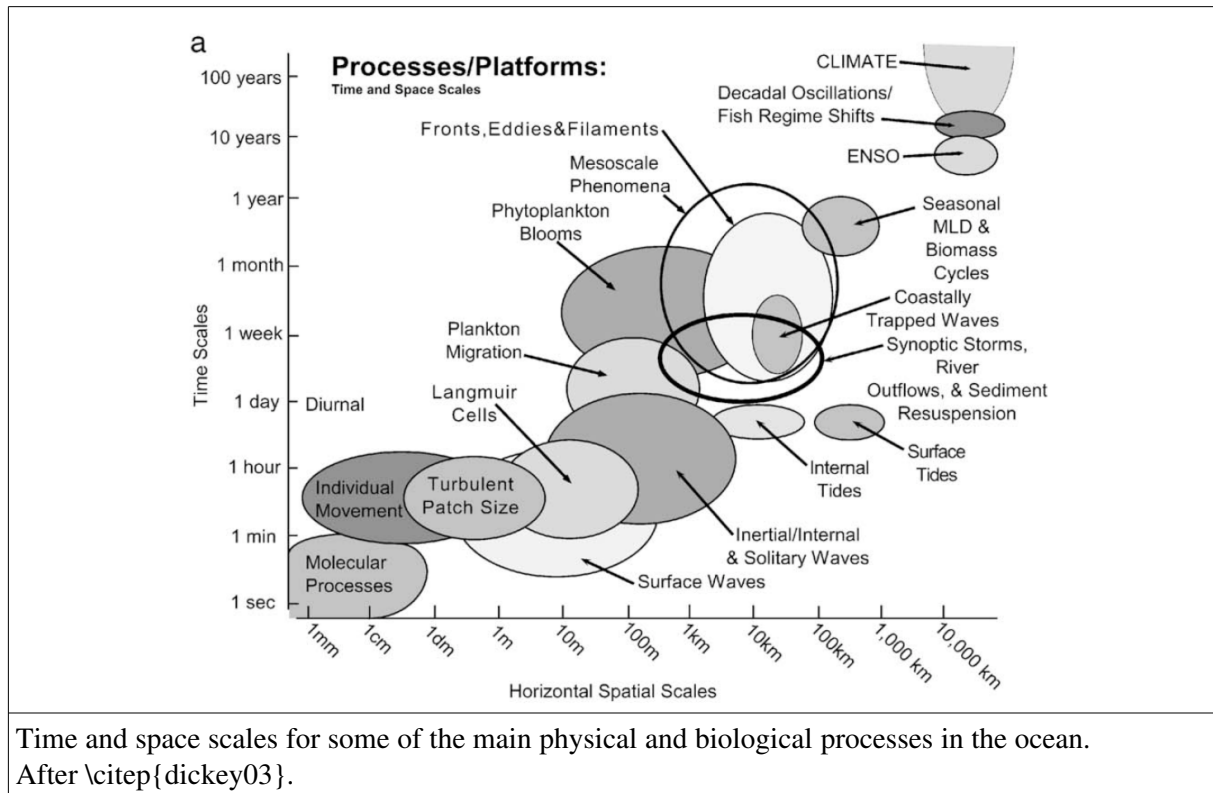
The sheer number of mesoscale eddies in the ocean make it highly likely that they will interact with one another. These interactions induce stretching of water masses which will generate new structures at scales smaller than the first internal Rossby radius of deformation ($R_{\text{R}} \approx \sqrt{gD/\sigma}$). These smaller structures (known as submesoscale) are typically non-geostrophic and their dynamics become three-dimensional. Their relatively small size makes them difficult to detect which is why it took some time to appreciate just how many such structures there are \citep{mcwilliams16}: they were too small and rapidly evolving for conventional ship-based measurements and also for early remote sensing satellites, as it was often difficult to distinguish them from inertial waves in fixed-point time series data or in vertical profiles. In addition, their non-linear nature complicated any theoretical predictions. It was only from the early 2000s that numerical circulation models reached a sufficient resolution to be able to represent them. Such modelling studies, in combination with the availability of very high resolution satellite imagery, formed the starting point for a more detailed study of these structures which has resulted in a rapidly growing interest over the past fifteen years.

Indeed, they could represent the 'missing link' in the energy cascade from the meso- to the dissipation scale \citep{ferrari09} and play a key role in the vertical transfer of heat and salt and in the injection of nutrients into the photic zone \citep{mahadevan16}.

As we move to even smaller scales we arrive at the so-called microscale where turbulence dominates the dynamics. The study of marine turbulence has, unlike the sub-mesoscale, a very long tradition. One typically assumes that at the microscale turbulence is homogeneous and stationary, which allows us to consider the flow at this scale as a superposition of a mean flow and a random component \citep{reynolds1895}. It is also at this microscale where we arrive at the final step of the energy cascade: eddies become so small that they are dissipated by the fluid viscosity and their kinetic energy is transformed into heat.

By generating important velocity gradients over small spatial scales, the physical process of turbulence mixing becomes dominant for both the transfer of mass and heat and for the dispersion of solutes and small organic and inorganic particles.

Despite the long history of the study of marine turbulence, several questions remain unanswered, particularly concerning issues of how turbulence can be represented in general circulation models and its role in the dispersion of biogeochemical tracers.

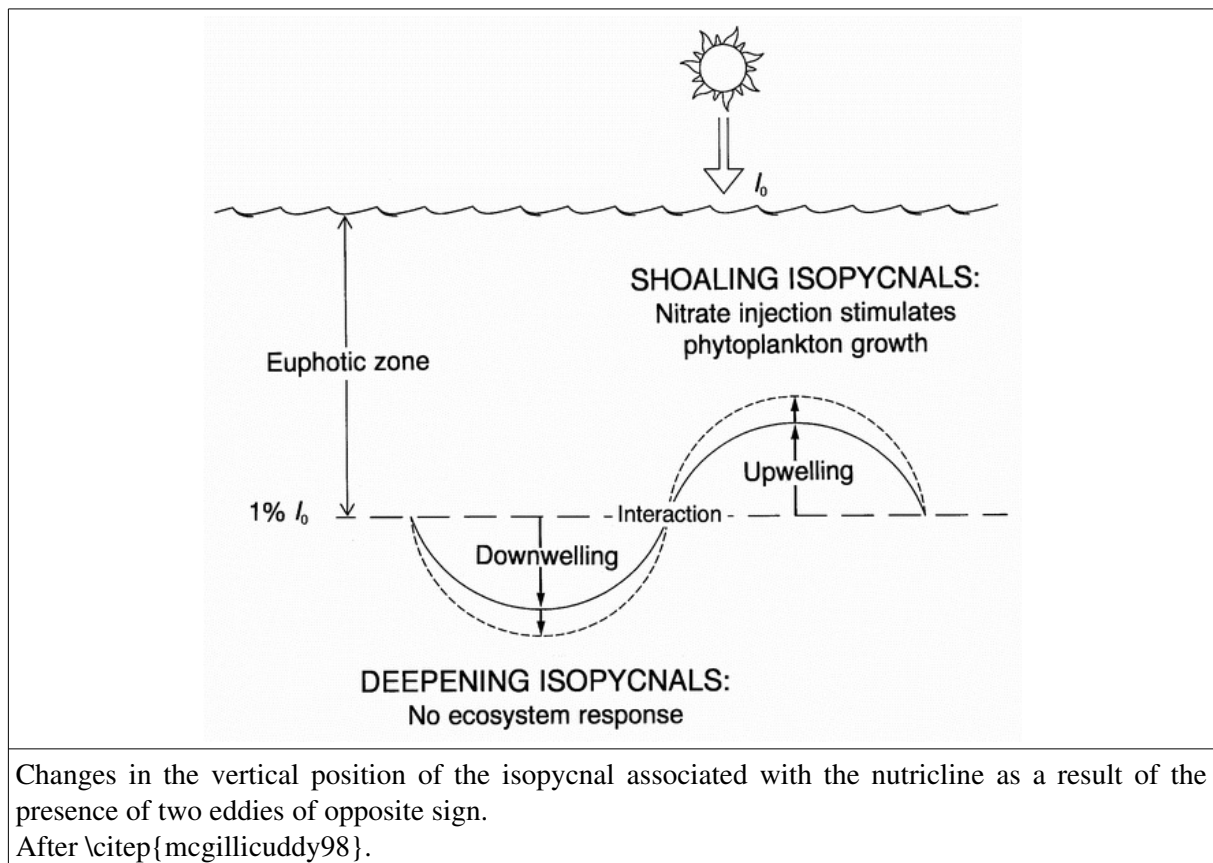


Since the works by \cite{riley42} and \cite{sverdrup53} on the role of vertical mixing on the dynamics of the phytoplankton spring bloom, or those by \cite{haury78} on the role of ocean dynamics on the spatial distribution of plankton (at the origin of the notion of “plankton patchiness”), it is generally accepted that the physics of the ocean affects the dynamics of planktonic communities \footnote{The term plankton has been used for a little over a century to define organisms living in water, more or less passively in suspension and transported by currents \cite[for a review of Lagrangian studies of plankton dynamics, see][]{hitchcock07}}.

The link with geochemistry has been recognised as early as the 1960s with the works by \cite{dugdale67} on the limitation of primary production by nutrients.

The emergence of the issue of global warming linked to the carbon cycle has led to the notion of the “biological pump” \cite{volk85,raven99} which further contributed to this interdisciplinary vision of the ocean and the recognition that an increase of our current understanding of ocean dynamics can only be achieved through a joint cross-disciplinary effort at the scales most relevant to the physical and biogeochemical processes.

The mesoscale plays a key role in ocean dynamics, for heat and mass transport, and for controlling biological activity \cite[e.g., \fig{mcgillicuddy}]; for a recent review see \cite{mcgillicuddy16}.



While numerical studies have shown the very importance of these processes, observational confirmations of these effects are difficult to obtain, mainly due to compatibility issues between the observational strategy required to obtain physical data and the strategy used to study the biogeochemistry. The task becomes particularly complicated in coastal waters due to the complexity of the near-shore circulation, the high variability in the distribution of species and geochemical quantities, and the difficulty of estimating the transfers of matter and energy between the coast and the open ocean and between the surface and the sea bed.

At smaller scales, vertical mixing and - especially in zones of deep water formation - winter convection play an equally important role as they can both bring up nutrients into the photic zone while transporting biomass and detritus to greater depths.

A good understanding of the physical processes that lead to the establishment/break-down of vertical stratification of the water column is pivotal to be able to investigate primary production in the context of seasonal cycles. Furthermore, turbulence can affect the competition between phytoplankton species or groups (e.g., flagellates vs diatoms) [Huisman 2004](#) and thus play a role in the seasonal succession of different species/groups. Vertical mixing due to turbulence also affects the dispersion of zooplankton and can therefore affect ecosystem structure and functioning.

At a global scale, climate change is expected to increase vertical stratification and the fact that turbulence is now better accounted for in coupled models should have some significant impact on the simulated global biogeochemical budgets [Klein 2009](#).

This stratification is also strongly dependent on the physical mesoscale activity (which is only poorly represented in global circulation models) and possible feedbacks between the mesoscale activity and turbulence.

For instance, eddies may be represented in different ways in biogeochemical models: in the closed model the eddy acts as a self-contained unit, while in the open model the eddy affects its environment and triggers biogeochemical reactions along its path [e.g., Nencioli 2008](#). [Olaiola et al., 1993](#), [Nencioli et al., 2008](#) - the choice of which model to use typically depends on the local hydrodynamics, particularly with regard to turbulence.

Attempts to try and answer these kinds of questions have led to significant advances in coupled physical-biogeochemical modelling over the past 30 years. Based on the fundamental conservation equations of matter and energy, while taking advantage of increasingly efficient numerical methods

and tools, coupled models can simulate the response of the planktonic ecosystem in terms of primary production and biomass, as well as geochemical flows associated with the variability of oceanic conditions across a range of temporal scales ranging from short (diurnal tidal cycles and radiative transfer, precipitation), over intermediate (passing atmospheric disturbances), to seasonal scales (seasonal variations in freshwater flows, winter convection, summer stratification).

Integrating this variability on annual, decadal, or even centennial time scales yields quantitative estimates of biogeochemical quantities and functional ecological groups and their behaviour in response to variability in the oceans' "climate".

Recent technological advances in instrumentation allow for (continuous) *in situ* biogeochemical measurements (e.g., ISUS - a high frequency nitrate sampler, or automated flow cytometry) which open up possibilities for exploring the effect of physical processes on the biogeochemistry across a continuum of spatial and temporal scales.

These measurements are essential to calibrate and validate both model results and remote sensing observations using satellites at the same time scales.

Example : Great frigatebirds and eddies in the Mozambique Channel

Foraging strategy of a top predator in tropical waters: great frigatebirds in the Mozambique Channel

personnel.univ-reunion.fr/lecorre/papers/Weimerskirchetal2004.pdf
www.legos.obs-mip.fr/fr/evenements/actualite/actu16.fr.pdf

Top marine predators, such as frigatebirds, have been observed to follow coherent structures in shallow oceans to find food.

<http://www.legos.obs-mip.fr/fr/evenements/actualite/actu16.fr.pdf>

Example : the Hawai'i eddy (Nencioli et al. 2008)

North Pacific Subtropical Gyre

Oligotrophic region:

- Nutrient Limited
- Low biomass and primary productivity
- Small size phytoplankton
- High regeneration rates (recycled nutrients)

(http://oceancolor.gsfc.nasa.gov/cgi/biosphere_globes.pl)

Primary Production and the Biological Pump

Regenerated Production: primary production supported by recycled nutrients

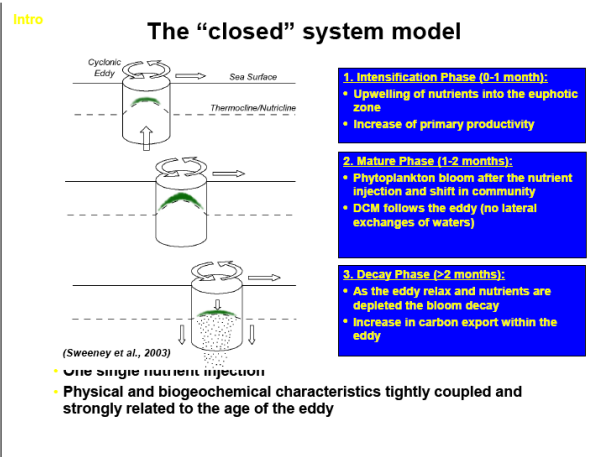
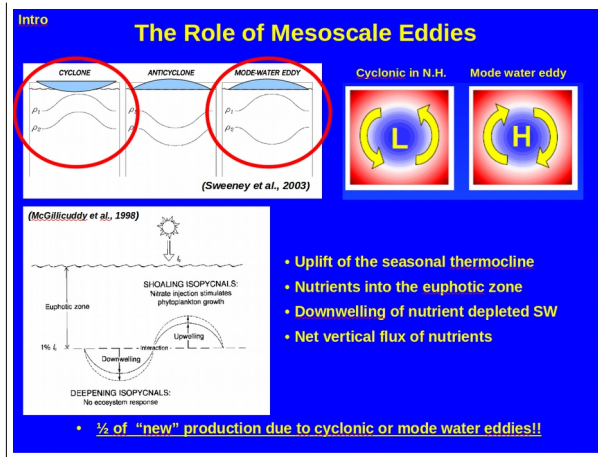
New Production: primary production supported by input of nutrients from outside the euphotic zone (Dugdale and Goering, 1997)

Biological Pump: Steady state over seasonal time scales: **New Production = Carbon Export** (Volk and Hoffert, 1985)

Subtropical Gyres:

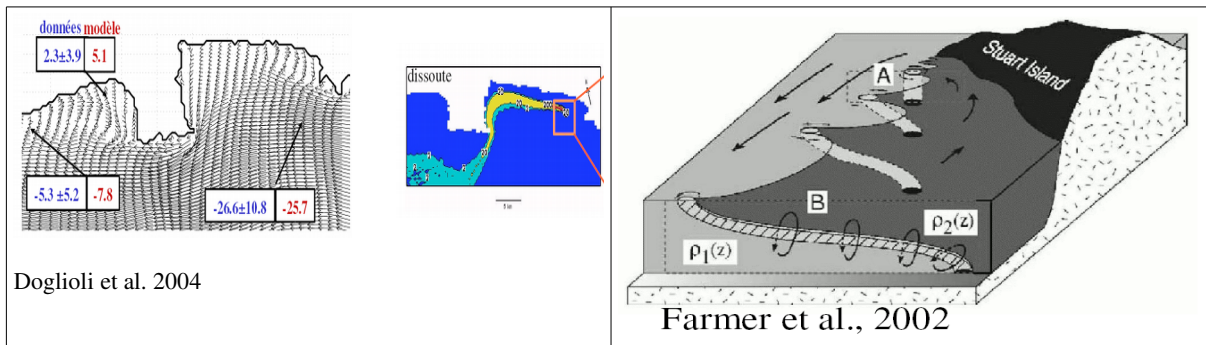
- New P. small fraction of Total P.
- They cover 75% of world oceans

Important sink term for the global carbon cycle!!!



NB : mode water—A term for water of exceptionally uniform properties over a large depth range, caused in most instances by convection. Mode waters represent regions of water mass formation; they are not necessarily water masses in their own right but contribute significant volumes of water to other water masses. Because they represent regions of deep sinking of surface water, mode water formation regions are atmospheric heat sources.

Example : the effects of eddies for the redistribution of solutes downstream from capes and headlands



by radii

The external or barotropic Rossby radius of deformation is given by the ratio between the propagation velocity of gravity waves in shallow water and the Coriolis parameter:

$$\delta_R = \frac{\sqrt{gh}}{f}$$

where h is the depth. It represents the spatial scale at which a barotropic gravity wave will start to be affected by the earth's rotation which causes a "deformation" of the flow.

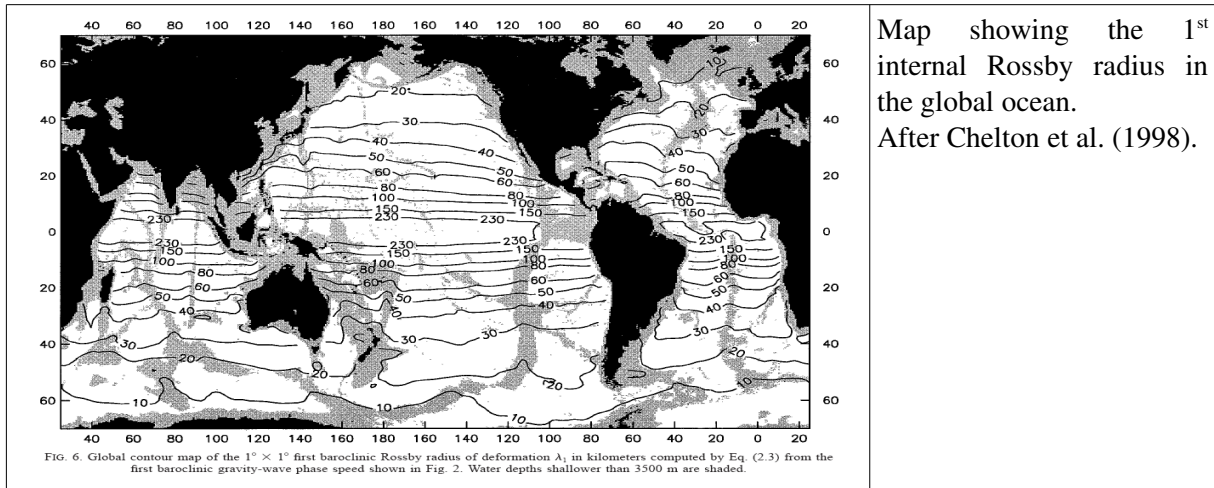
$$\delta'_R = \frac{\sqrt{g'D}}{f} \text{ with } g' = \frac{\rho_2 - \rho_1}{\rho_2} g \text{ being the reduced gravity}$$

is the first internal or baroclinic Rossby radius of deformation; it describes the propagation of a gravity wave in the top layer of a stratified ocean, with $\rho_2 > \rho_1$.

The external Rossby radius of deformation is of the order of 2000 km at mid latitudes and over depths of 4000m (for long waves with phase velocities, c , of ~200 m/s) and reduces to just 300km in shelf seas with depths of about 100m ($c \sim 30$ m/s). As for the internal Rossby radius, it ranges from about 10-30 km in the open ocean to a few kilometres (5-7 km) in shelf seas.

This internal Rossby radius is the natural spatial scale to which physical processes such as fronts and slope currents adjust. We can therefore define mesoscale processes as those that develop at spatial

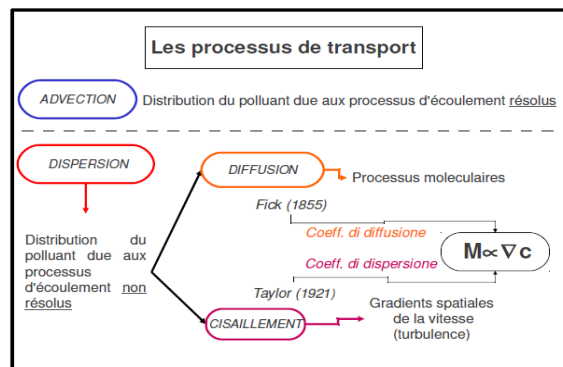
scales that are of the same order of magnitude as δ'_R .



1.3 Advection and dispersion

The term dispersion refers to the process of how a substance released into a fluid becomes distributed over time. While advection refers to the deterministic transport by ocean currents (i.e., the mean flow in the Reynolds sense), dispersion depends on random (diffusion) and shear processes.

Fick (1855) and Taylor (1921) parametrized the mass flux of solutes due to molecular diffusion and turbulence by assuming that the fluxes were proportional to the concentration gradients, with the constants of proportionality having been labelled the molecular and turbulence diffusivity, respectively.

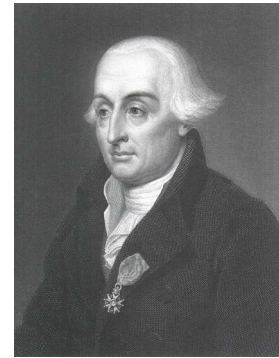


Then, Taylor extended this approach to the flux due to the combined effects of diffusion and shear by introducing the so-called dispersion coefficients.

Eulerian and Lagrangian approaches

Joseph Louis, Count of Lagrange (in Italian: Giuseppe Lodovico Lagrangia), born in Turin on 25 January 1736 and died in Paris on 10 April 1813, was a mathematician, mechanic, and astronomer. He was of French descent from his father's side and spent the first 30 years of his life in Piémont, the subsequent 21 in Berlin, and returned to Paris for his remaining years.

With only 19 years of age he was already appointed professor at the Turin School of Artillery in 1755 where he founded the Turin Academy of Sciences in 1758 through which he published his first works. He was admitted to the Berlin Royal Academy of Sciences by Euler whom he later succeeded as president. He then transferred to Paris where he published his *Mécanique analytique* (1787), just before the French Revolution. Only his genius allowed him to evade the measures of repression taken against foreigners at the time. Special decrees of the Committee of public health allowed him to continue exercising his functions. Having been admitted as a foreign associate member to the French Academy of Sciences in 1772, he became the academy's director in 1788 and a member of the mathematics chapter in 1795. He was appointed senator in the conservative senate in 1799. Together with Monge and Laplace, he was one of the scholars appointed to sit in this assembly.



https://en.wikipedia.org/wiki/Joseph-Louis_Lagrange

Best known for introducing analytical methods to geometry, he also studied other branches of mathematics and published important works in geometry, trigonometry, and mechanics. He is buried in the Pantheon in Paris.

Leonhard Paul Euler was born on 15 April 1707 in Basel and died on 18 September 1783 in Saint Petersburg. He was a Swiss mathematician and physicist who spent most of his life in Russia and Germany.

Euler made some important discoveries in fields as varied as infinitesimal calculus and graph theory. He also introduced much of the terminology and notation of modern mathematics, particularly in analysis where he introduced the concept of a mathematical function. He is also known for his contributions to mechanics, fluid mechanics, optics, and astronomy.



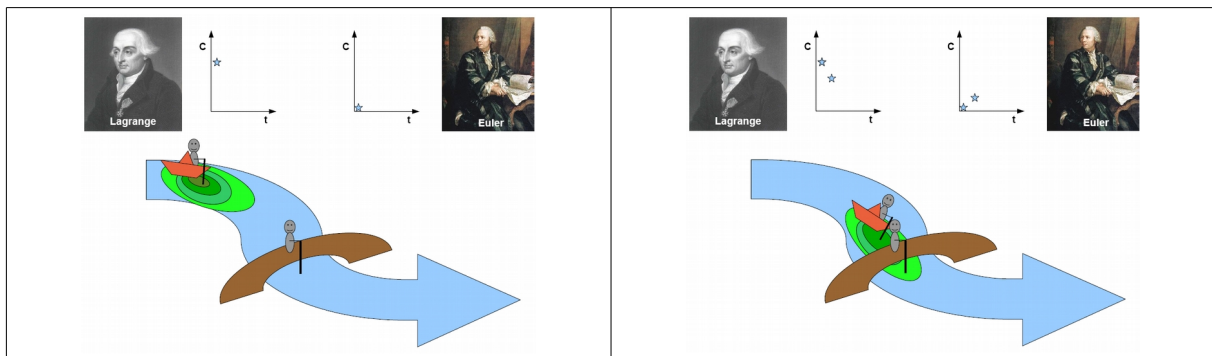
https://en.wikipedia.org/wiki/Leonhard_Euler

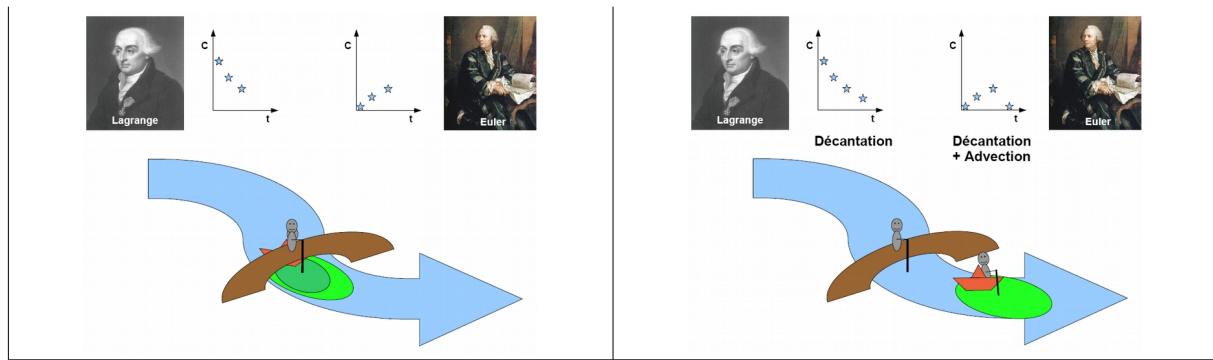
Euler is considered an eminent mathematician of the 18th century and one of the greatest and most prolific of all times. A quote attributed to Pierre-Simon Laplace about the influence of Euler on mathematics states: "Read Euler, read Euler, he is the master of us all".

Definition of the material or Lagrangian derivative:

$$\frac{DC}{Dt} = \frac{\partial C}{\partial t} + \vec{u} \cdot \nabla C = \frac{\partial C}{\partial t} + u \frac{\partial C}{\partial x} + v \frac{\partial C}{\partial y} + w \frac{\partial C}{\partial z}$$

Schematic comparing the Lagrangian and Eulerian approaches for measuring the concentration of a non-conserved tracer.

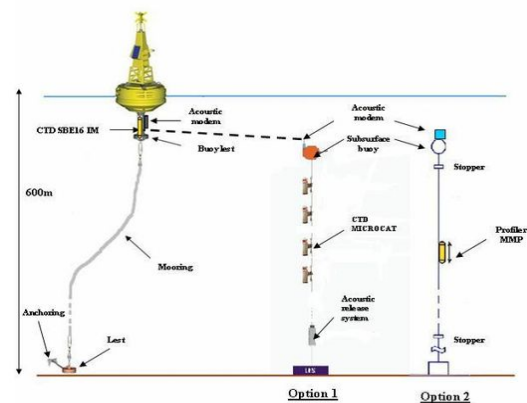




Examples for Eulerian and Lagrangian types of measurements

A) **The autonomous MOLA platform** consists of a buoy-type structure (MOBILIS model jet) with an approximate diameter of 3m and a height of about 5.5m. It contains a pyramidal setup on top which performs all atmospheric measurements (meteorological and GPS), contains a beacon, hosts the power supply (solar panels and batteries), as well as the electronic brain and all communication systems. A CTD SBE16+ sits below the floats on the central mast and collects salinity (conductivity), surface water temperature, fluorescence, and turbidity, together with oxygen and GTD sensors.

<http://observation.obs-banyuls.fr/spip.php?article106>



To simplify measurements and sensor maintenance operations, a second mooring line is deployed close-by which includes the following sensors: CTD, turbidity, fluorescence, O2d, and ADCP (Acoustic Doppler Current Profiler). This second line is equipped with an acoustic release system to facilitate recovery and maintenance and an acoustic modem to communicate with the main mooring. The scientific purpose of this second mooring is to obtain vertical profiles of the water column. In the future, this setup will be complemented by a deep environmental observatory that will utilize the MOLA platform as a field station by adding some biological sensors.

B) **Surface drifters** consist of a surface buoy attached to a floating anchor or drogue via cable (rope). This floating anchor drags the buoy along and allows it to follow the water mass on which it swims. Another name for this type of system is *surdrift*.

The buoy is usually small to minimize drag and wind resistance and is tracked by Argos satellites or through GPS. In the case of GPS, positions are stored internally for several days before being transmitted in bulk to Argos, Imersat, or other systems. This method has the advantage of minimizing the cost of satellite communication while being able to obtain more frequent and precise location measurements.

The line connecting the buoy to the drogue is usually quite thin, only a few millimetres in diameter to minimize parasitic drag. As it also needs to be fairly resistant it is typically made from Aramid fibres (highly resistant). The drogue is kept at a constant depth that typically ranges from tens of metres to a kilometre.

The drogue is designed for maximum drag so it can follow the water mass to be studied. Its drag must be at least 30 times larger than the drag of other elements of the assemblage. The drogue comes in a variety of shapes and forms but is often cylindrical (*Holey sock*) or diamond-shaped (*Tristar*). The latter type consist of 3 flaps made of fabric that are assembled at 90° angles to one another and are joined at their diagonals. The shape of the flaps is maintained through a system of rods.

A weight is attached at the base of the drogue to keep the assembly vertical.

Text and figure from <http://www.univ-brest.fr/lpo/instrumentation/16.htm>

446 / David L. Mackas, William R. Crawford and Pearn P. Niiler

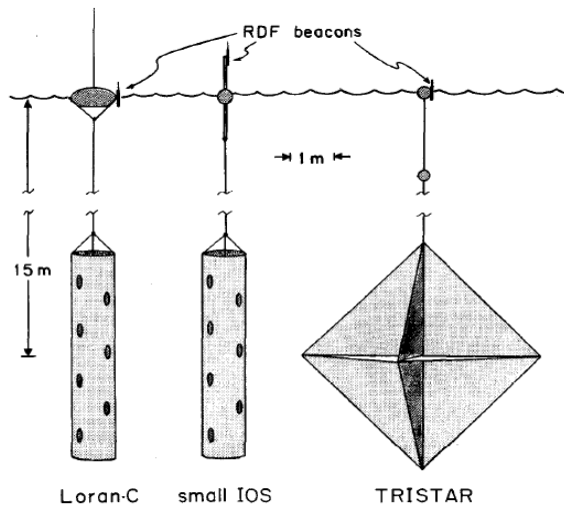
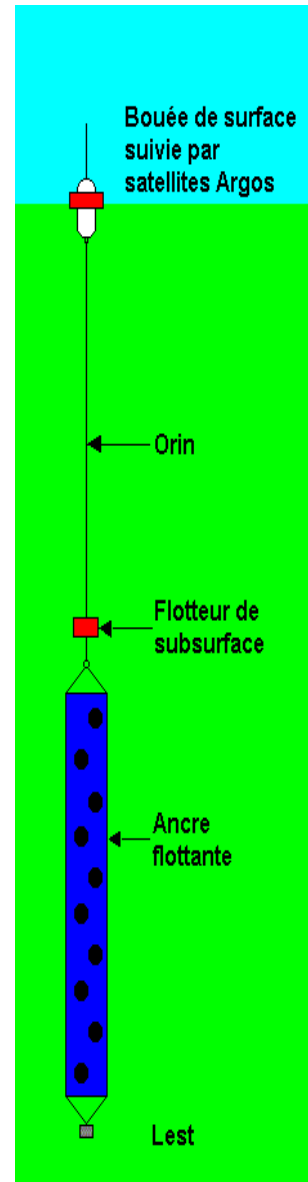


Fig.1 Relative size of float and drogue elements for the three drifter designs compared in this study. All drogues were centred at 15-m depth. Float : drogue frontal area ratios ranged from about 10 : 1 for the Lorán drifter to about 50 : 1 for the TRISTAR and the IOS small drifter. The TRISTAR uses two flotation spheres, with most of the buoyancy provided by the deeper float, allowing the tether to the surface (ARGOS transmitter) float to be slack much of the time and thus transmit less surface wave energy to the drogue.

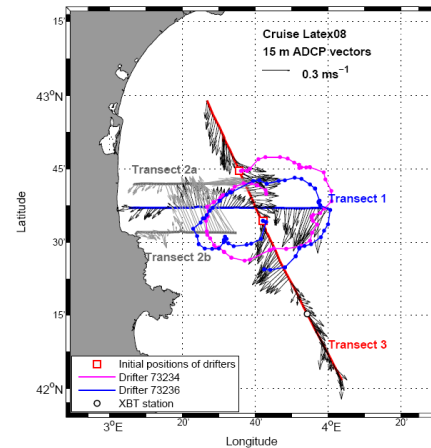


Surface current velocities as measured by hull mounted ADCP aboard Tethys II and the trajectories of two surface drifters.

Measurements carried out during the LATEX 2008 campaign:

The vectors are drawn every 4 minutes along three transects: Transect 1 (Sept. 1), Transects 2a and 2b (Sept. 3), and Transect 3 (Sept. 5);

The dots along the surface drifter trajectories mark their position every hour (Sept. 5 – 11).

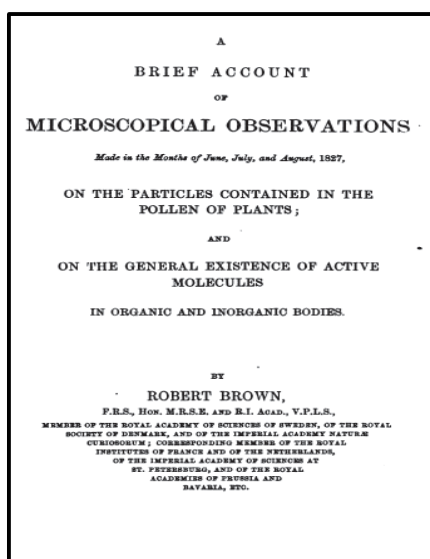


From Hu et al., 2009

Diffusion and Brownian motion

Diffusion refers to the process that distributes a substance in a liquid and thereby reduces concentration gradients. The same process not only acts on particulates but also on the fluid properties themselves such as density or salinity, if their distribution is non-uniform. While there are slight differences in how diffusion redistributes matter, kinetic energy, and momentum, these different mechanisms are tightly linked and interconnected. Diffusion is closely linked to Brownian motion, named after Robert Brown, who described this phenomenon for the first time at the beginning of the 19th century.

Robert Brown, born December 21 1773 in Montrose (Angus), died June 10 1858 in London, was a Scottish botanist. His most famous scientific legacy is not related to Botany but to physics: the random motion of particles suspended in a medium – named after him as Brownian motion. His discovery was partly owed due to the fact that he was one of the first to use a microscope routinely in his trade. Thus, in 1827, while observing pollen of *Clarkia pulchella* under his microscope, he noticed the presence of very small particles that were moving in all directions. He repeated this observation with other plants and initially believed that what he saw was the manifestation of a "vital fluid". Only when he made the same observations with inorganic particles did he change his mind.



<http://books.google.com/books?id=KwUAAAAYAAJ>

He published his results in 1828 in an account where he acknowledged that other scholars had preceded him in observing these erratic movements, the explication for which was not available until almost a century later when another famous scholar, Albert Einstein, published a paper on the movement of small particles suspended in stationary liquids and explained motion from the molecular-kinetic theory of heat. After having worked on pollen and (falsely) attributing the erratic motions he saw to a biological cause, he then started to work on a drop of water that was trapped inside a quartz crystal and could therefore not have been contaminated with pollen or other spores. Again, he observed the same erratic movements of small particles suspended in the water drop which led him to conclude that these movements could not have a biological origin but that they must be linked to a (still unknown) physical phenomenon.

About 80 years later, Albert Einstein suggested that the movement of pollen as observed by Brown and others could be expressed as a Random Walk: subject to constant collisions with water molecules, a suspended particle exhibits small displacements of random length and direction. By measuring how particles moved in response to Brownian motion, Einstein showed that it was possible to determine several important physical constants such as the atomic mass or Avogadro constant. This piqued the interest of many mathematicians who then began to study this phenomenon.

Today, Brownian motion can be found everywhere: it forms the basis of our understanding for all diffusive phenomena in physical, chemical, and biological systems and can even be found in economic theory. In 1900, Louis Bachelier developed a theory to describe the fluctuations observed at stock markets by employing a Random Walk approach. This approach was re-discovered for the field of economics in the 1970s and further refined, playing an important role in financial mathematics today.

The Random Walk model (representing Brownian motion) can explain the process of diffusion. Diffusion can be divided into 2 types: 1) self-diffusion: governed exclusively by Brownian motion; 2) forced diffusion: due to a force (electrostatic, chemical, physical) or a gradient in temperature and/or concentration.

A simple Lagrangian particle tracking model can be used to simulate the spatial and temporal evolution of a drop of ink released into a glass of water. It also allows us to reflect on how microscopic disorder can generate macroscopic order.



Yellow food colouring diffusing through water. The glass on the left contains hot water, while the glass on the right contains cold water. The food colouring was added to the cold water slightly before the colouring was added to the hot water, yet after a few seconds it has diffused more thoroughly through the hot water. The frames are roughly 1 second apart (so the animation is roughly 2x real-time).

en>User:CTho made this. It is available (along with the source images) at <http://ctho.ath.cx/pics/new/2006-09-24/> - It has been released into the public domain. [1]

<http://commons.wikimedia.org/wiki/Image:Diffusion.gif>

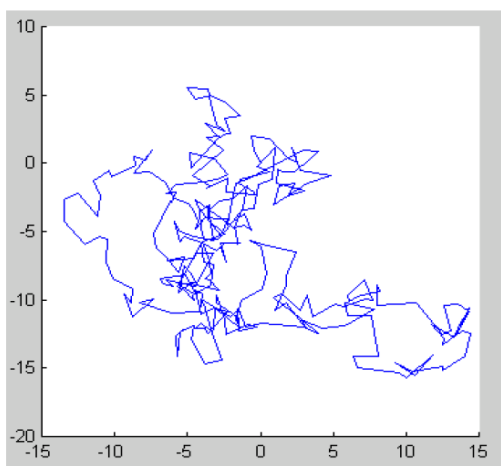


Figure 2 : Marche aléatoire d'une particule dans un espace à 2 dimensions

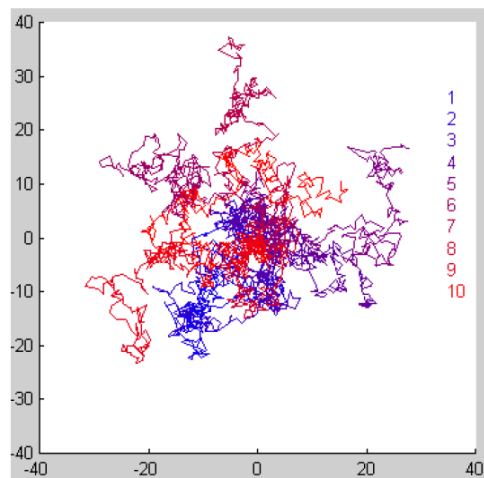


Figure 3 : Marche aléatoire de 10 particules indépendantes

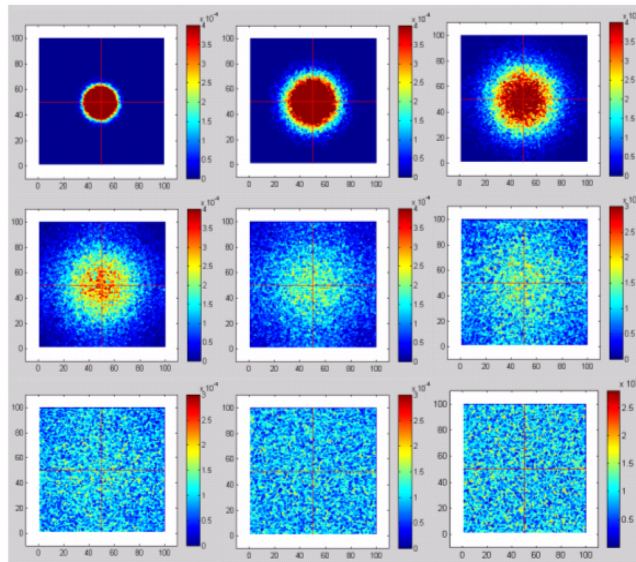
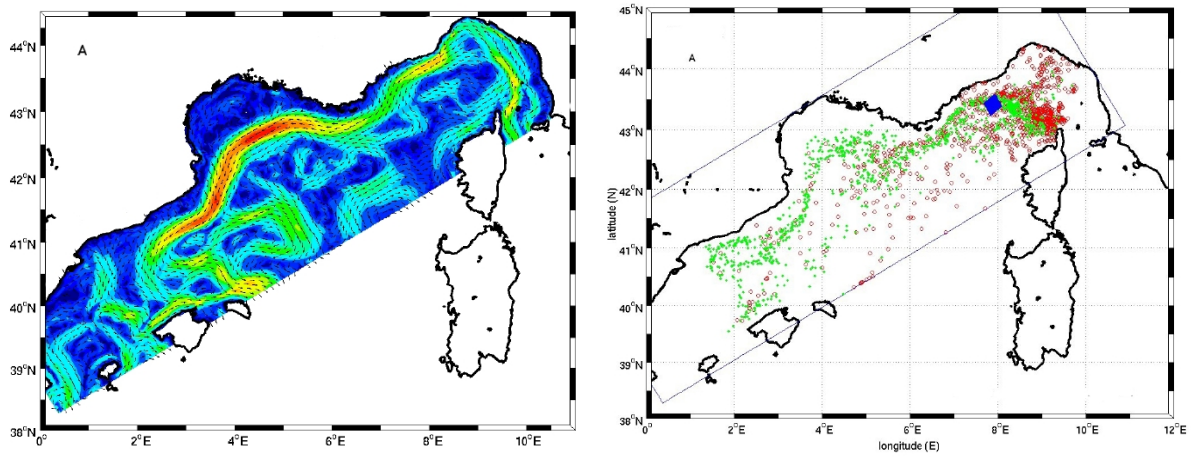


Figure 5 : Diffusion d'une goutte d'encre dans de l'eau

Lagrangian particle tracking simulation of a drop of ink diffusing in a glass of water.

Examples of Eulerian and Lagrangian models

Results from an Eulerian (left) and Lagrangian model (Qiu et al. 2011).



2. Fundamentals

2.1 The Continuity Equation

In classical fluid mechanics, the continuity equation is typically written in Eulerian form

$$\frac{\partial \rho}{\partial t} + \frac{\partial}{\partial x_i}(\rho u_i) = 0$$

where ρ is density, t time, and u_i the fluid velocity along the three coordinate axes x_i (with $i=1,2,3$; employing the so-called Einstein notation, see https://en.wikipedia.org/wiki/Einstein_notation). The equation expresses the idea that the local density changes only if there is a convergence or a divergence of the mass flux (ρu_i).

Another form of the equation is

$$\frac{d\rho}{dt} + \rho \frac{\partial u_i}{\partial x_i} = \frac{1}{\rho} \frac{d\rho}{dt} + \frac{\partial u_i}{\partial x_i} = 0 \quad (1.1)$$

with

$$\frac{d\rho}{dt} = \frac{\partial \rho}{\partial t} + u_i \frac{\partial \rho}{\partial x_i}$$

being the total time derivative of density, i.e., the rate of change of density along the particle track.

If we want to apply this equation to the coastal ocean, we realize that seawater is not such a simple substance! First, we need to consider changes in density due to the diffusion of salt. In fresh water, this can be neglected and the main causes of density variations are related to cooling and heating of the fluid. Both these effects are accounted for in Equation (1.1) if we consider that u_i also includes the expansions and thermal contractions. While these simplifying assumptions do not work in seawater, we can assume that as long as the heat and salt fluxes vary in realistic bounds, temperature and salinity variations occur very slowly and we can assume quasi-stationarity.

Density and relative density

Density is a fundamental parameter for oceanographers. Small horizontal variations in density (created, for instance, through solar irradiance) can produce important oceanographic currents.

Strictly speaking, relative density (or specific gravity) = (the mass of 1m^3 of seawater)/(the mass of 1m^3 of distilled water at 4°C) [without unit]. In oceanography, for practical reasons, the density of seawater is usually expressed as the actual density [kg m^{-3}] – 1000 and is denoted with the symbol σ .

The density of seawater depends on the salinity S , the temperature T , and on the pressure p . These three terms are related through the equation of state of seawater. It is an empirical relation that has been defined based on numerous laboratory studies. The first version of this equation was established in 1902 by Knudsen and Ekman and has since been replaced by "the international one-atmosphere equation of state (EOS-80)":

EOS-80 : *International One-Atmosphere Equation of State of Seawater*

$$\rho(S, t, p) = \rho(S, t, 0) \left[1 - p/K(S, t, p) \right]$$

with

$$\begin{aligned} \rho(S, t, 0) = & 999.842594 + 6.793952 \times 10^{-2} t - 9.095290 \times 10^{-3} t^2 + 1.001685 \times 10^{-4} t^3 - 1.120083 \times 10^{-6} t^4 \\ & + 6.536332 \times 10^{-9} t^5 + 8.24493 \times 10^{-1} S - 4.0899 \times 10^{-3} tS + 7.6438 \times 10^{-5} t^2 S - 8.2467 \times 10^{-7} t^3 S \\ & + 5.3875 \times 10^{-9} t^4 S - 5.72466 \times 10^{-3} S^2 + 1.0227 \times 10^{-4} tS^2 - 1.6546 \times 10^{-6} t^2 S^2 \\ & + 4.8314 \times 10^{-4} S^3 \end{aligned}$$

and

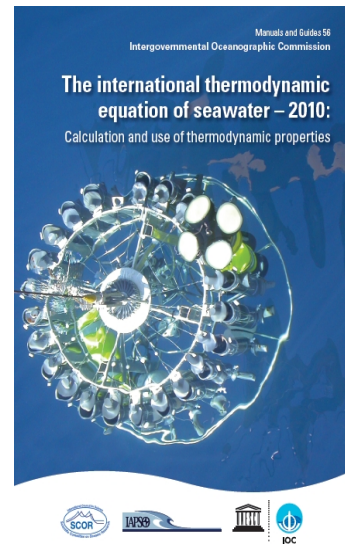
$$\begin{aligned} K(S, t, p) = & 19652.21 + 148.4206 t - 2.327105 t^2 + 1.360447 \times 10^{-2} t^3 - 5.155288 \times 10^{-5} t^4 + 3.239908 p \\ & + 1.43713 \times 10^{-3} tp + 1.16092 \times 10^{-4} t^2 p - 5.77905 \times 10^{-7} t^3 p + 8.50935 \times 10^{-5} p^2 \\ & - 6.12293 \times 10^{-6} tp^2 + 5.2787 \times 10^{-8} t^2 p^2 + 54.6746 S - 0.603459 tS + 1.09987 \times 10^{-2} t^2 S \\ & - 6.1670 \times 10^{-5} t^3 S + 7.944 \times 10^{-2} S^2 + 1.6483 \times 10^{-2} tS^2 - 5.3009 \times 10^{-4} t^2 S^2 + 2.2838 \times 10^{-3} pS \\ & - 1.0981 \times 10^{-5} tpS - 1.6078 \times 10^{-6} t^2 pS + 1.91075 \times 10^{-4} pS^2 - 9.9348 \times 10^{-7} p^2 S \\ & + 2.0816 \times 10^{-8} tp^2 S + 9.1697 \times 10^{-10} t^2 p^2 S \end{aligned}$$

<http://lecalve.univ-tln.fr/oceano/ies80/index.html>

More refined and recent formulations can be found in the literature (Anati, 1999; Feistel 2003, 2005), as well as formulations taking into account the geographic variability linked to the shape of the geoid (for the concept of "neutral density" see McDougall, 1987).

In June 2009, the Intergovernmental Oceanographic Commission (IOC), with the support of the Special Committee on Oceanic Research (SCOR) and the International Association of the Physical Sciences of the Oceans (IAPSO), adopted the Thermodynamic Equation of Seawater 2010 (TEOS-10) as official definition of the properties of seawater and sea ice.

Oceanographers are now strongly advised to use the algorithms and variables defined by TEOS-10 when reporting their results.



The fundamental differences between TEOS-10 and EOS-80 are that TEOS-10 uses:

- (1) Absolute Salinity (SA) to describe the salt content of seawater; Absolute Salinity takes into account the spatial variability of the composition of seawater. In the open ocean, the use of this new salinity has a non-trivial effect on the horizontal density gradient and thus on the velocities calculated using the Thermal Wind Equation.
- (2) Conservative Temperature (Q) which replaces the potential temperature (q). Both are derived quantities that are determined from thought experiments, namely, they represent the temperature that a water parcel would attain if adiabatically brought to a standard reference pressure. The Conservative Temperature offers a better representation of the heat content of seawater with a precision that is two orders of magnitude greater than with potential temperature.
- (3) The properties of seawater defined by TEOS-10 all derive mathematically from a Gibbs function (through differentiation) and are thus compatible with each other (unlike the now obsolete EOS-80 approach in which different mutually incompatible polynomials defined each thermodynamic variable). To allow any oceanographer to use the new TEOS-10 formalism, two software programs are available:
 - (i) the Gibbs SeaWater (GSW) oceanographic toolbox (for MATLAB and FORTRAN),
 - (ii) the Sea-Ice-Air (SIA) library (for Fortran and Visual Basic).

Both are freely available from <http://www.TEOS-10.org>.

2.2 The momentum equations

Using an Eulerian approach, Newton's Second Law (Equation of Motion) can be written as

$$\frac{d(\rho u_i)}{dt} = -\frac{\partial p}{\partial x_i} + \frac{\partial \tau_{ij}}{\partial x_j} + \rho b_i \quad (1.3)$$

On the left side of the equation we find the acceleration of a fluid parcel per unit volume while on the right we have the sum of all surface and volume forces. The former include the hydrostatic pressure gradients, p , and the divergence of the stress tensor τ_{ij} .

While the volume forces, ρb_i , have several origins (gravity, Coriolis) they are all proportional to the mass of the water particle.

The first index in τ_{ij} is used to define the direction of the shear (parallel to x_i) while the second index defines the plane on which this acts (perpendicular to x_i). x_3 represents the vertical axis. Thus, τ_{13} and τ_{23} are the shear stresses acting on the horizontal planes, while τ_{12} and τ_{21} act on the lateral walls of the imaginary water parcel.

The stress tensor components acting on the horizontal planes are particularly important in shallow water as they transmit the effect of wind forcing onto the surface layer and bottom friction to the bottom layers.

By using the continuity equation for an incompressible fluid (Eq. 1.2) the right side of Eq. 1.3 can be rewritten as

$$\frac{d(\rho u_i)}{dt} = \frac{\partial(\rho u_i)}{\partial t} + \frac{\partial}{\partial x_j}(\rho u_i u_j) \quad (1.4)$$

The second term on the right is the divergence of the flow from the momentum caused by the flow itself. It represents the redistribution of momentum in space which fortunately is only non-negligible in a limited part of the flow field. In fact, this non-linear term causes many mathematical difficulties (see section on "the Reynolds tensor").

Volume forces

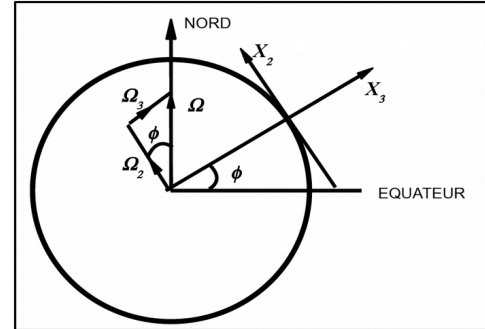
The velocity components, u_i , are measured in a rotating frame of reference: Earth. Volume forces therefore include the centrifugal force and the Coriolis pseudo-force associated with the rotation of the Earth. The centrifugal force is usually contained in the gravity term and the volume forces are written as

$$\begin{aligned} b_i &= 2 \epsilon_{ijk} u_j \Omega_k + g_i \\ g_i &= -g \delta_{i3} \end{aligned} \quad (1.5)$$

where Ω_k represents the Earth's angular velocity components in local coordinates and g the acceleration due to local gravity.

The gravitational pulls by the Moon and Sun are also part of the volume forces. They are important mainly in the deep ocean, while in shelf seas we mostly study the effects of tidal propagation rather than the processes of its generation.

Schematic of the local coordinate system showing the horizontal (x_1, x_2) and vertical (x_3) axes at latitude ϕ and the angular velocity components.



The Earth's angular velocity, Ω , is 2π radians per 24 h, thus

$$\Omega = 0.7292 \cdot 10^{-4} \text{ s}^{-1}.$$

By combining Eqs. (1.4) and (1.5) with Eq. (1.3) we obtain

$$\frac{\partial(\rho u_i)}{\partial t} + \frac{\partial}{\partial x_j}(\rho u_i u_j) = -\frac{\partial p}{\partial x_i} - g \rho \delta_{i3} + 2\rho \epsilon_{ijk} u_j \Omega_k + \frac{\partial \tau_{ij}}{\partial x_j} \quad (1.6)$$

In this form, the equation of motion becomes nearly impossible to solve analytically. In order to obtain suitable models to study simple flows in shelf seas, Eq. (1.6) needs to be simplified.

2.3 The quasi-horizontal movement approximation

In shelf seas, the ratio between vertical and horizontal velocities is small. This is partly due to the small ratio between the vertical (depth) and horizontal scales which is of the order of 10^{-3} . By using simple geometrical considerations we can estimate that the ratio between vertical and horizontal velocities (at the basin scale) will have the same ratio. Furthermore, the water column is often vertically stratified which further impedes vertical exchanges.

As $|u_3| \ll |u_1|, |u_2|$ the components of the Coriolis acceleration term in the equation of motion become

$$\begin{aligned} 1^{\text{st}} \text{ eq. } & 2(u_2 \Omega_3 - u_3 \Omega_2) \cong 2 u_2 \Omega_3 \\ 2^{\text{nd}} \text{ eq. } & 2(u_3 \Omega_1 - u_1 \Omega_3) \cong -2 u_1 \Omega_3 \end{aligned}$$

through geometrical considerations we find

$$\Omega_3 = \Omega \sin \phi$$

where ϕ = latitude. We can now introduce the Coriolis parameter

$$f = 2 \Omega \sin \phi = 1.458 \cdot 10^{-4} \sin \phi \quad [\text{s}^{-1}]$$

which yields

$$\begin{aligned} &\text{in the 1}^{\text{st}} \text{ eq.} && f u_2 \\ &\text{and in the 2}^{\text{nd}} \text{ eq.} && -f u_1 \end{aligned}$$

At mid-latitudes around 41° , f is about 10^{-4} s^{-1} . f is generally taken as positive in the northern hemisphere.

2.4 The hydrostatic and Boussinesq approximations

While Eq. (1.6) needs to be applied separately to each spatial dimension, gravity is typically only important for vertical movements. The vertical component of the Equation of Motion is

$$\frac{d u_3}{d t} = -\frac{1}{\rho} \frac{d p}{d x_3} - g + 2(u_1 \Omega_2 - u_2 \Omega_1) + \frac{1}{\rho} \frac{\partial \tau_{3j}}{\partial x_j} \tag{1.7}$$

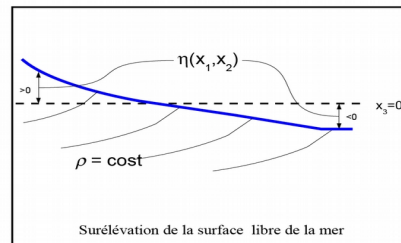
The gravitational acceleration, g , is about 10 m s^{-2} ; we have already seen that horizontal movements in the coastal ocean are typically of the order of 0.1 up to 1.0 m s^{-1} ; the Coriolis acceleration is of the order of 10^{-5} to 10^{-4} m s^{-2} . The gradients of the Reynolds stress tensor can reach values of 0.1 N m^{-2} (0.1 Pa) = 0.1 kg m s^{-2} on a layer of 10 m . Thus the last term is of the order of 10^{-5} ms^{-2} . The typical maximum vertical velocities in the coastal ocean are about 10^{-2} ms^{-1} and the minimum time scales about 10^3 s which yields vertical accelerations of the order of 10^{-5} ms^{-2} . As a result, we essentially have a quasi-horizontal motion where the dominant acceleration by gravity is balanced by the pressure gradient:

$$\frac{\partial p}{\partial x_3} = \rho g \tag{1.8}$$

Given that this balance is the same as for a fluid at rest, this is called the hydrostatic approximation. If the fluid was truly at rest, this equation would tell us that the free surface of the ocean would be at $x_3 = 0$. However, a fluid in motion may have a free surface that shows a certain inclination with respect to the horizontal. One typically uses a function like $\eta = \eta(x,y)$ to indicate the position of the free surface of the ocean (the so-called *sea surface height, ssh*). Negative values of η indicate a depression in the free surface below the mean reference level while positive values indicate an elevation about the mean.

If we integrate Eq. (1.8) between a certain level x_3 and the surface, we obtain

$$p = p_a + \int_{x_3}^{\eta} \rho g dx_3 \tag{1.9}$$



where p_a is the atmospheric pressure.

The Equation of Motion in the horizontal (Eq. 1.6 with $i=1,2$) contains the pressure gradients which can be calculated from the hydrostatic approximation (Eq. 1.9) as:

$$\frac{\partial p}{\partial x_i} = \frac{\partial p_a}{\partial x_i} + \rho_{surf} g \frac{\partial \eta}{\partial x_i} + \int_{x_3}^{\eta} g \frac{\partial \rho}{\partial x_i} dx_3 \quad (i=1,2) \quad (1.10)$$

This equation tells us that the pressure gradient in the water column is the sum of three terms: (i) the atmospheric pressure gradient, (ii) the gradient due to deviations of SSH from the mean, and (iii) the gradient of the internal density field.

The atmospheric pressure gradient represents an external forcing, however, in shallow water this term can often be neglected as wind forcing dominates.

The second term represents the acceleration due to the inclined free surface, which can be thought of as water particles on the surface rolling down a slope.

The third term concerns buoyancy effects that stem from density differences along horizontal surfaces (or better geopotentials). Under typical coastal flow conditions, this last term can be further simplified.

Vertical density differences in the coastal ocean are of the order of one per thousand, which means that we can replace ρ_{surf} with a reference density ρ_0 in Eq. (1.10) without committing too great of an error. However, horizontal density variations ($\partial \rho / \partial x_i$, $i=1,2$) are non-negligible. Boussinesq suggested to write density as

$$\rho = \rho_0(1+\epsilon) \quad \text{with } \epsilon = O(10^{-3}) \quad (1.11)$$

and to only retain those buoyancy terms that are of the same order of magnitude.

Neglecting the atmospheric pressure, Eq. (1.10) becomes

$$\frac{1}{\rho_0} \frac{\partial p}{\partial x_i} = g \frac{\partial \eta}{\partial x_i} + \int_{x_3}^{\eta} g \frac{\partial \epsilon}{\partial x_i} dx_3 = g \frac{\partial}{\partial x_i} [\eta - \eta_d(x_3)] \quad (i=1,2) \quad (1.12)$$

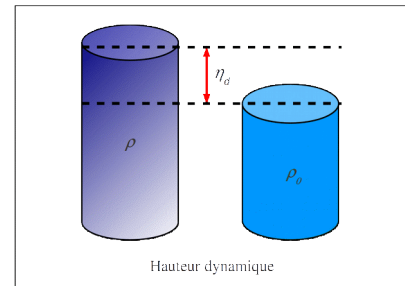
η_d is the difference in sea surface height between a water column of density ρ_0 and a water column with the “real” density $\rho(x_3)$. In short, the Boussinesq approximation allows replacing the real density with its reference value, ρ_0 , everywhere except in the gravity acceleration term. In the pressure terms, this only leaves the parts with ϵ which is called the dynamic height and is the main driver of the resulting flow.

One often uses the higher density value as reference density so ϵ is always negative and the dynamic height is zero or positive.

If the pressure gradient $-\partial p / \partial x_i$ disappears at a certain depth $x_3 = -h$, Eq. (1.12) becomes

$$\eta = \eta_d(-h) \quad (1.13)$$

where we have chosen an appropriate zero level for the free surface that allows us to neglect the constant of integration. In this case, the sea level topography can be directly determined from the density distribution (Sverdrup, 1942). In shallow water, it is not usually possible to assume that the pressure gradients vanish at a certain depth, and the simplification from Eq. (1.13) can only be made if the total water depth, H , is much greater than the reference depth h . This constraint essentially eliminates any possibility to simplify the equations in coastal waters which are highly dynamic and typically exhibit strong density gradients.



However, by carefully choosing the reference level, h , we can regard h_d as a contribution to the dynamic height of something that is relative to the density distribution and on which there is a distribution of $h - h_d$ that is not necessarily related to the internal density distribution.

The typical velocities in coastal oceans are of the order of 0.1 m s^{-1} with time scales of days (e.g., storm events), i.e., 10^5 s . This corresponds to a mean acceleration of 10^{-6} m s^{-2} . An inclination of the free surface of just 10^{-7} (1 cm on 100 km) creates the same level of acceleration making it an important quantity to consider when assessing the momentum balance.

A constant density anomaly, ϵ , of 1 part per 1000 over a 30 m surface layer yields a 3 cm contribution to the dynamic height relative to a 30 m depth. On a typical scale of 100 km a 10^{-7} density gradient is created if a surface layer is 30 m deep at one point and 20 m deep at a distance 100 km away. Density differences of this order (and above) are almost always present in coastal oceans, so it can be said that all physical processes that control the density field can affect horizontal momentum balances in a highly significant way.

The Reynolds stress tensor

Flow in coastal waters is generally turbulent, especially in the surface and bottom layers, and the time scales of such flows are typically greater than the time scales associated with turbulence. Whenever this is true, it is possible to use the so-called Reynolds decomposition which divides the overall flow and pressure into a mean (non-turbulent) component and a component due to turbulence

$$u_i = \bar{u}_i + u_i'$$

$$p = \bar{p} + p'$$

The time averages of the fluctuating components, u_i' and p' , are zero by definition. As a result, all terms containing these fluctuations in the equations of continuity and motion disappear and only the products of the form $\rho \overline{u_i' u_j'}$ remain, the so-called Reynolds stresses. The divergence of these terms is very similar to the role played by the means of the viscous terms in the equation of motion, as a result these terms are often combined and placed on the same side of the equation:

$$\tau_{ij} = \bar{\tau}_{ij} - \rho \overline{u_i' u_j'}$$

With a few exceptions, the contribution by molecular viscosity is usually negligible in comparison to turbulence viscosity and we will therefore always consider the viscous terms as Reynolds stresses and that Eq. (1.3) is applied to the mean flow, even if we will omit the overbars (symbolizing the means) in the notation from now on for practical reasons.

REMINDER (see Course OPB205)

Average flow equations (Reynolds)

For a turbulent flow, rather than looking for the instantaneous speed given by the Navier-Stokes equations, we are looking for a velocity that is averaged over time, that is to say, averaged over a certain period of time that depends on the type of phenomenon being investigated.

At the same time, for each of the variables (components of velocity and pressure) we do the following decomposition $u = \bar{u} + u'$, where \bar{u} is the mean and u' the variability about the mean such that $\overline{u'} = 0$:

$$\bar{u} = \frac{1}{T} \int_0^T u \, dt \quad \overline{u'} = \frac{1}{T} \int_0^T u' \, dt = 0$$

This approach was developed by Osborne Reynolds (http://en.wikipedia.org/wiki/Osborne_Reynolds). As an example, let us calculate the mean of the product of two independent components u and v :

$$\overline{uv} = \frac{1}{T} \int_0^T uv \, dt = \frac{1}{T} \int_0^T \bar{u}\bar{v} \, dt + \frac{1}{T} \int_0^T \bar{u}v' \, dt + \frac{1}{T} \int_0^T u'\bar{v} \, dt + \frac{1}{T} \int_0^T u'v' \, dt$$

so

$$\overline{uv} = \bar{u}\bar{v} + \overline{u'v'} + \overline{u'\bar{v}} + \overline{\bar{u}v'}$$

but since $\overline{u'} = \overline{v'} = 0$

$$\overline{uv} = \bar{u}\bar{v} + \overline{u'v'}$$

T represents a period of time that is sufficiently long so the mean values are independent of time. We have similar definitions for v , w , and p . Even if $\overline{u'} = 0$, it should be noted that the fluctuations themselves can be of the same order of magnitude as u . Furthermore, these fluctuations that are superimposed on the mean vector are always three-dimensional, i.e., u', v', w' are always non-zero even if the flow is one- or two-dimensional.

It can be shown that all linear terms of the Navier-Stokes Equation keep the same form for both the mean and instantaneous flows; however, the advection terms (to show in the exercise) become:

$$\overline{\vec{V} \cdot \nabla u} = \overline{\vec{V} \cdot \nabla \bar{u}} + \underbrace{\overline{u' \frac{\partial u'}{\partial x}} + \overline{v' \frac{\partial u'}{\partial y}} + \overline{w' \frac{\partial u'}{\partial z}}}_{\text{termes turbulents}}$$

The Reynolds equations thus differ from the Navier-Stokes Equation in that they contain turbulence terms. They are often referred to as the *Reynolds-averaged Navier-Stokes (RANS) equations*.

Reynolds stress and turbulence viscosity

We show that the continuity equation for an incompressible fluid

$$\frac{\partial u}{\partial x} + \frac{\partial v}{\partial y} + \frac{\partial w}{\partial z} = 0$$

satisfies the following mean flow equation (to show in the exercise):

$$\frac{\partial \bar{u}}{\partial x} + \frac{\partial \bar{v}}{\partial y} + \frac{\partial \bar{w}}{\partial z} = 0$$

Using the definitions of \bar{u} and u' we obtain:

$$\frac{\partial \bar{u}}{\partial x} = \frac{1}{T} \int_0^T \frac{\partial u}{\partial x} dt = \frac{\partial}{\partial x} \left[\frac{1}{T} \int_0^T u dt \right] = \frac{\partial}{\partial x} \left[\frac{1}{T} \int_0^T (\bar{u} + u') dt \right] = \frac{\partial \bar{u}}{\partial x}$$

By subtracting ($u' = u - \bar{u}$) we can deduce that

$$\frac{\partial u'}{\partial x} + \frac{\partial v'}{\partial y} + \frac{\partial w'}{\partial z} = 0$$

We can therefore write the turbulence terms as follows (without them changing value – according to Ox):

$$\overline{u' \frac{\partial u'}{\partial x}} + \overline{v' \frac{\partial u'}{\partial y}} + \overline{w' \frac{\partial u'}{\partial z}} + \overline{u' \left(\frac{\partial u'}{\partial x} + \frac{\partial v'}{\partial y} + \frac{\partial w'}{\partial z} \right)} = \frac{\partial \overline{u'u'}}{\partial x} + \frac{\partial \overline{u'v'}}{\partial y} + \frac{\partial \overline{u'w'}}{\partial z}$$

and the Reynolds equation for the u component can be written as:

$$\frac{\partial \bar{u}}{\partial t} + \bar{u} \frac{\partial \bar{u}}{\partial x} + \bar{v} \frac{\partial \bar{u}}{\partial y} + \bar{w} \frac{\partial \bar{u}}{\partial z} = -\frac{1}{\rho_0} \frac{\partial \bar{P}}{\partial x} + f_v + \nu \left[\frac{\partial^2 \bar{u}}{\partial x^2} + \frac{\partial^2 \bar{u}}{\partial y^2} + \frac{\partial^2 \bar{u}}{\partial z^2} \right] - \frac{\partial \overline{u'u'}}{\partial x} - \frac{\partial \overline{u'v'}}{\partial y} - \frac{\partial \overline{u'w'}}{\partial z}$$

where the last three terms are the so-called Reynolds stress terms.

J.V. Boussinesq (1842–1929) proposed to relate these Reynolds stresses to the gradients in the mean flow as:

$$\overline{u'u'} = -A_x \frac{\partial \bar{u}}{\partial x} ; \quad \overline{u'v'} = -A_y \frac{\partial \bar{u}}{\partial y} ; \quad \overline{u'w'} = -A_z \frac{\partial \bar{u}}{\partial z} ;$$

where the coefficients A are called turbulent exchange coefficients (where the symbol A comes from *Austausch* = exchange in German) or *eddy viscosity*.

If we neglect the spatial variability of these coefficients the turbulence terms take a form that is identical to the

form of molecular friction as illustrated for the x component:

$$\frac{d\bar{u}}{dt} = -\frac{1}{\rho_o} \frac{\partial \bar{P}}{\partial x} + f\bar{v} + \nu \left[\frac{\partial^2 \bar{u}}{\partial x^2} + \frac{\partial^2 \bar{u}}{\partial y^2} + \frac{\partial^2 \bar{u}}{\partial z^2} \right] + A \left[\frac{\partial^2 \bar{u}}{\partial x^2} + \frac{\partial^2 \bar{u}}{\partial y^2} + \frac{\partial^2 \bar{u}}{\partial z^2} \right]$$

and since they are much smaller (in the ocean 10^{-5} to 10^{-6} in the vertical and 10^{-10} to 10^{-12} in the horizontal) they are typically neglected entirely.

However, care must be taken with these simplifications because unlike ν , the A coefficients are no properties of the fluid but of the flow. They vary spatially and depend on the chosen averaging time. In oceanography, we typically distinguish between coefficients for the horizontal $A_x = A_y = A_h$ and vertical dimension A_z .

2.5 Surface and bottom friction

While the diagonal components of the Reynolds stress tensor represent a small correction of the hydrostatic pressure, the components $\tau_{xy} = \tau_{yx} = \overline{u'v'}$ represent the turbulence momentum flux, the divergence of which is very important for the horizontal components of the equation of motion. In practice, the value of τ_{xy} is rarely larger than 1 Pa and its spatial scale of variability usually greater than 10 km. The divergence term thus becomes

$$\frac{\partial \tau_{xy}}{\partial x}, \frac{\partial \tau_{xy}}{\partial y} \approx O(10^{-7}) \text{ m s}^{-2} < \frac{\partial \tau_{xz}}{\partial z}, \frac{\partial \tau_{yz}}{\partial z} \quad (\text{see below})$$

Although the vertical divergence is larger, the difference is not large enough to completely eliminate τ_{xy} and τ_{yx} , although Csanady (1982) pointed out that it is difficult to demonstrate that the effects of lateral friction play a rather significant role in general circulation problems in coastal waters.

In contrast, the horizontal Reynolds stresses $\tau_{xz} = \overline{u'w'}$ and $\tau_{yz} = \overline{v'w'}$ are really important in shallow water. Wind friction at the surface represents the main forcing for the main flow and is transmitted to the sub-surface via these terms. Likewise, bottom friction represents a key process for coastal flows.

If we use $\vec{F} = (F_x, F_y)$ ($z=0$) to denote the components of surface friction due to wind, the continuity condition at the air-sea interface requires

$$\tau_{xz} = F_x \quad \tau_{yz} = F_y$$

Generally, wind friction occurs along the wind direction and its intensity can be calculated from a quadratic law.

$$\vec{F} = \frac{\rho_a}{\rho_w} C_{10} \vec{W} |\vec{W}| \quad (1.23)$$

with $\vec{W} \equiv (W_x, W_y)$ the wind velocity, ρ_a/ρ_w the ratio between the densities of air and water, and C_{10} a drag coefficient which, by definition, refers to the wind speed at an altitude of 10 m above sea level. The value of C_{10} can be estimated with field measurements. Csanady (1982) proposed the following:

$$C_{10} = 1.6 \times 10^{-3}, \quad (W \leq 7 \text{ m s}^{-1})$$

$$C_{10} = 2.5 \times 10^{-3}, \quad (W \geq 10 \text{ m s}^{-1})$$

with intermediate values for wind speeds between 7 and 10 m s^{-1} . C_{10} varies with wind speed as larger wind speeds increase the surface roughness of the water (creating ripples and increasingly large

waves) which in turn increases friction.

These values of C_{10} correspond to those for a Nikuradse roughness (see box) of 1.4 cm for weak winds that create capillary waves and 10 cm for stronger winds that create foam-capped waves.

For a wind speed of 7 m s^{-1} Eq. (1.23) gives $F = 10^{-4} \text{ m}^2 \text{ s}^{-2}$ where $\tau = 0.1 \text{ Pa}$.

Another reason why the terms $\tau_{xz} = \overline{u'w'}$ and $\tau_{yz} = \overline{v'w'}$ are so important is because they also transmit the bottom friction toward shallower layers. A typical sea floor slope near the coast is of the order of 10^{-2} - 10^{-3} thus practically horizontal (NB: over distances of the order of kilometres the irregularities in the bottom topography can be considered as a type of “roughness”).

If we denote the bottom roughness with $\vec{B} = (B_x, B_y)$ ($z = -H$), we can write

$$\tau_{xz} = B_x \quad \tau_{yz} = B_y \quad (1.25)$$

in analogy to Eq. (1.22) and the bottom friction can be treated with a quadratic law that is similar to Eq. (1.23)

$$\vec{B} = C_d \vec{U}_1 |\vec{U}_1| \quad (1.26)$$

where C_d is again a drag coefficient and $\vec{U}_1 \equiv (U_1, V_1)$ the current velocity at a certain height above the sea bed, typically at 1 m. It is often difficult to determine C_d through *in situ* observations and one often employs a fixed value of $C_d = 2 \cdot 10^{-3}$.

Using this value we see that the typical intensity of bottom friction for a water velocity of 0.2 m s^{-1} roughly corresponds to the amount of wind friction caused by moderate wind velocities. A bottom water velocity of 1 m s^{-1} would correspond to the wind friction caused by a hurricane. So the divergence of both the surface and bottom friction $\partial \tau_{(x,y)z} / \partial z$ are important.

2.6 Eddy viscosity

Bottom and surface friction are not uniformly distributed throughout a water column of 100 m. There are typically two mechanisms that prevent a uniform distribution: rotation and stratification.

In a viscous and homogeneously rotating fluid, friction on a boundary that is not parallel to the axis of rotation generates layers of limited depth in which the friction is reduced to zero (Ekman 1905). The depth of the viscous Ekman layer is of the order of

$$\sqrt{2 \frac{\nu}{f}}$$

with ν the kinematic viscosity. Outside the Ekman layer the flow remains practically frictionless. When the Ekman layer is turbulent (nearly always in coastal waters) the Reynolds stresses are also limited to a layer of limited depth, as if turbulence itself was some form of viscosity that prevented further distribution through the water column. The thickness of the turbulent boundary layer is independent of the properties of the fluid and is of the order of

$$0.1 \frac{u_*}{f} \quad \text{where } u_* = \left(\frac{\tau}{\rho} \right)^{1/2} \text{ is a friction velocity with } \tau \text{ the amount of stress exerted against the boundary}$$

For a typical stress value of $t = 0.1 \text{ Pa}$, $u_* = 1 \text{ cm s}^{-1}$, the thickness of the Ekman layer is of the order of 10 m at mid latitudes, while for a hurricane producing stresses of 3 Pa or above, the bottom and surface Ekman layers in a 100m water column may start to overlap.

Stratification due to surface heating or as a result of freshwater inflow can lead to a slight reduction in the thickness of the surface and bottom layers. As the bottom and surface layers remain well mixed by turbulence, any density variations are confined to the interior of the water column, the intermediate depths between both layers where strong changes in density can sometimes be observed. While Reynolds stresses can also be generated through wave action, these stresses are usually smaller (by about 2 orders of magnitude) than the stresses generated by bottom or surface friction. There can be exceptions at the layer interfaces depending on the magnitude of density variations, with abrupt

changes in flow velocity.

In order to make the equation of motion solvable, it is necessary to parametrize the Reynolds stresses inside the fluid τ_{13} , τ_{23} in terms of velocities. With a little care and knowledge, we can write these stresses as proportional to the flow velocity gradients

$$\tau_{xz} = K_z \frac{\partial u}{\partial z}, \tau_{yz} = K_z \frac{\partial v}{\partial z} \quad \text{where } K_z \text{ is the turbulence eddy viscosity} \quad (1.27)$$

Whenever you use these relations you need to remember that K_z is a property of the fluid and not of the flow. *A priori*, it is therefore not reasonable to use a single value for the entire water column and neither for the entire boundary layer. In fact, in a boundary layer of 1 m K_z varies very rapidly with depth near the sea bed and the surface, in fact near any interface (e.g., the thermocline). In general, the velocity vector changes rapidly across these surfaces but the Reynolds stress does not. If we are trying to characterize the flow within the boundary layer we can use a logarithmic law. In coastal oceanography, the study of boundary layers is very complicated and our understanding of them remained very limited for a long time. Modern instruments now make it possible to embark on more detailed *in situ* studies (see figures of observations with the SEPTR).

Outside boundary layers, in a flow region with homogeneous turbulence shear, the eddy viscosity can be considered constant and proportional to the velocity and length scale of the flow. In regions influenced by surface and bottom stresses, we can have a proportional relationship with the friction velocity and the depth of the mixed layer:

$$K_z = \frac{u_* h}{Re} \quad \text{where } Re \text{ is the friction Reynolds number.} \quad (1.28)$$

Field observations suggest that Re is between 12 and 20.

Inside a continuously stratified water column, hence without interfaces of sharp density changes, there are no observations that can help to determine K . An typical estimate of the order of magnitude is $K=1 \text{ cm}^2 \text{ s}^{-1} = 10^{-4} \text{ m}^2 \text{ s}^{-1}$, i.e., two orders of magnitude smaller than the typical value for a well-mixed boundary layer using Eq. (1.28).

At interfaces where density varies abruptly, it is better to use a quadratic law of the type of Eqs. (1.23) and (1.26). Then, if we denote the stress components with $\vec{I} = (I_x, I_y)$ ($z = -h_I$), we can write

$$I_i = C_s \vec{U}_I |\vec{U}_I| \quad (1.29)$$

where C_s a friction coefficient appropriately chosen for this kind of interface and \vec{U}_I represents the velocity change across the interface. In a laboratory setup a value of $C_s = 0.5 \times 10^{-3}$ has been observed but it is very difficult to verify whether this value also applies *in situ*.

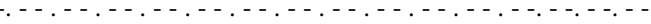
In summary, it is possible to use Eq. (1.27) with $K = \text{constant}$ in a homogeneous layer and to use Eqs. (1.23), (1.26), and (1.29) at the boundaries (see schematic on right).

Obviously, in this case the procedure to calculate the stresses and velocity distribution becomes very complex as we need to apply the quadratic laws and scale the eddy viscosity with the boundary stresses.

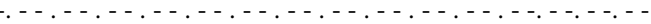


$$\tau_{(x,y)z} = \vec{F} = \frac{\rho_a}{\rho_w} C_{10} \vec{W} |\vec{W}| \quad (1.23)$$

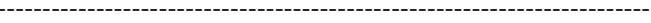
$$\tau_{(x,y)z} = \rho K_z \frac{\partial(u, v)}{\partial z} \quad \text{with} \quad K_z = \frac{u_* h}{Re} \quad \text{where} \quad K_z = 10^{-4} \quad (1.27)$$



$$\tau_{(x,y)z} = I_i = C_s \vec{U}_1 |\vec{U}_1| \quad (1.29)$$



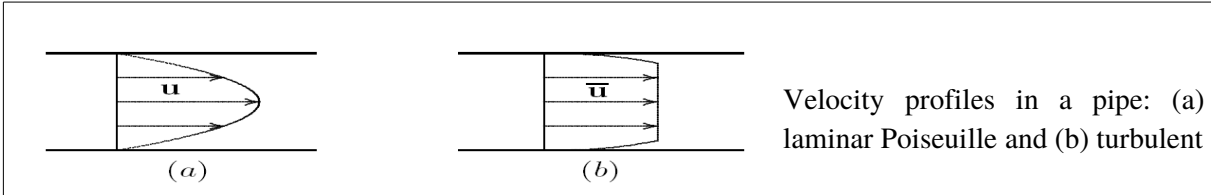
$$\tau_{(x,y)z} = \rho K_z \frac{\partial(u, v)}{\partial z} \quad \text{with} \quad K_z = \frac{u_* h}{Re} \quad \text{where} \quad K_z = 10^{-4} \quad (1.27)$$

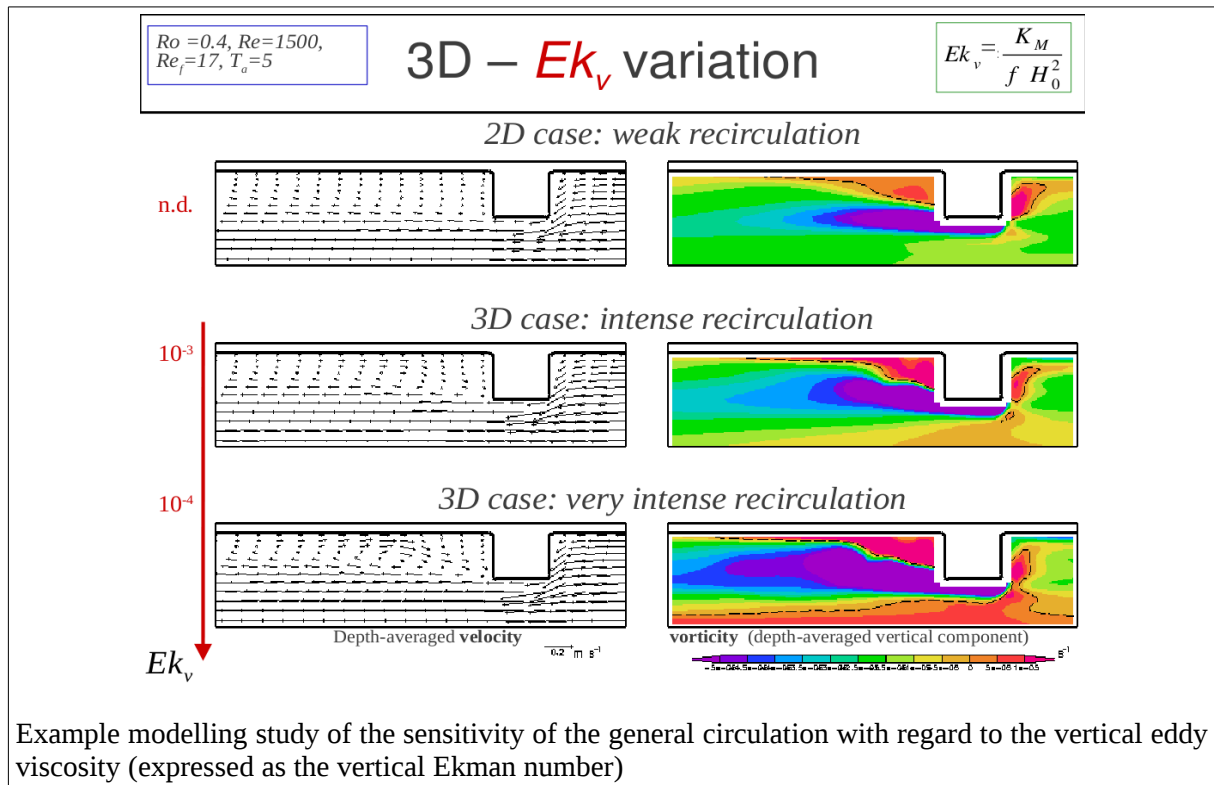


$$\tau_{(x,y)z} = \vec{B} = C_d \vec{U}_1 |\vec{U}_1| \quad (1.26)$$



While it is often possible to simplify the relationship between the stresses at the boundaries and within the fluid and the flow velocity without incurring too great of an error, it should be noted that the presence of the bottom and surface layers cannot be neglected altogether if we wish to obtain a realistic distribution of the internal flow velocities. For example, if we were to impose a no-slip condition at the solid borders and a constant eddy viscosity in the interior of a viscous fluid flow, one would observe the same difference between the calculated and observed profiles as between the Poiseuille distribution for laminar flow and the turbulent velocity profile in a pipe.





2.8 Linearising the equations

When Eq. (1.27) is inserted into the horizontal components of the equation of motion, the latter takes on the form of the Navier-Stokes equations, which – in their non-linear form – cannot be solved analytically. They can be simplified by neglecting the internal stresses which are assumed to be distributed in a simplified fashion or by neglecting the advection terms, a transformation known as “linearisation”.

In general, we can assume that the advection of momentum in geophysical problems can be neglected if the ratio between the non-linear terms and the Coriolis force (i.e., the Rossby number) is small:

$$\frac{u \frac{\partial u}{\partial x}}{f v} \simeq \frac{U}{f L} = Ro \ll 1 \tag{1.30}$$

where U and L are appropriate velocity and length scales, respectively. This criterion focuses on balancing the momentum across the flow (cross-section).

In contrast, if one wants to create a balance along the flow direction, since there is no Coriolis term the comparison is made between the non-linear terms and the wind/bottom friction terms. The non-linear terms are negligible if

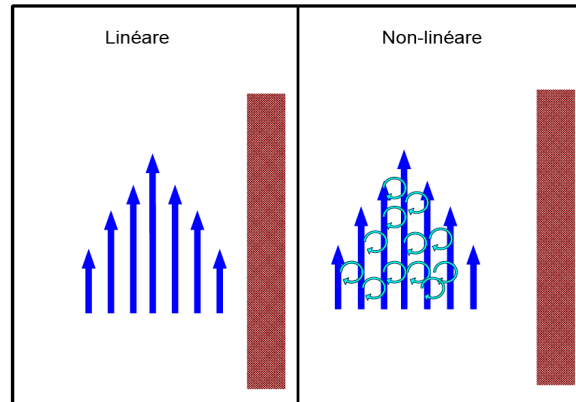
$$\frac{u \frac{\partial v}{\partial x}}{\frac{u_*^2}{h}} \simeq \frac{U^2}{u_*^2} \cdot \frac{h}{L} \ll 1 \tag{1.31}$$

where h is the thickness of the layer across which the stress ρu_*^2 is distributed.

In coastal waters, neither criterion (1.30) nor (1.31) are typically met, as Ro in (1.30) and the ratio in (1.31) are usually of the order of 1. This means that the advection of momentum could be important. However, if we examine what the actual effects of the advection of momentum really are, we find that they consist of readily understandable and predictable modifications of the structures (patterns) created and governed by the linear terms (Coriolis, local accelerations, wind and bottom friction). The

reason for this behaviour is that the non-linear terms have the form of a divergence and therefore disappear near the boundaries. Their role is thus to transfer the momentum from one part of the basin to another, without modifying the magnitude of momentum.

If we consider the example of a coastal jet, i.e., a strong and fairly narrow wind-driven current along the coast, balancing the linear terms implies that it should stay near the coast, but if we also consider the non-linear terms we see that under certain conditions the advection of momentum would move this current away from the coast toward the open sea, but without modifying any of its basic characteristics such as its horizontal extent or strength.



Clearly, this effect is very important and must be understood, but it is also true that by using just the linear terms we can already understand a significant amount such as the spatial and temporal scale, oscillation frequencies, or the number of waves that contribute to an oscillatory movement.

In summary, the purpose of using a linear theory is to provide theoretical models that are simple enough to highlight some important physical relationships in otherwise overly complicated problems. The limitations of linear theory become particularly apparent in stratified fluids with large vertical and horizontal displacements of fluid parcels, as generated by wind or other forcings in a narrow coastal strip. The effects of these displacements are not only included in the momentum transport terms but also in the first order variations of the distribution of pressure caused by the distortions of the density field. As we have already seen, a water parcel tends to keep its temperature and salinity for periods of about one day, and a rapid vertical displacement yields a similar increase in elevation as a rapid change in dynamic height η_d Eq. (1.12). If these changes in elevation are confined to a narrow coastal strip, this creates significant pressure gradients. Nevertheless, linear theory, although assuming only small vertical displacements, can still be useful to understand the initial phase of these types of dynamics.

2.8 Shallow water equations

Previously, we saw that the evolution of the mean horizontal velocity (in the sense of turbulence) of a geophysical fluid parcel is described by the Navier-Stokes equations:

$$\begin{aligned} \frac{\partial u}{\partial t} + u \frac{\partial u}{\partial x} + v \frac{\partial u}{\partial y} + w \frac{\partial u}{\partial z} &= -\frac{1}{\rho_o} \frac{\partial P}{\partial x} + f v - \frac{\overline{\partial u' u'}}{\partial x} - \frac{\overline{\partial u' v'}}{\partial y} - \frac{\overline{\partial u' w'}}{\partial z} \\ \frac{\partial v}{\partial t} + u \frac{\partial v}{\partial x} + v \frac{\partial v}{\partial y} + w \frac{\partial v}{\partial z} &= -\frac{1}{\rho_o} \frac{\partial P}{\partial y} - f u - \frac{\overline{\partial v' u'}}{\partial x} - \frac{\overline{\partial v' v'}}{\partial y} - \frac{\overline{\partial v' w'}}{\partial z} \end{aligned}$$

$u, v,$ and w are the horizontal and vertical non-turbulent velocity components or “means”;

$u', v',$ and w' are the turbulent velocity components;

f is the Coriolis parameter;

P is the pressure;

ρ_o is the reference density of sea water in the Boussinesq sense.

The first term corresponds to the local variations in velocity over time. The second to fourth terms represent horizontal advection along the three axes, and the fifth term is the pressure gradient. The sixth term is the Coriolis term that accounts for the influence of the Earth’s rotation; if the flow has a sufficiently small length scale, the Earth’s surface can be approximated by its tangent plane and we can consider the Coriolis term i) constant: f -plane, $f = f_o$, e.g., for coastal dynamics or ii) varying

linearly along a meridian: approximation of β -plane, $f = f_o + \beta y$, e.g., for regional and large-scale dynamics.

The last three terms account for turbulence. In what is known as “Newtonian closure”, we can, similarly to molecular viscosity, introduce coefficients of turbulence eddy viscosity and replace the means of the products between the turbulence velocities with the mean flow velocity:

$$\begin{aligned} \overline{u'u'} &= -A_x \frac{\partial u}{\partial x} ; & \overline{u'v'} &= -A_y \frac{\partial u}{\partial y} ; & \overline{u'w'} &= -A_z \frac{\partial u}{\partial z} ; \\ \overline{v'u'} &= -A_x \frac{\partial v}{\partial x} ; & \overline{v'v'} &= -A_y \frac{\partial v}{\partial y} ; & \overline{v'w'} &= -A_z \frac{\partial v}{\partial z} . \end{aligned}$$

For typical scales of oceanic flows, the equation for the vertical velocity component reduces to the hydrostatics equation which reflects the balance between pressure and gravitational forces. It yields the pressure:

$$P(z) = P_a + g \int_z^\eta \rho \cdot dz$$

where P_a is the atmospheric pressure, g is gravitational acceleration, and η the surface elevation with respect to the mean. $z = \eta(x, y, t)$ thus represents the free surface of the ocean while $z = -h(x, y)$ marks the bottom. ρ is the density. Using Boussinesq's approximation of $\rho \equiv \rho_o + \rho'(x, y, z, t)$ with $\rho' \ll \rho_o$, the horizontal derivatives become

$$\begin{aligned} \frac{1}{\rho_o} \frac{\partial P}{\partial x} &= \frac{1}{\rho_o} \frac{\partial P_a}{\partial x} + g \frac{\partial \eta}{\partial x} + \frac{g}{\rho_o} \int_z^\eta \frac{\partial \rho'}{\partial x} dz \\ \frac{1}{\rho_o} \frac{\partial P}{\partial y} &= \frac{1}{\rho_o} \frac{\partial P_a}{\partial y} + g \frac{\partial \eta}{\partial y} + \frac{g}{\rho_o} \int_z^\eta \frac{\partial \rho'}{\partial y} dz \end{aligned}$$

The second and third term on the right-hand-side are the barotropic and baroclinic contributions to the pressure gradient, respectively.

If we neglect the baroclinic and atmospheric pressure contributions, the horizontal gradient can be written as:

$$\nabla_H P = \rho_o g \nabla_H \eta$$

This equation states that the forces acting on the fluid are purely horizontal, which allows us to assume that the horizontal velocity components are independent of z . This causes the fourth terms in the Navier-Stokes equations to vanish while the turbulence eddy viscosity term is replaced by the boundary conditions, i.e., wind forcing at the surface $\vec{F} \equiv (F_x, F_y)$ and frictional forcing at the bottom $\vec{B} \equiv (B_x, B_y)$.

While the wind forcing (F_x, F_y) represents an external forcing, the bottom friction terms can be rewritten using the quadratic law

$$B_x = C_d u (u^2 + v^2)^{1/2}, \quad B_y = C_d v (u^2 + v^2)^{1/2} \quad (z = -H)$$

While the velocities at $z = -H$ are the velocities above the bottom layer, in calculations they are often taken as extrapolated velocities assuming a constant eddy viscosity in the interior layers with a drag coefficient adapted to this velocity.

The equations of motion become

$$\frac{\partial u}{\partial t} + u \frac{\partial u}{\partial x} + v \frac{\partial u}{\partial y} = -g \frac{\partial \eta}{\partial x} + f v + A_h \left[\frac{\partial^2 u}{\partial x^2} + \frac{\partial^2 u}{\partial y^2} \right] + F_x + B_x \quad (1)$$

$$\frac{\partial v}{\partial t} + u \frac{\partial v}{\partial x} + v \frac{\partial v}{\partial y} = -g \frac{\partial \eta}{\partial y} - f u + A_h \left[\frac{\partial^2 v}{\partial x^2} + \frac{\partial^2 v}{\partial y^2} \right] + F_y + B_y \quad (2)$$

We thus have two equations for three unknowns (the two velocity components and the surface elevation). To close the system, we need to add the continuity equation rewritten as a function of the same three unknowns.

We start with the continuity equation for an incompressible fluid:

$$\nabla \cdot \vec{u} = \frac{\partial w}{\partial z} + \left(\frac{\partial u}{\partial x} + \frac{\partial v}{\partial y} \right) = 0$$

By integrating from the sea bed to the free surface and considering that the velocities and their derivatives are independent of z we obtain:

$$w_{z=\eta} - w_{z=-h} + (h+\eta) \left(\frac{\partial u}{\partial x} + \frac{\partial v}{\partial y} \right) = 0 \quad .$$

At the surface we have

$$w_{z=\eta} = \frac{d\eta}{dt} = \frac{\partial \eta}{\partial t} + u \frac{\partial \eta}{\partial x} + v \frac{\partial \eta}{\partial y} \quad .$$

At the bottom, considering that the bathymetry does not change with time, we obtain

$$w_{z=-h} = -\frac{dh}{dt} = -u \frac{\partial h}{\partial x} - v \frac{\partial h}{\partial y} \quad .$$

Through substitution we obtain:

$$\frac{\partial \eta}{\partial t} + \frac{\partial(Hu)}{\partial x} + \frac{\partial(Hv)}{\partial y} = 0 \quad \text{with } H = h + \eta \quad (3)$$

The ensemble of Eqs. (1-3) constitutes the so-called shallow water (SW) equations. As for the hydrostatic approximation, these equations are valid as long as the water depth is shallow in comparison to the relevant horizontal scales.

The SW equations are useful to study, among other things, long gravity or gyroscopic waves. For this we need to consider the linearised version of the equations, without eddy viscosity, and assume that $\eta \ll h$. Furthermore, if $h = const$, $f = 0$, and if any motion depends on x only (1D flow), the equations become:

$$\begin{array}{lll} \frac{\partial u}{\partial t} = -g \frac{\partial \eta}{\partial x} & \text{if we differentiate} & \frac{\partial}{\partial x} \frac{\partial u}{\partial t} = -g \frac{\partial^2 \eta}{\partial x^2} \\ & \text{by} & \\ & \frac{\partial}{\partial x} & \text{we obtain } \frac{\partial^2 \eta}{\partial t^2} - gh \frac{\partial^2 \eta}{\partial x^2} = 0 \end{array}$$

$$\begin{array}{lll} \frac{\partial \eta}{\partial t} + h \frac{\partial u}{\partial x} = 0 & & \frac{\partial^2 \eta}{\partial t^2} + h \frac{\partial}{\partial t} \frac{\partial u}{\partial x} = 0 \end{array}$$

This last equation is a wave equation with the solution $\eta = F(x - ct)$ with $c = \sqrt{gh}$.

The above set of equations provides a fairly accurate description of the dynamics in a well-mixed coastal ocean. The SW equations are sometimes also referred to as Saint-Venant equations.

Local and global applications

When applying the above equations, the problem of predicting the response of a coastal ocean under

some forcing can be conveniently divided into a local and global problem.

Once an appropriate approximation has been chosen for A_z , Eqs. (1.32) and (1.33) can be solved for $u(z)$, $v(z)$ using the sea surface slope (gradient of η) as external input (forcing). The resulting velocity distribution can be obtained from a local calculation of the pressure at each (x,y) .

We then need to calculate the distribution of the pressure, or rather the elevation, on the basin scale, i.e., "globally". This can be done by vertically integrating the equations or transport equations. Integration on the vertical implies that we define the horizontal transport from the velocity components

$$U = \int_{-H}^0 u dz, \quad V = \int_{-H}^0 v dz \quad (1.34)$$

yields

$$\begin{aligned} \frac{\partial U}{\partial t} - fV &= -gH \frac{\partial \eta}{\partial x} + F_x - B_x \\ \frac{\partial V}{\partial t} + fU &= -gH \frac{\partial \eta}{\partial y} + F_y - B_y \\ \frac{\partial U}{\partial x} + \frac{\partial V}{\partial y} &= -\frac{\partial \eta}{\partial t} \end{aligned} \quad (1.35)$$

In Eqs. (1.34) and (1.35) small variations in surface elevation $\eta(x,y)$ have been neglected with respect to the depth $H(x,y)$. Surface friction (F_x, F_y) is accounted for as an external input. Bottom friction can be calculated from the velocity distributions obtained from the local calculations.

The above equations, called transport equations, constitute a closed ensemble of three equations for three unknowns U , V , and η which can be solved globally.

While the solution of the global problem is usually difficult, the problem can be simplified by neglecting bottom friction or by expressing it as another transport term

$$B_x = C_d U (U^2 + V^2)^{1/2}, \quad B_y = C_d V (U^2 + V^2)^{1/2}$$

which yields solutions to many interesting problems.

To solve the transport equations it is necessary to define the boundary conditions at the coast and at the open boundaries. At the coast, we have a closed boundary which means that the cross-boundary transport is zero while at the open boundaries the cross-boundary transport and changes in η need to be continuous.

Unfortunately, several problems arise when an open boundary is located between the coastal ocean and the deep ocean and a simultaneous solution of the two regions is not always possible.

2.9 Simple models

A small number of basic models have played an important role in advancing our understanding of atmospheric and oceanic dynamics as they have been able to elucidate some of the more complex dynamics in the coastal ocean. Below, we study three elementary models based on the shallow water equations which provide solutions to the local and global problems.

Geostrophic balance

If we consider the case in which (i) both wind and bottom friction are negligible, (ii) the fluid is homogeneous, and (iii) the flow stationary, then all derivatives in the transport equations vanish. While this case is rather unrealistic, it could represent a scenario where a current that has been generated by an earlier event and is now weakening very slowly. Without loss of generality, we can align the y axis with the main flow direction which means that $U = 0$.

The transport equations then become:

$$\begin{aligned}
 -fV &= -gH \frac{\partial \eta}{\partial x} \\
 0 &= -gH \frac{\partial \eta}{\partial y} \\
 \frac{\partial V}{\partial y} &= 0
 \end{aligned}
 \tag{1.42}$$

The first and third equations are only adequate if $\partial(H/f)/\partial y=0$, i.e., if the transport occurs along isobaths while the sea surface slope is perpendicular to the coast.

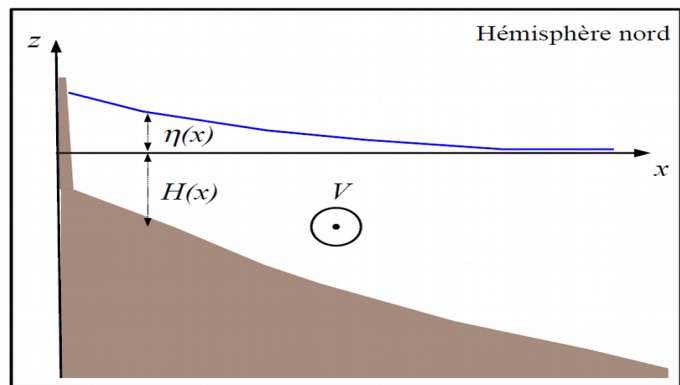
The balance of forces is not trivial except in the direction perpendicular to the coast along which the Coriolis force is balanced by the pressure gradient.

In the absence of any sea surface elevation and bottom friction, the solution to the local problem is simply

$$v = \frac{V}{H} = \frac{g}{f} \frac{\partial \eta}{\partial x} \quad \forall z, y$$

with $g \approx 10 \text{ m s}^{-2}$ and $f=10^{-4} \text{ s}^{-1}$ we have a gradient of just 10^{-5} (1 cm on 1 km) which gives a geostrophic flow velocity of 1 m s^{-1} .

This type of flow satisfies the “coastal constraint” condition for all x and is therefore valid if the coast line is parallel to the y -axis. It can be considered as a basic coastal flow.



Ekman drift

When considering the flow far from any boundaries we can assume $h = 0$ everywhere. Let us assume that the flow is forced by wind friction rF in the y direction and that the flow is stationary. We further assume that the water column is sufficiently deep so that bottom friction can be neglected (we will return to this later on).

The transport equations (1.35) then become

$$\begin{aligned}
 -fV &= 0 \\
 +fU &= F_y \\
 \frac{\partial U}{\partial x} + \frac{\partial V}{\partial y} &= 0
 \end{aligned}$$

with the following solutions

$$\begin{aligned}
 U &= \frac{F_y}{f} \\
 V &= 0
 \end{aligned}$$

This results in a transport to the right of the main flow (in the Northern hemisphere where f is positive) with a magnitude of F/f . For typical values of $F = 10^{-4} \text{ m}^2 \text{ s}^{-2}$ and $f = 10^{-4} \text{ s}^{-1}$ we obtain $U = 1 \text{ m}^2 \text{ s}^{-1}$ (equivalent to a current velocity of 0.1 m s^{-1} over a depth of 10 m). This transport is known as Ekman

transport and the movement that sets off this transport is called Ekman drift. The local problem has no trivial solution in this case. We use Eq. (1.27) to calculate the eddy viscosity and assume that K is constant below a surface layer of negligible thickness, and considering that the horizontal gradients are zero as per our assumption, then Eq. (1.32) becomes

$$-f v = A_z \frac{\partial^2 u}{\partial z^2}$$

$$f u = A_z \frac{\partial^2 v}{\partial z^2}$$

with boundary conditions

$$A_z \frac{du}{dz} = 0, \quad A_z \frac{dv}{dz} = F_y, \quad (z=0)$$

$$\frac{du}{dz} = \frac{dv}{dz} = 0, \quad (z \rightarrow -\infty)$$

The spatial scale is the Ekman depth

$$D = \sqrt{\frac{2 A_z}{f}} \tag{1.50}$$

and the solution can be written as

$$u = \frac{F_y}{f D} e^{z/D} \left(\cos \frac{z}{D} - \sin \frac{z}{D} \right)$$

$$v = \frac{F_y}{f D} e^{z/D} \left(\cos \frac{z}{D} + \sin \frac{z}{D} \right) \tag{1.51}$$

At a depth $-z \gg D$ velocities and turbulence stresses disappear and it becomes reasonable to neglect bottom friction for sufficiently deep water columns.

Empirically, we have already seen that for a turbulent Ekman layer the Ekman depth is

$$D \approx 0.1 \frac{u_*}{f} \tag{1.52}$$

and from Eq. (1.50) we get

$$K = \frac{u_*^2}{200 f} = \frac{u_* D}{20}$$

which has the same form as Eq. (1.28) and tells us that for a homogeneous Ekman layer the turbulent Reynolds number is about 20.

Eq. (1.52) also shows that the term $u_* f D$ from Eq. (1.51) is of the order of 10. Hence the velocity components at $z=0$, i.e., up to just below the surface layer, are $u = v = 10 u_*$ and these velocities are at a 45° angle with respect to the wind direction.

While the properties of the surface layer are not well known, we can apply a logarithmic profile of the form

$$\frac{v_s - v}{u_*} = \frac{1}{k} \ln \frac{|z|}{r} + 8.5$$

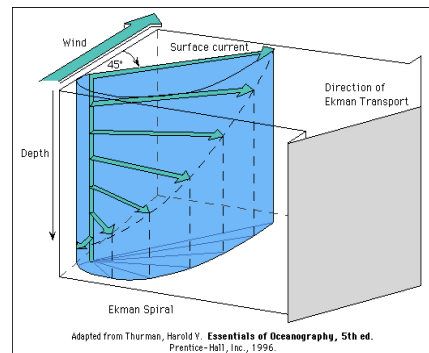
where k is von Karman's constant (≈ 0.4) and r the corresponding surface roughness. The latter can become rather large (of the order of 1 m for moderate wind speeds) such that the contribution of the logarithmic term for a depth of $-z = 1$ m becomes negligible. The velocity variation across the surface layer is thus about $8.5u^*$ between the free surface and the lower limit of the layer at $z = -r$.

The velocity distribution in a turbulent Ekman layer with the surface boundary layer is shown as a hodograph. The surface flow is at an angle of about 45° to the right of the wind direction and has a velocity of about $20u^*$, which, according to Eq. (1.23), represents about 3% of the wind speed.

For a typical value of $u^* = 0.01 \text{ m s}^{-1}$ which corresponds to a wind speed of $W = 7 \text{ m s}^{-1}$ and with $f = 10^{-4} \text{ s}^{-1}$ the Ekman depth, D , is 10 m.

The current velocity becomes negligible at a depth of about $z = -3D$ or 30 m. The water column is often sufficiently homogeneous for this depth to be realistic.

However, we should not forget that in this model the coast is supposedly absent. In fact, the Ekman spiral shown in the figure below is incompatible with the presence of a coast in any direction as there would always be a flow perpendicular to the coast at all depths. However, it is also possible to insert a thin lateral layer to resolve this problem.



[www-pord.ucsd.edu/~ltalley/sio210/Wind forcing/](http://www-pord.ucsd.edu/~ltalley/sio210/Wind_forcing/)

2.10 Inertial currents and oscillations

If we consider a flow far from the coast we can assume that the sea surface elevation is zero everywhere ($\eta = 0$). By assuming that both bottom and surface friction are negligible and that the flow has been generated by some previous event, the transport equations become

$$\begin{aligned}\frac{\partial U}{\partial t} - fV &= 0 \\ \frac{\partial V}{\partial t} + fU &= 0 \\ \frac{\partial U}{\partial x} + \frac{\partial V}{\partial y} &= 0\end{aligned}\tag{1.44}$$

This system represents a balance between local accelerations and the Coriolis force and has the following solution

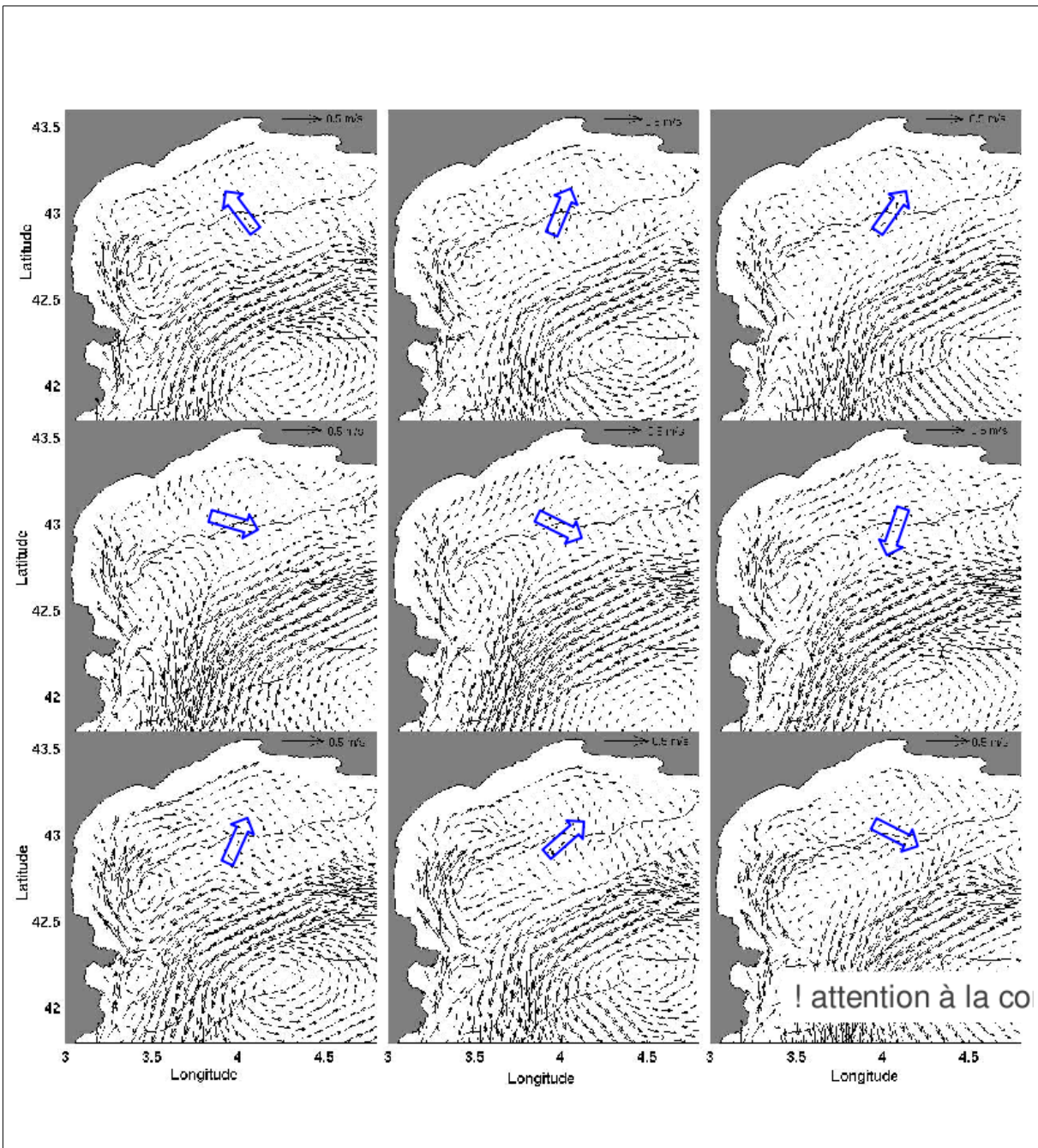
$$U = U_o \cos ft \quad V = -U_o \sin ft$$

where $U_o = \text{const}$. If the coordinate system is chosen such that $V = 0$ at $t = 0$ then the internal velocities simply are

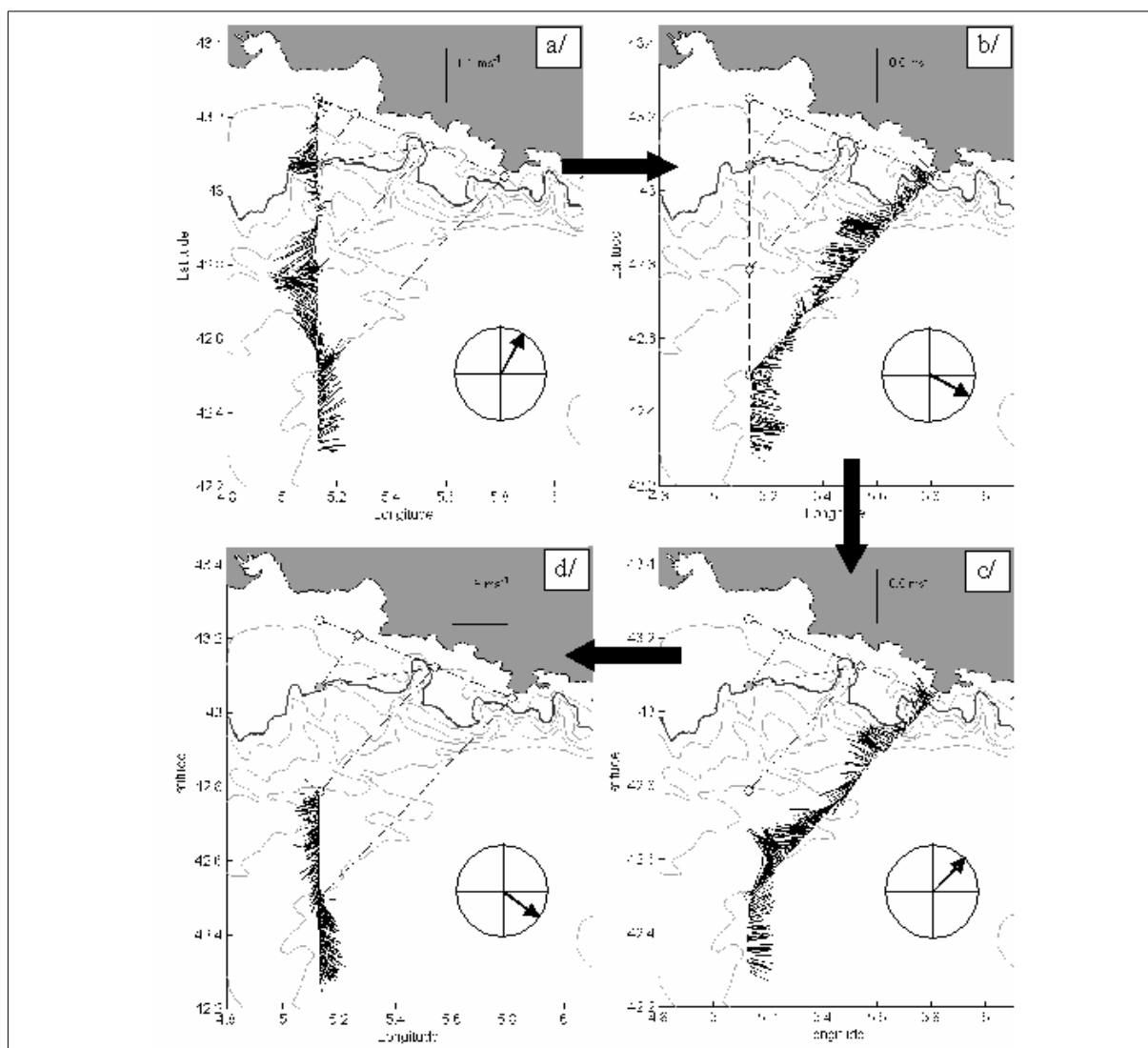
$$\begin{aligned}u &= \frac{U}{H} = u_o \cos ft, \\ v &= \frac{V}{H} = -u_o \sin ft\end{aligned}$$

The flow is periodic with a period of $T = 2\pi/f$ which is about 17 h at mid latitudes. The entire water mass oscillates in phase and the water particles travel along circular paths with a radius of u_o/f . For a velocity of $u_o = 1 \text{ m s}^{-1}$, and given that $f = 10^{-4} \text{ s}^{-1}$, we obtain a radius of 10 km.

These types of motions are called inertial oscillations. They are usually not observed near coasts although Eqs. (1.44) and the implied balance of forces can be observed in areas characterised by strong winds such as the Gulf of Lion.



Simulation of the flow velocity in the Gulf of Lion during the Moogli-2 campaign (June 1998) using the Symphonie model. The arrows represent the temporal evolution of the flow at 32 m every 3 hours. At the centre of the Gulf we can observe an inertial oscillation. (C. Dufau et A. Petrenko)



Currents measured by hull-mounted ADCP at 16 m depth in chronological order (following the bold arrows) on transects a/ 1-66b, b/ 66-6a et 6-7a, c/ 7-6a and 6-66a, and d/ 66-4a. The flow directions at Station 6 are shown in the circular inset at the bottom right of each panel.

| Station 6 | Date et heure | Direction des courants | $\Delta t = t_i - t_{i-1}$ en heure | $\Delta \theta_{obs} = \theta_i - \theta_{i-1}$ en degré | $\Delta \theta_{calc} = \theta_i - \theta_{i-1}$ en degré |
|------------------|-----------------|------------------------|-------------------------------------|--|---|
| sur 1-66b | 13 juin à 20h13 | 35° | XXXXXX | XXXXXX | XXXXXXX |
| sur 66-6a / 6-7a | 14 juin à 00h47 | 124° | 4,57h | 89° | 94° |
| sur 7-6a / 6-66a | 14 juin 15h15 | 49° | 14,47h | 285° | 298° |
| sur 66-4a | 14 juin 18h59 | 128° | 3,73h | 79° | 77° |

Tableau III.XX : pour chaque trajet de la campagne GOLTS juin 2002, au passage à la station 6, le tableau donne : la date du passage, la direction des courants mesurés, le laps de temps écoulé et la différence d'orientation des courants mesurés entre deux passages et la rotation que doit effectuer une oscillation d'inertie pendant le laps de temps mesuré.

(figure and table courtesy of J. Gatti).

(Lecture given by A.Petrenko)

Summary: Inertial oscillations (or waves), in a rotating reference frame, consist of a horizontal and circular motion of a particle only subject to the Coriolis force and moving frictionlessly on a gravitationally equipotential surface (locally, a horizontal plane) with a non-zero initial velocity. While undergoing one cycle of this oscillation, a water particle describes a circle, called an inertial circle, which it follows in a clockwise direction in the Northern hemisphere with a periodicity that is called the inertial period.

Bibliography

Chereskin T.K., M.D. Levine, A.J. Harding, L.A. Regier, *Observations of near-inertial waves in Acoustic Doppler Current Profiler measurements made in the Mixed Layer Dynamics Experiment*, J. Geophys. Res., 94 (C6) (1989), pp. 8135–8145

C. Millot, *The Gulf of Lion's hydrodynamics*, Cont. Shelf Res., 10 (9–11) (1990), pp. 885–894

Millot and Crepon, 1981, *Inertial oscillations on the Continental Shelf of the Gulf of Lions – Observations and Theory*, JPO vol 11, 5.

Petrenko A., C. Dufau and C. Estournel (2008), *Barotropic eastward currents in the western Gulf of Lion, north-western Mediterranean Sea, during stratified conditions*. J. Marine Syst., doi:10.1016/j.jmarsys.2008.03.004

Petrenko A., Y. Leredde, and P. Marsaleix (2005), *Circulation in a stratified and wind-forced Gulf of Lions, NW Mediterranean Sea: in-situ and modeling data*. Continental Shelf Res., 25, 5-27, doi:10.1016/j.csr.2004.09.004

Petrenko, A.A. (2003), *Circulation features in the Gulf of Lions, NW Mediterranean Sea; importance of inertial currents*, Oceanol. Acta, 26, pp. 323–338

Reminder from the L3 course (Ocean Dynamics. A. Doglioli et A. Petrenko ; and remember Section 2.9 of this course)

If a particle is not subjected to any external force, its acceleration in an inertial reference frame obeys Newton's 2nd law. The equations of motion can be simplified as follows:

$$\begin{aligned}\frac{du}{dt} &= fv \\ \frac{dv}{dt} &= -fu\end{aligned}$$

by solving for u and substitution we get

$$\begin{aligned}v &= \frac{1}{f} \frac{du}{dt} \\ \frac{1}{f} \frac{d^2u}{dt^2} &= -fu \quad \text{i.e.} \quad \frac{d^2u}{dt^2} + f^2u = 0\end{aligned}$$

The general solution of this second degree differential equation is:

$$\begin{aligned}u &= +V_o \cos(ft + \phi) \quad \text{and if we replace } u \text{ by this solution in the } v\text{-equation:} \\ v &= -V_o \sin(ft + \phi)\end{aligned}$$

where the velocity V_o and phase ϕ depend on the initial conditions.

For example, if we consider the case where the oscillations are triggered by Mistral events off the

Marseille coast, by positioning the axes as shown in the figure below, we can set the following initial conditions:

Initial flow velocity in the direction of the wind: $u_{t=0}=0$. Then

$$u_{t=0} = V_o \cos(\phi) = 0 \text{ et } \phi = \pi/2$$

Substituting this into the v -equation

$$v = -V_o \sin(ft + \pi/2) \text{ and thus}$$

$$v_{t=0} = -V_o \sin(\pi/2) = -V_o$$

The flow velocity depends on the wind speed. For example, for a wind speed of 80 km h^{-1} the surface velocity reaches approximately 50 cm s^{-1} .

See for example:

<http://www.dot.state.fl.us/rddesign/dr/Research/CE/Wind-Generated-Currents.pdf>

As $f = 2\Omega \sin \lambda$ [rad.s^{-1}] where λ is the latitude, we obtain for Marseilles with a latitude of about 43°N the approximate:

$$f \approx 2 \frac{2\pi}{24} \sin\left(\frac{\pi}{4}\right) \approx \frac{2\pi}{17} \text{ [rad.h}^{-1}\text{]}$$

i.e., a period of $T \approx 17$ [h]

NB: To calculate this value more precisely, use the length of a sidereal day of 23 h 56 min 4 s and the exact latitude of Marseilles of 43° instead of 45° ($\pi/4$ was used in the above equation) (this yields a more precise value for T of 17h33').

For a period of $T=16\text{h}$ (have fun checking which latitude this corresponds to) the calculations become very simple and through substitution in the u - and v -equations we obtain

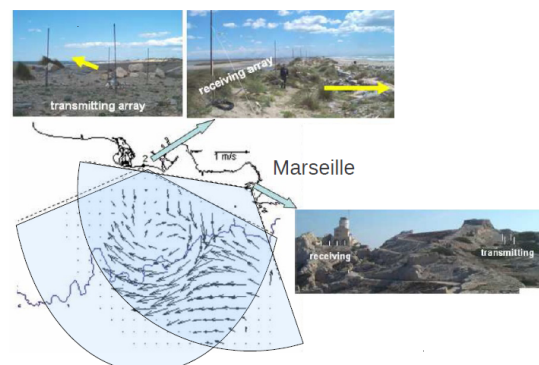
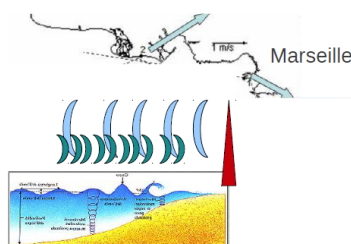
$$\vec{v}_{t=0} \equiv (0, -0.5) V_o, \quad \vec{v}_{t=4\text{h}} \equiv (-0.5, 0) V_o, \quad \vec{v}_{t=8\text{h}} \equiv (0, +0.5) V_o \text{ and}$$

$$\vec{v}_{t=12\text{h}} \equiv (+0.5, 0) V_o$$

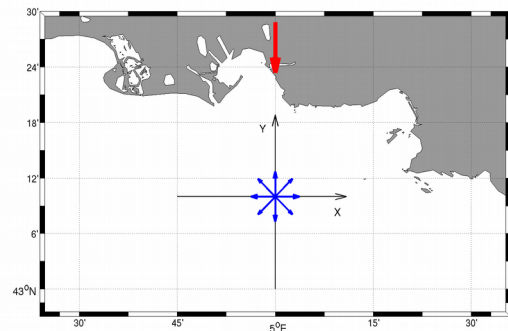
Measurements carried out using a coastal radar by some colleagues from the MIO (formerly LSSET-Laboratoire des Sondages Électromagnétiques) at Toulon have corroborated this analytical model.

Mesure du courant de surface par radar cotier à haute resolution

Le radar est un système qui utilise les ondes radio pour détecter et déterminer la distance et/ou la vitesse d'objets tels que les avions, bateaux, ou encore la pluie. Un émetteur envoie des ondes radio, qui sont réfléchies par la cible et détectées par un récepteur, souvent situé au même endroit que l'émetteur. La position est estimée grâce au temps de retour du signal et la vitesse est mesurée à partir du changement de fréquence du signal par effet Doppler.



Note: these radar systems are currently installed at the Toulon and Nice coasts.



In red the wind vector, in blue the inertial current vectors whose direction varies over time (Matlab script available in the L3 course (see A. Doglioli's web site).

By integrating again with $u = \frac{dx}{dt}$ and $v = \frac{dy}{dt}$ we obtain the trajectory:

$$x = x_o + \frac{V_o}{f} \sin(ft + \phi)$$

$$y = y_o - \frac{V_o}{f} \cos(ft + \phi)$$

$$(x - x_o)^2 + (y - y_o)^2 = \left(\frac{V_o}{f}\right)^2$$

This last set of equations shows that the trajectory of a fluid particle “trapped” in an inertial oscillation is indeed a circle centred at (x_o, y_o) with radius $|V_o|/f$.

Since the Coriolis force acts to the right of any movement in the Northern Hemisphere, the particle travels the circle in a clockwise direction. This is reversed in the Southern Hemisphere.

The time it takes a particle to complete one full circle is the time T which depends only on the inertial frequency f .

As the Coriolis force is zero at the equator, there are no inertial motions at those low latitudes.

In this circular movement, the centrifugal force is compensated by the Coriolis force (remember TD1 Course on Oceanic Dynamics; Doglioli and Petrenko):

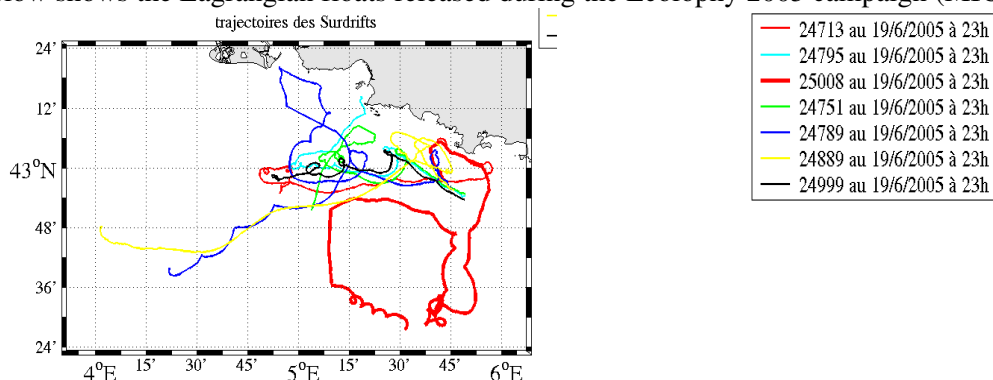
$$m \omega^2 r = m \left(\frac{u^2}{r}\right) = mfu$$

$$f = \frac{u}{r}$$

Therefore $T = \frac{2\pi}{f} = \frac{2\pi r}{u}$

At any given latitude, there is a fixed relationship between the velocity at which a fluid particle travels along the inertial circle and the radius of the circle. The larger the absolute value of the velocity (which depends on the forcing) the greater the radius. However, the period of rotation (inertial period) does not change.

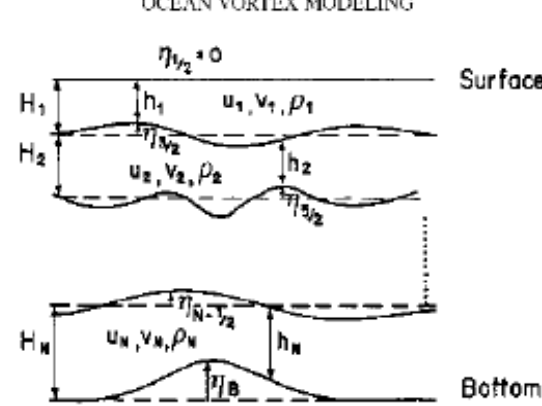
It is difficult to observe perfect circles in nature as friction is always present, but they are often observed with Lagrangian floats as circular trajectories that gradually vanish with time. The figure below shows the Lagrangian floats released during the Ecology 2005 campaign (MIO/Ifremer)



Inertial currents are generated by local variations in atmospheric forcing. They are most commonly observed during periods of vertical stratification which creates a two-layered water column. The inertial current in the lower layer is then offset by half an inertial period (phase shift of π).

Theory

(taken from Millot and Crepon, 1981, Inertial oscillations on the Continental Shelf of the Gulf of Lions – Observations and Theory, JPO vol 11, 5)

| | |
|---|---|
| <p>The density variation of the ocean is simplified by using a two-layer fluid. This is a crude, but realistic assumption corresponding to retention of only the first internal mode, which is the most important for small motions (Lightill, 1969; Gill and Clarke, 1974). Because of the small depths of the Gulf of Lions we will also investigate the effects of bottom friction on the motions.</p> <p>Hydrostatic and Boussinesq assumptions are employed and we deal with the vertically averaged equations of hydrodynamics in each layer. Since we consider small perturbations from rest, the equations are linearized.</p> | <p style="text-align: center;">OCEAN VORTEX MODELING</p>  <p style="text-align: center;">Figure 2a. Vertical cross-section of a N-layer shallow-water model.</p> |
| <p><i>In the upper fluid</i></p> $\frac{\partial}{\partial t} \mathbf{u}_1 + f\mathbf{z} \times \mathbf{u}_1 = -g\nabla\zeta_1 + \frac{1}{\rho_1 h_1} (\boldsymbol{\tau} - \boldsymbol{\tau}_I) \quad (4)$ $\frac{\partial}{\partial t} (\zeta_1 - \zeta_2) + \nabla h_1 \mathbf{u}_1 = 0. \quad (4)$ <p><i>In the lower fluid</i></p> $\frac{\partial}{\partial t} \mathbf{u}_2 + f\mathbf{z} \times \mathbf{u}_2 = -g\epsilon\nabla\zeta_2 - g(1 - \epsilon)\nabla\zeta_1 + \frac{1}{\rho_2 h_2} (\boldsymbol{\tau}_I - \boldsymbol{\tau}_b), \quad (4)$ $\frac{\partial}{\partial t} \zeta_2 + \nabla h_2 \mathbf{u}_2 = 0. \quad (4)$ | <p>The terms are defined as follows:</p> <ul style="list-style-type: none"> ζ_1 (ζ_2) elevation at sea surface (interface) from rest \mathbf{u}_1 (\mathbf{u}_2) averaged velocity in the upper fluid (lower fluid) f Coriolis parameter g acceleration of the gravity ϵ fractional change in density $[(\rho_2 - \rho_1)/\rho_2]$ ∇ two-dimensional operator $\partial/\partial x, \partial/\partial y$ \mathbf{z} unit vector along the vertical axis, positive upward h_1 (h_2) thickness of the upper layer (lower layer) at rest $\boldsymbol{\tau}$ stress at the sea surface $\boldsymbol{\tau}_I$ stress at the interface $\boldsymbol{\tau}_b$ bottom stress. |

See Section 6 (Carton 2005) of this course for the shallow water (SW) equations in a multi-layered system (Figure 2a below). Here, we will only consider 2 layers.

See Section 2.8 (SW equations) for the notation used in the equation of conservation of mass.

Given the spatio-temporal scales of the process, we can assume that both f and the total depth $H = h_1 + h_2$ are constant.

Thompson and O'Brien (1973) showed that the stress at the interface (τ_I) is about one order of magnitude smaller than τ_b and τ . Hence any coupling between the two layers is due to pressure forces. The bottom stress is considered proportional to the flow velocity:

$$\tau_b = \rho_2 h_2 \nu u_2$$

where ν is an attenuation coefficients ($[t^{-1}]$).

How to resolve the problem

The study is carried out along a rectilinear dimension $x = 0$ (using the typical orientation of the coordinate axes with x being positive towards the east and y positive towards the north) with a transient wind (i.e., VARIABLE). We assume that the solution will be independent of y (the derivative with respect to y is zero).

By performing a Laplace transform of the elevation (see Section 4.3 for a summary of Laplace and the Laplace transform method) with respect to time, the velocities and stress tensor become:

$$Z_i(p, x) = \int_0^\infty e^{-pt} \zeta_i(t, x) dt = \mathcal{L}(\zeta_i),$$

$$U_i(p, x) = \int_0^\infty e^{-pt} \mathbf{u}_i(t, x) dt = \mathcal{L}(\mathbf{u}_i),$$

$$\mathbf{T}(p, x) = \int_0^\infty e^{-pt} (\mathbf{x}\tau^x + \mathbf{y}\tau^y) dt = \mathcal{L}(\boldsymbol{\tau}).$$

Based on the SW equations (4.1) and (4.3), we can determine U_i from Z_i . If we then substitute U_i in the derivatives of equation of conservation of mass (4.2 et 4.4) we obtain:

$$\begin{aligned} & \frac{\partial^2}{\partial x^2} Z_1 - (p^2 + f^2)(Z_1 - Z_2) \frac{1}{gh_1} \\ &= \frac{1}{\rho_1 g h_1} \left(\nabla \mathbf{T} + \mathbf{z} \frac{f}{p} \nabla \times \mathbf{T} \right) \\ & \times (p + \nu) \frac{\partial^2}{\partial x^2} [(1 - \epsilon)Z_1 + \epsilon Z_2] \\ & - p[(p + \nu)^2 + f^2] Z_2 \frac{1}{gh_2} = 0. \end{aligned} \quad (4.6)$$

Then:

If $\boldsymbol{\tau}$ does not depend on x , and taking into account the radiation condition (the motions must vanish as x tends to infinity), the solution of (4.6) is

$$\left. \begin{aligned} Z_1 &= A_1 e^{-\alpha_1 x} + A_2 e^{-\alpha_2 x} \\ Z_2 &= B_1 e^{-\alpha_1 x} + B_2 e^{-\alpha_2 x} \end{aligned} \right\}, \quad (4.7)$$

where

$$B_i = \left(1 - \alpha_i^2 \frac{gh_1}{p^2 + f^2} \right) A_i,$$

The solution of the homogeneous differential equation associated with (4.6) is of the form

$$Z = A e^{\pm \alpha_i x},$$

where α_i is a positive eigenvalue of Eq. (4.6).

$$\begin{aligned} A_i &= (-1)^i \frac{1}{\rho_1 (gh_1)^2 \epsilon} (fT^y + pT^x) \\ & \times \frac{p^2 + f^2 - \alpha_{3-i}^2 g \epsilon h_1}{(\alpha_1^2 - \alpha_2^2) p \alpha_i}. \end{aligned}$$

Here A_i does not depend on x ; it is determined by the boundary condition $\mathbf{u}_i(t, 0) = 0$.

1) Simplification – Case where the attenuation coefficient, ν , is zero (= no bottom stress)

This scenario has been studied many times (see O'Brien et al, 1977).

The Eigenvalue solutions for α_i are as follows:

$$\alpha_1^2 = \frac{p^2 + f^2}{c_1^2} \quad \text{and} \quad \alpha_2^2 = \frac{p^2 + f^2}{c_2^2}$$

with $c_1 = (gH)^{1/2}$ the long barotropic wave velocity

et $c_2 = \left(\frac{g \epsilon h_1 h_2}{H} \right)^{1/2}$ the long baroclinic wave velocity

with r_i the associated deformation radii $r_i = \frac{c_i}{f}$

Generally, we have $c_1 \gg c_2$ (e.g., in the Gulf of Lion, $\frac{c_2}{c_1} \approx 2.10^{-2}$) and $r_1 \gg r_2$

We typically distinguish between two cases:

1a – case where the wind blows perpendicular to the coast

1b – case where the wind blows parallel to the coast

For case 1a we have $\tau = \tau_0 Y(t)x$ with $Y(t)=1$ for $t \geq 0$ and $Y(t)=0$ for $t < 0$

We find an upwelling near the coast in the elevation term (see the paper for more details) and obtain the following velocities for the two-layer system when $0 < x < r_2 \leq r_1 \wedge ft > 2$:

$$\left. \begin{aligned} \mathbf{u}_1 &= \frac{\tau_0}{\rho_1 f H} \frac{h_2}{h_1} \left\{ (e^{-x/r_2} - 1)\mathbf{y} + (x/r_2) \right. \\ &\quad \times (ft)^{-1/2} (2/\pi)^{1/2} [\cos(ft - \pi/4)\mathbf{x} \\ &\quad \left. - \sin(ft - \pi/4)\mathbf{y}] \right\} \\ \mathbf{u}_2 &= -\frac{h_1}{h_2} \mathbf{u}_1 \end{aligned} \right\} \quad (4.16)$$

The spin-up time of (4.16) is $T = 2f^{-1}$. The inertial oscillations are polarized clockwise. The currents are baroclinic. The mean currents and the inertial oscillations in the upper and the lower layers have opposite phases, in agreement with the observations of Section 3.

For the case 1b we have $\tau = \tau_0 Y(t)y$ with $Y(t)=1$ for $t \geq 0$ and $Y(t)=0$ for $t < 0$

We again find an upwelling near the coast in the elevation term and when $0 < x < r_2 \leq r_1$ and $ft > 2$ we find the following velocities for the two layers:

$$\left. \begin{aligned} \mathbf{u}_1 &= \frac{\tau_0}{\rho_1 H f} \frac{h_2}{h_1} \left\{ \left(\frac{h_1}{h_2} + e^{-x/r_2} \right) fty \right. \\ &\quad + (1 - e^{-x/r_2})\mathbf{x} + (x/r_2)(ft)^{-1/2} \\ &\quad \times (2/\pi)^{1/2} [\sin(ft - \pi/4)\mathbf{x} \\ &\quad \left. + \cos(ft - \pi/4)\mathbf{y}] \right\} \\ \mathbf{u}_2 &= \frac{\tau_0}{\rho_1 H f} \left\{ (1 - e^{-x/r_2})(fty - \mathbf{x}) \right. \\ &\quad - (x/r_2)(ft)^{-1/2} (2/\pi)^{1/2} \\ &\quad \left. \times [\sin(ft - \pi/4)\mathbf{x} + \cos(ft - \pi/4)\mathbf{y}] \right\} \end{aligned} \right\} \quad (4.20)$$

where the spin-up time of (4.20) is $T = 2f^{-1}$.

There is thus a coastal jet flowing in the y-direction.

We should also note that this case is more complex than the previous one with

$$u_1 = A + B \quad \text{and} \quad u_2 = \frac{-h_1}{h_2} B$$

On the continental shelf, the behavior of currents is similar to that in (4.16). The inertial oscillations are polarized clockwise. The mean current perpendicular to the shore and the inertial oscillations are in opposite phases in the two layers, but the mean current parallel to the shore increases linearly with time and has a tendency to become semi-barotropic for distances off the shore of the order of r_2 . This agrees with the observations of currents off the Oregon shore where the wind is parallel to a straight coastline (Smith, 1974).

- 2) Case where the attenuation coefficient, ν , is non-zero; here, the solution is more complicated (see Appendix of the paper by Millot and Crepon, 1981, Inertial oscillations on the Continental Shelf of the Gulf of Lions – Observations and Theory, JPO vol 11, 5.)

Example observations

Phase shift of π below the thermocline visible in the vertical profiles.

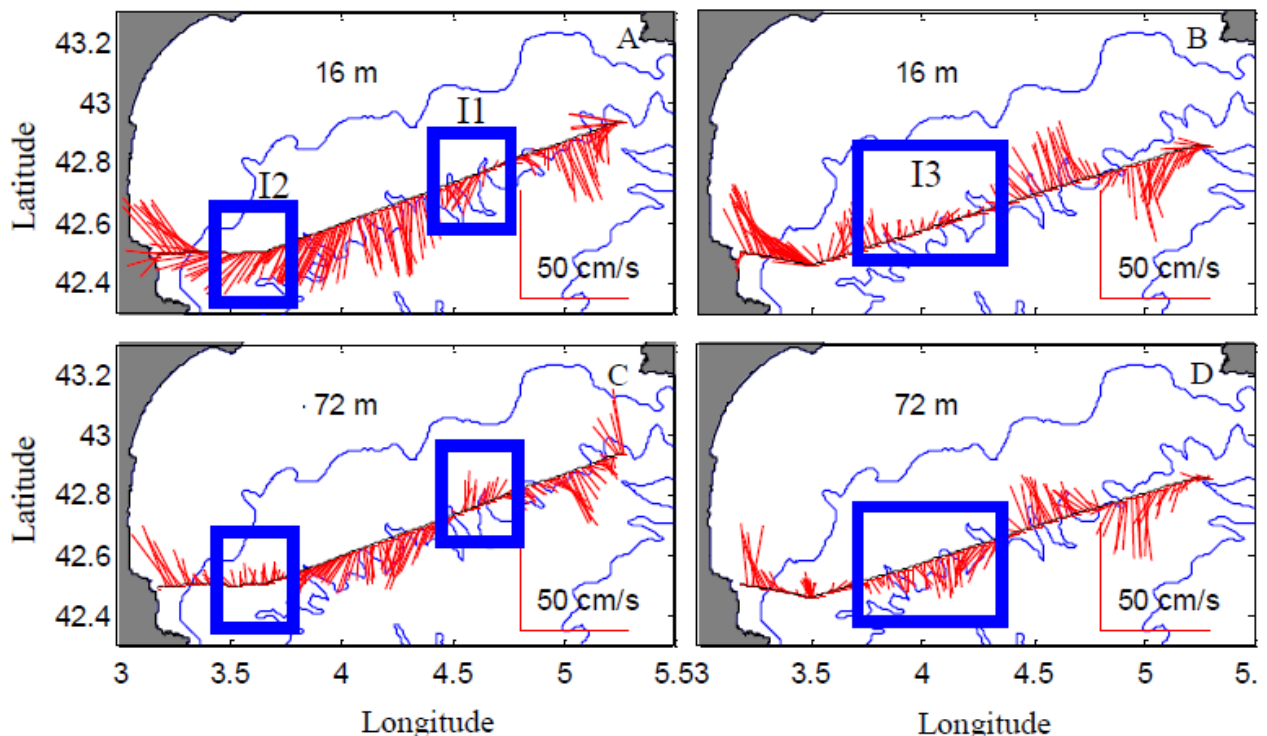


Fig. - Horizontal currents during MOOGLI 2 at A) 16 m and C) 72 m along transect TR1, and B) 16 m and D) 72 m along transect TR2. The boxes isolate the zones with inertial currents. At 16 m, they are labelled (I1, I2, and I3) in the chronological order currents were measured. Isobaths 100 m, 1000 m, and 2000 m are shown. (Fig 9 taken from **Petrenko A.** (2003), *Circulation features in the Gulf of Lions, NW Mediterranean Sea; importance of inertial currents.* Oceanol. Acta, 26, 323-338)

and associated text:

“The presence of inertial currents can also be verified on the spatial maps of TR1 and TR2 currents. For example, surface inertial currents are oriented southwestward at the end of TR1 (I2) and northward in the center of TR2 (I3), about 10 hours after (Figure 9 and Table 1). A full rotation of 360 degrees representing 17.5 hours, it is expected that the inertial currents rotate by 126 degrees (taking into account the geostrophic component of the NC) clockwise in 10 hours. The observed clockwise rotation is ~ 120 degrees, in nearly perfect agreement with the one calculated. The inertial currents compared are separated by 50 to 75 km. This shows that our horizontal coherence assumption was acceptable. No coherence is found between I1 and I2, nor between I1 and I3.”

Detecting intrusions

When the local currents already exist before a sudden wind event, they can continue to exist once the wind event occurs, resulting in a simple superposition of the two types of flow. For example, the Northern Current (in the Gulf of Lion) is considered a superposition of quasi-geostrophic and inertial currents.

Here are several possibilities to filter out inertial currents in order to study any pre-existing currents.

a) Modelling

In the output from numerical simulations the currents can be very well defined. In the above example, the currents are shown over an inertial period (Figure 9). The inertial currents are mainly visible to the south and east of the plateau. The part of the current that is on top of the plateau also tends to turn clockwise but slightly out of phase with the offshore inertial current (phase shift or merely a slight difference in period?).

To get around this problem, if we want to “remove” any influence from inertial currents, it should suffice to simply average any simulated velocities over the inertial period, or over a period close to the inertial period (e.g., daily, although this runs the risk of aliasing).

From Petrenko A., Y. Leredde, and P. Marsaleix (2005), *Circulation in a stratified and wind-forced Gulf of Lions, NW Mediterranean Sea: in-situ and modeling data*. Continental Shelf Res., 25, 5-27, doi:10.1016/j.csr.2004.09.004

“A strong inertial oscillation, with maximum amplitude of 60 cm/s, is clearly observed at the western side of the gulf due to the absence of the NC there. The model also exhibits this oscillation, and provides its temporal variations. The analysis, closely coupling in situ measurements and model results, provides information that would not have been obtained using either data separately.”

(see full article for further details)

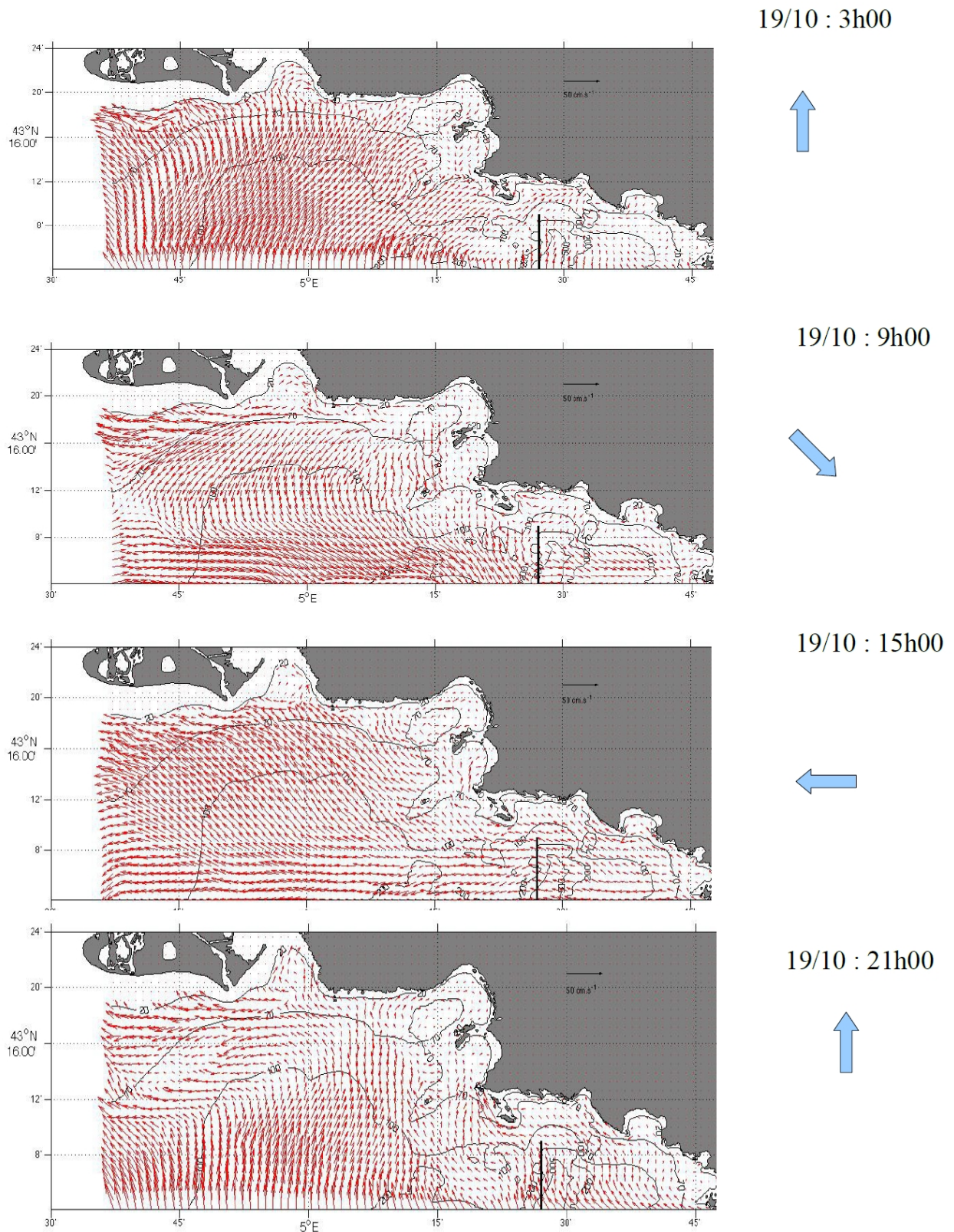


Fig.  Model run for the coast off Marseilles using MARS 3D – Rhoma (courtesy F. Desbiolles, student of I. Pairaud and A. Petrenko, 2010)

b) In situ *current measurements*

From Petrenko, A.A. (2003), *Circulation features in the Gulf of Lions, NW Mediterranean Sea; importance of inertial currents*, *Oceanol. Acta*, 26, pp. 323–338.

“The summer stratification allows the development, after strong wind variations, of inertial currents with their characteristic 2-layer baroclinic structure. In the surface layer, the speed of

the inertial oscillation can locally be as high as 200 % the NC speed. Otherwise the inertial current is about 2/3 the NC. Horizontal spatial coherence of inertial currents is found on scales up to 50 - 75 km. The contribution of these inertial currents to the measured circulation can not be neglected but is hard to estimate without the detailed and local analysis done in this article. The situation is different with time series data sets where high frequency motions such as inertial currents are classically filtered out. Spatial interpolation technique [Candela *et al.*, 1992] was tried unsuccessfully on the MOOGLI 1 ADCP data to isolate inertial currents (Durrieu de Madron, pers. comm.). The retrieval of the inertial component from the circulation is one of the main problems that oceanographers and modelers, working on the circulation in the Gulf of Lions and elsewhere, are presently dealing with.”

Depending on the type of available observational data, several methods can be used:

- 1 Plotting $u+iv$
- 2 Phase unwrapping
- 2 Overlaying the current with a sinusoid
- 3 Band-pass filtering

1) Plotting $u+iv$ - With u and v being the easterly and northerly current velocity components, we can create a plot of $u+iv$. If the curve turns around 0 during one inertial period, we are dealing with an inertial current. If the curve turns around a point (u_0, v_0) in an inertial period, then we are dealing with an inertial current superimposed on a fixed current of magnitude (u_0, v_0) .

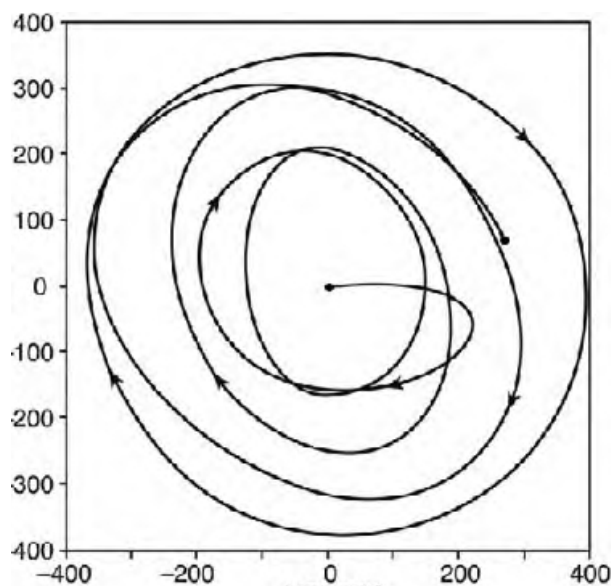


Fig. Inertial circles observed by a current meter in the main thermocline of the Atlantic Ocean at a depth of 500 m; 28°N, 54°W. Five inertial periods are shown. The inertial period at this latitude is 25.6 h. (Courtesy Carl Wunsch, MIT, via J. Marshall and A. Plumb “Atmosphere, Ocean and Climate Dynamics”, Elsevier book, 2008, Fig 6.16).

2) Phase unwrapping (Chereskin, JGR, 1989)

“The summer stratification allows the development, after strong wind variations, of inertial currents with their characteristic two-layer baroclinic structure. In the top layer, the speed of the inertial oscillation can locally be as high as 200% the NC speed. Otherwise in the surface layer, inertial current is about 2/3 the NC. Horizontal spatial coherence of inertial currents is found on scales up to 50–75 km.” taken from Petrenko (2003).

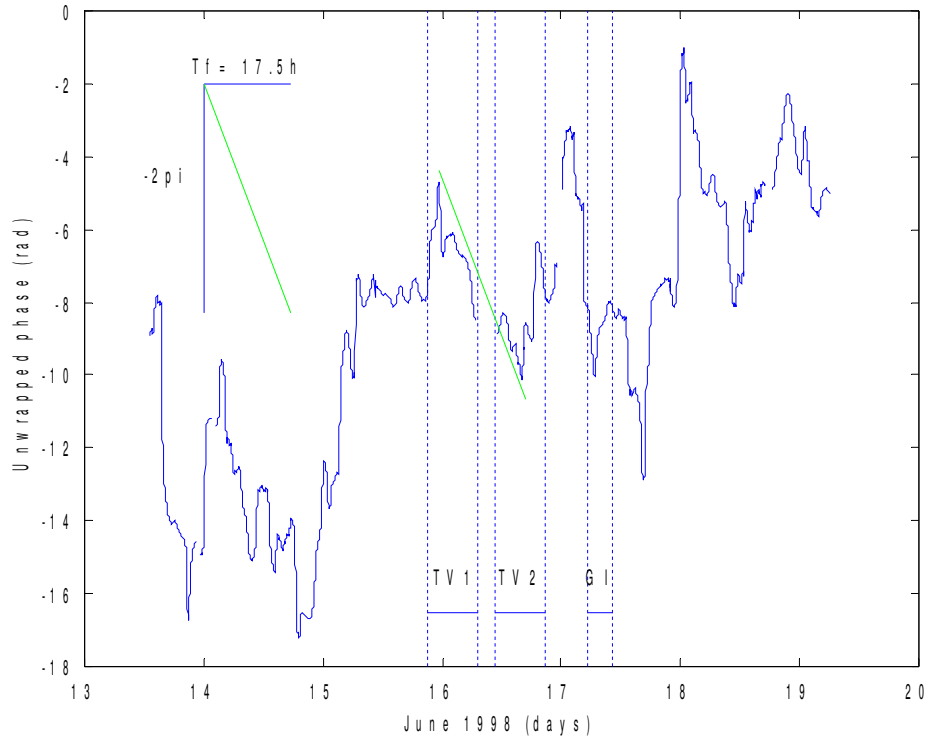
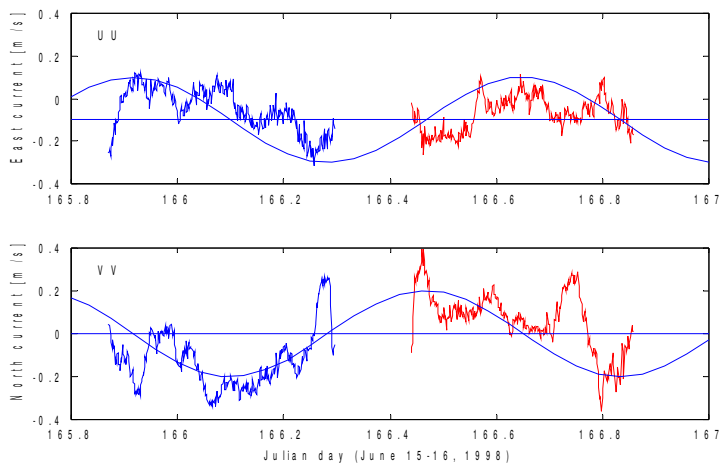


Fig. - Phase unwrapping of the horizontal current shear (16 m - 72 m) during June 13-19, 1998 (Moogli 2 cruise). The negative slope corresponding to the Coriolis factor is shown. Transects TR1, TR2, and GI were done during the periods indicated by the dotted vertical lines. (Fig. 8 from **Petrenko A.** (2003), *Circulation features in the Gulf of Lions, NW Mediterranean Sea; importance of inertial currents.* Oceanol. Acta, 26, 323-338)

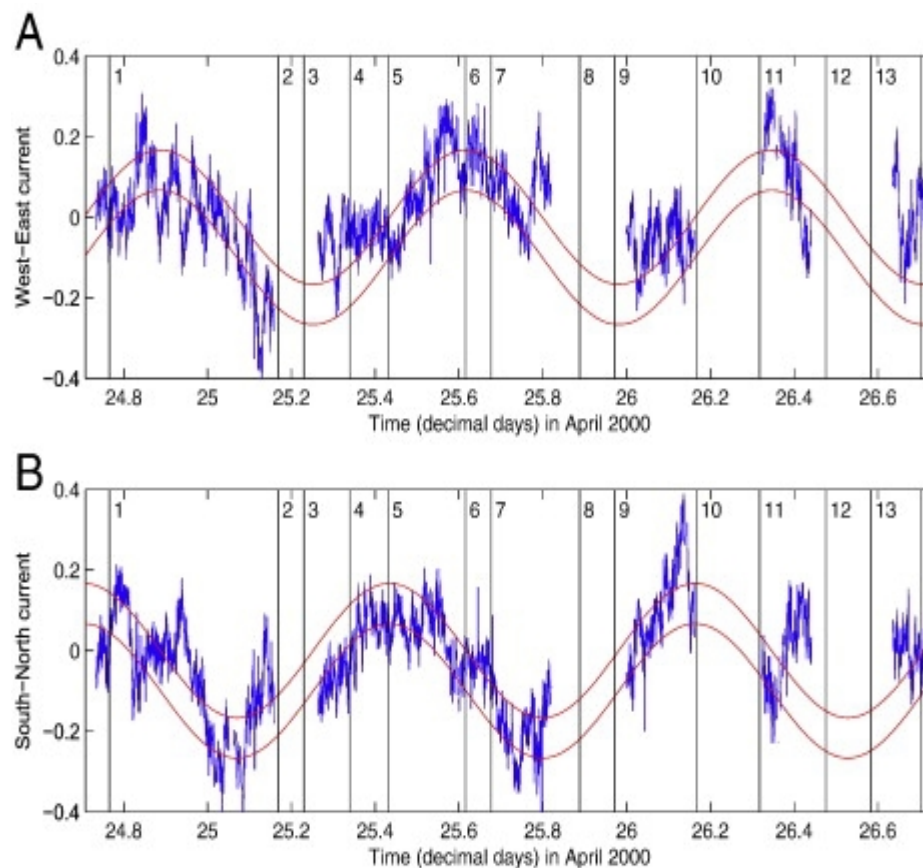
3) Overlaying the current with a sinusoid



Time series of A) the eastward and B) northward current components, at 16 m depth, along transects TR1 and TR2 of MOOGLI 2. Superimposed is a sinusoidal curve of inertial period, shifted by $+\pi/2$ in A) compared to B). The horizontal blue line shows the means of the two components: A) -0.10 m/s; and B) 0 m/s. (Fig 12 from **Petrenko A.** (2003), *Circulation features in the Gulf of Lions, NW Mediterranean Sea; importance of inertial currents*. *Oceanol. Acta*, 26, 323-338).

and associated text:

“The mean current of the eastward component is around -10 cm/s, corresponding to the average westward speed of the NC. The mean component of the northward component is zero. The amplitude of the sinusoidal curve, corresponding to the inertial current, is about 20 cm/s. Hence, at that depth (16 m), the speed of the inertial oscillation can be locally as high as 200% the NC speed. Otherwise, the average speed of the NC in its core is about 30 cm/s; so the inertial current is about 2/3 the NC. It is important to remember that the thickness of the top layer of the inertial oscillation is about 30 m while the NC extends over 200 m; hence, the inertial oscillation energy is much smaller than the NC energy.”



Time series of the ADCP current differences between two depths, in m/s A) $u(12\text{ m})-u(48\text{ m})$, u being the west-east (+ east) component of the horizontal current and B) $v(12\text{ m})-v(48\text{ m})$, v being the south-north (+ north) component during Sarhygol 2, April 2000. A sinusoid at the Coriolis frequency, representing the inertial oscillation is added to A and shifted by $\pi/2$ in B. (from Petrenko A., C. Dufau and C. Estournel (2008), *Barotropic eastward currents in the western Gulf of Lion, north-western Mediterranean Sea, during stratified conditions*. *J. Marine Syst.*, doi:10.1016/j.jmarsys.2008.03.004, Fig 2)

3rd-pass filtering

papier à venir

D. Allain, 2014, Numerical filtering of geophysical data : methods and application on ocean inertial waves.

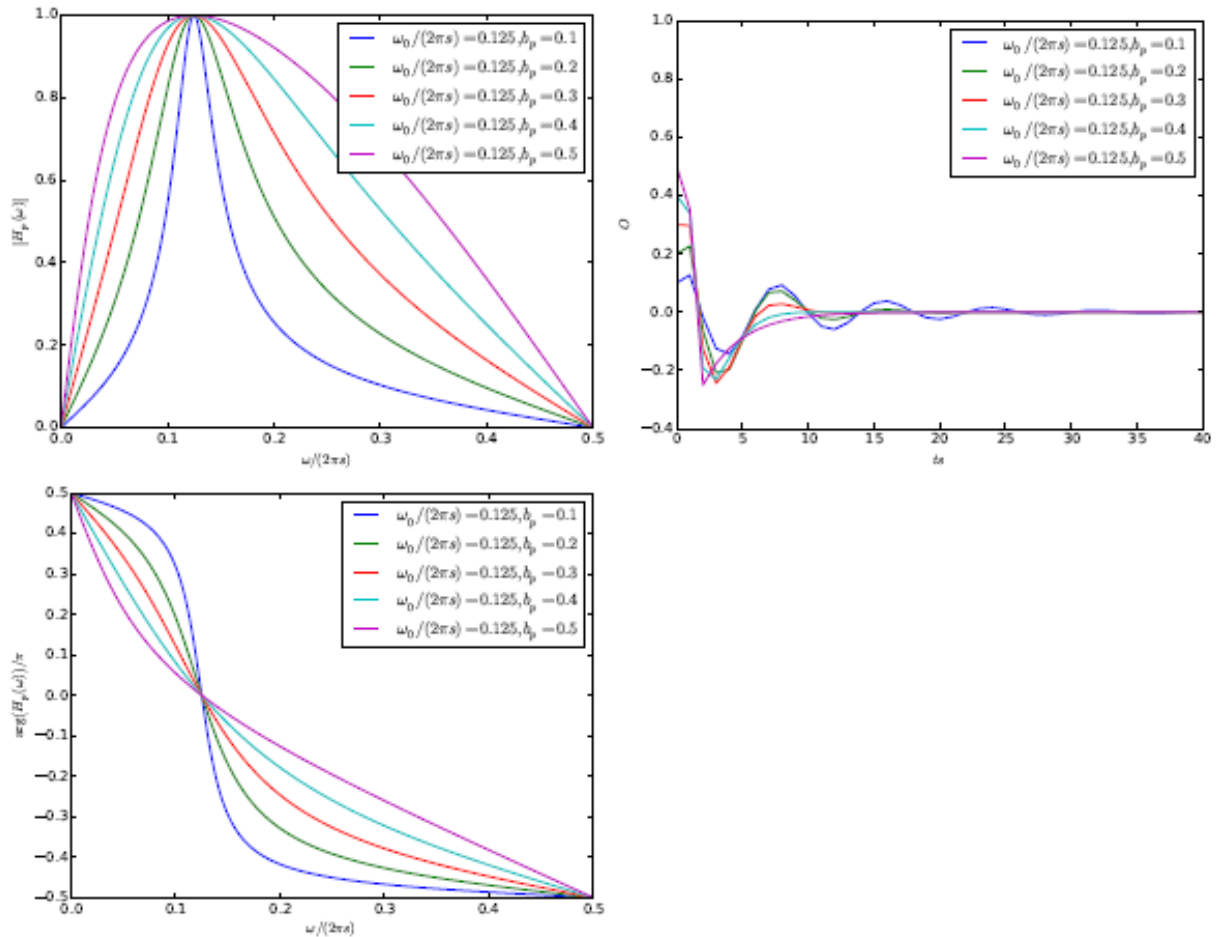
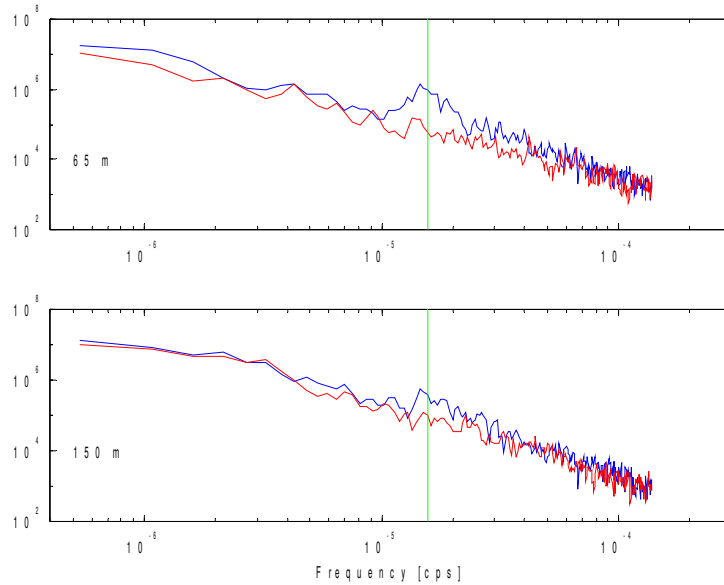


Figure 2: Amplitude and phase diagrams and convolution kernels of the DF-II IIR BP filter for different values of b_p

For more details contact D. Allain (SHOM-founded CNRS research engineer working within the ECOLA team, damien.allain@legos.obs-mip.fr)

4) Rotary spectra



Rotary spectra versus frequency (bottom x-axis) for A) 65 m, B) 150 m currents measured at SOFI during April to June 1998. The black (grey) line is the clockwise (counter-clockwise) component of the spectra. Note that, at the inertial frequency (indicated by the vertical line), the clockwise component is much higher than the counter-clockwise component. (Fig 11 extraite de **Petrenko A.** (2003), *Circulation features in the Gulf of Lions, NW Mediterranean Sea; importance of inertial currents.* Oceanol. Acta, 26, 323-338).

5) Wavelet analysis

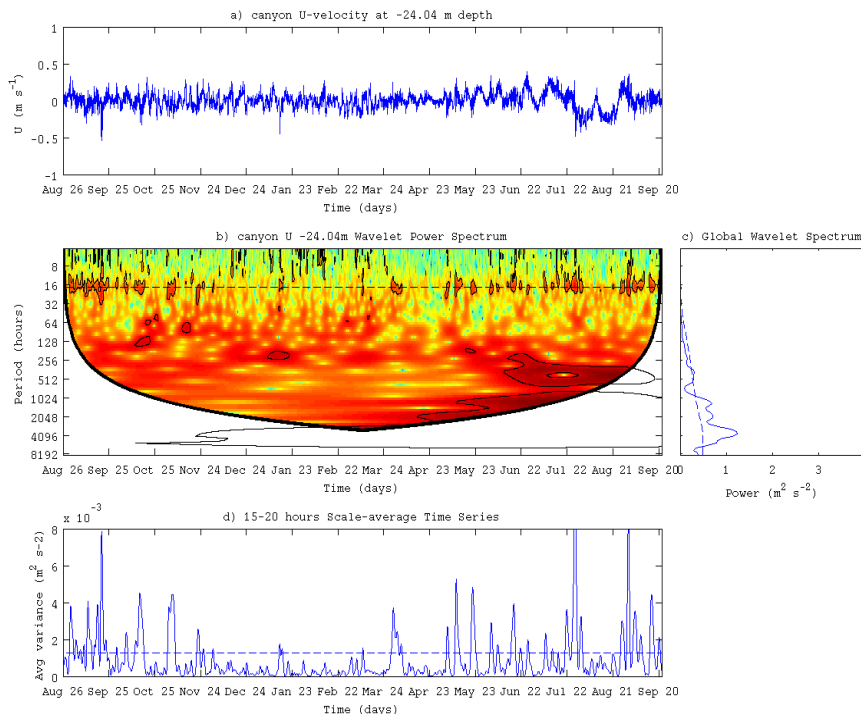


Fig – Wavelet analysis of a velocity time series acquired during the Latex campaign (from the mooring in the canyon) between August 2009 and August 2010 (Courtesy F. Nencioli) – spectral analysis tool from Torrence and Compo, 1998.

2.11 Omega Equation for estimating vertical velocities (lecture by A.Petrenko)

A INSERER 

3. Coastal eddies

Fundamentals

The potential flow simultaneously satisfies the following relations

$$\nabla \times \vec{v} = 0 \quad \text{and} \quad \nabla \cdot \vec{v} = 0$$

i.e., the velocity field is irrotational and incompressible.

If the velocity fields are irrotational (or conservative), given that by definition $\nabla \times (\nabla \Phi) = 0$, there must exist a scalar velocity potential Φ whose velocity field (also termed potential flow) is

$$\vec{v} = \nabla \Phi \quad (3.1)$$

If the velocity field is solenoidal (or incompressible), given that by definition $\nabla \cdot (\nabla \times \vec{\Psi}) = 0$, there must exist a vector velocity potential $\vec{\Psi}$ whose velocity field (potential flow) is

$$\vec{v} = \nabla \times \vec{\Psi} \quad (3.2)$$

If the flow is planar (2D horizontal), we have $\vec{\Psi} \equiv (0, 0, \Psi)$ and the scalar velocity potential $\Psi \equiv \Psi(x, y)$ is a function of the flow.

These potential flows are equivalent to electrostatic problems in a vacuum. They will occur whenever we can neglect any viscous effects.

Examples

Uniform parallel flow

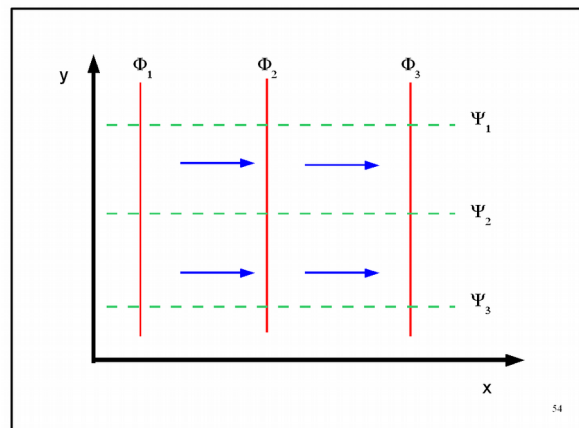
$$v_x = U \quad v_y = 0$$

Using Eqs. (3.1) and (3.2) we obtain

$$v_x = \partial_x \Phi = \partial_y \Psi \quad \text{and} \quad v_y = \partial_y \Phi = -\partial_x \Psi$$

which yields

$$\Phi = Ux \quad \text{and} \quad \Psi = Uy$$



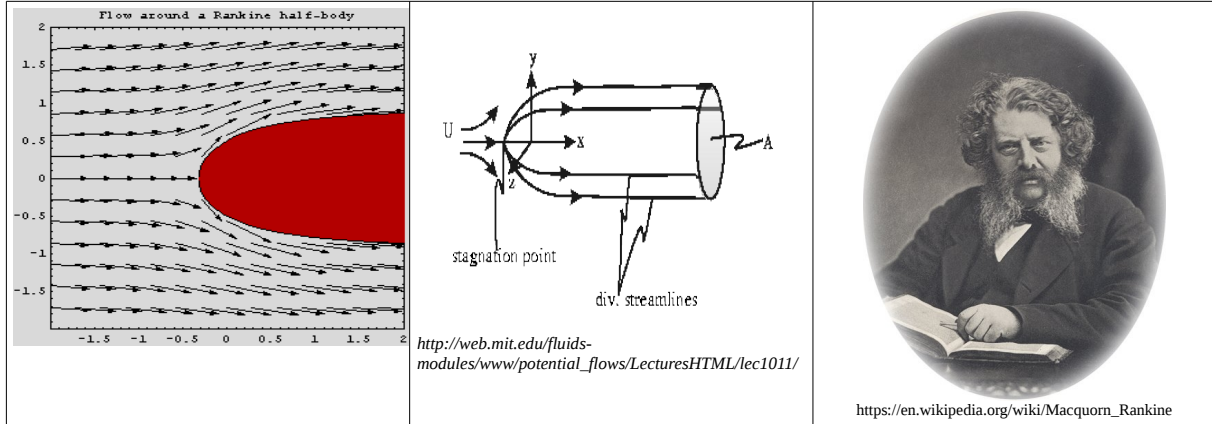
| | | |
|---------------|---|--|
| <p>Source</p> | $v_r = \frac{Q}{2 \pi r} \quad v_\theta = 0$ $\Phi = \frac{Q}{2 \pi} \log \left(\frac{r}{r_o} \right)$ $\Psi = \frac{Q}{2 \pi} \theta$ | |
| <p>Eddy</p> | $v_r = 0 \quad v_\theta = \frac{\Gamma}{2 \pi r}$ $\Phi = \frac{\Gamma}{2 \pi} \theta$ $\Psi = \frac{\Gamma}{2 \pi} \log \left(\frac{r}{r_o} \right)$ | |
| <p>Dipole</p> | $v_r = \frac{p \cos \theta}{2 \pi r^2} \quad v_\theta = \frac{p \sin \theta}{2 \pi r^2}$ $\Phi = -\frac{Qd \cos \theta}{2 \pi r}$ $\Psi = \frac{Qd \sin \theta}{2 \pi r}$ | |

The superposition of simple flows above allows us to introduce potential flows that are a little more complex.

| | |
|------------------------------|--|
| <p>Uniform flow + Source</p> | |
| <p>Uniform flow + Dipole</p> | |

In these types of flow there are so-called stagnation points where the flow velocity is zero. The curve representing the flow, the streamline, contains the stagnation point(s) and divides the domain into two regions in which the fluid is driven by two basic flows. One could replace such a dividing streamline by a solid obstacle without modifying the main flow.

In 3D one speaks of a “Rankine half-body” named after the researcher who has developed this technique while studying the design of boats.



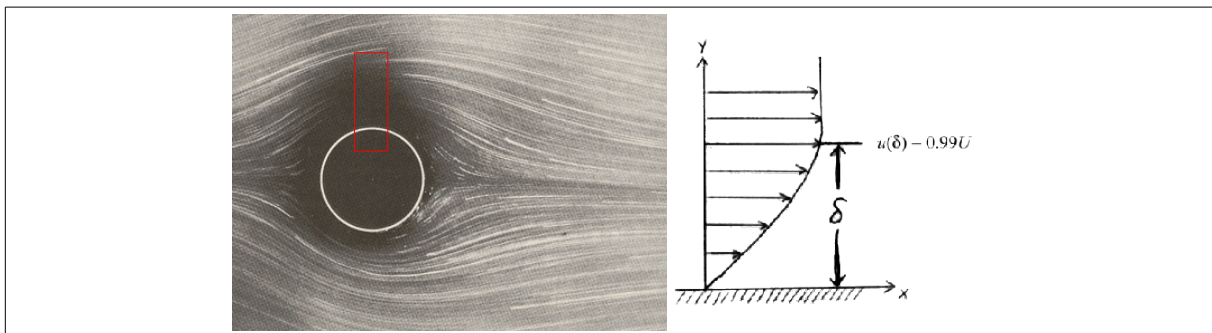
Laminar boundary layer

Far from the body and as long as the incoming flow is not turbulent the viscosity terms in the equation of motion (Navier -Stokes equation)

$$\frac{d\vec{u}}{dt} = -\frac{1}{\rho} \nabla p + \vec{g} + \nu \nabla^2 \vec{u}$$

are negligible and the flow basically has the same profile as a perfect fluid.

The connection between the perfect/ideal fluid solution and the zero-velocity (so-called no-slip) condition on the surface of a solid body occurs in the so-called boundary layer, the thickness of which decreases as the Reynolds number $Re = \frac{UL}{\nu}$ increases. In this region, both the viscosity and advection terms must be taken into account. The idea of a boundary layer links two otherwise separate domains of fluid mechanics: the potential flows of perfect/ideal fluids and the experimental study of viscous flows.



Generation of relative vorticity

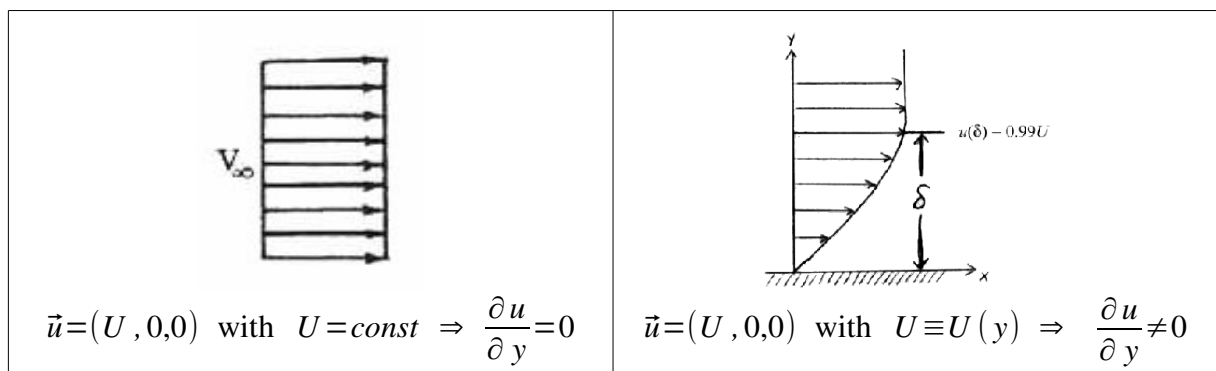
Relative vorticity is the vertical component of the velocity curl

$$\zeta = \vec{k}(\nabla \times \vec{V}) = \frac{\partial v}{\partial x} - \frac{\partial u}{\partial y}$$

Relative vorticity describes the tendency of a fluid to turn/rotate. The sign of ζ can be illustrated using the following schematics:

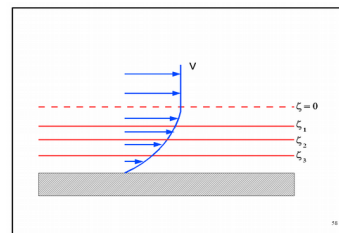


It is termed “relative” vorticity because it is measured with respect to the Earth’s rotation. It is generated by the no-slip condition on a solid object. Let us compare the viscous and non-viscous cases:



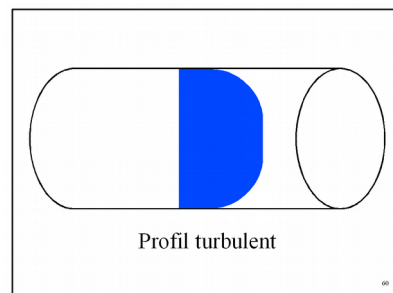
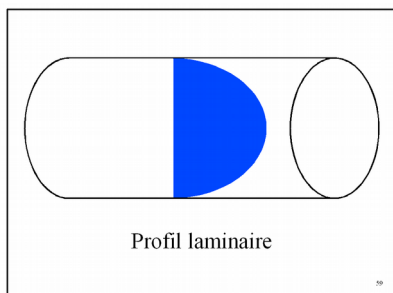
It is thus in the boundary layer where relative vorticity is being created.

If we plot the isolines we can show how the vorticity is concentrated in the boundary layer



Turbulent boundary layer

Until now, whenever we spoke of viscosity we meant the molecular viscosity and all boundary layers were laminar. Prandtl has adapted the idea of a boundary layer to the case of turbulence. In the laminar scenario, the transport of momentum is due to molecular viscosity and we have a diffusive transport. If the advective transport of momentum becomes more important than the diffusive transport we are in a turbulent flow and the velocity profiles change considerably. The Reynolds experiment clearly showed this for the case of a cylindrical tube: in the laminar case the Poiseuille velocity profile is parabolic while in the turbulent case it is flatter.



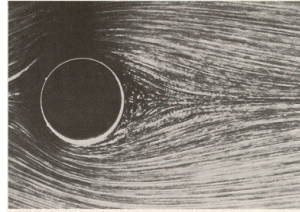
In both cases there is a boundary layer. In the turbulent case this layer is also turbulent and is the place where vorticity is being generated.

Different flow regimes

Depending on the flow velocity and geometry, the transport of momentum can be dominated by diffusive or advective phenomena. The relative importance of these terms is expressed as the Reynolds number which can also be interpreted as the ratio between the characteristic time scales of momentum diffusion and momentum advection.

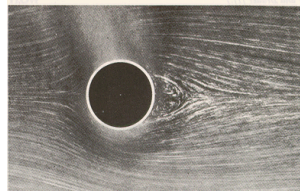
The following experiment can be used to visualize the different flow regimes: a cylinder of diameter D is placed parallel to the z -axis in a flow of velocity U flowing along the x -axis. In the actual laboratory setup, the fluid is typically at rest and the cylinder is being moved through the fluid at a velocity U . Small particles are often added to the fluid, illuminated by a sheet of light arriving at a right angle to visualize the streamlines. Depending on the magnitude of Re we can distinguish different regimes.

For $Re \ll 1$ the flow velocity is small (or the liquid very viscous - this scenario does not really interest us in oceanography), the flow is laminar and perfectly symmetrical between the up- and downstream sides of the cylinder. We have a situation very similar to the solution to the Rankine half-body problem.

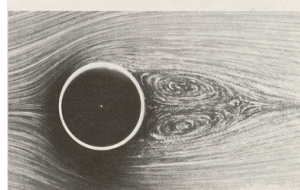


$Re = 1.54$

For $Re \approx 1$ we start to observe two counter-rotating eddies downstream from the cylinder (recirculating flow). The size of the recirculation zone increases with increasing Re .



$Re = 13.1$

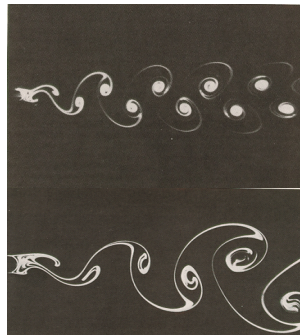


$Re = 26$

For $Re \approx 50$ the flow is no longer stationary and the flow velocity becomes time dependent: small vortices are constantly being shed from the downstream side of the cylinder and form two lines of eddies called the "von Karman vortex street". The shedding frequency is characterised by the Strouhal number

$$Sr = f \frac{D}{u}$$

with f being the frequency of vortex shedding. Physically, it represents the ratio between the advection time scale and characteristic time scale of non-stationarity. If $Sr \ll 1$, the flow is called quasi-stationary. Dans ce cas est constant et de l'ordre de 1.



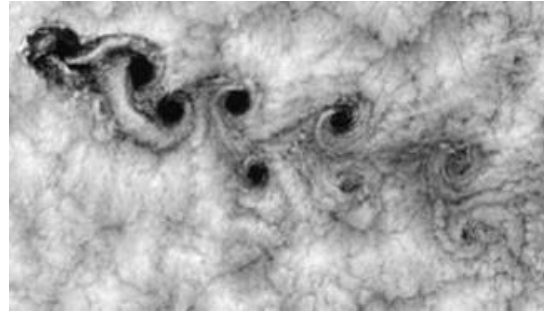
$Re = 105$

$Re = 150$

<http://www.media.mit.edu/physics/pedagogy/nmm/student/95/aries/mas864/obstacles.html>

For $Re \gg 1$ there is a superposition of these larger coherent structures and the incoherent motions. The spatial scales become smaller the larger Re . In practice, their minimum size decreases with $1/\sqrt{Re}$.

The von Karman vortex street can be observed up to very high Reynolds numbers in both oceanographic and atmospheric flows in the lee of islands or other large-sized obstacles.

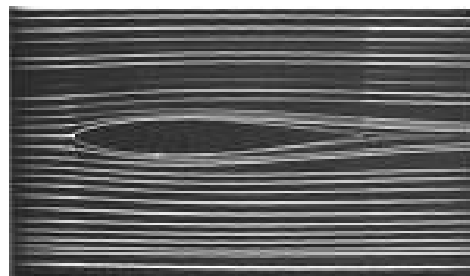


The image on the right shows a von Karman vortex street observed in the atmosphere off the Chilean coast near Juan Fernandez island.

Flow separation

What happens to vorticity once it has been generated?

The vorticity generated near a wall is carried along by the flow into the downstream wake of the obstacle. In the case of a wing-shaped obstacle placed in a uniform flow, there is only a very small wake downstream.



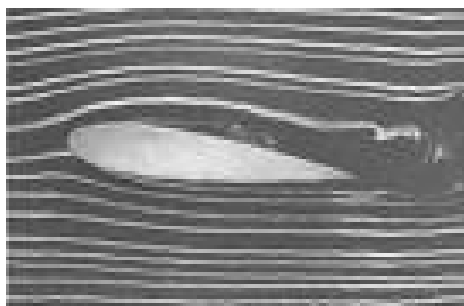
If you place a less streamlined body in the flow the flow changes more significantly. *Re* changes because *L* changes.

If we use a cylinder, for instance, the boundary layer only exists on the upstream side of the cylinder while on the downstream side there is a turbulent wake, the size of which is comparable to the cylinder itself.



This phenomenon is called flow separation (or boundary layer separation). In this scenario the downstream flow is far from a perfect fluid and the energy dissipation and drag force on the body are both considerably increased.

Below are two examples of flow separation in the wake of an air plane wing. What causes the Reynolds number to vary?



Integrating the relative vorticity equation in the vertical dimension

The formation and evolution of vortices downstream of headlands can be explained more “simply” in terms of the production, advection, and dissipation of vorticity.

To describe the phenomena that interest us, the simplest equations to use are the shallow water equations as they still contain all the relevant physics while allowing for certain simplifications.

For a homogeneous fluid and using the hydrostatic approximation, the momentum and continuity equations can be written as [Signell and Geyer, 91]:

$$\partial_t \vec{u} + \vec{u} \cdot \nabla \vec{u} + f(\vec{k} \times \vec{u}) = -g \nabla \eta - \frac{c_D \vec{u} |\vec{u}|}{h + \eta} + \nabla \cdot (A_H \nabla \vec{u}) \quad (\text{A})$$

$$\partial_t \eta + \nabla \cdot [\vec{u}(h + \eta)] = 0 \quad (\text{B})$$

The vertically averaged vorticity can be obtained from the curl of Eq. (A). We will now analyse each term of the equation. The first term becomes

$$\nabla \times \partial_t \vec{u} = \partial_t \nabla \times \vec{u} = \partial_t \vec{\zeta}$$

The second term is

$$\begin{aligned} \nabla \times (\vec{u} \cdot \nabla \vec{u}) &= \nabla \times (\vec{\zeta} \times \vec{u}) = \\ &= \vec{u} \cdot \nabla \zeta - (\vec{\zeta} \cdot \nabla) \vec{u} + (\nabla \cdot \vec{u}) \zeta + \vec{u} (\nabla \cdot \vec{\zeta}) = \\ &= \vec{u} \cdot \nabla \zeta - (\vec{\zeta} \cdot \nabla) \vec{u} - \frac{\zeta}{H} (\partial_t \eta + \vec{u} \cdot \nabla H) \end{aligned}$$

where $\vec{u} (\nabla \cdot \vec{\zeta})$ is zero as it is the divergence of the velocity curl and we have substituted the velocity divergence from (B) and $H = h + \eta$.

The Coriolis term can be written as

$$\nabla \times f(\vec{k} \times \vec{u}) = f[\vec{k}(\nabla \cdot \vec{u}) - \vec{u}(\nabla \cdot \vec{k}) + (\vec{k} \cdot \nabla) \vec{u} - (\vec{u} \cdot \nabla) \vec{k}] = f \vec{k}(\nabla \cdot \vec{u}) = -\frac{f}{H} \vec{k}(\partial_t \eta + \vec{u} \cdot \nabla H)$$

The gravity term is zero as it is the curl of a gradient

$$\nabla \times (g \nabla \eta) = 0$$

The bottom friction term can for now be written as

$$\nabla \times \frac{c_D \vec{u} |\vec{u}|}{h + \eta}$$

and finally the viscous term, assuming a constant eddy viscosity, becomes

$$\nabla \times A_H \nabla^2 \vec{u} = A_H \nabla^2 (\nabla \times \vec{u}) = A_H \nabla^2 \vec{\zeta}$$

In 2D, the vorticity $\vec{\zeta} = \vec{k}(\partial_x v - \partial_y u)$ is a vector where only the vertical component is non-zero, we can write the equation for this component

$$\partial_t \zeta + \vec{u} \cdot \nabla \zeta = \frac{\zeta + f}{H} [\partial_t \eta + \vec{u} \cdot \nabla H] - \left[\nabla \times \left(\frac{C_D \vec{u} |\vec{u}|}{H} \right) \right] \cdot \vec{k} + A_H \nabla^2 \zeta$$

The left-hand-side describes the rate of change of the vorticity and its advection, i.e., the change in vorticity while following a fluid parcel of constant mass.

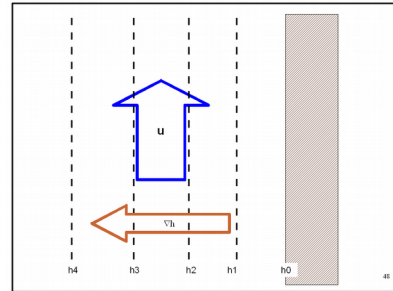
The right-hand-side represents the processes that cause these changes:

- i) the first term is the production of vorticity due to compression (or stretching) and planetary vorticity;
- ii) the second term is the production of vorticity due to bottom friction.
- iii) the third term is the diffusion of vorticity due to turbulence.

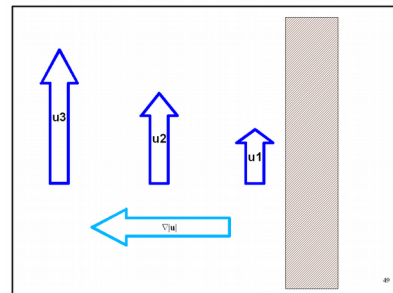
Due to the shallow depth of coastal areas, the second term can be very important. If we expand this term we obtain three more terms:

$$\left[\nabla \times \left(\frac{C_D \vec{u} |\vec{u}|}{H} \right) \right] \cdot \vec{k} = \frac{C_D |\vec{u}|}{H^2} [\vec{u} \times \nabla H] \cdot \vec{k} - \frac{C_D (\vec{u} \times \nabla |\vec{u}|)}{H} + \frac{C_D |\vec{u}| \zeta}{H}$$

a) slope torque: the production of vorticity when there is a velocity component perpendicular to the bathymetry gradient. Physically, this means that the water closer to the coast experiences a higher (vertically integrated) amount of friction than the water offshore.



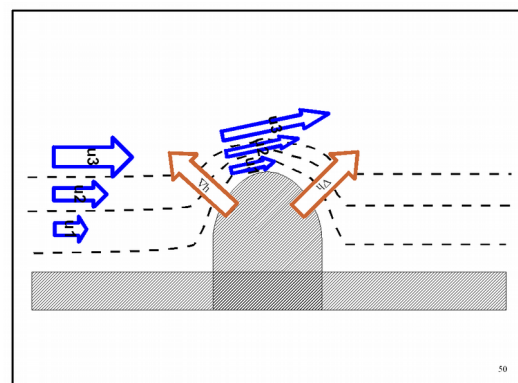
b) velocity torque: vorticity is produced when there is a velocity component perpendicular to the velocity gradient itself. This phenomenon is linked to the fact that friction obeys a quadratic law. A faster flow is much more delayed than a slightly slower flow.



c) dissipation of vorticity due to friction. The time scale of this phenomenon is $\tau = \frac{H}{C_D |\vec{u}|}$

Near a cape or headland there are several mechanisms that can lead to the production of vorticity.

The shallow depth and strong bathymetric gradients can invoke both mechanisms a) and b) from above. Indeed, flow that follows a bathymetric gradient, but also strong gradients in velocity of the component perpendicular to the main flow direction. A third source for vorticity is the no-slip condition at the coast.



Near a cape, we therefore find high amounts of vorticity although this does not necessarily mean that we observe any vortices. For vortices to form, the vorticity must be transported away from the fluid's boundary layer, i.e., offshore. If the flow remains parallel to the coast, vortices can only form if there is flow separation; it is therefore necessary to study the conditions required for separation to occur.

Flow separation near a cape

By adopting a suitably oriented coordinate system, the derivatives along the coordinate axis parallel to the coast, x_1 , are much smaller than those in the direction perpendicular to the coast x_2 .

The equations for the parallel component and for continuity can be written as:

$$\partial_t u_1 + u_1 \frac{\partial u_1}{\partial x_1} + u_2 \frac{\partial u_1}{\partial x_2} = -g \frac{\partial \eta}{\partial x_1} - \frac{c_D U_o u_1}{h} + A_H \frac{\partial^2 u_1}{\partial x_2^2} \tag{C}$$

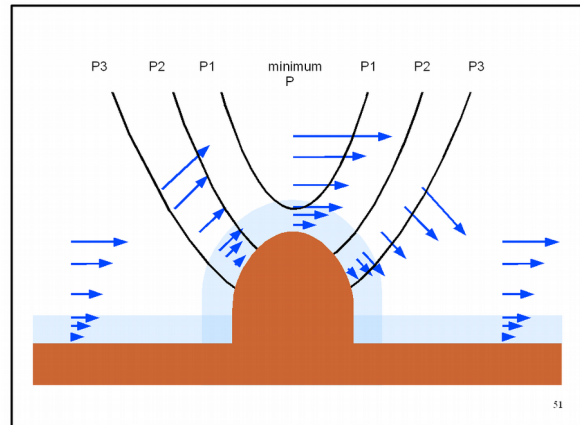
$$\partial_{x_1} u_1 h + \partial_{x_2} u_2 h = 0 \tag{D}$$

where U_o is the flow velocity far from the cape (in particular for tidal currents). Without bottom friction and topography, these equations are equivalent to the Prandtl equations for the boundary layer of a 2D flow.

We first consider the case of a stationary flow without bottom friction.

Outside the boundary layer the flow accelerates as it approaches the tip of the cape. It then starts to slow down as soon as the tip has been passed.

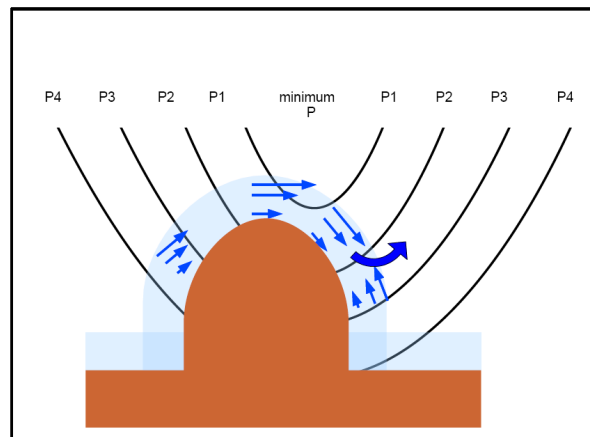
According to Bernoulli's law this generates a local pressure minimum at the tip of the cape. Along the edge of the boundary layer there is thus a favourable pressure gradient (in the sense that P decreases in the direction of the flow) upstream and an adverse gradient downstream.



Upstream, the favourable pressure gradient maintains the flow direction in the boundary layer because it compensates for the loss of momentum in the boundary layer.

Downstream, the adverse pressure gradient retards the boundary layer flow and decreases its momentum.

If the amount of advection of upstream momentum is insufficient, the main flow starts to veer off. For reasons of continuity, this deceleration of the boundary layer flow that is parallel to the coast must be accompanied by a flow away from the coast (and out of the boundary layer).



The point along the edge of the layer boundary where the flow parallel to the coast becomes zero is called the separation point. Here, the streamline at the edge of the boundary layer veers away from the coast towards the interior of the main flow.

The distance between the point of minimum pressure and the point of separation depends on the momentum flux and the strength of the unfavourable pressure gradient (and thus the flow).

For a viscous fluid without bottom friction the advection terms are all very small near the boundary layer and the balance of momentum (Eq. C) is made between the pressure gradient and the diffusion terms

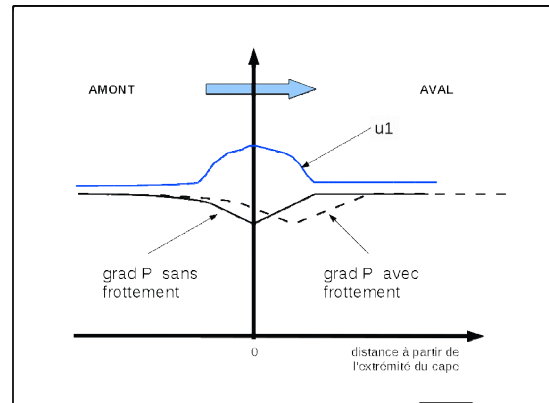
$$g \frac{\partial \eta}{\partial x_1} = A_H \frac{\partial^2 u_1}{\partial x_2^2} \tag{C'}$$

An adverse pressure gradient only requires that the flow has a negative curvature near the boundary

layer and, as a result, that the velocity profile parallel to the coast has an inflection point. Physically, this means that there won't be any separation if the momentum flux is sufficiently strong to compensate the adverse pressure gradient.

However, in coastal flows bottom friction is very important and the velocity maximum no longer coincides with the pressure minimum because the pressure gradient needs to balance not only advection but also friction.

The pressure minimum therefore moves downstream from the velocity maximum.



A momentum balance is thus created between the pressure gradient and the pressure term.

$$(C'') \quad g \frac{\partial \eta}{\partial x_1} = - \frac{c_D U_o u_1}{h}$$

Note that now the adverse pressure gradient requires that u_1 have an opposite sign: thus, if the gradient is ever reversed then there is an immediate separation because u_1 changes sign. The separation problem therefore is linked to the inversion of the pressure gradient.

Using an analytical model, Signel and Geyer (1991) demonstrated that (in the absence of any tides) there is an inversion of the pressure gradient when the advection term dominates over friction.

For a cape/headland of shape a/b , the importance of the advection terms is measured by the equivalent flow Reynolds number:

$$Re_f = \frac{H}{C_D a}$$

In a similar fashion to the Reynolds number, we observe different flow regimes downstream of a cape based on the variation of Re_f [Doglioli et al, 2004 and presentation below].

3.5 Example : circulation around the Portofino peninsula

Capes → coastal currents dynamics and associated transport.

Leeward eddies → local distributions of:

- sediments;
- pollutants;
- nutrients;
- marine species.

Previous numerical studies:

- Flat bathymetry;
- Tidal forcing;
- 2D models.

This numerical study:

- Steep slope;
- Inflow steady current;
- 2D & 3D model.

Bibliography

Boyer and Tao, 1984, J.Fluid.Mech.
 Freeland, 1990, Atmosphere-Ocean
 Veron et al., 1991, Fluid Dynamics Res.
 Signell and Geyer, 1991, J.Geoph. Res.
 Davies et al., 1995, J. Coastal Res.

Study area and measurements

Latitude: 44°N, 20°00'

Longitude: 9°E, 10°, 20°, 30°

Legend: ■ Currentmeters position; ▬ mean velocity [m s⁻¹]

IOF-CNR, 1972-82; ENEA, 1986-88, 1991-94, 1997; (Airoldi and Manca, 1982)

Physical system

simplified coastline

simplified bathymetry

$H = H_0 e^{-2x/(45000)}$
 $H_0 = 20$
 $\lambda = 0.0002$

Numerical setting

Radiation (Orlanski Condition)

Free sleep wall 5 km 0.25°

Prescribed inflow (Flather Condition)

Numerical domain: 202 x 81 grid points ↔ **Physical domain: 100 x 50 km**

Horizontal resolution: $Dx = 500m$ $200m < Dy < 1000m$

Vertical resolution: 31 sigma layers

Inflow current

Flather boundary condition $U = U_e + \sqrt{gH}(\eta - EL_e)$

1) Constant inflow: $U_e = 0.067, 0.025, 0.50$ m/s

2) Gaussian jets:

$U_e = -U_{max} e^{-\frac{(y-Y_H)_{100}^2}{\xi}}$

t.c. $\int_{H=0}^{H=300} U_e dy = -0.5$ Sv

Western boundary condition test

(comparison between boundary results of a small grid and internal value of a big grid)

UA transport along shore component: very good agreement

EL elevation of free surface: little shift

Numerical experiments

$Ro = \frac{U_0}{f a}$
 $Re = \frac{U_0 a}{A_M}$
 $Re_f = \frac{H_0}{C_D a}$
 $Ek_v = \frac{K_M}{f H_0^2}$
 $Sb = g \frac{\Delta \rho}{\rho} \frac{H_0}{f^2 a^3}$

| Exp. | Ro | Re | Re _f | Ek _v | Sb |
|---------------------|-----------|------------|-----------------|---|---------|
| C _D 2D | 0.4 | 1500 | 4 - 83 | n.d. | n.d. |
| U ₀ 2&3D | 0.1 - 0.8 | 360 - 3000 | 17 | 1.5 × 10 ⁻³ | 0 - 6.4 |
| K _M 3D | 0.4 | 1500 | 17 | 1.5 × 10 ⁻⁵ - 1.5 × 10 ⁻² | 0 - 6.4 |
| H ₀ 2D | 0.4 | 1500 | 1 - 17 | n.d. | n.d. |

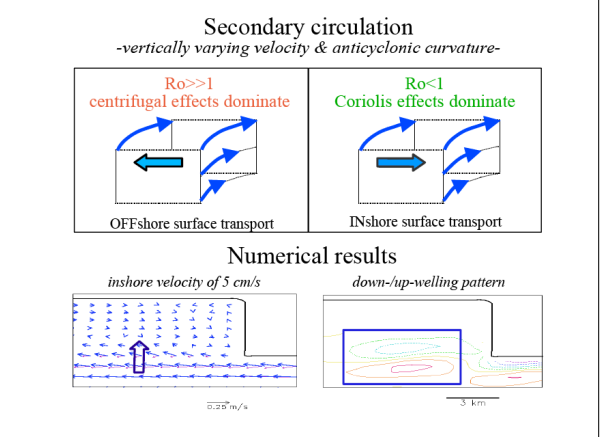
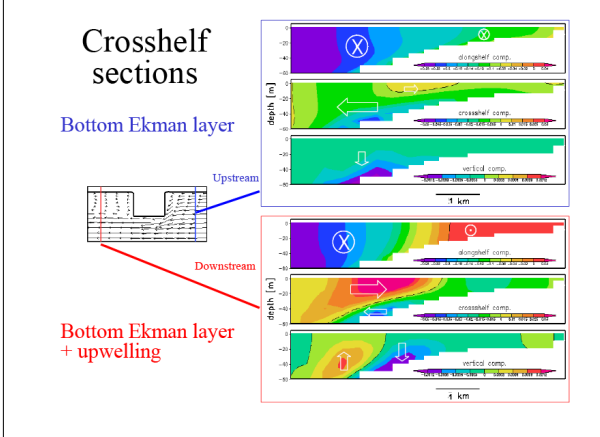
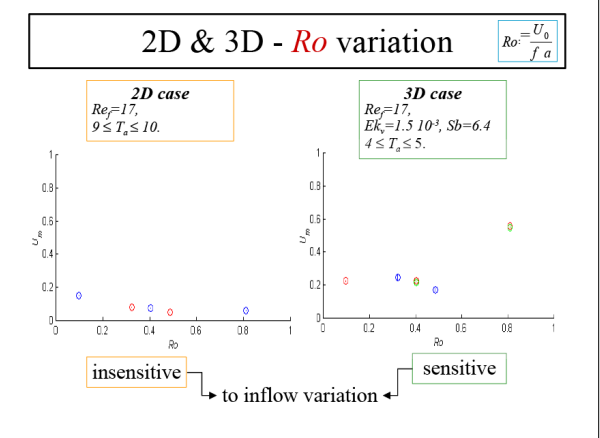
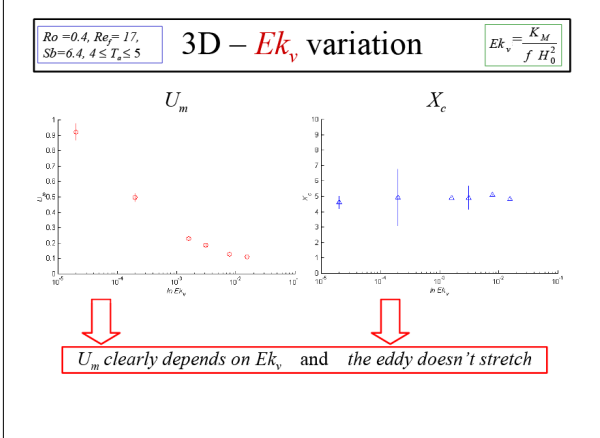
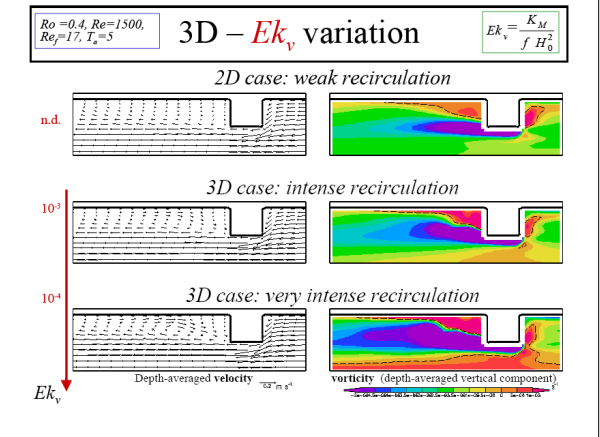
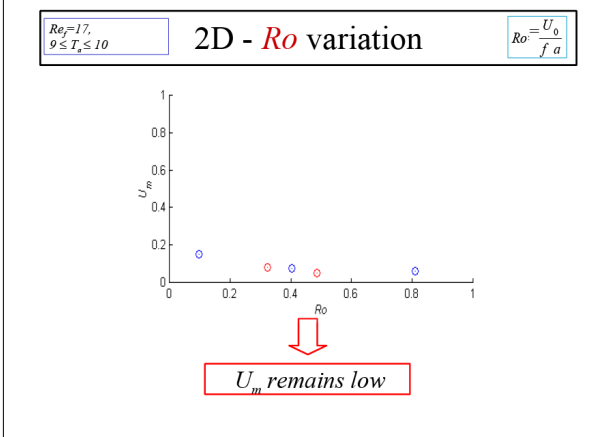
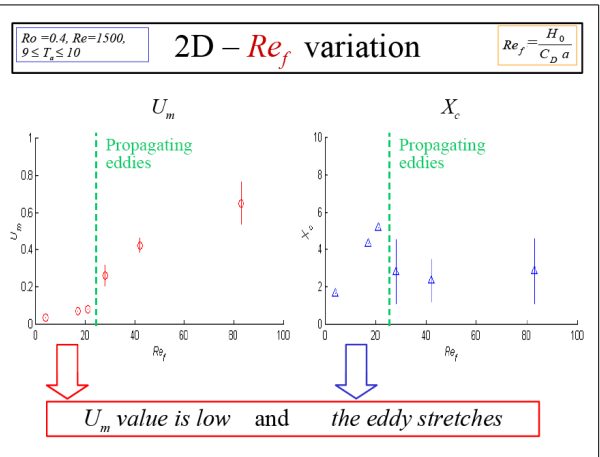
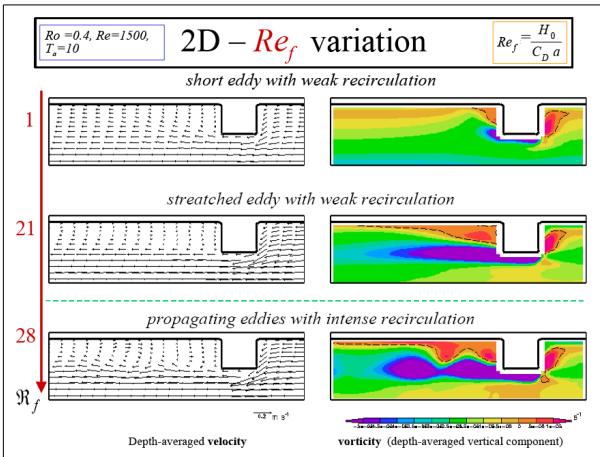
Varying parameters:
bottom friction: $10^{-4} < C_D < 10^{-2}$, linear & quadratic drag;
inflow: $0.06 < U_0 < 0.50$ [m s⁻¹], uniform & gaussian jet
vertical kinematic viscosity (3D): $10^{-4} < K_M < 10^{-1}$ [m² s⁻¹]

Observables

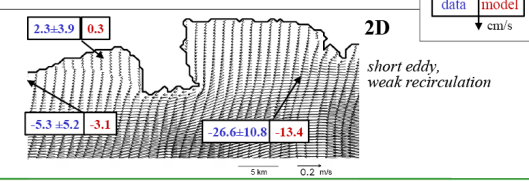
- X_c : dimensionless distance where the recirculation starts
- U_m : dimensionless maximum value of the recirculation current

a and U_0 used to normalise length and velocities, average and std on a $t_f = \frac{H_0}{C_D U_0}$ period

5 km color interval [m/s]: 0.064 0.068 0.072 0.076 0.080 0.084 0.3 m/s

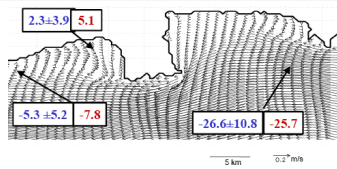


Real bathymetry ($Ro=0.4, Re_f=17$)



3D $Ek_v=1.6 \cdot 10^{-4}$

short eddy, intense recirculation



Conclusions

- in the case of *inflow steady current + narrow shelf + steep slope* the 2D models might not be appropriate;
- in 3D, the resolved bottom Ekman layer and secondary circulation could explain the leeward eddy intensification;
- with the realistic bathymetry 3D model, a good calibration is obtained varying both Re_f and Ek_v ;

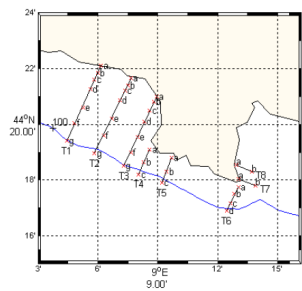
Outlooks

- time varying inflow;
- real stratification;
- new data.

Grigliato:

Metodo

misure idrologiche
17 giugno: 35 stazioni
9 agosto: 36 stazioni



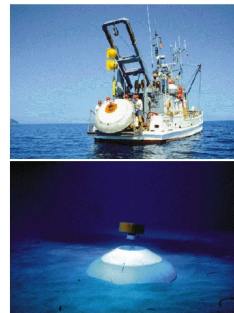
Sonda IDRONAUT
OCEAN SEVEN 316 CTD
multiparameter probe ???

Conducibilita'
Temperatura
Salinita'
O2
Chl-A



Metodo

misure correntometriche e idrologiche

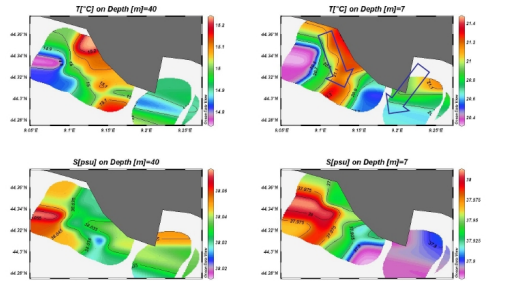


SEPTR
(Shallow water Environmental Profiler in Trawl-safe Real-Time)



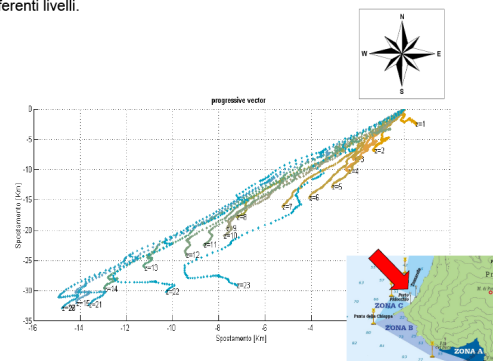
CTD
17 giugno

Risultati



Vettori progressivi della corrente ricampionata ogni 6h a differenti livelli.

Risultati



3.6 Example : eddies in the western Gulf of Lion

| | | | | | |
|---|---|---|--|---|---|
| <p>Motivations – Question ouvertes</p> <p>Les processus de (sub)mesoéchelle peuvent avoir une grande influence sur la biogéochimie (e.g. budgets de la production primaire, disponibilité nutriments)</p> <p>(Sweeney et al., 2003)</p> <p>(McGillicuddy et al., 1998)</p> <p>Études récentes intéressants en océan ouvert (e.g. Benitez-Nelson et al. 2007, McGillicuddy et al. 2007, Dickey et al 2008)</p> <table border="1"> <tr> <td>TOURBILLONS Cyclones Anticyclones</td> <td>TYPE D'EAU oligotrophique eutrophique</td> <td>BIOLOGICAL PUMP sousestimation surestimation</td> </tr> </table> | TOURBILLONS Cyclones Anticyclones | TYPE D'EAU oligotrophique eutrophique | BIOLOGICAL PUMP sousestimation surestimation | <p>Motivations – Question ouvertes</p> <p><i>En plus, peu est connu en eaux côtières</i></p> <p>Comment se forment ces tourbillons? Quel est leur dynamique?</p> <p>Y a-t-il des circulations secondaires? Avec des fortes vitesses secondaires? Quel est leur rôle dans la dispersion?</p> <p>Facilitent-ils le transfert horizontal de matière au travers du plateau et de la pente continentale? Peuvent-ils piéger des larves?</p> <p>Nof, 1999</p> <p>Hernandez Garcia d'Ovidio</p> | |
| TOURBILLONS Cyclones Anticyclones | TYPE D'EAU oligotrophique eutrophique | BIOLOGICAL PUMP sousestimation surestimation | | | |
| <p>Study zone: Gulf of Lion (GoL)</p> <p>Forcings:</p> <ol style="list-style-type: none"> 1- Rhone plume 2- Winds : Tramontane, Mistral. 3- Northern Current (NC) | <p>Zone d'étude : Golfe du Lion</p> <p>Le Courant Nord est partie intégrante de la circulation générale de la Méditerranée</p> <p>Millot and Taupier-Letage, 2005</p> <ul style="list-style-type: none"> — principale/permanente — saisonnière — secondaire/retour circulation ••••• tourbillons et mélanges (instabilités du courant) ••••• front Nord-Est-Sud ••••• zone de convection hivernale ••••• tourbillon induit par le vent <p>l approximation : courant géostrophique, i.e. barrière dynamique reputation de stabilité par rapport aux courants coté sud, mais aussi comportement turbulent</p> | | | | |
| <p>Zone d'étude : Golfe du Lion</p> <p>Circulation anticyclonique dans l'ouest</p> <p>Millot, 1979</p> <p>Millot, 1982</p> | <p>LATEX - LAgrangian Transport Experiment</p> <p>PIs: Anne Petrenko and Frédéric Diaz financement LEFE/IDAO&CYBER – Région PACA Pilot project 2007 – Main project 2008-11</p> <p>Objectif comprendre le rôle de la dynamique couplée physique-biogéochimie à (sub) mésoéchelle dans les échanges de matière et d'énergie entre les zones côtière et hauturière</p> <p>Méthode utilisation sélective et combinée de modélisation numérique et d'observations in situ (Lagrangian floats, SF6, ADCPs de coque, mouillages, images satellitaires, gliders, radars)</p> | | | | |
| <p>LATEX - LAgrangian Transport Experiment</p> <table border="1"> <tr> <td style="text-align: center;">MODÉLISATION</td> <td style="text-align: center;">EXPÉRIMENTAL</td> </tr> <tr> <td> <p>Hydrodynamique (Symphonie) with C.Estoumel et P.Marsaleix [POC, Toulouse]</p> <p>Analyse en ondelettes (WATERS)</p> <p>Particules numériques (ARIANE) with B.Blanke et N.Grimas [LPO, Brest]</p> <p>Couplage Physique (Symphonie) Biogéochimie (Eco-3M)</p> </td> <td> <p>Sept 2007 - Tests de communication et mesure de concentration ambiante du traceur</p> <p>Sept 2008 – Identification d'un tourbillon</p> <p>Sept 2009 – Mouillages & Identification d'un tourbillon</p> <p>Oct 2009 – Test du dispositif SF6</p> <p>Sept 2010 – campagne avec Suroit and Thélys II</p> </td> </tr> </table> | MODÉLISATION | EXPÉRIMENTAL | <p>Hydrodynamique (Symphonie) with C.Estoumel et P.Marsaleix [POC, Toulouse]</p> <p>Analyse en ondelettes (WATERS)</p> <p>Particules numériques (ARIANE) with B.Blanke et N.Grimas [LPO, Brest]</p> <p>Couplage Physique (Symphonie) Biogéochimie (Eco-3M)</p> | <p>Sept 2007 - Tests de communication et mesure de concentration ambiante du traceur</p> <p>Sept 2008 – Identification d'un tourbillon</p> <p>Sept 2009 – Mouillages & Identification d'un tourbillon</p> <p>Oct 2009 – Test du dispositif SF6</p> <p>Sept 2010 – campagne avec Suroit and Thélys II</p> | <p>MODÉLISATION – étude de sensibilité</p> <p>Modèle aux équations primitives Symphonie</p> <p>modeled velocity intensity (July 25, 2001) at 20 m boxes: model domains</p> <p>Emboîtement 1-km resolution One – Way Nesting</p> <p>Coefficient d'atténuation introduit dans le schéma d'advection-diffusion</p> <p>[Hu et al., 2009]</p> |
| MODÉLISATION | EXPÉRIMENTAL | | | | |
| <p>Hydrodynamique (Symphonie) with C.Estoumel et P.Marsaleix [POC, Toulouse]</p> <p>Analyse en ondelettes (WATERS)</p> <p>Particules numériques (ARIANE) with B.Blanke et N.Grimas [LPO, Brest]</p> <p>Couplage Physique (Symphonie) Biogéochimie (Eco-3M)</p> | <p>Sept 2007 - Tests de communication et mesure de concentration ambiante du traceur</p> <p>Sept 2008 – Identification d'un tourbillon</p> <p>Sept 2009 – Mouillages & Identification d'un tourbillon</p> <p>Oct 2009 – Test du dispositif SF6</p> <p>Sept 2010 – campagne avec Suroit and Thélys II</p> | | | | |

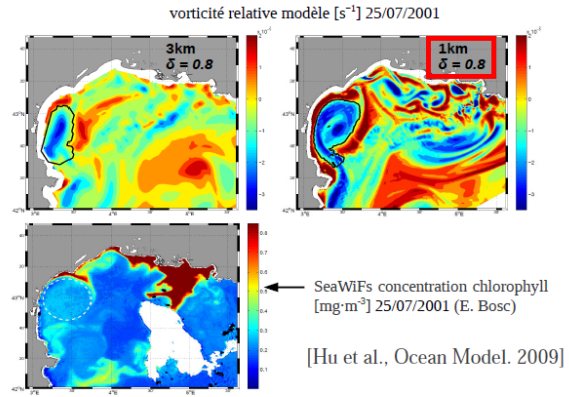
I-2. Sensitivity study

Advection – Diffusion Scheme in Symphonie (upwind + Leapfrog time-stepping):

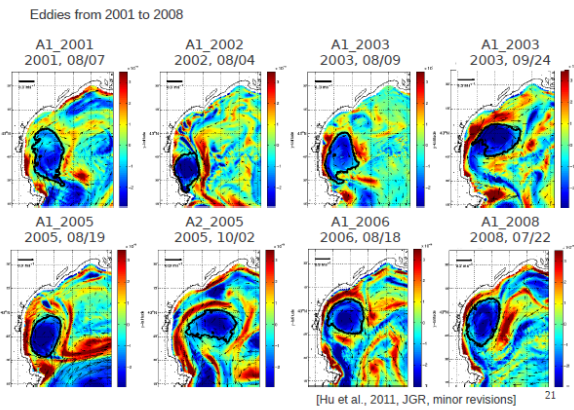
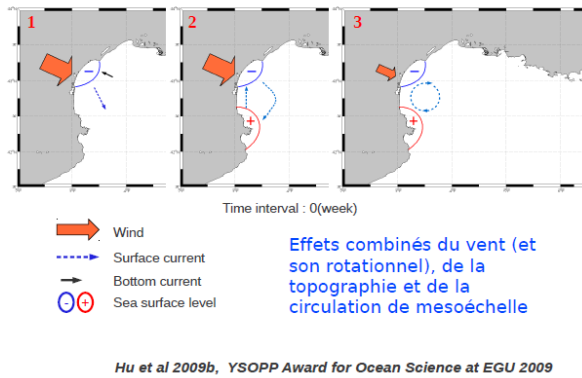
$$\frac{\phi_i^{t+\Delta t} - \phi_i^{t-\Delta t}}{2\Delta t} = \underbrace{-\frac{u_{i+1/2} \phi_i^t + \phi_{i+1}^t}{\Delta x} + \frac{u_{i-1/2} \phi_i^t + \phi_{i-1}^t}{\Delta x}}_{\text{Advection}} + \underbrace{\frac{A_{i+1/2} (\phi_{i+1}^{t-\Delta t} - \phi_i^{t-\Delta t})}{\Delta x} - \frac{A_{i-1/2} (\phi_i^{t-\Delta t} - \phi_{i-1}^{t-\Delta t})}{\Delta x}}_{\text{Numerical diffusion}}$$

Viscosity Coefficient: $A = |u| \frac{\Delta x}{2} \rightarrow \bar{A} = \delta \cdot |u| \frac{\Delta x}{2}$
 $\delta \in [0,1]$
 $\delta = 0$ No dissipation effect
 $\delta = 1$ Dissipation totally taken into account

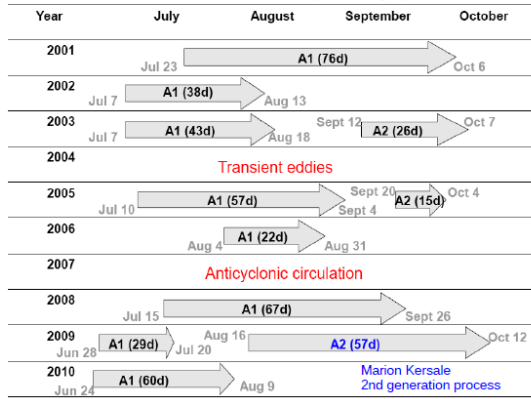
MODÉLISATION – étude de sensibilité



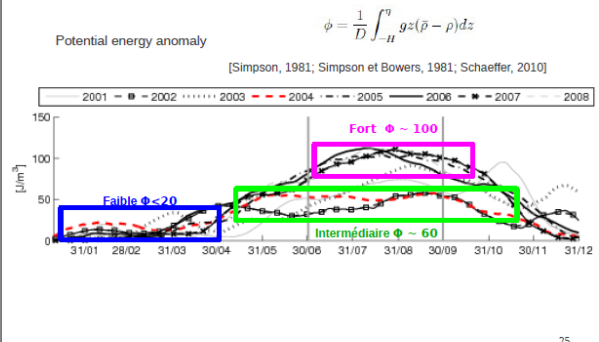
MODÉLISATION – hyp. génération du tourbillon



Presence of eddies (>15 days)



Influence of stratification on the eddy



Generation process

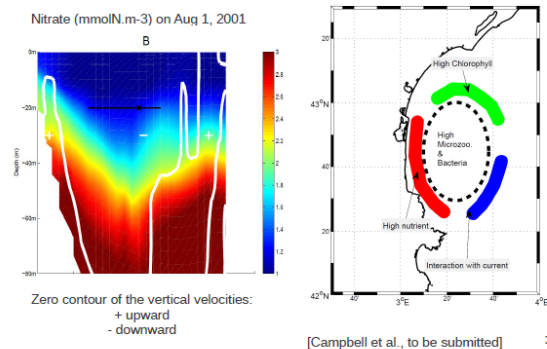
2 conditions are necessary to generate a long-life eddy:
 - strong North-West wind (Tramontane)
 - strong stratification

| Wind | weak | strong | strong | strong | strong & persistent | strong & persistent |
|----------|-------------|--------|--------------|-----------|---------------------|--------------------------|
| Stratif. | strong weak | no | intermediate | strong | intermediate | strong |
| Eddy | no | no | transient | long-life | long-life | anticyclonic circulation |

winter spring
 early summer, end of fall, summer 2004
 summers: 2001, 2003, 2005, 2006, 2008
 summer 2002
 summer2 007

[Hu et al., 2011, JGR, minor revisions]

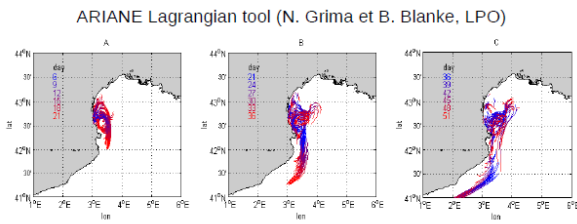
Coupled Physical (Symphonie) - Biogeochemical (Eco3M) Modeling



Zero contour of the vertical velocities:
 + upward
 - downward

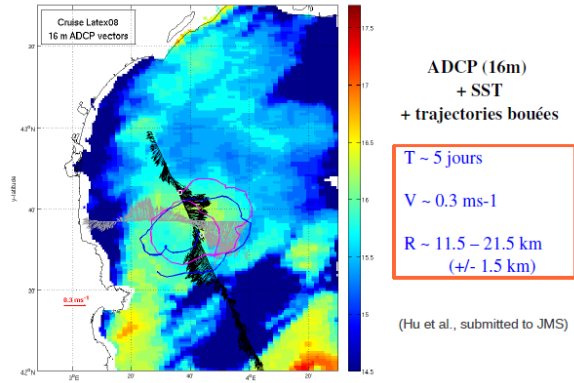
[Campbell et al., to be submitted]

MODÉLISATION – échanges (résultats préliminaires)



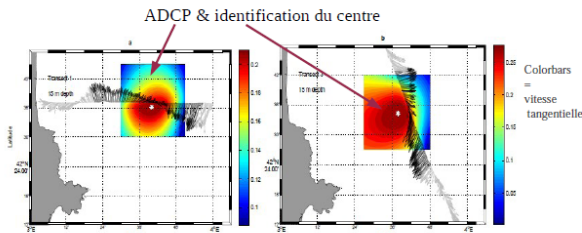
170 particules lancées le 11/08/2001 dans un transect de A1 eddy (toute la colonne d'eau) et intégrées pour 51 jours

EXPERIMENTAL - Latex08, 1-6 Septembre 2008



(Hu et al., submitted to JMS)

EXPERIMENTAL - Latex08, 1-6 Septembre 2008

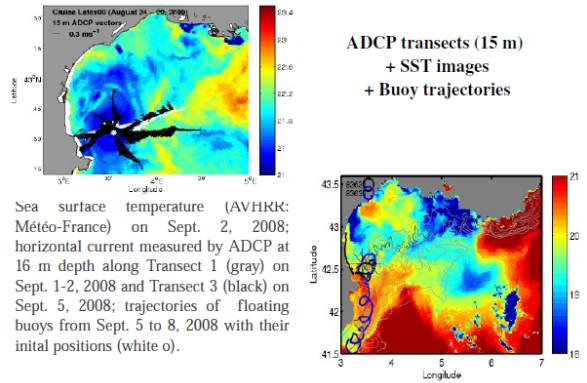


collaboration avec F. Nencioli, UCSB)

Center moved ~ 4 km in 5 days - Drift velocity 1.4 cm/s

Hu et al., submitted to JMS

EXPERIMENTAL - Latex09, 24-29 Août 2009



EXPERIMENTAL - Latex08 & Latex09

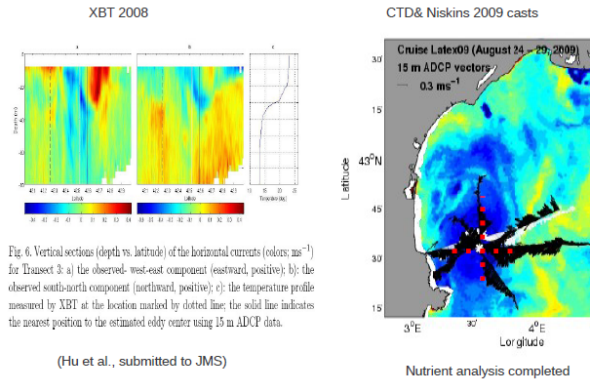
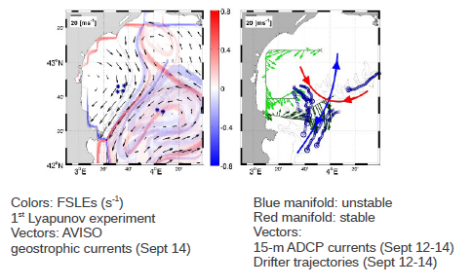


Fig. 6. Vertical sections (depth vs. latitude) of the horizontal currents (colors: ms^{-1}) for Transect 3 a) the observed west-east component (eastward, positive); b) the observed south-north component (northward, positive); c) the temperature profile measured by XBT at the location marked by dotted line; the solid line indicates the nearest position to the estimated eddy center using 15 m ADCP data.

(Hu et al., submitted to JMS)

Nutrient analysis completed

Latex10 (September 2010)
Example of Lyapunov exponents real-time experiments



[Nencioli et al., GRL, 2011]

38

Conclusions

- Physical model: 10 years of realistic simulations 2001 – 2010
- Characteristics of the eddies
- Eddy-induced coastal plankton community changes
- Generation process of the eddy : wind forcing + stratification

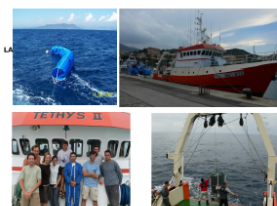
Perspectives

- Second generation mechanism (M. Kersale, PhD)
- Quantification of the coast-offshore exchanges; 2 cases :
 - 1) when the eddy is present : eddy-retention on the coastal shelf ? eddy interaction with the NC ?
 - 2) when there is no eddy : corridors as potential exit pathways ? (Latex10 case)
- Estimation of *in situ* eddy diffusivity (tracers and SCAMP)


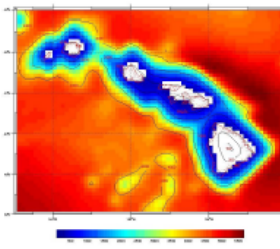
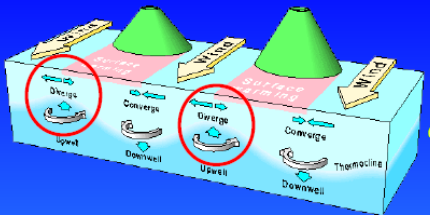
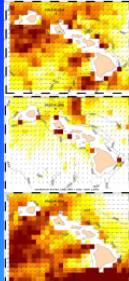
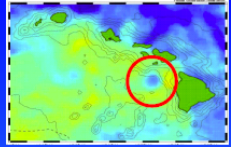
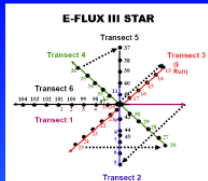
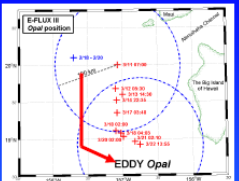
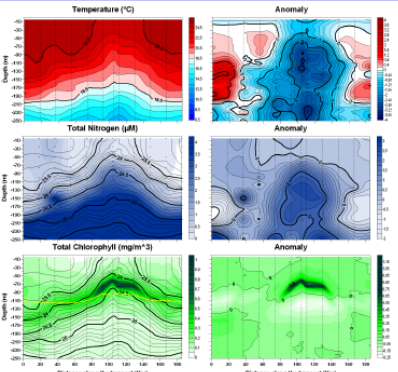
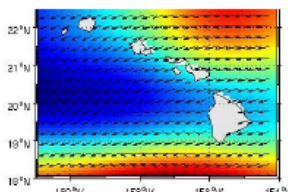
39

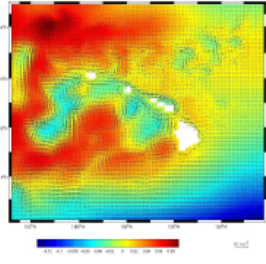
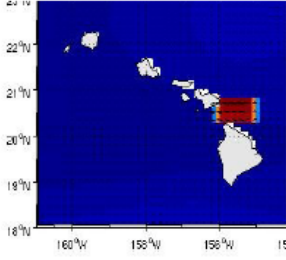
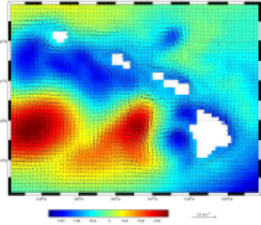
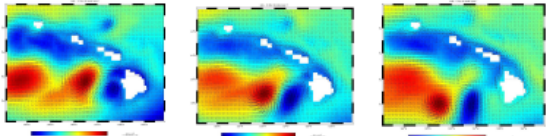
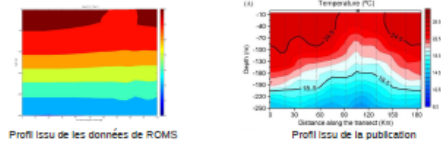
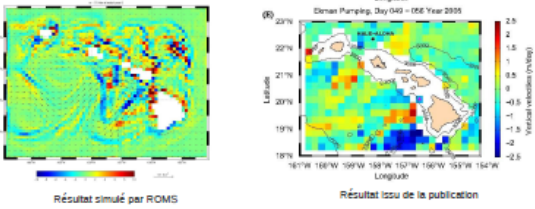
LATEX web site

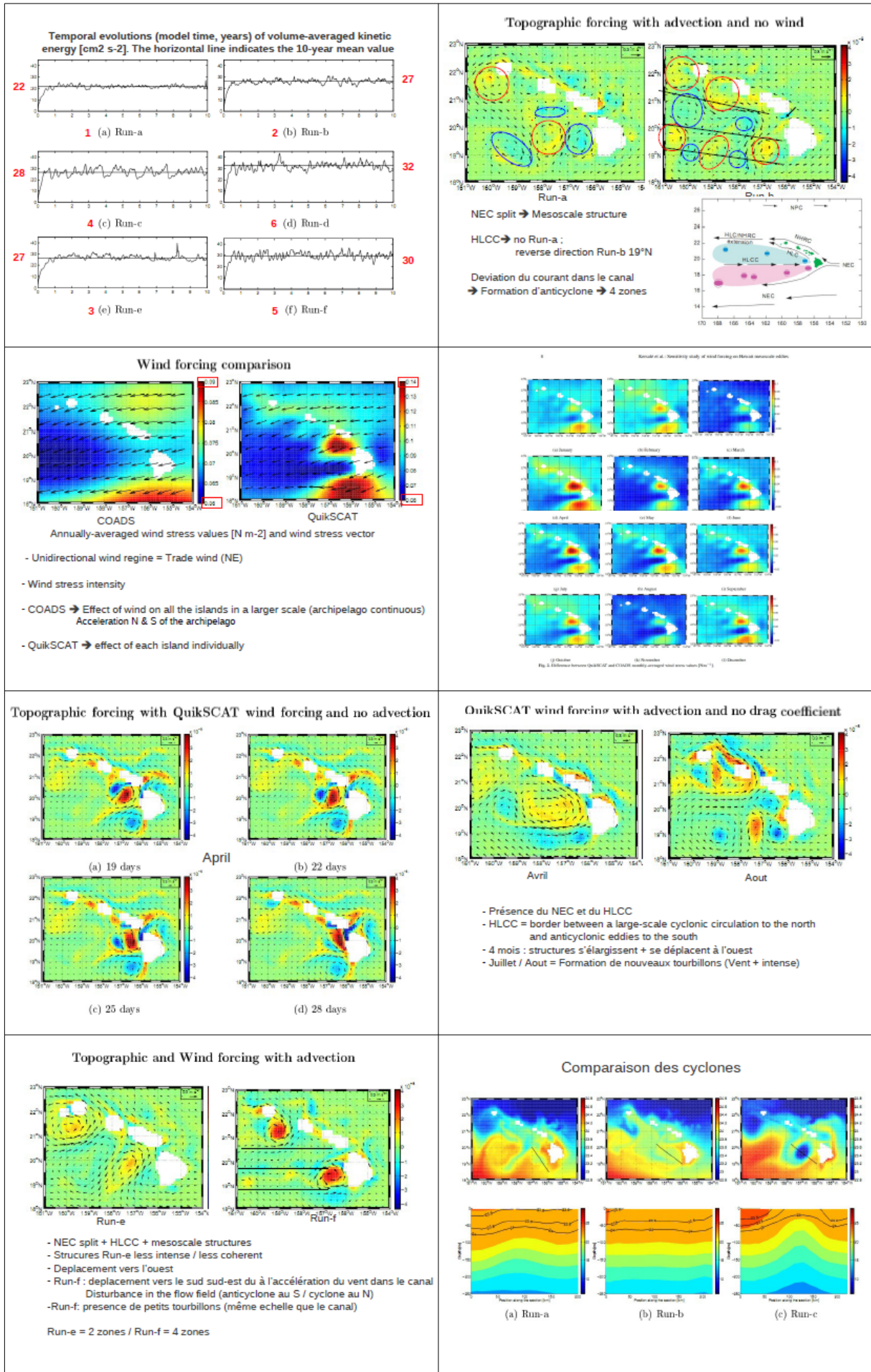
<http://www.com.univ-mrs.fr/LOPB/LATEX>

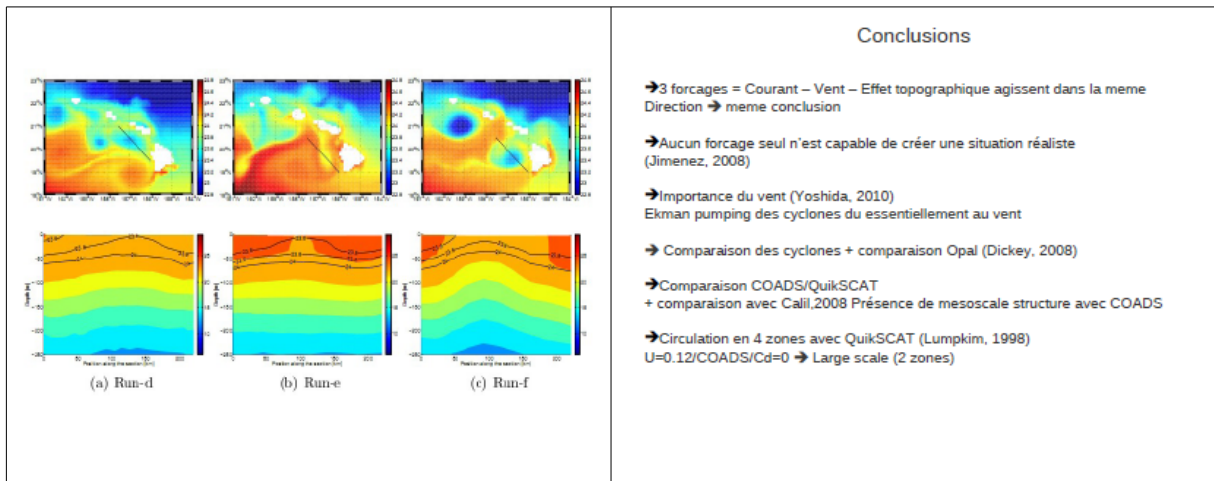


3.7 Example : circulation around the Hawai'ian islands

| | |
|---|--|
| <p>Introduction Modèle ROMS Résultats Conclusion</p> <p>→ Caractéristiques de la zone d'étude</p>  <ul style="list-style-type: none"> • Longitude : 154°40' - 162°W • Latitude : 16°55' - 23°N • Plus longue chaîne d'île au monde (2451 km de long) • Topographie élevée • Climat de type tropical | <p>Introduction Modèle ROMS Résultats Conclusion</p> <p>→ Implémentation du modèle</p>  <ul style="list-style-type: none"> • Construction de la grille : Lonmin=154°W - Lonmax=161°W Latmin=18°N - Latmax=23°N Frontières ouvertes : Nord, Sud, Est, Ouest Résolution : dl=1/10° Script <code>make_grid.m</code> → Figure de la bathymétrie + paramètres de la grille L=70, M=54, N=32 • Mise en place des forçages et des conditions initiales : Script <code>make_forcing.m</code> et <code>make_clim.m</code> • Calcul du pas de temps interne et externe Script <code>ad_cfl.m</code> → $\Delta t_i=720s$, $\Delta t_e=12s$ |
| <p>E-Flux Eddy formation in the lee of Hawaii</p>  <p>(Chevonne et al., 2002)</p> <ul style="list-style-type: none"> • Trade winds accelerate between islands • Different Ekman transport between channels and island wakes • Result in alternating divergences/convergences and up/downwelling • Spin up of cyclonic and anti-cyclonic eddies • Cyclonic eddies are biologically productive | <p>E-Flux The E-Flux Project</p> <p>Objective of the project was to study the physical and biogeochemical interactions within cyclonic eddies in the lee of Hawaii Islands.</p> <p>Three field experiments:</p> <ul style="list-style-type: none"> • E-Flux I (November 4-22, 2004): Cyclone Noah • E-Flux II (January 10-28, 2005): no eddies • E-Flux III (March 10-28, 2005): Cyclone Opal  |
| <p>Cyclone Opal E-Flux III: Cyclone Opal</p>  <p>Cold core of Opal appeared in GOESS SST in the second week of February</p> <p>(Courtesy of Carrie Leonard)</p> <p>Sampling strategy:</p> <p>Collected Data: CTD, ADCP, Optical Properties, Biogeochemical Variables and Microscopy from water samples</p> <p>Three week field experiment:</p> <ul style="list-style-type: none"> • Week 1 (Mar. 10 to 15): 6 Transects across the center of Opal • Week 2 (Mar. 16 to 22): Time series at the center of Opal (IN-stations) • Week 3 (Mar. 24 to 27): Time series outside Opal (OUT-stations) | <p>Cyclone Opal First week: 6 Transects</p>  <p>Planned spatial arrangement</p> <p>~160 Km North to South migration</p>  <p>6 transect had to be rearranged to follow Opal's migration</p> <p>Focus on transect 3 (red):</p> <ul style="list-style-type: none"> • closest to the center • Water samples |
| <p>Cyclone Opal CTD and Biogeochemical variables: Transect 3</p>  <ul style="list-style-type: none"> • Intense doming • ~80 km radius • Deep feature • Nutrients upwelled into the euphotic zone • Shoaling and intensification of the DCML • Diatom bloom!! | <p>Introduction Modèle ROMS Résultats Conclusion</p> <ul style="list-style-type: none"> • Simulations effectuées 1- Implémentation du modèle décrite précédemment Données de forçage du modèle : COADS Analyse des vecteurs et vitesse du vent au mois de Mars  <p>Aucune amplification du vent à la sortie du canal d'Alenuihaha</p> |

| Introduction | Modèle ROMS | Résultats | Conclusion | | | | | | | | | | | | | | | | | | | | | | | | | | | | |
|--|--------------|---|---|--------------|-------------------|---------------------|---|---|------|-----|---|---|------|-----|---|----------|---|-----|---|----------|------|------|---|-------|------|-----|---|----------|------|-----|--|
| <p>2- Domaine de simulation plus grand</p> <p>Analyse des vecteurs et vitesse du vent → Aucune amplification</p> | |  <p>Analyse des vecteurs du courant et du champ d'élévation le 8 Mars → Circulation océanique régionale (Lumpkin,1998)</p> | | | | | | | | | | | | | | | | | | | | | | | | | | | | | |
| | |  | <p>3- Modification du script <code>make_forcing.m</code> → impose une augmentation du vent dans le canal d'Alenuihaha</p> | | | | | | | | | | | | | | | | | | | | | | | | | | | | |
| <p>Visualisation du résultat</p> | |  <p>Analyse du champ d'élévation en surface le 14 Mars → Formation du tourbillon cyclonique OPAL</p> | | | | | | | | | | | | | | | | | | | | | | | | | | | | | |
| | |  <p>Champ d'élévation le 17/03/07, le 23/03/07, le 08/04/07</p> <p>Déplacement vers le Sud ensuite vers l'ouest</p> <p>Dans la publication : Déplacement du cyclone OPAL vers le sud et ensuite vers l'est.</p> <p>→ Propagation des tourbillons problématique</p> | <p>• Comparaison avec des résultats issues de la publication de Dickey & al. (2008)</p> <p>➢ Comparaison de la trajectoire du cyclone</p> | | | | | | | | | | | | | | | | | | | | | | | | | | | | |
| <p>➢ Comparaison d'un profil vertical en fonction de la température</p> | |  <p>Profil issu de les données de ROMS</p> <p>Profil issu de la publication</p> <p>Différence : Remontée des isothermes</p> <p>Similitude : 'Outcropping' d'une isotherme</p> | | | | | | | | | | | | | | | | | | | | | | | | | | | | | |
| | |  <p>Résultat simulé par ROMS</p> <p>Résultat issu de la publication</p> <p>Zones d'upwelling → $w = +2,5$ m/jour</p> <p>Zone de downwelling → $w = -2,5$ m/j</p> | <p>➢ Comparaison de la composante verticale de la vitesse du courant</p> | | | | | | | | | | | | | | | | | | | | | | | | | | | | |
| <p>IV- PREMIÈRE CONCLUSION</p> <ul style="list-style-type: none"> • Ile d'Hawaïi → Rôle important dans la circulation océanique et atmosphérique → Formation de tourbillons cycloniques et anticycloniques • Tourbillon + Alycée Nord → Variations locales de la température et de la salinité des eaux • Les structures du vent à méso-échelle doivent être incluses dans le forçage des modèles océaniques • Résultats difficiles à généraliser → Perturbations locales des flux dues à la présence de ces îles • Mêmes perturbations observées aux îles Canaries et aux îles du Cap-Vert | | <p>Différentes simulations</p> <table border="1"> <thead> <tr> <th>Run</th> <th>Wind forcing</th> <th>Advection (m s-1)</th> <th>Topographic forcing</th> </tr> </thead> <tbody> <tr> <td>a</td> <td>∅</td> <td>0.12</td> <td>oui</td> </tr> <tr> <td>b</td> <td>∅</td> <td>0.24</td> <td>oui</td> </tr> <tr> <td>c</td> <td>QuikSCAT</td> <td>∅</td> <td>oui</td> </tr> <tr> <td>d</td> <td>QuikSCAT</td> <td>0.12</td> <td>Cd=0</td> </tr> <tr> <td>e</td> <td>COADS</td> <td>0.12</td> <td>oui</td> </tr> <tr> <td>f</td> <td>QuikSCAT</td> <td>0.12</td> <td>oui</td> </tr> </tbody> </table> | Run | Wind forcing | Advection (m s-1) | Topographic forcing | a | ∅ | 0.12 | oui | b | ∅ | 0.24 | oui | c | QuikSCAT | ∅ | oui | d | QuikSCAT | 0.12 | Cd=0 | e | COADS | 0.12 | oui | f | QuikSCAT | 0.12 | oui | |
| Run | Wind forcing | Advection (m s-1) | Topographic forcing | | | | | | | | | | | | | | | | | | | | | | | | | | | | |
| a | ∅ | 0.12 | oui | | | | | | | | | | | | | | | | | | | | | | | | | | | | |
| b | ∅ | 0.24 | oui | | | | | | | | | | | | | | | | | | | | | | | | | | | | |
| c | QuikSCAT | ∅ | oui | | | | | | | | | | | | | | | | | | | | | | | | | | | | |
| d | QuikSCAT | 0.12 | Cd=0 | | | | | | | | | | | | | | | | | | | | | | | | | | | | |
| e | COADS | 0.12 | oui | | | | | | | | | | | | | | | | | | | | | | | | | | | | |
| f | QuikSCAT | 0.12 | oui | | | | | | | | | | | | | | | | | | | | | | | | | | | | |





Conclusions

- 3 forcages = Courant – Vent – Effet topographique agissent dans la meme Direction → meme conclusion
- Aucun forçage seul n'est capable de créer une situation réaliste (Jimenez, 2008)
- Importance du vent (Yoshida, 2010)
Ekman pumping des cyclones du essentiellement au vent
- Comparaison des cyclones + comparaison Opal (Dickey, 2008)
- Comparaison COADS/QuikSCAT
+ comparaison avec Calif,2008 Présence de mesoscale structure avec COADS
- Circulation en 4 zones avec QuikSCAT (Lumpkin, 1998)
 $U=0.12/COADS/Cd=0$ → Large scale (2 zones)

Add here a few slides on Marquises

4. Isolated eddies

Definition (Carton, 2005)

Recirculations can happen at virtually any scale in the ocean, from large ocean gyres ($L = O(5000\text{km})$) to small-scale turbulence ($L = O(1\text{km})$). Between these two extremes we have so-called mesoscale eddies ($L = O(100\text{km})$) which are particularly interesting: although present in different forms and produced by different mechanisms, they are highly energetic and persist for a long time. They often travel great distances and play a very important role in ocean dynamics which is why we study them.

Apart from a long lifespan, oceanic eddies are characterised by an intense and closed flow that is typically blocked in the horizontal plane by planetary rotation and stratification. Often they have an almost circular shape with radii of 20 to 200 km and a relative vorticity that can reach a considerable fraction of the planetary vorticity.

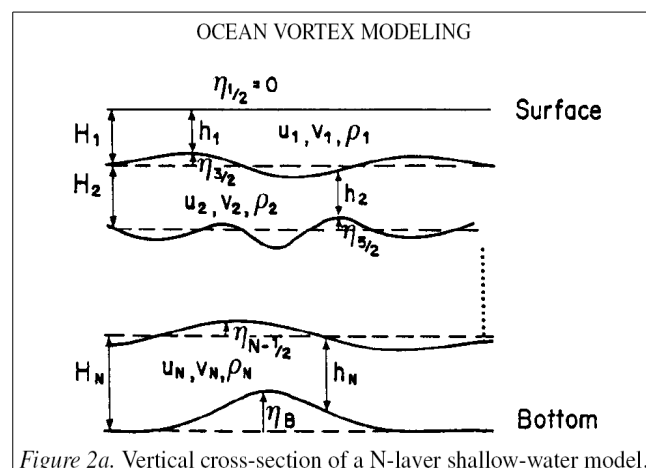
The characteristic recirculation times at the radius of maximal velocity are of the order of a few days. Beyond this radius, the tangential velocities decrease rapidly as a function of distance from the centre. Except in their areas of formation, mesoscale eddies typically are isolated structures with large distances in-between them so they do not typically interact with other eddies for long periods of time. However, if such an interaction does occur, the result can be highly destructive. Mesoscale eddies can also disappear rather quickly whenever they interact with strong currents or when they encounter strong topographic gradients. Dispersion, dissipation, and heat exchange with the atmosphere are processes that generally lead to a more gradual destruction of the eddies.

Ocean eddies can trap characteristic water masses at their core for long periods of time. In fact, they are often the end product of local instabilities and trap bodies of water from their region of origin. This water is then transported by the eddies across the ocean with only little mixing occurring at the eddy's outer perimeter.

In areas of eddy formation, fine filaments or small-scale convective movements (in the case of static instabilities) can also contribute to energy transfers and local mixing processes. Vortices can also affect local thermodynamics by promoting the propagation of inertial waves and the penetration of atmospheric fluxes or the subduction of water from the mixing layer under large-scale fronts.

6.1 Equations describing the dynamics of isolated eddies

The ocean can be approximated as a succession of homogeneous layers (isopycnal model). In general, the thickness of each layer varies from some 10m to 100-200m, while horizontal mesoscale motions occur on scales ranging from tens to hundreds of kilometres. This large difference in scales allows us to employ the Boussinesq approximation, the hydrostatic approximation, and the shallow water equations.



$$\begin{aligned}
\frac{Du_j}{Dt} - f v_j &= \partial_t u_j + u_j \partial_x u_j + v_j \partial_y u_j - f v_j = \frac{-1}{\rho_j} \partial_x p_j + F_{xj}, \\
\frac{Dv_j}{Dt} + f u_j &= \partial_t v_j + u_j \partial_x v_j + v_j \partial_y v_j + f u_j = \frac{-1}{\rho_j} \partial_y p_j + F_{yj}, \\
\frac{Dh_j}{Dt} + h_j \vec{\nabla} \cdot \vec{u}_j &= \partial_t h_j + u_j \partial_x h_j + v_j \partial_y h_j + h_j (\partial_x u_j + \partial_y v_j) = 0 \quad (1)
\end{aligned}$$

where $u_j, v_j, p_j, h_j, \rho_j, F_j$, represent, respectively, the horizontal velocity components, pressure, the layer thickness, density, and the volume forces in the j^{th} layer (where j varies from 1 at the surface to N at the seabed).

f is the Coriolis parameter on a horizontal plane β , $f = f_o + \beta y$.

The local layer thickness is $h_j = H_j + \eta_{j-1/2} - \eta_{j+1/2}$ with H_j the thickness of the layer at rest and $\eta_{j+1/2}$ the interface between layers j and $j+1$ due to local movement. In the vertical, one often applies a rigid-lid approximation at the surface, i.e., ($\eta_{1/2} = 0$), while the bottom topography is described by $\eta_{N+1/2} = \eta_B(x, y)$.

Finally, the hydrostatic balance is

$$p_j = p_{j-1} + g(\rho_j - \rho_{j-1})\eta_{j-1/2}.$$

Oceanic eddies can be considered circular and the dynamic equations can be reformulated in polar coordinates (omitting the index j):

$$\begin{aligned}
\frac{Dv_r}{Dt} - \frac{v_\theta^2}{r} - f v_\theta &= \partial_t v_r + v_r \partial_r v_r + \frac{v_\theta}{r} \partial_\theta v_r - \frac{v_\theta^2}{r} - f v_\theta = \frac{-1}{\rho} \partial_r p + F_r, \\
\frac{Dv_\theta}{Dt} + \frac{v_r v_\theta}{r} + f v_r &= \partial_t v_\theta + v_r \partial_r v_\theta + \frac{v_\theta}{r} \partial_\theta v_\theta + \frac{v_r v_\theta}{r} + f v_r = \frac{-1}{\rho r} \partial_\theta p + F_\theta, \\
\frac{Dh}{Dt} + h \vec{\nabla} \cdot \vec{v} &= \partial_t h + v_r \partial_r h + \frac{v_\theta}{r} \partial_\theta h + \frac{h}{r} (\partial_r (r v_r) + \partial_\theta v_\theta) = 0, \quad (2)
\end{aligned}$$

In the absence of any forcing and dissipation ($F = 0$), a circular eddy is an invariant solution to these equation on the f -plane ($\beta = 0$). Hence, if $\partial_t = 0, v_r = 0, \partial_\theta = 0$ then then last two equations disappear and the first equation reduces to

$$-\frac{v_\theta^2}{r} - f_0 v_\theta = \frac{-1}{\rho} \frac{dp}{dr}. \quad (3)$$

This equation is called the *gradient wind balance* (Cushman-Roisin, 1994). It describes the balanced state between centrifugal forces created by the eddy's rotation, the Coriolis force, and the radial pressure gradient. Whenever the centrifugal force is negligible (i.e., the rotation is weak) the balance simply becomes the geostrophic balance.

Satellite-derived altimetry

add slides from Jerome here

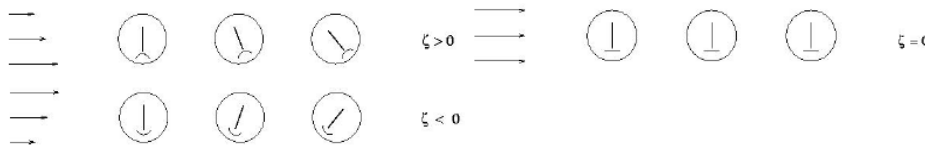
4.2 Vorticity

Relative vorticity

It is defined as the vertical component of the velocity curl

$$\zeta = \vec{k}(\nabla \times \vec{V}) = \frac{\partial v}{\partial x} - \frac{\partial u}{\partial y}$$

The relative vorticity denotes the tendency of a fluid to rotate. The sign of ζ can be illustrated using the schematic below:



It is termed “relative” vorticity as it is measured relative to the Earth’s rotation.

Planetary vorticity

The vorticity of a solid body in rotation equals twice its angular velocity. At a latitude Φ the angular velocity is $\Omega \sin \Phi$ which yields a vorticity of

$$2 \Omega \sin \Phi = f$$

A water column at rest on a rotating Earth therefore possesses a so-called “planetary” vorticity f . The planetary vorticity corresponds to the Coriolis parameter under the so-called “quasi-geostrophic” approximation (see TD4).

Absolute vorticity

We take the momentum equations for the horizontal components which we assume to be invariant on the vertical. By neglecting viscosity and friction (i.e., by positioning ourselves outside the Ekman and boundary layers along western coastlines):

$$\begin{aligned} \frac{\partial u}{\partial t} + u \frac{\partial u}{\partial x} + v \frac{\partial u}{\partial y} - fv &= -\frac{1}{\rho_o} \frac{\partial p}{\partial x} \\ \frac{\partial v}{\partial t} + u \frac{\partial v}{\partial x} + v \frac{\partial v}{\partial y} + fu &= -\frac{1}{\rho_o} \frac{\partial p}{\partial y} \end{aligned}$$

Cross differentiation and subtraction $\partial_x(2) - \partial_y(1)$

$$\begin{aligned} \frac{\partial}{\partial y} \frac{\partial u}{\partial t} + \frac{\partial u}{\partial y} \frac{\partial u}{\partial x} + u \frac{\partial^2 u}{\partial y \partial x} + \frac{\partial v}{\partial y} \frac{\partial u}{\partial y} + v \frac{\partial^2 u}{\partial y^2} - \frac{\partial f}{\partial y} v - f \frac{\partial v}{\partial y} &= -\frac{1}{\rho_o} \frac{\partial^2 p}{\partial y \partial x} \\ \frac{\partial}{\partial x} \frac{\partial v}{\partial t} + \frac{\partial u}{\partial x} \frac{\partial v}{\partial x} + u \frac{\partial^2 v}{\partial x^2} + \frac{\partial v}{\partial x} \frac{\partial v}{\partial y} + v \frac{\partial^2 v}{\partial x \partial y} + \frac{\partial f}{\partial x} u + f \frac{\partial u}{\partial x} &= -\frac{1}{\rho_o} \frac{\partial^2 p}{\partial x \partial y} \end{aligned}$$

yields a single equation (remembering that $\frac{df}{dt} = \frac{\partial f}{\partial t} + u \frac{\partial f}{\partial x} + v \frac{\partial f}{\partial y}$)

$$\frac{\partial}{\partial t} \left(\frac{\partial v}{\partial x} - \frac{\partial u}{\partial y} \right) + \frac{\partial u}{\partial x} \left(\frac{\partial v}{\partial x} - \frac{\partial u}{\partial y} \right) + u \frac{\partial}{\partial x} \left(\frac{\partial v}{\partial x} - \frac{\partial u}{\partial y} \right) + \frac{\partial v}{\partial y} \left(\frac{\partial v}{\partial x} - \frac{\partial u}{\partial y} \right) + v \frac{\partial}{\partial y} \left(\frac{\partial v}{\partial x} - \frac{\partial u}{\partial y} \right) + \frac{df}{dt} + f \left(\frac{\partial u}{\partial x} + \frac{\partial v}{\partial y} \right) = 0$$

which can be written as

$$\frac{\partial}{\partial t} \zeta + \frac{\partial u}{\partial x} \zeta + u \frac{\partial \zeta}{\partial x} + \frac{\partial v}{\partial y} \zeta + v \frac{\partial \zeta}{\partial y} + \frac{df}{dt} + f \left(\frac{\partial u}{\partial x} + \frac{\partial v}{\partial y} \right) = 0$$

Regrouping terms 1, 3, and 5 which represent the total derivative of relative vorticity and also terms 2 and 4

$$\frac{d\zeta}{dt} + \zeta \left(\frac{\partial u}{\partial x} + \frac{\partial v}{\partial y} \right) + \frac{df}{dt} + f \left(\frac{\partial u}{\partial x} + \frac{\partial v}{\partial y} \right) = 0$$

and finally

$$\frac{d(\zeta + f)}{dt} + (\zeta + f) \left(\frac{\partial u}{\partial x} + \frac{\partial v}{\partial y} \right) = 0$$

This equation states the principle of the conservation of absolute vorticity $\zeta_{abs} = (\zeta + f)$ for those flows for which friction can be neglected: the absolute value of absolute vorticity increases in a converging flow ($\nabla_H \vec{u} < 0$) and decreases in a diverging flow ($\nabla_H \vec{u} > 0$) .

Potential vorticity

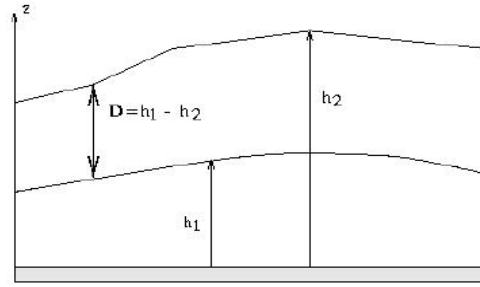
Let us assume a layer of thickness D in which the density is homogeneous.

The continuity equation becomes:

$$\frac{\partial u}{\partial x} + \frac{\partial v}{\partial y} + \frac{\partial w}{\partial z} = 0$$

and we can write:

$$\frac{\partial w}{\partial z} = \frac{\left(\frac{dh_1}{dt} - \frac{dh_2}{dt} \right)}{(h_1 - h_2)} = \frac{1}{D} \frac{dD}{dt}$$



which - through substitution in the continuity equation - yields

$$\frac{1}{D} \frac{dD}{dt} = - \left(\frac{\partial u}{\partial x} + \frac{\partial v}{\partial y} \right)$$

We can then replace the horizontal divergence in the conservation equation for absolute vorticity and obtain

$$\frac{d}{dt} \left(\frac{\zeta + f}{D} \right) = 0$$

NB: We have used the quotient rule to find the derivative:

$$\frac{d}{dt} \left(\frac{\zeta_a}{D} \right) = 0 \rightarrow \left(\frac{d\zeta_a}{dt} D - \zeta_a \frac{dD}{dt} \right) \frac{1}{D^2} = 0 \rightarrow \frac{d\zeta_a}{dt} \frac{1}{D} - \zeta_a \frac{dD}{dt} \frac{1}{D^2} = 0 \rightarrow \frac{d\zeta_a}{dt} - \zeta_a \frac{dD}{dt} \frac{1}{D} = 0$$

If we compare the dimension of all four types of vorticity: relative, planetary, absolute, and potential, we have

$$\zeta_{rel} : \left[\frac{LT^{-1}}{L} \right] = [T^{-1}] \quad \zeta_{pla} : [T^{-1}] \quad \zeta_{abs} : [T^{-1}] \quad \zeta_{pot} : \left[\frac{T^{-1}}{L} \right] = [T^{-1}L^{-1}]$$

The odd one out is thus the potential vorticity.

NB: A more general formulation of potential vorticity also accounts for effects of density, temperature, salinity and other environmental parameters and the dimension depends on the type of parameters that have been taken into account.

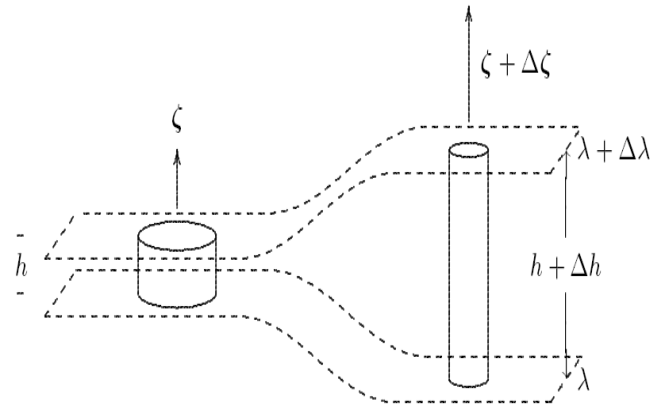
$$\frac{d}{dt} \left(\zeta_{abs} \cdot \frac{\nabla \lambda}{\rho} \right) = 0$$

Example: Intensification of stretched vortices

If we place ourselves on the f -plane

$$\left(\frac{\zeta}{D}\right) = \text{const}$$

then, a column of water, moving between two surfaces on which λ must be conserved, must change in order to satisfy the laws of conservation of mass and angular momentum. The greater the height of the water column the greater its rotational velocity.



$$\Delta D > 0 \rightarrow \Delta \zeta > 0$$

$$\Delta D < 0 \rightarrow \Delta \zeta < 0$$

From Mattioli (1995) Principi Fisici di Oceanografia e Meteorologia, Fig.48.1

Potential vorticity anomaly

Considering that the rotation of a vortex is associated with a displacement of the isopycnals, a physical variable that combines both quantities and the Coriolis parameter would be most suitable for characterizing the vortex dynamics. This variable is the potential vorticity (PV) which is conserved in models based on shallow water equations without friction.

$$\frac{d \Pi_j}{dt} = 0 \quad \Pi_j = \frac{\zeta_j + f}{h_j}$$

where ζ_j is the relative vorticity and f the planetary vorticity.

In reality, the vortex dynamics can be fully characterized by knowing the difference in potential vorticity between the inside and outside of the vortex. In addition, the meridional variability of the planetary vorticity is typically much weaker than the relative vorticity. We can therefore define the PV-anomaly:

$$Q_j = \Pi_j - \Pi_j^o = \frac{\zeta_j + f_o}{h_j} - \frac{f_o}{H_j} = \frac{1}{h_j} \left(\zeta_j - f_o \frac{\delta \eta_j}{H_j} \right)$$

with $\delta \eta_j = h_j - H_j$ the vertical variation in isopycnal surfaces inside the vortex. Remember that the PV-anomaly itself is not conserved and that interactions with planetary vorticity can have significant consequences such as vortex drift.

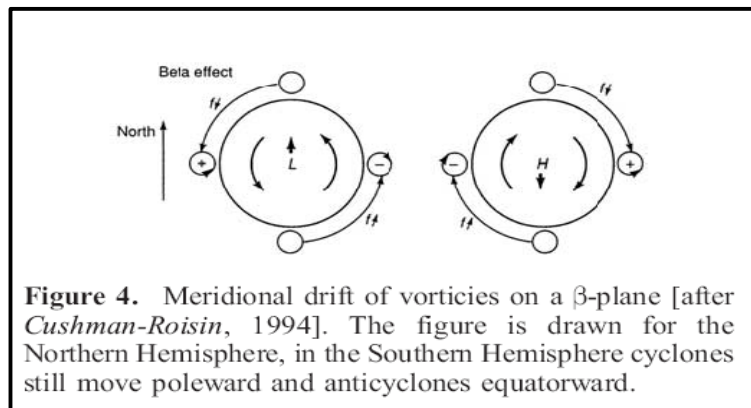
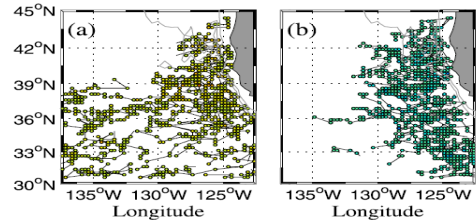
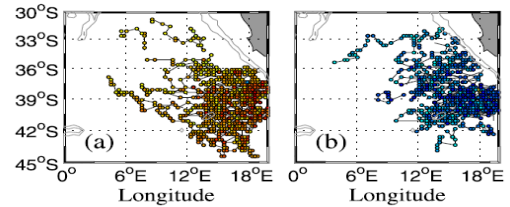
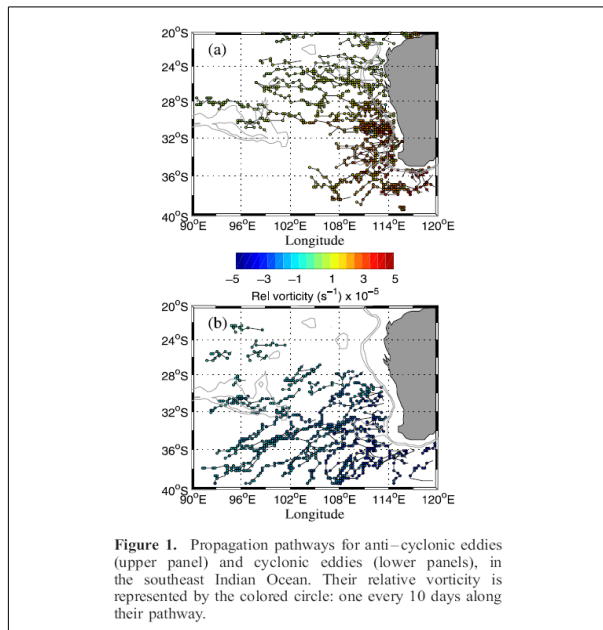


Figure 4. Meridional drift of vortices on a β -plane [after Cushman-Roisin, 1994]. The figure is drawn for the Northern Hemisphere, in the Southern Hemisphere cyclones still move poleward and anticyclones equatorward.



4.3 Example: Meddies

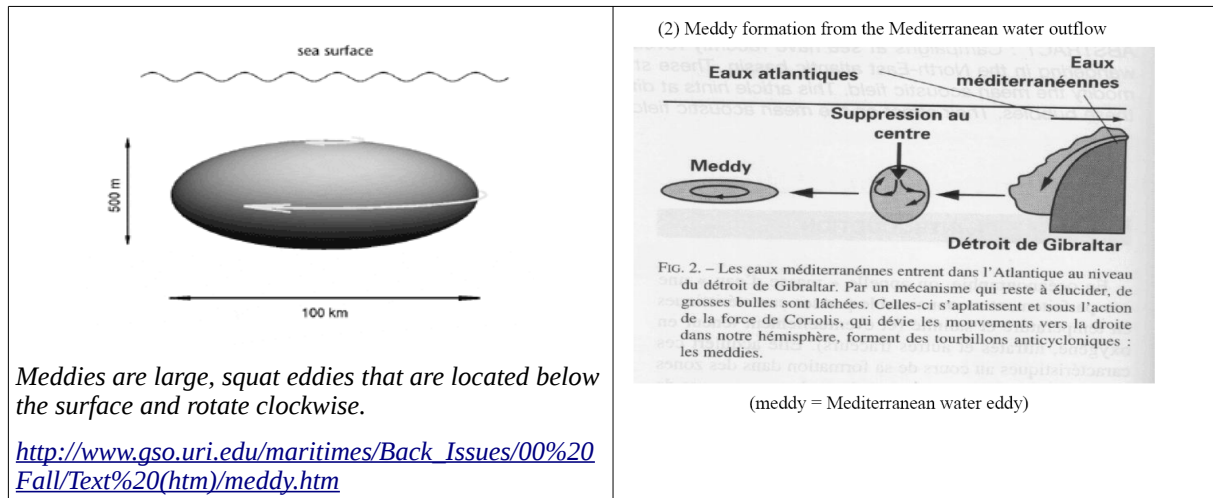
Historically, the discovery of meddies is based on an error (see McDowell and Rossby's online article [http://www.gso.uri.edu/maritimes/Back_Issues/00%20Fall/Text%20\(htm\)/meddy.htm](http://www.gso.uri.edu/maritimes/Back_Issues/00%20Fall/Text%20(htm)/meddy.htm)). First of all, in 1976, researchers discovered a huge whirlpool off the Bahamas that was very hot and very salty. This led them to conclude that this eddy was of Mediterranean origin. This discovery provided the impetus to start searching for similar structures. A systematic study was carried out between 1984 and 1986 in the North-East and North-West Atlantic. Although some meddies were indeed discovered in the NE Atlantic, none had the size of the by then famous "Bahamas Meddy". No meddy was detected in the NW basin. The researchers honestly admitted their mistake, which forced them to seek an alternative explanation for the origin of this eddy. The solution was found much later, in the 90s: the Bahamas Meddy had originated from the North Atlantic Current, an extension of the Gulf Stream, after it had turned northwards at the level of the Grand Banks of Newfoundland. From time to time, the waters meander and detach from the main current to become anti-cyclonic eddies with relatively warm (10.8°C observed) and salty (35.4 g/l observed) cores. The "double irony" of which the authors speak is therefore based on the fact that it was the "false" Bahamas Meddy which led to the discovery of real meddies, although their error led to the discovery that the North Atlantic Current can generate vortices capable of moving over distances exceeding 4000 km along the North American continent.

In his 1985 paper, McWilliams provided the figure below and the following explanation:

For lack of more complete observations, we identify this water with the end-state of the convection process; this would indicate a dilution of the outflow water with 1-2 times as much Atlantic water, depending upon the depths at which the entrainment occurs. The relatively well mixed blobs then undergo an adjustment process and acquire a geostrophic or cyclostrophical anticyclonic circulation (process(2) in Figure 5) (see appendix, note 2). This protects the core water mass from straining and diffusion by the general circulation as the latter advects Meddies into the interior of the Atlantic, approximately along the $\sigma = 27.6$ potential density surface.

Cross sections of the locally anomalous salinity cores are shaded at processes (3) and (4) in Figure 5, where the horizontal scale has been exaggerated by a factor of 5 relative to the abscissa. These particular Meddies are depictions of the observations of Arnni and Zenk [1984] for Meddy (3) and of McDowell and Rossby [1978] and McDowell r1985a-I for Meddy (4). From maps of the salinity anomalies the approximate dimensions of Meddy (3) are $L = 40$ km and $h = 300$ km, while for Meddy (4), $L = 60$ km and $h = 200$ km. Adjacent to the cross sections are values for the local maximum S , maximum salinity anomaly relative to the local environment $5S$, N for the environment at the depth of the Meddy core, and latitude. In the migration away from Gibraltar, S and $5S$ systematically decrease, consistent with weak diffusion en route. Between Meddies (3) and (4) there is also a change of core volume and shape: the volume increases by about 50% (again a sign of diffusion), and the aspect ratio h/L decreases from about 0.0075 to 0.0033. The latter might be an indication of anisotropic diffusion (horizontal dominating vertical), but it may also reflect a partial compensation for the changing N/f of the Meddy environment in such a way as to tend to preserve the B value for the SCV:

N/f changes from 42 to 70, so that B only changes from 0.32 to 0.23. The lifetime of the Meddy at (4) is more than 4 years by the previous estimate of the general circulation transport rate. Destruction of a Meddy (process (5)) probably occurs when interactions with other currents fragment the core water mass.



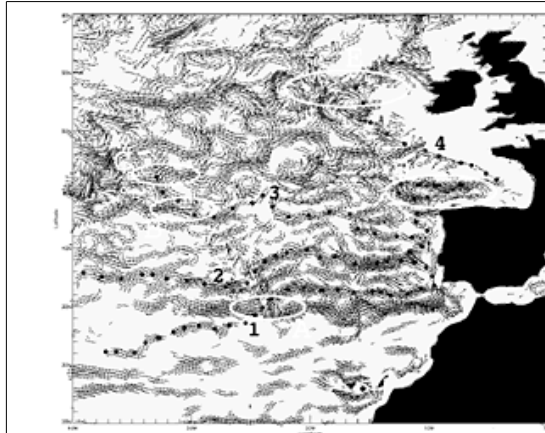
Meddies are large, squat eddies that are located below the surface and rotate clockwise.

[http://www.gso.uri.edu/maritimes/Back_Issues/00%20Fall/Text%20\(htm\)/meddy.htm](http://www.gso.uri.edu/maritimes/Back_Issues/00%20Fall/Text%20(htm)/meddy.htm)

Mediterranean waters swirl in the Atlantic

From http://www.mercator-ocean.fr/html/actualites/news/actu_meddies_fr.html

Off Gibraltar, the Mediterranean and Atlantic waters meet. The Atlantic waters enter the Mediterranean at the surface while Mediterranean water, being more dense, flows out into the Atlantic at the bottom of the strait, forming a Mediterranean water vein. Under certain conditions, this vein can give rise to eddies which will then propagate across the Atlantic. These are the so-called meddies or Mediterranean lenses. The high resolution Mercator model of the Atlantic is able to simulate such events.



Mean velocity (averaged over 3 years) at a depth of 870 m derived from the PAM model: the presence of Mediterranean water is marked by zones of higher velocities (appearing darker in the figure). The dotted lines show the main trajectories of the four main Mediterranean water veins. Credit: Yann Drillet et al., 2005 (click to enlarge)

The Strait of Gibraltar (250m deep, 15 to 20 km across) is the only location where the Mediterranean exchanges water with the outside. The warmer, saltier, and denser Mediterranean water flows into the Atlantic at the bottom of the strait at an average rate of around 0.57 Sv. In order to restore the balance, Atlantic water (colder and less salty) enters the Mediterranean at the surface. As the Mediterranean loses more water due to evaporation than it receives from rain and riverine inflows, there is more Atlantic water coming in than Mediterranean water going out.

Upon crossing the Gibraltar Strait, the denser Mediterranean water plunges between 800 and 1200m into the Gulf of Cadiz where total water depths reach 4000 to 5000m. The main outflow turns northward and continues to flow up along the Portuguese coast and into the Bay of Biscay where it flows along the continental slope and continues its way to the coast of Ireland at around 50°N.

Another branch of the Mediterranean water flows west, leaving the Spanish coast near Cape St-Vincent, at 36°N, from where it flows out to 25°W. The outflow velocity of Mediterranean water near the bottom of the Strait of Gibraltar is of the order of 15 cm/s. Between the sill and a depth of 700m, in an area centred at about 6.5°W and 36°N, this speed can reach 1 m/s. The flow then stabilizes downstream from Cap St-Vincent at a depth of 1000 m with speeds of the order of 15 cm/s. Salinity is also a crucial factor for identifying Mediterranean water. We define a high salinity core as having salinities greater than 35.8 g/kg.

Mediterranean water lenses (or Mediterranean eddies or meddies) are eddies (typically anticyclonic,

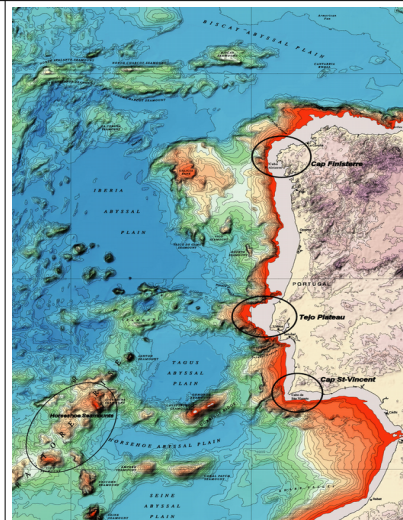
i.e., rotating clockwise) with relatively warm and salty cores, born out of instabilities generated by the passage through the Gibraltar Strait and as it passes over rough topography (e.g., the passage of Cape St Vincent near the south-western tip of Spain, the Tejo Plateau off Lisbon, and Cape Finisterre at the north-western tip of Spain).

The meddy rotation period (time to complete a complete revolution) can vary from 3 to 24 days with an average of 8 days. Their typical translation speed is of the order of 2 cm/s. It is estimated that about 70% collide with the Horseshoe Seamounts (west-southwest of Cape St. Vincent) and either disintegrate or at least weaken significantly. The remaining 30% bypass the seamounts to the north and reach the Canary Basin.

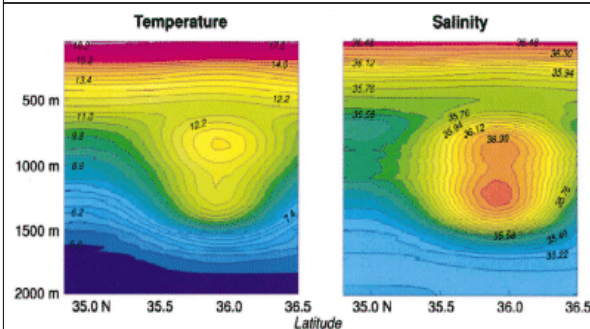
The average lifespan of a newly formed meddy is estimated to be 1.7 years, although some have been observed to last 5 years. It is estimated that around 20 meddies are formed each year which, considering their their lifespan, suggests that about 30 meddies are constantly roaming the North Atlantic.

We have observed two meddies colliding and also the opposite: their separation.

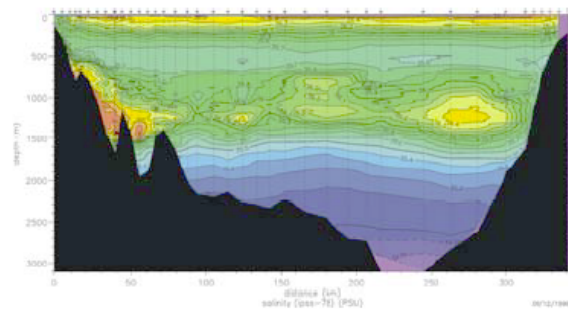
North Atlantic Deep Water is partly fed by these Meddies which add both heat and salt.



Bathymetry of the meddy generation zone. Credit: [Bulletin de la Société Géologique de France](#)



Vertical sections of temperature and salinity through a meddy measured in July 1993 in the Canary Basin at around 36°N, 28°W. This meddy had two local maxima for both temperature and salinity with values reaching 13.2°C and 34.4 g/l at 850 m and 12.3°C and 34.5 psu at 1250 m. The anomaly with respect to the surrounding water reached 4.1°C and 1.1 g/l at 1250 m. The total diameter was 120 km
Credit: Tychensky and Carton, 1998

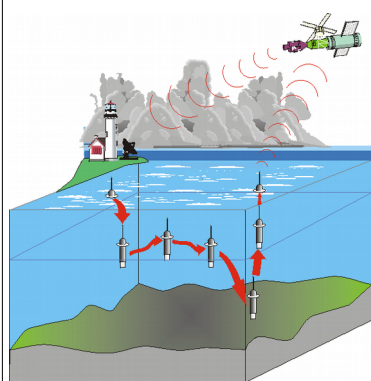


Salinity section between Portugal (left) and Morocco (right), along 8.2°W, from measurements made during the Semane campaign in July 1999. A cyclonic eddy can be seen near the centre of the transect and a meddy toward the Moroccan coast.

Credit : V. Thierry, X. Carton and J. Paillet.

Researchers aboard an oceanographic research vessel need a great deal of luck to be able to observe a meddy and observations are indeed rare. Since the altimetry signal is quite weak, they cannot be located using remote sensing data (some studies have investigated this issue, see for example <http://conference.iproms.org/presentation/145>), however, the few observations that exist have been published in specialized journals (Richardson et al., 2000, Tychensky and Carton, 1998). The observed meddy radii were between 20 and 80 km and their vertical extents between 800 and 1400 m, with the meddy core at about 1000 m depth. At the meddy core, salinities reached up to 36.37 g/l and a temperature of 13.2°C. Other observations have been made using Argo floats (sensors periodically diving to 2000 m to measure temperature and salinity along their trajectory and relaying their data to the Argos satellites when they return to the surface).

The international Argo program



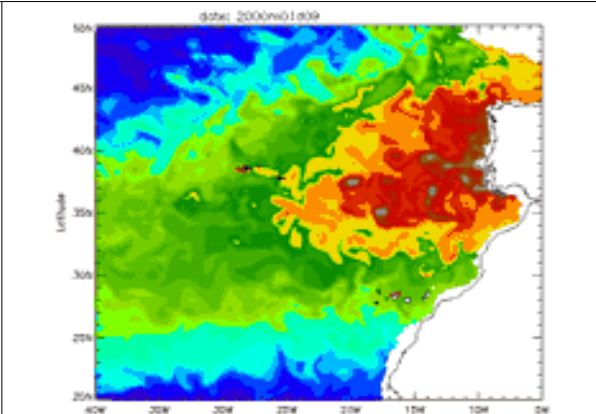
http://www.mercator-ocean.fr/html/actualites/news/actu_argo2000_fr.html

By the mid-1990s, pioneers of ocean forecasting had understood that altimetry data from satellites, essential for operational oceanography, did not provide sufficient information to construct detailed models of the processes taking place in the deep ocean. In 2000, the deployment of Argo floats began as part of an international program.

Argo aims to deploy and maintain a network of around 3000 profiling floats, globally distributed on a 3° × 3° grid, measuring temperature and salinity profiles down to depths of 2000 m, hence their name "Argo profiler". In addition, they measure the current speed at several depths. Through data assimilation these three parameters are then fed into models to improve their accuracy. The Argo program was initiated as a support for operational oceanography and seasonal and inter-annual climate forecasting programs. Each float rises to the surface every ten days and transmits its data to [Argos](#) satellites (also other systems such as Iridium are being used) before diving back down to 2000 m. The data is distributed free of charge and without any restrictions in real time via the Global Transmission System (GTS) as well as over the internet. 17 countries plus the European Union participate in the Argo network. The [Coriolis](#) project is the French Argo partner; it contributes instrumentation (development of the Provor model), facilitates instrument deployment, and provides data processing (Coriolis is one of the two Argo Global Data Centres).

An in-depth study carried out by the Mercator Ocean modelling team aimed to assess the capacity of the North Atlantic Mediterranean Prototype (PAM) to simulate these structures.

This experiment was carried out without data assimilation. Apart from a realistic bathymetry and some initial climatological conditions (an average state of the ocean) the model was only forced with atmospheric parameters (wind, heat flux, evaporation, precipitation). The model has a horizontal resolution of 5 to 7 km and covers the Atlantic Ocean and Mediterranean Sea. In the vertical, the resolution ranges from 6m near the surface to 300m near the bottom. The mean layer thickness is about 100 m in the Mediterranean (surface layers are thinner than deep layers to better represent complex surface phenomena). The simulation covers the 5 years period from 1998 to 2002.

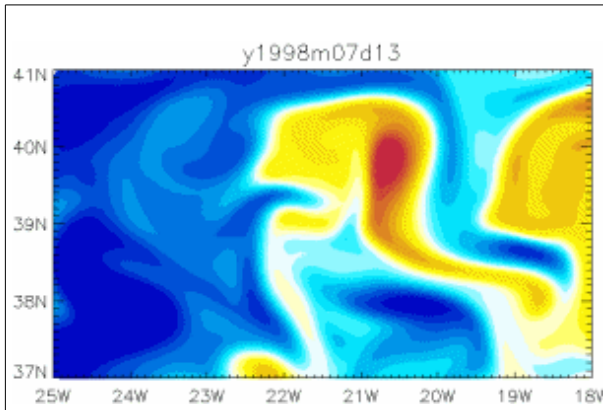


PAM simulation for the year 2000 showing the salinity at 870m; meddies can be identified by their grey coloured centres. Credit: Yann Drillet

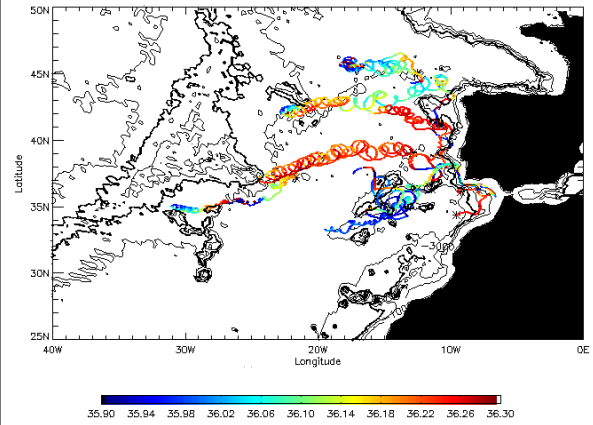
The results demonstrated the model’s capability to simulate meddies. Such simulations improve our understanding of meddy formation and allow us to study their preferred routes during their voyage into the Atlantic.

The model can also simulate processes like meddy collisions and separation (see animation below). A method for monitoring meddies using Lagrangian trajectories makes it possible to follow the trajectory of the vortices as illustrated in the figure below. Although a 5-year simulation is not long enough to study the full formation process of meddies along the Spanish and Portuguese coasts, we were able to follow a few meddies over a period of 4 years and a greater number over a period of one year. The simulated trajectories are very realistic if we compare them to observations which have been made during oceanographic campaigns: formation often occurs near St Vincent Cape and the Tejo Plateau or near Cape Finistere, then they travel westward, south-westward, or northward. One particular eddy that formed at the start of the simulation could be followed for 5 years until reaching the Atlantic ridge at 30°W/35°N. Meddies have been observed at this location, in particular during the Semaphore oceanographic campaign. Longer simulations will make it possible to study a complete meddy lifecycle, in particular their potential ability to cross the seamounts that rise in the middle of the Atlantic.

The 5-year simulation also provided new estimates for the amount of salt transported across the Atlantic and the contribution made by meddies to this process which is essential to maintain the thermohaline circulation.



PAM simulation showing the salinity at 870 m, from 13/07/98 till 30/11/98 at 20d intervals. Note the meddy collision and subsequent separation into two separate structures. Credit: Yann Drillet



Trajectories of floats simulated by the model. The colour represents the salinity at the float's position which, in this example, varies between 33.9 and 34.3 g/kg of seawater, i.e., about 0.5 to 0.6 g/kg more than in the surrounding water. Credit: Yann Drillet et al., 2005

4.4 Example : Numerical study of a meddy colliding with a seamount

Meddies (Mediterranean eddies) are vortices that contain relatively warm and salty Mediterranean water at their core. They are prominent hydrological structures of the North Atlantic. As they travel, meddies face many topographical obstacles. The objective of this internship study is to study the dynamics and processes involved in the collision of a meddy with a seamount. High resolution simulations were carried out in order to model this collision. A preliminary study, without seamounts, was carried out in order to understand the evolution and structure of the meddy without any disturbances. Its propagation is affected primarily by the β effect and a hetonic (dipolar) interaction with an underlying cyclonic structure developing. A sensitivity analysis of the physical parameters of the model was performed using different seamount characteristics. In all simulations, the meddy survived the collision with the seamount and split into two independent structures: a main meddy and a secondary meddy. A change in the main meddy's vertical vorticity structure indicated a rapid evolution towards a hetonic structure. The main meddy then continued to travel south-west. In one of the simulations, the evolution towards a hetonic structure was so important that a stable structure emerged that travelled eastward. Erosion, aggregation, and filamentation were also analysed.

| <p>INTRODUCTION</p> <ul style="list-style-type: none"> Impact de l'eau Méditerranéenne dans l'Atlantique Meddies (<i>Mediterranean Eddies</i>) - tourbillons anticycloniques Dérive sud-ouest + Obstacles topographiques → <p>COLLISION</p> <p>[Richardson et al., 2000] [http://www.gso.uri.edu]</p> | <p>INTRODUCTION</p> <ul style="list-style-type: none"> Observations bouées lagrangiennes Observation Meddy 26 [Richardson et al., 2000] Hypothèse : Séparation du Meddy en deux Meddies <p>[Cenedese, 2002]</p> <ul style="list-style-type: none"> Observations de collisions rares Compréhension des processus dynamiques faibles | | | | | | | | |
|--|---|--|------------|---|---|--|--|--|---|
| <p>INTRODUCTION</p> <ul style="list-style-type: none"> Expériences en laboratoire de la collision d'un vortex cyclonique lors de sa collision avec un cylindre [Cenedese, 2002] <p>[Cenedese, 2002]</p> <ul style="list-style-type: none"> Approche 2D Tourbillons cycloniques barotrope (anticyclones instables) <p>→ Extrapolation des résultats pour les cyclones à des anticyclones</p> | <p>INTRODUCTION</p> <p>Objectif : Analyser la dynamique d'un Meddy lors de sa collision avec une montagne sous-marine</p> <p>Méthode : Simulation numérique 3D à haute résolution</p> | | | | | | | | |
| <p>Matériels & Méthodes</p> <p>Modèle numérique</p> <p>Résultats Discussion Conclusion</p> <p>ROMS Roms-tools [http://roms.mpl.ird.fr/]</p> <table border="1"> <tr> <th>Surface</th> <th>Fond</th> <th>Frontières</th> </tr> <tr> <td>Flux atmo. (Q, E, P) nul Tension frottement ($\tau_{x,y}$) nul</td> <td>Tension frottement $\tau_{b,x,y}$ linéaire Coeff. de traînée $C_d = 3.10^{-4}$</td> <td>Surface ouverte / nudging Conservation volume Vitesse courant (u, v) nulle</td> </tr> </table> <p>Equations primitives 3D → 3 jours ρ, η, T, u, v</p> <table border="1"> <tr> <td>Horizontal Grille Arakawa C Schéma advection avec ordre 2 Coeff. viscosité turb. $A_h = 10 \text{ m}^2 \text{ s}^{-1}$ Coeff. $K_h^2 = 0 \text{ m}^2 \text{ s}^{-1}$ diffusivité turb.</td> <td>Vertical Coordonnées sigma Schéma advection centré ordre 4 Coeff. viscosité / diffusivité turb. $A_z = K_z^2 = 1.10^{-3} \text{ m}^2 \text{ s}^{-1}$</td> </tr> </table> | Surface | Fond | Frontières | Flux atmo. (Q, E, P) nul Tension frottement ($\tau_{x,y}$) nul | Tension frottement $\tau_{b,x,y}$ linéaire Coeff. de traînée $C_d = 3.10^{-4}$ | Surface ouverte / nudging Conservation volume Vitesse courant (u, v) nulle | Horizontal Grille Arakawa C Schéma advection avec ordre 2 Coeff. viscosité turb. $A_h = 10 \text{ m}^2 \text{ s}^{-1}$ Coeff. $K_h^2 = 0 \text{ m}^2 \text{ s}^{-1}$ diffusivité turb. | Vertical Coordonnées sigma Schéma advection centré ordre 4 Coeff. viscosité / diffusivité turb. $A_z = K_z^2 = 1.10^{-3} \text{ m}^2 \text{ s}^{-1}$ | <p>Matériels & Méthodes</p> <p>Résultats Discussion Conclusion</p> <p>Domaine - Grille</p> <p>Approximation β-plan</p> <p>Domaine : 800 x 800 km Grille : 160x160 pts Résolution = $1/20^\circ$ (~5km) 30 niveaux sigma</p> <p>La montagne sous-marine</p> <ul style="list-style-type: none"> Forme d'une Gaussienne $h_t(r) = H_t e^{-\frac{r^2}{\mu^2}}$ <p>[Richardson et al., 2000]</p> |
| Surface | Fond | Frontières | | | | | | | |
| Flux atmo. (Q, E, P) nul Tension frottement ($\tau_{x,y}$) nul | Tension frottement $\tau_{b,x,y}$ linéaire Coeff. de traînée $C_d = 3.10^{-4}$ | Surface ouverte / nudging Conservation volume Vitesse courant (u, v) nulle | | | | | | | |
| Horizontal Grille Arakawa C Schéma advection avec ordre 2 Coeff. viscosité turb. $A_h = 10 \text{ m}^2 \text{ s}^{-1}$ Coeff. $K_h^2 = 0 \text{ m}^2 \text{ s}^{-1}$ diffusivité turb. | Vertical Coordonnées sigma Schéma advection centré ordre 4 Coeff. viscosité / diffusivité turb. $A_z = K_z^2 = 1.10^{-3} \text{ m}^2 \text{ s}^{-1}$ | | | | | | | | |

Matériels & Méthodes Résultats Discussion Conclusion

Conditions initiales : Meddy isolé

Pression

$$P_{Meddy}(x, y, z) = P_b + e^{-\frac{r^2}{2R_v^2}} e^{-\frac{(z-z_0)^2}{H^2}}$$

Equilibre hydrostatique

Densité

Élévation de la surface libre

Fonction linéaire

Température

Equilibre géostrophique

Comp. horizontales de la vitesse en surface

Méthode dynamique

Profil vertical de la vitesse

R_v Rayon du vortex
 Z_v Profondeur centrale
 H Epaisseur

Matériels & Méthodes Résultats Discussion Conclusion

La vorticité relative

- Définition : Composante verticale du rotationnel de vitesse

$$\xi = \frac{\partial v}{\partial x} - \frac{\partial u}{\partial y}$$
- Expression de la **tendance d'un fluide à tourner**
- Utilité : Suivi du **centre du Meddy** (minimum local de vorticité relative)
Structure horizontale et verticale du Meddy

Matériels & Méthodes Résultats Discussion Conclusion

Les simulations

Impact avec Great Meteor

Simulation n°1: Meddy de référence

Simulation n°2: Impact au Centre

Simulation n°3: Impact au Sud

Simulation n°4: Impact au Nord

Simulation n°5: Impact avec Irving au centre

▪ Comparaison à l'observation [Richardson et al., 2000]

▪ Trajectoire du Meddy sans perturbation

▪ Structure de la vorticité relative

▪ Généralités sur la collision et différences selon la géométrie de l'impact

▪ Comparaison avec les expériences en laboratoire de [Cenedese, 2002]

Matériels & Méthodes Résultats Discussion Conclusion

Simulation n°1 - Meddy de référence

- Déplacement d'un anticyclone vers l'ouest et vers l'équateur :
 - Effet β
 - Déplacement des particules environnantes
 - Effet d'éirement / écrasement

[Cushman-Roisin et al., 1990; Cushman-Roisin et Beckers, 2010]

Matériels & Méthodes Résultats Discussion Conclusion

Simulation n°1 - Meddy de référence

- Changement de la structure de la vorticité relative du Meddy

- Formation d'une structure hétéronique [Morel et McWilliams, 2003]
Création de vorticité positive en profondeur → Dipôle penché → Circulation cyclonique se développe en-dessous du Meddy → Interaction hétéronique

Matériels & Méthodes Résultats Discussion Conclusion

Simulation n°2 - Impact au centre

- **Changement de la structure verticale après la collision très important**
- Evolution vers une structure hétéronique **accéléérée**
- **Modon** = structure hétéronique stable et persistante + Propagation vers l'est
- **Séparation : Meddy principal / Meddy secondaire**

Matériels & Méthodes Résultats Discussion Conclusion

La collision

Simulations n°2-3-5

- Formation d'une langue de vorticité cyclonique qui s'enroule dans le sens horaire
- **Séparation** de la structure : Meddy principal (1) – Meddy secondaire (2)
- Le Meddy principal dérive vers le sud-ouest ou vers l'est

Simulation n°4

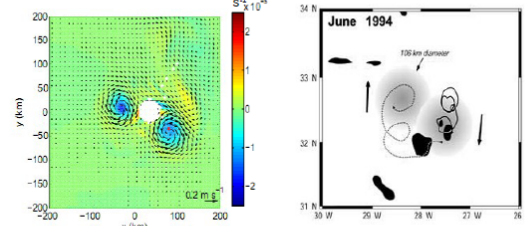
Matériels & Méthodes Résultats Discussion Conclusion

Expériences en laboratoire de Cenedese (2002)

- Etude de l'évolution d'un **vortex cyclonique** lors de sa collision avec un **cylindre** → **Extrapolation des résultats pour les cyclones à des anticyclones**

| Cenedese (2002) | Cette étude |
|---|--|
| Formation d'un streamer dans le sens horaire autour du cylindre | Formation d'une langue de vorticité dans un sens horaire autour de la montagne sous-marine |
| Formation d'un nouveau pôle de vorticité en aval du cylindre | Formation du Meddy secondaire en aval de la montagne sous-marine |
| Séparation pour un impact au Nord et au centre du cylindre | Séparation pour un impact au Sud et au centre de la montagne sous-marine |

- Mécanisme de formation du nouveau vortex = Tourbillons de l'allée de Von-Karman

| Matériels & Méthodes | Résultats | Discussion | Conclusion |
|--|-----------|------------|------------|
| Simulation n°5 – Impact Irving | | | |
| Observation Meddy 26 [Richardson et al., 2000] | | | |
|  | | | |
| <ul style="list-style-type: none"> ▪ Séparation du Meddy ▪ Dérive vers le nord du Meddy secondaire - Dérive vers le Sud du Meddy principal | | | |
| Confirmation de l'hypothèse issue de l'observation | | | |
| | | | 1 |

| Matériels & Méthodes | Résultats | Discussion | Conclusion |
|--|-----------|----------------------------|------------|
| Meddy | | | |
| Propagation Sud-ouest + interaction hétéronique | | | |
| Collision avec une montagne sous-marine | | | |
| Processus de séparation | | | |
| Meddy principal | | Meddy secondaire | |
| Structure hétéronique accélérée | | Allée de Von-Karman | |
| Impact au nord → Processus d'agrégation entre le Meddy principal et le Meddy secondaire en aval de la montagne sous-marine | | | |
| | | | 1 |


4.5 Techniques for identifying and tracking vortices

A proper definition of a vortex and the implementation of an algorithm to automatically identify and follow mesoscale and submesoscale structures are fundamental to study vortex dynamics using large databases such as those from satellite altimetry or the outputs from circulation models. Different methods have been proposed, either based on the physical characteristics or the geometry of the study area.

Methods based on physical characteristics identify vortices using a specific parameter, e.g., the value of the chosen parameter exceeds a predefined threshold. Methods based on the flow field geometry identify vortices based on the shape or curvature of streamlines. These automated detection algorithms can be classified into three types (Nencioli et al, 2009): 1) based on physical parameters; 2) based on the geometry of the flow field; and 3) hybrid methods that utilise both physical parameters and the flow field geometry.

In theory, the particle velocity, u , in a vortex (and, therefore, the vortex itself) can vary in several ways depending on the distance r from the axis. We distinguish between two important cases: (i) an irrotational vortex and (ii) a rigid body vortex.

If u is inversely proportional to r , then an imaginary test balloon placed in the vortex will not spin on its own axis but maintain the same orientation while moving in a circle around the axis of the vortex. In this case, the vorticity $\vec{\omega}$ is zero everywhere except on the axis of the vortex and the flow is called irrotational.

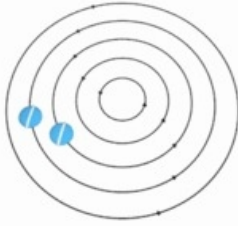
| | |
|--|---|
| $\vec{\Omega} = (0, 0, \alpha r^{-2}), \quad \vec{r} = (x, y, 0),$ $\vec{u} = \vec{\Omega} \times \vec{r} = (-\alpha y r^{-2}, \alpha x r^{-2}, 0),$ $\vec{\omega} = \nabla \times \vec{u} = 0.$ |  <p>http://en.wikipedia.org/wiki/Vortex</p> |
|--|---|

In the absence of external forces, a vortex usually moves fairly rapidly towards the irrotational flow pattern where u is inversely proportional to r . For this reason, irrotational vortices are also called free vortices. For an irrotational vortex, the flow is zero along any closed contour that does not contain the axis of the vortex. The flow has a constant value, Γ , for any contour encircling the axis once. The tangential component of the particle velocity is then $u_\theta = \frac{\Gamma}{2\pi r}$.

However, an irrotational vortex is not physically realistic as this would imply that the velocity of the water particles (and therefore the force necessary to keep them on their circular trajectories) would increase without limit as one approaches the axis of the vortex. What happens in a real vortex is that there is always a core region surrounding the axis where the speed of water particles no longer increases. At some point, the velocity actually starts to decrease towards zero as r tends to zero. In this region, the flow is no longer irrotational, the vorticity $\vec{\omega}$ becomes non-zero and its vector is roughly parallel to the axis of the vortex. Rankine's vortex is a model that assumes a rotational rigid body flow where r is less than a fixed distance r_0 and an irrotational flow outside that central region.

A rotating vortex can only be maintained in this state in the presence of an additional external force that is not generated by the movement of the fluid itself. For example, if a bucket of water is rotated at a constant angular velocity w about its vertical axis the water will eventually turn like a rigid body and the water particles will move along circular trajectories with a speed $u = w r$. In this scenario, the free surface of the water will assume a parabolic shape and the resulting pressure gradient will be directed towards the interior of the bucket, thus preventing the flow from evolving from a rigid body flow to an irrotational one. In this type of flow with a fluid of constant density, the dynamic pressure is proportional to r^2 . In a constant gravity field, the free surface of the liquid is a concave paraboloid.

If the fluid rotates as a rigid body – that is, if the angular velocity, Ω , is uniform, such that u increases proportionally with r – a small ball placed in the vortex would also rotate about its own axis as if it were part of that rigid body. In such a flow, the vorticity is constant – equal to 2Ω – throughout and its direction parallel to the axis of rotation.

| | |
|---|--|
| $\vec{\Omega} = (0, 0, \Omega), \quad \vec{r} = (x, y, 0),$ $\vec{u} = \vec{\Omega} \times \vec{r} = (-\Omega y, \Omega x, 0),$ $\vec{\omega} = \nabla \times \vec{u} = (0, 0, 2\Omega) = 2\vec{\Omega}.$ |  <p>http://en.wikipedia.org/wiki/Vortex</p> |
|---|--|

The study by McWilliams (1990) was among the first to investigate the automated detection of vortices. They developed an algorithm to quantitatively measure the specific properties of coherent vortices from a numerical solution of the 2D circulation problem. It is based on the notion that rotation dominates in a vortex and relative vorticity, ζ , can be used as a physical parameter for its detection. The vortex centres can be identified by local minima and maxima of ζ while the vortex edges are defined by the contour line where $\frac{\zeta}{\zeta_{center}} < 0.2$. A series of geometrical constraints is applied to the detected structures and only those that are not too axisymmetric are considered to represent a vortex. For this reason, this method belongs to the last category,

In the detection algorithms that are based on physical parameters, the Okubo-Weiss parameter, W, is among the most commonly used (Okubo 1970; Weiss 1991). This parameter is calculated from the horizontal velocity field

$$W = s_n^2 + s_s^2 - \omega^2 \quad \text{where} \quad \omega = \frac{\partial v}{\partial x} - \frac{\partial u}{\partial y} \quad s_n = \frac{\partial u}{\partial x} - \frac{\partial v}{\partial y} \quad s_s = \frac{\partial v}{\partial x} + \frac{\partial u}{\partial y}$$

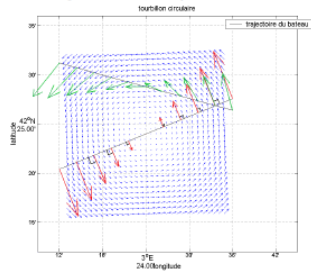
where s_n and s_s are the deformation de cisaillement et de déformation, respectively, et ω est la composante verticale de la vorticité. Here, W quantifies the relative importance of deformation vs rotation. Since the velocity field in a vortex is dominated by rotation, ocean eddies are generally characterized by negative values of W. It is therefore possible to identify these functions as closed contours of $W = W_0$, where W_0 is a chosen threshold value. This process was often used for detecting vortices in sea surface altimetry data (SSH) (e.g., Isern-Fontanet et al., 2003; Morrow et al., 2004; Chelton et al., 2007). However the velocity derivatives cause additional noise in the W fields. This noise can be reduced by applying a smoothing algorithm which can of course also remove part of the signal we are trying to detect. Several studies have demonstrated that this method also has its limits (Sadarjoen and Post 2000; Chaigneau et al., 2008) in that it tends to yield false positives, i.e., it falsely identifies vortices, a problem that appears to persist even after smoothing the W field. Furthermore, when long time series are analysed, the threshold value W_0 must be continuously adjusted according to the variation of the turbulence properties of the velocity field.

An approach known as the winding angle method has been proposed by Sadarjoen and Post (2000). This approach belongs to the second category and is based on the assumption that vortices can be identified from their approximately circular or spiralling shape around their cores (Robinson, 1991). As a first step, the instantaneous streamlines are derived from the velocity field; then, the change in mean direction of the segments that make up a given streamline (winding angle) is calculated for each streamline. Vortices are identified by current lines that have a winding angle $|\alpha| \geq 2\pi$ that corresponds to a closed circular or spiralling shape.

This method was used by Chaigneau et al. (2008) to analyse vortex activity in the eastern part of the South Pacific using SSH altimetry data. By comparing the results from their method with those obtained with the Okubo-Weiss method they could demonstrate that the winding angle method was better at detecting vortices and, more importantly, exhibited a much lower rate of false positives. However, this improved accuracy comes at the price of a higher computational cost. Chaigneau et al. (2008) could reduce the computational effort by applying this method only to regions where eddies had been identified through local maxima/minima in SSH. For this reason, their method belongs to the third (hybrid) category: a physical quantity (SSH) is used to identify potential vortex candidates before using geometric characteristics of the flow zone (streamlines) to define the vortex boundaries.

Introduction

Importance dans l'estimation des coordonnées du centre d'un tourbillon
 Lorsque la trajectoire passe par le centre, le point de vitesse nulle correspond aux coordonnées du centre
 Cas idéal
 Les vecteurs sont orthogonaux au transect (composante tangentielle uniquement, pas de radiale)
 Trajectoire aléatoire, décomposition des vecteurs



Calcul du centre grâce à la méthode de Nencioli:

Décomposition des vecteurs
 Méthode tangentielle: meilleure estimation du centre = point où la somme des composantes tangentielles est maximale
 Méthode radiale: meilleure estimation du centre = point où la somme des composantes radiales est minimale

Exemple:

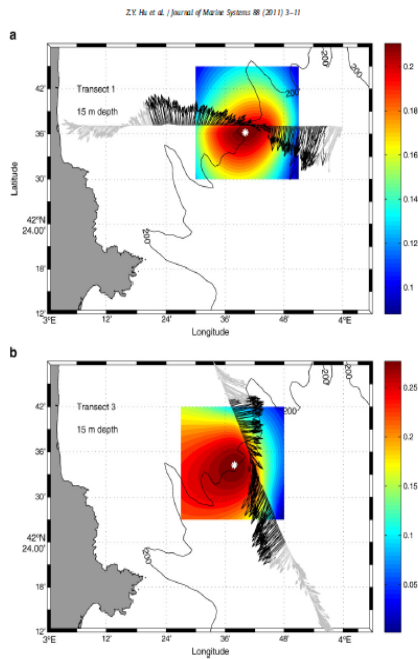
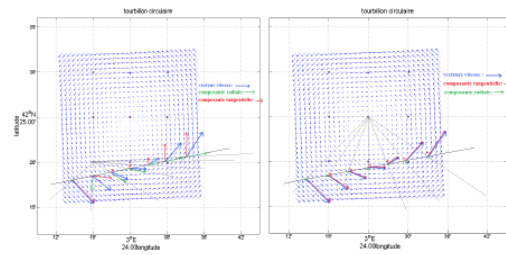


Fig. 4. Estimated center location of an eddy (white asterisk) for Transect 1 (left) and Transect 3 (right) at 15 m depth. Tangential components of the black vectors were computed for each point within the grids. For each transect, the center of the eddy was defined as the point for which the mean absolute value of tangential velocity was maximal. The contours in the square areas indicate values of equal mean absolute tangential velocity (ms^{-1}). Bath at 200 m is plotted with black line.

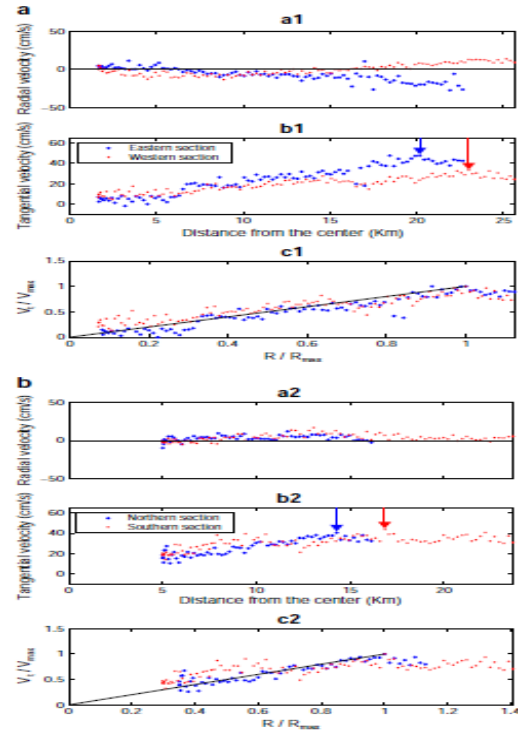


Fig. 5. Distribution of (a) radial and (b) tangential velocities with respect to radial distance from the center; (c) distribution of normalized tangential velocity with respect to normalized radial distance for both Transect 1 (left column) and Transect 3 (right column). Arrows in (b) indicate the locations of maximum velocity magnitude for two sections; the solid lines in (c) indicate values of equal angular velocity (V_{max}/R_{max}).

Here nencioli slides

4.6 Example : tracking vortices in the Cape Basin and the Gulf of Lion



MPO - RSMAS

Study of Cape Basin eddies and Indian-Atlantic interocean exchange in a regional model.

A.M. Doglioli¹,
B. Blanke¹, A. Griffa^{2,3}, G. Lapeyre⁴, S. Speich¹, M. Venziani^{2,5}

¹Laboratoire de Physique des Océans, UMR 6523 CNRS-IFREMER-UBO, Brest, France.
²RSMAS-MPO, University of Miami, Miami, USA
³ISMAR-CNR, La Spezia, Italy
⁴Laboratoire de Mécanique Dynamique/PSL, Ecole Normale Supérieure, Paris
⁵now at UC Santa Cruz, USA

Miami, 10 July 2006

PROJECT GOALS


- identifying mesoscale eddies with an objective method,
- time-tracking these eddies and
- evaluating their properties and the water mass they transfer.

Wavelets Analysis for Time-tracking Eddies in Regional models
<http://www.ifremer.fr/lpo/adoglioli/WATERS/>

Acknowledgments
 A. M. Doglioli is supported by SHOM, under contract number CA 2003/03/CMO (Contact: Alain Sèpète). This study is also a contribution to InterUp, a project funded by the French Programme national Atmosphère et Océan à Multiéchelles (PATOM).

Study Area

Cape Caudron: zone of turbulent stirring and mixing in the southeastern Cape Basin [Boebel et al, 2003]



[...] Here at the Agulhas retroflection, "leakage" of water occurs within an array of cyclonic (clockwise) and anticyclonic (anticlockwise) eddies that are injected into the vigorous stirring and mixing environment of the Cape Basin [...].
 Gordon, Nature 2002

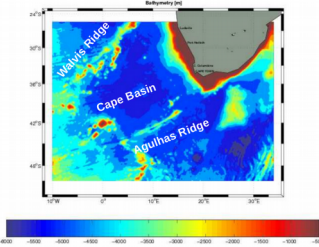
Ocean Model - Configuration

ROMS code
IRD version with ROMSTOOLS [Penven, 2003]

Horizontal resolution: 1/10°

11-year run

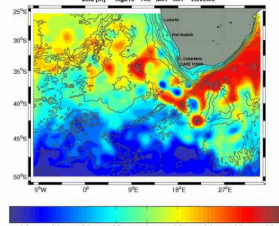
Output : 2-day average



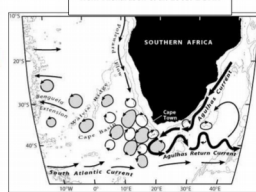
| Climatologies | | |
|-----------------|--------------|---------------------------|
| Open boundaries | Wind forcing | Heat & Fresh water fluxes |
| OCCAM 1/4° | QuikSCAT | COADS 1/2° |

Ocean Model - Animations

Sea Surface Height



from Richardson et al. 2003. DSRH



Wavelet Analysis – Eddy identification

The wavelet analysis consists in the decomposition of the signal into orthogonal, multiresolution wavepackets, in a manner similar to Fourier decomposition. MATLAB tools using Wavelab library [http://www-stat.stanford.edu/wavelab/]

Fourier

Signal → Transform

Constituent sinusoids of different frequencies

Wavelet

Signal → Transform

Constituent wavelets of different scales and positions

The algorithm we use has four different sub-steps:

- a best basis is found to minimize a cost function (here the Shannon entropy). This basis changes for each time step considered and it allows to find the best location for the wave packets.
- the model relative vorticity is decomposed on this basis.
- the wavelets are sorted as a function of their spectral coefficients. Only a few of them are kept (with a number that depends on the dimension of the basis: usually 9% of the initial set of wavelets). The reconstructed signal is virtually zero where there is no identified pattern.
- we extract structures so that adjacent points along x and y axes belong to the same pattern.

Following this method, we obtain localized structures in space, which allows us to define eddies.

Wavelet Analysis – Eddy identification

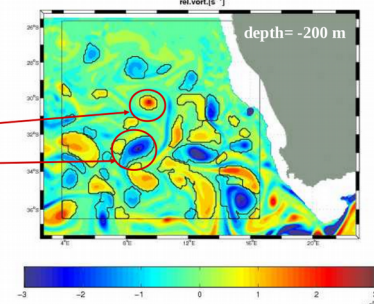
Decomposition of an horizontal slice of relative vorticity

MATLAB tools using Wavelab library [http://www-stat.stanford.edu/wavelab/]

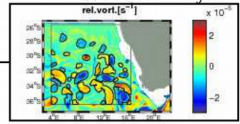
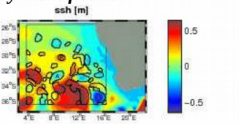
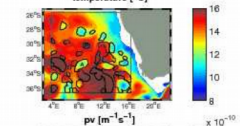
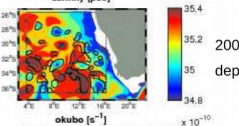
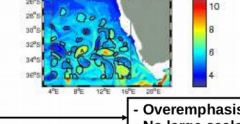
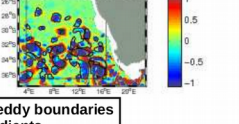
Research Area
256 x 256 [gridcells]

Numbering and Naming
Anticyclone
PANORAMIX
Cyclone
ASTERIX

Center definition
(ic,jc)=max(|ξ|)



Wavelet Analysis – Eddy identification

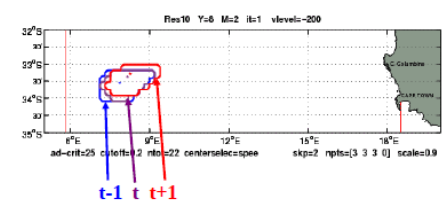







200-m depth

- Overemphasis of eddy boundaries
- No large scale gradients

Wavelet Analysis – Time tracking

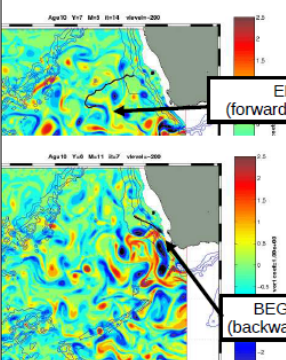
Forward Tracking: $C_t \in \mathcal{E}_{t-\Delta t}$
Eddy center Set of eddy points



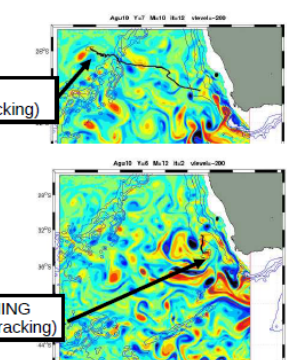
Backward = Forward

Wavelet Analysis – Time tracking

Cyclone Asterix



Anticyclone PANORAMIX

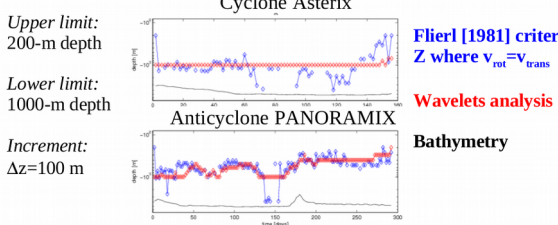


END (forward tracking)
BEGINNING (backward tracking)

Wavelet Analysis – Vertical Tracking

Downward Tracking: $C_z \in \mathcal{E}_{z-\Delta z}$
Eddy center Set of eddy points

Upper limit: 200-m depth
Lower limit: 1000-m depth
Increment: $\Delta z=100$ m



Flierl [1981] criterion
Z where $v_{rot} = v_{trans}$

Wavelets analysis
Bathymetry

$$V = \sum_{k=1}^{iz_L} A_k \cdot \Delta z$$

Wavelet Analysis – 4D tracking

Velocity

$$v \equiv v(t) = \frac{1}{iz_L} \sum_{k=1}^{iz_L} v_k$$

$$v_{err} = \frac{\sigma_z(u)}{v}$$

Volume

$$V = \sum_{k=1}^{iz_L} A_k \cdot \Delta z$$

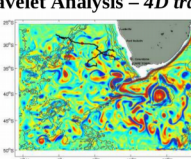
$$V_{err}(t) = \frac{\Delta z \pi \left(\frac{D}{2}\right)^2}{V} + \frac{4 \Delta x \Delta z \sum_{k=1}^{iz_L} A_k D_k^{-1}}{V}$$

Diameter

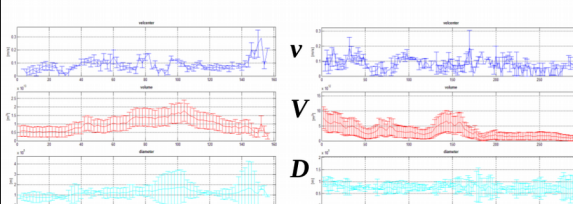
$$D = \frac{1}{2 iz_L} \sum_{k=1}^{iz_L} (D_k^{EW} + D_k^{NS})$$

$$D_{err} = \frac{\frac{1}{2 iz_L} \sum_{k=1}^{iz_L} |D_k^{EW} - D_k^{NS}|}{D}$$

Wavelet Analysis – 4D tracking

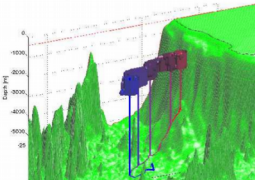


Cyclone ASTERIX Anticyclone PANORAMIX

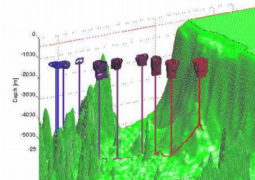


Wavelet Analysis – 4D tracking

Cyclone ASTERIX



Anticyclone PANORAMIX



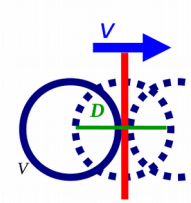
January-June January to October

Vel = 0.09 [ms⁻¹] Vel = 0.08 [ms⁻¹]
Diam = 121 [km] Diam = 75 [km]
Vol = 9.7 10¹² [m³] Vol = 3.1 10¹² [m³]

| | Boebel et al., 2003 | | Van Ballegooyen et al., 1994 | |
|---|---------------------|---------------|------------------------------|--------------|
| | Cyclones | Agulhas Rings | Cyclones | Anticyclones |
| Diameter [km] | 120 | 200 | 160 | 190 – 320 |
| Velocity [m/s] | 0.036 | 0.038 | 0.046 | 0.04 – 0.09 |
| Volume [10 ¹² m ³] | - | - | - | 11.2 - 33.8 |

Divergent pathways
(Morrow et al., 2004)


Wavelet Analysis – transport



$$Tr = V \cdot \Delta t^{-1}$$

$$Tr = v \cdot V \cdot D^{-1}$$

$$D = \frac{1}{2 iz_L} \sum_{k=1}^{iz_L} (D_k^{EW} + D_k^{NS})$$

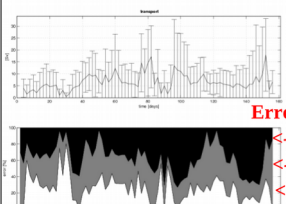
$$D_{err} = \frac{\frac{1}{2 iz_L} \sum_{k=1}^{iz_L} |D_k^{EW} - D_k^{NS}|}{D}$$


Wavelet Analysis – Transport

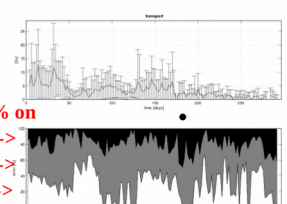
$Tr = v \cdot V \cdot D^{-1}$

$$Tr_{err} = v_{err} + V_{err} + D_{err}$$

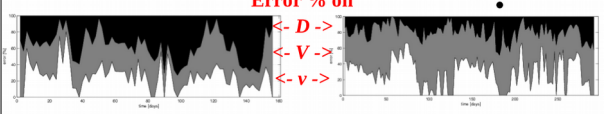
Cyclone ASTERIX



Anticyclone PANORAMIX



Error % on



<Tr> = 6.6 [Sv] <Tr> = 3.3 [Sv]

Wavelet Analysis

SUMMARY

- the wavelet analysis proved successful in tracking eddies;
- tracked mesoscale eddies present realistic dynamics;
- wavelets diagnostic offer estimates of eddy mass transport.

Reference:
 Doglioli, A.M., Blanke, B., Speich, S., Lapeyre, G. (2006). *Wavelets Analysis for Tracking Eddies in Regional Models. Application to Cape Basin Eddies*. J. Geophys. Res., In revision.

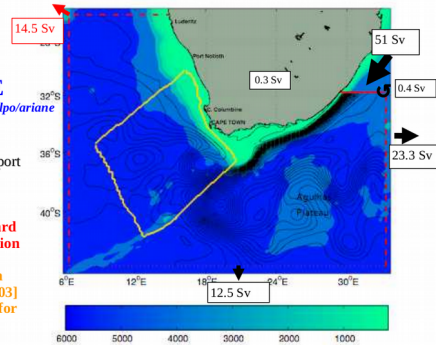
Lagrangian particles – Interocean Exchange

ARIANE
<http://www.univ-brest.fr/lpo/ariane>

Compute total, cross-section transport from them.

Forward/Backward
 7-yr time integration

Cape Cauldron
 [Boebel_et al, 2003]
 6-hour sampling for spin analysis



Lagrangian particles – Spin parameter

$$\Omega = \frac{\langle u'dv' - v'du' \rangle}{2 \Delta t \text{ EKE}}$$

Veneziani et al., 2004. JPO 34, 1884-1906

The eddy field properties in the subsurface northwestern Atlantic are due to the **superposition** of two different regimes: the regime of the **coherent vortices (loopers)** and that of the **background field (non-loopers)**

The observed features can be parameterized through a first-order **LSM Lagrangian Stochastic Model** with **bi-modal distributed spin Ω**

Veneziani et al., 2005a. JMR 63, 753-788

The majority (85%) of looping trajectories are core-loopers, which provide estimates of Ω :
 - very similar to the **vortex core relative vorticity** and
 - whose temporal changes are directly connected to the actual **vortex evolution**.

Only the remaining 15% of loopers sample the vortex edge

Lagrangian particles – Spin parameter

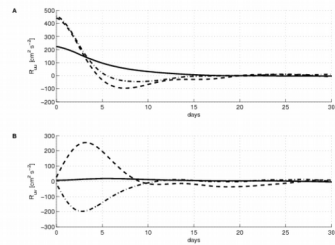
Two 10% random subsets

30-day chunks

Thresholds:

$$\Omega_{\text{surf}} = 0.30 \text{ days}^{-1}$$

$$\Omega_{\text{deep}} = 0.15 \text{ days}^{-1}$$



Lagrangian particles

SUMMARY

- high resolution ocean model reproduces fairly well the vigorous stirring and mixing processes of the study area;
- the Lagrangian particle-following technique provided an estimate of Agulhas leakage of about 14 Sv, which is consistent with observations and previous results from lower resolution models;
- looper regime accounts for about 30% of the estimated interocean exchange, with a remarkable contribution due to cyclones;
- Lagrangian computations coupled with spin analysis revealed promising results, and it would be worth conducting a more complete study

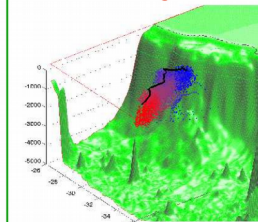
Reference:
 Doglioli, A.M., Veneziani, M., Blanke, B., Speich, S., Griffa, A. (2006). *A Lagrangian analysis of the Indian-Atlantic interocean exchange in a regional model*. Geophys. Res. Lett., In press.

OUTLOOK

Wavelets & Lagrangian particles

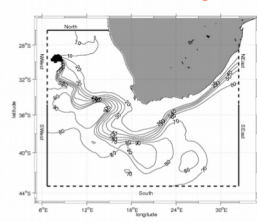
Coherent eddies

Eddy-life
 time integration



Remote Origins

Multiple-years
 backward time integration



5. Advection-diffusion

Fundamentals

5.1 Conservation theorem

The law of conservation of a generic density ψ can be written as

$$\frac{\partial \psi}{\partial t} + \nabla \cdot (\psi \mathbf{u}) = 0,$$

a special case of the conservation law is the continuity equation where the density is conserved

$$\frac{\partial \rho}{\partial t} + \nabla \cdot (\rho \mathbf{v}) = 0,$$

A more general form is

$$\frac{\partial \psi}{\partial t} + \nabla \cdot (\psi \mathbf{u}) = \gamma.$$

which also accounts for the presence of possible sinks and sources of ψ , represented by γ . This term can be divided into two other terms, a non-divergent contribution ξ and the divergence of a certain vector $-\chi$

$$\gamma = \xi - \nabla \cdot \chi.$$

to yield

$$\frac{\partial \psi}{\partial t} + \nabla \cdot (\psi \mathbf{u}) + \nabla \cdot \chi = \xi,$$

which is the most general form of a conservation equation.

Divergence Theorem

https://en.wikipedia.org/wiki/Divergence_theorem

In [vector calculus](#), the **divergence theorem**, also known as **Gauss's theorem** or **Ostrogradsky's theorem**, is a theorem which relates the [flux](#) of a [vector field](#) through a closed [surface](#) to the [divergence](#) of the field in the volume enclosed, i.e., the [surface integral](#) of a vector field over a closed surface, which is called the *flux* through the surface, is equal to the [volume integral](#) of the divergence over the region inside the surface:

$$\iiint_V \operatorname{div} \vec{F} \, dV = \iint_S \vec{F} \cdot d\vec{S}$$

where V is the reference volume and S the surface containing V .

By integrating this equation over a finite reference volume and by applying the Divergence Theorem one obtains the integral form of the Conservation Theorem

$$\frac{d}{dt} \int_V \psi \, dV + \oint_S \psi \mathbf{v} \cdot d\mathbf{S} + \oint_S \chi \cdot d\mathbf{S} = \int_V \xi \, dV,$$

This formulation demonstrates that the local temporal variation of the property ψ in the volume V (first term) is linked to the sum of three terms:

- a transport term $\psi \mathbf{v}$, linked to the entrainment of a property by the moving fluid;
- a flux term, i.e., effects impacting the surface, linked to χ which result in a loss or increase in a certain quantity in the finite volumes, but with $\chi=0$ on the surface (but not necessarily throughout the entire volume occupied by the fluid). This term thus redistributes the property inside the fluid or distributes it through actions seeking to introduce or export the property through the surface.

- a dissipation or generation term, i.e., volume effects linked to ξ which represents any change in ψ due to forces distributed in space, which could also be zero (individually or overall), although the term mostly represents the fact that the property ψ is not conserved, and, in any case, is never conserved locally.

EXAMPLE: estimating the net production in an oceanic eddy (LATEX project)

NB: in this case the diffusion coefficients correspond to turbulence (see below) and not molecular diffusion.

Mass budget for a Lagrangian control volume

$$\frac{d}{dt} \int_V \psi dV + \oint_S \psi \mathbf{u} \cdot d\mathbf{S} + \oint_S \chi \cdot d\mathbf{S} = \int_V \xi dV$$

Temporal variation

Advection
(to be neglected)

Boundary exchanges
horiz+vert

Sources & sinks
(null for SF₆)

where $\psi = O_2, C, SF_6$

This method makes possible to close the biogeochemical budgets

Net Community Production $\Delta t=5-6$ days

$$NCP_{O_2} = \Delta O_2 + F_{sea-air} + F_{hor} + F_{ver}$$

$$NCP_{DIC} = \Delta DIC + F_{sea-air} + F_{hor} + F_{ver}$$

& comparison with incubations

NB :

SF₆ Sulfur hexafluoride

Carbon export

$$C_{exp} = NCP_{DIC} - \Delta POC - \Delta DOC$$

in situ bottle (in situ)

We can now take the property ψ as

$$\psi = \rho S$$

with S being salinity in parts per thousand.

By applying the law for the conservation of mass and the definition of a Lagrangian derivative we obtain

$$\begin{aligned} \frac{\partial(\rho S)}{\partial t} + \nabla \cdot (\rho S \mathbf{u}) &= \rho \frac{\partial S}{\partial t} + S \frac{\partial \rho}{\partial t} + S \nabla \cdot (\rho \mathbf{u}) + \rho \mathbf{u} \cdot \nabla S = \\ &= \rho \left(\frac{\partial S}{\partial t} + \mathbf{u} \cdot \nabla S \right) + S \left(\frac{\partial \rho}{\partial t} + \nabla \cdot (\rho \mathbf{u}) \right) = \rho \frac{dS}{dt}. \end{aligned}$$

The equation for the conservation of salinity then becomes

$$\rho \frac{dS}{dt} + \nabla \cdot \chi = \xi$$

In general, one always assumes that the flux of a property is proportional to the negative gradient of said property, i.e.

$$\chi = -k_s \nabla S$$

with k_s the proportionality constant. The conservation equation then becomes

$$\rho \frac{dS}{dt} = \nabla \cdot (k_s \nabla S) + \xi$$

and since we can assume the spatial variability of k_s to be negligible,

$$\frac{dS}{dt} = \kappa_s \nabla^2 S + \frac{\xi}{\rho}$$

with $\kappa_s = \frac{k_s}{\rho}$ the molecular diffusion coefficient.

Molecular diffusion has relatively long time scales compared to diffusion by turbulence and we will therefore neglect molecular diffusion in what follows. However, in the absence of any turbulence molecular diffusion must always be considered as it is the only process that can cause any redistribution of a property. Without sources/sinks, molecular diffusion acts to reduce any concentration gradients in accordance with the second law of thermodynamics.

For what follows, it will be useful to study the case of molecular diffusion in a fluid at rest. Under these conditions we have

$$\frac{\partial S}{\partial t} = \kappa_s \nabla^2 S + \frac{\xi}{\rho}.$$

If $\xi = 0$, a possible solution is

$$\mathcal{G}(\mathbf{r}, t) = \frac{1}{(4\pi\kappa_s t)^{3/2}} e^{-\frac{r^2}{4\pi\kappa_s t}},$$

with $r^2 = x^2 + y^2 + z^2$. This solution represents a 3D Gaussian centred at the origin with a variance of $\sigma^2 = 2\kappa_s t$.

In the initial state, the property S is entirely concentrated in a single point (for simplicity, we will place this point at the origin of the coordinate system). Then the concentration of property S spreads

at a rate $\sqrt{\frac{2\kappa_s}{t}}$. In other words, the radius of the (circular) volume into which the point source

property diffuses increases with the square root of time while the rate of expansion decreases at the same rate; for typical values of molecular diffusivity, κ_s , this process is very very slow. In the sea, the value of κ_s for salt (or mass in general) is about $1.5 \times 10^{-9} \text{ m}^2 \text{ s}^{-1}$. This value tells us that a high salinity water pocket occupying 1 m^2 will take 10,000 days to grow just 0.5 m^2 (1 day = $86400 \text{ s} \sim 10^5 \text{ s}$)! The molecular diffusivity for temperature, κ_T , is about $1.5 \times 10^{-7} \text{ m}^2 \text{ s}^{-1}$. This implies that, while still slow, the diffusion of temperature occurs about 100 times faster than the diffusion of salt. The kinematic viscosity (i.e., the molecular diffusion of momentum) at a temperature of 20°C and a salinity of 39 psu is about $1.0 \times 10^{-6} \text{ m}^2 \text{ s}^{-1}$.

The slowness of these transport processes allows us to use passive tracers to mark certain flow fields (e.g., a particular current).

In addition, this homogeneous 3D solution can be broken down into a product of three 1D solutions:

$$\mathcal{G}(\mathbf{r}, t) = \frac{1}{(4\pi\kappa_s t)^{3/2}} \left(e^{-\frac{x^2}{4\pi\kappa_s t}} \right) \left(e^{-\frac{y^2}{4\pi\kappa_s t}} \right) \left(e^{-\frac{z^2}{4\pi\kappa_s t}} \right)$$

each of which is the solution to the 1D diffusion equation

$$\frac{\partial S}{\partial t} = \kappa_s \frac{\partial^2 S}{\partial x_i^2},$$

in cui $x_i = x, y, z$ per $i = 1, 2, 3$.

These solutions allow us to find a solution for the case where $\xi \neq 0$ starting from a certain initial concentration S_0 :

$$S(\mathbf{r}, t) = \int_0^t \int_V \mathcal{G}(\mathbf{r} - \mathbf{r}', t - t') \frac{\xi(\mathbf{r}', t')}{\rho} d\mathbf{r}' dt' + \int_V \mathcal{G}(\mathbf{r} - \mathbf{r}', t) S_0(\mathbf{r}') d\mathbf{r}' .$$

Thus, to follow the evolution of a diffusing substance, we consider the distribution present at the beginning, or a certain concentration added later, and take it as the sum of several point sources. We then follow the evolution of each point source and eventually sum them to obtain the overall concentration field. Predicting diffusion is therefore relatively simple as long as there is no movement (and turbulence).

5.2 Turbulence as a stochastic process

Turbulence can be considered as resulting from an unstable flow, or from a flow in which the infinitesimal disturbances due to movements at the molecular level tend to increase until they reach an intensity comparable to that of the main flow itself.

The transition from stable to unstable is random, although the transition from stable to unstable typically occurs more rapidly than the reverse transition in which the flow becomes laminar again.

In addition to vibrations, the surface roughness of obstacles and other irregularities can promote the transition to a turbulent state.


The Reynolds number provides a threshold for determining the changeover from laminar to turbulent.

When a flow becomes turbulent it is not necessary to describe its evolution in every minute detail since the fluctuations affect all spatial and temporal scales and are highly irregular. Instead, a probabilistic approach is usually employed to focus on the mean flow/displacement.

| | |
|--|--|
| <p>Temporal mean:</p> $\bar{\xi} = \frac{1}{T} \int_0^T \xi dt$ <p>where T is a sufficiently long time period to contain a sufficiently large number of the random fluctuations we wish to neglect.</p> | <p>Spatial mean:</p> $\bar{\xi} = \frac{1}{V} \int_V \xi dV$ <p>where V is a region of space with volume V around our point of interest that is sufficiently large to contain a large number of random fluctuations.</p> |
|--|--|

The ensemble mean $\langle \xi \rangle(\mathbf{r}, t)$ is defined as the mean at each point in time and space obtained by repeating the same experiment an infinite number of times.

In a stationary situation, the ergodic hypothesis yields $\bar{\xi} = \langle \xi \rangle$, i.e., we can obtain the ensemble average from the temporal and spatial averages of just one single realisation of the experiment.



https://en.wikipedia.org/wiki/Ergodic_hypothesis

physics and thermodynamics, the ergodic hypothesis says that, over long periods of time, the time spent by a system in some region of the phase space of microstates with the same energy is proportional to the volume of this region, i.e., that all accessible microstates are equiprobable over a long period of time.

Liouville's theorem states that, for Hamiltonian systems, the local density of microstates following a particle path through phase space is constant as viewed by an observer moving with the ensemble (i.e., the convective time derivative is zero). Thus, if the microstates are uniformly distributed in phase space initially, they will remain so at all times. But Liouville's theorem does not imply that the ergodic hypothesis holds for all Hamiltonian systems.

The ergodic hypothesis is often assumed in the statistical analysis of computational physics. The analyst would assume that the average of a process parameter over time and the average over the statistical ensemble are the same. This assumption—that it is as good to simulate a system over a long time as it is to make many independent realizations of the same system—is not always correct (see, for example, the Fermi–Pasta–Ulam–Tsingou experiment of 1953).

Assumption of the ergodic hypothesis allows proof that certain types of perpetual motion machines of the second kind are impossible.

Systems that are ergodic are said to have the property of ergodicity; a broad range of systems in geometry, physics and stochastic probability theory are ergodic. Ergodic systems are studied in ergodic theory.

5.3 Eulerian and Lagrangian approaches to solving the equation of conservation of a solute in

the presence of turbulence

As we have seen in the introduction, the relationship between the total time derivative in a Lagrangian reference frame and the partial time and space derivatives in an Eulerian frame of reference are linked as

$$\frac{d}{dt} = \frac{\partial}{\partial t} + \mathbf{v} \cdot \nabla$$

There are thus two possible mathematical approaches to address the advection-diffusion problem:

- Eulerian: one assumes a stationary reference system; the balances of momentum, energy, and mass depend on the fluxes that pass through the walls of a volume V which is fixed with respect to the coordinate system. We integrate the advection- diffusion equations in such a system.
- Lagrangian: the fluid is interpreted as a set of particles and each particle is assigned its own characteristics, such as a certain concentration of pollutant and certain randomness in its movements; the concept of trajectories is used to track the path of each fluid particle; along the trajectories particles can undergo transformations depending on the environmental conditions.

Eulerian approach

This type of approach is based on solving the conservation equation of mass for each particle type (pollutant, plankton cell, salt, etc.) and the associated concentration $c(x,y,z,t)$. The conservation equation can be written as:

$$\frac{\partial c}{\partial t} + (\mathbf{v} \cdot \nabla) c = \kappa_s \nabla^2 c + \frac{\xi}{\rho},$$

and one assumes that the velocity \mathbf{v} can be represented as the sum of a mean and a fluctuating component (Reynolds decomposition):

$$\mathbf{v} = \bar{\mathbf{v}} + \mathbf{v}'$$

While $\bar{\mathbf{v}}$ represents the part of the flow that can be measured experimentally or determined using hydrodynamic models, \mathbf{v}' is a stochastic variable that contains information about the turbulence diffusivity and for which the temporal mean is zero by definition $\overline{\mathbf{v}'} = 0$. For the concentration we can write in the same fashion

$$c = \bar{c} + c' \quad \text{with} \quad \bar{c}' = 0$$

Oceanic turbulence is characterised by the superposition of several time scales avec une amplitude variable avec continuité and the choice of an appropriate time interval therefore not be made unequivocally. It will depend on an arbitrary choice of the time scale which we may want to average movement or not.

Once an appropriate value for T has been chosen, based on the problem under investigation, we can start to decompose the flow into two components:

- a mean flow that varies slowly;
- a turbulent flow that varies rapidly.

The ergodic hypothesis then yields

$$\langle \mathbf{v} \rangle = \bar{\mathbf{v}} \quad \langle \mathbf{v}' \rangle = \overline{\mathbf{v}'} = 0 \quad \langle c \rangle = \bar{c} \quad \langle c' \rangle = \overline{c'} = 0$$

Substituting this into the conservation equation yields:

$$\frac{\partial \bar{c}}{\partial t} + \frac{\partial c'}{\partial t} + (\bar{\mathbf{v}} + \mathbf{v}') \cdot \nabla (\bar{c} + c') = \kappa_c (\nabla^2 \bar{c} + \nabla^2 c') + \frac{\xi}{\rho}$$

$$\frac{\partial \bar{c}}{\partial t} + \frac{\partial c'}{\partial t} + \bar{\mathbf{v}} \cdot \nabla \bar{c} + \bar{\mathbf{v}} \cdot \nabla c' + \mathbf{v}' \cdot \nabla \bar{c} + \mathbf{v}' \cdot \nabla c' = \kappa_c (\nabla^2 \bar{c} + \nabla^2 c') + \frac{\xi}{\rho}$$

by taking the mean of the equation and applying the following definitions

$$\frac{\partial \bar{c}}{\partial t} + \bar{\mathbf{v}} \cdot \nabla \bar{c} + \overline{\mathbf{v}' \cdot \nabla c'} = \kappa_c (\nabla^2 \bar{c}) + \left\langle \frac{\xi}{\rho} \right\rangle$$

a “new” term appears which can be re-written as

$$\overline{\mathbf{v}' \cdot \nabla c'} = \overline{\mathbf{v}' \cdot \nabla c'} + \overline{c' \nabla \cdot \mathbf{v}'} = \nabla \cdot \overline{c' \mathbf{v}'}$$

where $\overline{c' \nabla \cdot \mathbf{v}'} = 0$ if we apply the velocity decomposition to the continuity equation for an incompressible fluid

$$\nabla \cdot \mathbf{v} = 0, \quad \nabla \cdot (\bar{\mathbf{v}} + \mathbf{v}') = \nabla \cdot \bar{\mathbf{v}} + \nabla \cdot \mathbf{v}' = 0 \quad \text{with} \quad \nabla \cdot \bar{\mathbf{v}} = \overline{\nabla \cdot \mathbf{v}} = 0 \quad \text{and thus} \quad \nabla \cdot \mathbf{v}' = 0$$

The term $\overline{c' \mathbf{v}'} = \langle c' \mathbf{v}' \rangle$ represents the turbulent diffusion; K theory (or Newtonian closure) suggests to take

$$\langle c' \mathbf{v}' \rangle = -\mathbf{K} \nabla \langle c \rangle$$

with K the diagonal of the turbulence diffusion tensor, the elements of which are estimated from *in situ* measurements or using numerical models: for oceanic flow we distinguish between horizontal and vertical phenomena

$$\langle c' u' \rangle = -K_H \frac{\partial c}{\partial x} \quad \langle c' v' \rangle = -K_H \frac{\partial c}{\partial y} \quad \langle c' w' \rangle = -K_V \frac{\partial c}{\partial z}$$

where K_H, K_V are the horizontal and vertical turbulence diffusivities, respectively.

Considering that turbulence diffusivities are typically several orders of magnitude larger than their molecular counterpart, molecular diffusion can usually be neglected entirely.

The main difference between turbulence and molecular diffusion is that the former are no property of the fluid but of the flow; they are often determined *a posteriori* in accordance with observational data. Turbulence diffusion is of the same order of magnitude as turbulence (or eddy) viscosity which describes the diffusion of momentum.

If we consider the example of pollutants that do not degrade in any way (i.e., $\langle \xi / \rho \rangle = \xi / \rho$), then Eq. 3.5 becomes

$$\frac{\partial \bar{c}}{\partial t} + \bar{\mathbf{v}} \cdot \nabla \bar{c} = K_H (\nabla_H^2 \bar{c}) + K_V \left(\frac{\partial^2 \bar{c}}{\partial z^2} \right) + \left\langle \frac{\xi}{\rho} \right\rangle$$

Symbols indicating time averaging have been omitted as is customary in the literature, but we should never forget the reasoning behind this (e.g., Reynolds decomposition), the approximations (e.g., incompressible fluid), and the hypotheses (e.g., ergodicity) that have led to this formulation of the conservation equations for a solute containing turbulence diffusivity.

Solutions of the type $\langle c(\mathbf{r}, t) \rangle$ for this equation can be found analytically by making certain simplifying assumptions (e.g., stationarity) or numerically by employing different approaches (finite differences, finite elements, spectral).

Lagrangian approach

The Lagrangian approach is based on the diffusion equation of a solute of a certain concentration $c(x,y,z,t)$:

$$\langle c(\mathbf{r}, t) \rangle = \int_{-\infty}^t \int_{\mathcal{V}} P(\mathbf{r}, t | \mathbf{r}_0, t_0) \xi(\mathbf{r}_0, t_0) d\mathbf{r}_0 dt_0$$

where $P(\mathbf{r}, t | \mathbf{r}_0, t_0)$ is the probability density that a particle which is at r_0 at time t_0 will be at the new location r at time t . As in the Eulerian case, this equation can be integrated analytically if we assume a certain probability distribution for P (often a Gaussian distribution is used as we speak of Gaussian models) and make certain simplifying assumptions. Alternatively, the integration can be solved numerically.

7.4 Lagrangian particle tracking models

Dispersion can be simulated with Lagrangian particle tracking models in two ways:

- models using one single particle: the movement of each particle is independent of the others;
- models using two or more particles: reproducing the relative dispersion between particles.

In the single-particle models, the particles move during each time step with a velocity \mathbf{v}_e that is equivalent to the real velocity \mathbf{v} . If \mathbf{v} defines the particle displacement during a certain time interval $\Delta t = t_2 - t_1$ according to

$$\mathbf{r}_2 = \mathbf{r}_1 + \int_{t_1}^{t_2} \mathbf{v}(\mathbf{r}(t), t) dt,$$

the equivalent velocity is defined as:

$$\mathbf{v}_e = \frac{1}{\Delta t} \int_{t_1}^{t_2} \mathbf{v}(\mathbf{r}(t), t) dt.$$

\mathbf{v}_e can be estimated using observations of Eulerian models of \mathbf{v} using

$$\mathbf{v}_e = \bar{\mathbf{v}} + \mathbf{v}',$$

where

- $\bar{\mathbf{v}}$ represents the deterministic part of the transport that is based on the Eulerian observations/hydrostatic modelling of the current strength;
- \mathbf{v}' represents the random/diffusive component, i.e., a numerical perturbation whose magnitude is linked to the turbulence intensity and the characteristics of the smallest eddies that are not accounted for in the mean velocity field.

To estimate \mathbf{v}' there are two possibilities:

- in the deterministic calculation we use a relation that can be obtained from K -theory of diffusion in a grid:

$$\mathbf{v}' = -\frac{\mathcal{K}}{c} \nabla c,$$

where c is the concentration calculated from the number of particles in a grid cell;

- in the statistical calculation \mathbf{v}' is treated stochastically using so-called Monte-Carlo approaches.

From https://en.wikipedia.org/wiki/Monte_Carlo_method



Monte Carlo methods, or **Monte Carlo experiments**, are a broad class of [computational algorithms](#) that rely on repeated [random sampling](#) to obtain numerical results. The underlying concept is to use [randomness](#) to solve problems that might be [deterministic](#) in principle. They are often used in [physical](#) and [mathematical](#) problems and are most useful when it is difficult or impossible to use other approaches. Monte Carlo methods are mainly used in three problem classes:[\[1\]](#) [optimization](#), [numerical integration](#), and generating draws from a [probability distribution](#).

In physics-related problems, Monte Carlo methods are useful for simulating systems with many [coupled degrees of freedom](#), such as fluids, disordered materials, strongly coupled solids, and cellular structures (see [cellular Potts model](#), [interacting particle systems](#), [McKean–Vlasov processes](#), [kinetic models of gases](#)).

Other examples include modeling phenomena with significant [uncertainty](#) in inputs such as the calculation of [risk](#) in business and, in mathematics, evaluation of multidimensional [definite integrals](#) with complicated [boundary conditions](#). In application to systems engineering problems (space, [oil exploration](#), aircraft design, etc.), Monte Carlo–based predictions of failure, [cost overruns](#) and schedule overruns are routinely better than human intuition or alternative "soft" methods.[\[2\]](#)

In principle, Monte Carlo methods can be used to solve any problem having a probabilistic interpretation. By the [law of large numbers](#), integrals described by the [expected value](#) of some random variable can be approximated by taking the [empirical mean](#) (a.k.a. the sample mean) of independent samples of the variable. When the [probability distribution](#) of the variable is parametrized, mathematicians often use a [Markov chain Monte Carlo](#) (MCMC) sampler.[\[3\]\[4\]\[5\]](#) The central idea is to design a judicious [Markov chain](#) model with a prescribed [stationary probability distribution](#). That is, in the limit, the samples being generated by the MCMC method will be samples from the desired (target) distribution.[\[6\]\[7\]](#) By the [ergodic theorem](#), the stationary distribution is approximated by the [empirical measures](#) of the random states of the MCMC sampler.

In other problems, the objective is generating draws from a sequence of probability distributions satisfying a nonlinear evolution equation. These flows of probability distributions can always be interpreted as the distributions of the random states of a [Markov process](#) whose transition probabilities depend on the distributions of the current random states (see [McKean–Vlasov processes](#), [nonlinear filtering equation](#)).[\[8\]\[9\]](#) In other instances we are given a flow of probability distributions with an increasing level of sampling complexity (path spaces models with an increasing time horizon, Boltzmann–Gibbs measures associated with decreasing temperature parameters, and many others). These models can also be seen as the evolution of the law of the random states of a nonlinear Markov chain.[\[9\]\[10\]](#) A natural way to simulate these sophisticated nonlinear Markov processes is to sample multiple copies of the process, replacing in the evolution equation the unknown distributions of the random states by the sampled [empirical measures](#). In contrast with traditional Monte Carlo and MCMC methodologies these [mean field particle](#) techniques rely on sequential interacting samples. The terminology *mean field* reflects the fact that each of the *samples* (a.k.a. particles, individuals, walkers, agents, creatures, or phenotypes) interacts with the empirical measures of the process. When the size of the system tends to infinity, these random empirical measures converge to the deterministic distribution of the random states of the nonlinear Markov chain, so that the statistical interaction between particles vanishes.

From https://en.wikipedia.org/wiki/Linear_regression

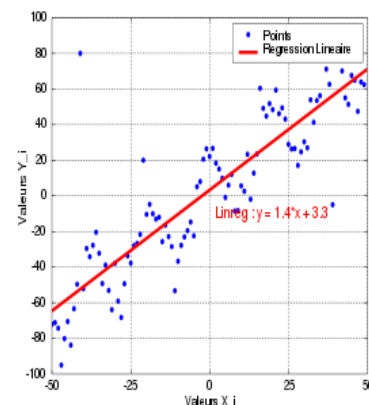
In statistics, given a random sample $(Y_i, X_i), i = 1, \dots, n$ of n statistical units, a linear regression model assumes that the relationship between the dependent variable Y and regressor X is [linear](#):

$$Y_i = aX_i + b, \quad i = 1, \dots, n$$

In **linear regression** the main task consists of estimating the values a and b and of quantifying the validity of these estimates through the **linear correlation coefficient**. This can be generalised for p explanatory variables/predictors

$$Y_i = a_0 + a_1X_{i1} + a_2X_{i2} + \dots + a_pX_{ip}$$

which is then called [multiple linear regression](#).



This second approach is more flexible and more common.

The velocity distribution of particles dispersing in turbulent flow can be written using autoregressive models. An autoregressive process is a [regression](#) model for time series data, the evolution of which can be fully explained from its past evolution.

The autoregressive models are thus discrete models where the velocity at a given instant is a linear combination of its past values plus a time-dependent random term.

An autoregressive model of order p is denoted with the acronym $AR(p)$ and for the case of velocities it becomes

$$\mathbf{v}'_n = \alpha_1 \mathbf{v}'_{n-1} + \alpha_2 \mathbf{v}'_{n-2} + \dots + \alpha_p \mathbf{v}'_{n-p} + \mathbf{v}$$

where \mathbf{v} is a random velocity component.

Zero-order autoregressive models or “random walks”

In this type of model, one makes the assumption that Brownian motion can be described as a zero-order autoregressive model $AR(0)$ where the random velocity component, being the result of random collisions between fluid particles, simply is:

$$\mathbf{v}'_n = \mathbf{v}$$

By using the analogy between molecular diffusion and the diffusion of particles immersed in the fluid by turbulence, one can consider the displacements due to the small eddies as purely random. A numerical model that makes use of this approximation calculates the particle displacements as follows:

$$\mathbf{r}_{n+1} - \mathbf{r}_n = \bar{\mathbf{v}}_n \Delta t + \boldsymbol{\mu}_n$$

where $\boldsymbol{\mu} = \mathbf{v} \Delta t$. To each component of $\boldsymbol{\mu} = (\mu_x, \mu_y, \mu_z)$ we assign a randomly chosen value from the corresponding probability density function.

First-order autoregressive models

A first-order autoregressive model, $AR(1)$, applies if we consider pollutant particles that are both small enough for the molecules around them to produce random variations in their velocity but also large enough to experience friction with the molecules of the liquid which causes a reduction in their velocity.

The equation of motion takes the form of the stochastic Langevin equation:

$$\frac{d\mathbf{v}'}{dt} = -\beta \mathbf{v}' + \mathbf{v}$$

In this equation, the particle acceleration is divided into two terms that describe different aspects of the particle-fluid interactions:

$\beta \mathbf{v}'$ describes the fluid as a continuous, macroscopic medium that exerts a friction force on the particle that is proportional to the particle velocity;

\mathbf{v} is a term that represents random forcing due to collisions, which therefore describes the behaviour of the fluid as a set of random variations due to the random particle accelerations.

The displacement of a particle immersed in a fluid moving with velocity $\bar{\mathbf{v}}$ is then given by the sum of the fluid velocity and the random velocity as obtained from the Langevin equation. It will therefore be necessary to solve the following set of equations numerically:

$$\begin{aligned} \mathbf{r}_{n+1} - \mathbf{r}_n &= [\bar{\mathbf{v}}_n + \mathbf{v}'_n] \Delta t \\ \mathbf{v}'_n - \mathbf{v}'_{n-1} &= -\beta [\mathbf{v}'_{n-1} + \mathbf{v}_n] \Delta t \end{aligned}$$

The second equation becomes

$$\mathbf{v}'_n - \mathbf{v}'_{n-1} = (1 - \beta \Delta t) \mathbf{v}'_{n-1} + \mathbf{v}_n \Delta t = \Phi \mathbf{v}'_{n-1} + \mathbf{v}_n \Delta t$$

With the series $\{v_n\}$ being entirely random and stationary with zero mean, the ensemble mean becomes

$$\langle v'_n \rangle = \Phi \langle v'_{n-1} \rangle$$

and in the steady state we have $\langle v'_n \rangle = 0$.

The covariance is

$$\langle v'_n v'_{n-1} \rangle = \Phi \langle v'^2_{n-1} \rangle$$

considering $\langle v_n v'_n \rangle = 0$ v is independent of v' .

In the steady state, by using the covariance $C_o = \langle v'^2_n \rangle$ the preceding equation can be written as

$$C_1 = \Phi C_o$$

and more generally

$$C_k = \Phi C_{k-1} \text{ or } C_k = \Phi^k C_o$$

We can define a correlation coefficient

$$\rho_k = \frac{C_o}{C_k} = \Phi^k$$

which, since $|\Phi| < 1$, will have the shape shown on the right

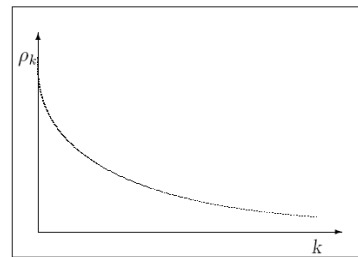


Figura 3.4: Andamento del coefficiente di correlazione.

The variance of $\{v'_n\}$ is linked to the variance of $\{v_n\}$ by the following relation where $2 \Phi \langle v_n v'_{n-1} \rangle = 0$

$$\langle v'^2_n \rangle = \Phi^2 \langle v'^2_{n-1} \rangle + \langle v^2_n \rangle \text{ or } \langle v'^2_n \rangle = \frac{1}{1-\Phi^2} \langle v^2_n \rangle$$

The series $\{v'_n\}$ can thus be calculated iteratively:

$$\begin{aligned} v'_1 &= \Phi v'_o + v_1 \\ v'_2 &= \Phi^2 v'_o + \Phi v_1 + v_2 \\ \dots \\ v'_n &= \Phi^n v'_o + \sum_{i=0}^{\infty} \Phi^i v_{n-1} \end{aligned}$$

but since Φ^n decreases quickly, v_n quickly loses its “memory” of the initial state. Asymptotically (in the steady state) we will have

$$v'_n \approx \sum_{i=0}^{\infty} \Phi^i v_{n-1}$$

The series $\{v'_n\}$ thus tends to be a moving average exponentially weighted based on the past evolution of $\{v_n\}$.

7.5 Implementing a “Random Walk” and an advection-diffusion model

For the moment, we will consider a zero mean velocity and consider a situation comparable to a drop of ink diffusing in a glass of water.

Our model then simply looks like this

$$r_{n+1} - r_n = \mu$$

and we need to calculate μ .

Truly random numbers can be produced with hardware that takes advantage of certain stochastic physical properties (e.g., the noise of a resistance) but this would be impractical for a numerical model. We therefore use a so-called pseudo-random number generator (PRNG) which is an algorithm that generates a sequence of numbers with certain properties of chance. For example, numbers must be largely independent of each other and it should be difficult to spot groups of numbers that follow a certain rule (group behaviour). However, it should be remembered that the output of any PRNG is never entirely random; they only approximate the ideal properties of completely random numbers. [John von Neumann](#) insisted on this fact with the following remark: "Anyone who considers arithmetical methods of producing random digits is, of course, in a state of sin". A rigorous mathematical analysis is necessary to determine the degree of randomness of a PRNG.

Pseudo-random methods are often used on computers for various tasks such as the Monte-Carlo simulations (see above) or [cryptographic](#) applications.

Most pseudo-random algorithms try to produce outputs that are uniformly distributed, typically with a uniform probability distribution between 0 and 1. However, to simulate diffusion in a liquid we need a Gaussian distribution of probability densities instead.

Afin d'obtenir un tirage gaussien, d'espérance et d'écart type paramétrable, une manipulation du tirage uniforme est à effectuée :

Une variable r possède une distribution de probabilité uniforme, entre 0 et 1. On définit une variable $r' = r - 1/2$, qui aura alors une distribution de probabilité uniforme entre $-1/2$ et $1/2$, une moyenne $\langle r' \rangle = 0$ et une variance :

$$\sigma^2 = \int_{-1/2}^{+1/2} r'^2 \cdot dr = \left[\frac{r'^3}{3} \right]_{-1/2}^{+1/2} = 1/12$$

Considérons maintenant la variable R définie tel que

$$R = \sum_{i=1}^n r'_i$$

$$\langle R \rangle = \sum_{i=1}^n \langle r'_i \rangle$$

On a donc

$$\sigma_R^2 = \sum_{i=1}^n \sigma_{r'_i}^2$$

En sommant des nombres r' tirés uniformément entre $-1/2$ et $+1/2$, on change la distribution de probabilité : une suite de n variable aléatoire indépendante (comme R) tend pour $n \rightarrow \infty$ à une distribution gaussienne $G(\langle R \rangle, \sigma^2)$. Lorsque n est grand, R a effectivement plus de chance d'être égale à 0 qu'à $1/2$ (où il faudra n tirages de r' égal à $1/2$!).

Si nous prenons $n=12$, nous avons $\langle R \rangle = 0$ et $\sigma_R^2 = 1$, nous tombons sur le théorème centrale limite.

$$g = \left[\sum_{i=1}^{12} r'_i \right] \cdot \sigma$$

Nous pouvons calculer maintenant le nombre g tel que

Le nombre g est alors un nombre tiré d'une distribution de probabilité gaussienne approximativement avec une moyenne nulle et un écart type σ , comme le montre la figure 1.

```

devst=10;
imax=1000;

for j=1:imax
    g=0;
    for i=1:12
        r=rand(1);
        g=g+(r-0.5);
    end
    gg(j)=g.*devst;
end

edges=[-100:1:100];
N=histc(gg,edges);
bar(edges,N./imax,'histc')

var=devst^2;
y=1/sqrt(2*pi*var).*exp(-edges.^2/(2*var));

line(edges,y,'color','r')
    
```

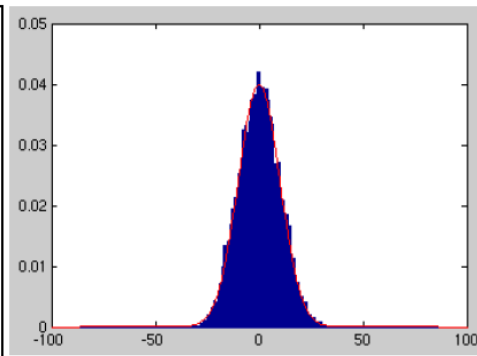


Figure 1 : Comparaison de l'histogramme de gg (en bleu) avec y une gaussienne théorique (en rouge)

Random walk in two spatial dimensions

For the purposes of this analysis, and in order to simplify the modelling of Brownian motion, we will consider only two spatial dimensions. Let us consider the case of a single particle for the moment. This particle performs a random walk when each step is of random direction and random length. For example, if (x_i, y_i) denote the particle coordinates after time step i , then the particle coordinates one time step later $(i + 1)$ will be given by:

$$x(i+1)=x(i)+depx$$

$$y(i+1)=y(i)+depy$$

where $depx$ and $depy$ are random variables taken from the Gaussian probability density distribution mentioned above, centred on 0 with a standard deviation of 1 ($devst$ in the code). The particle thus performs a random walk with independent steps as shown in the following figure.

```

figure(1);hold on;
devst=1;
x(1)=0;
y(1)=0;
itmax=300;

for it=2:itmax
    g=0;
    for j=1:12
        r=rand(1);
        g=g+(r-0.5);
    end
    depx=g.*devst;
    g=0;
    for j=1:12
        r=rand(1);
        g=g+(r-0.5);
    end
    depy=g.*devst;

    x(it)=x(it-1)+depx;
    y(it)=y(it-1)+depy;
end

line(x,y)
hold off;
    
```

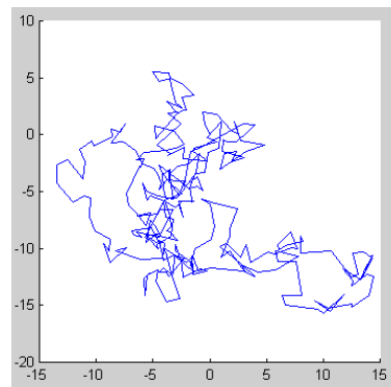


Figure 2 : Marche aléatoire d'une particule dans un espace à 2 dimensions

To model more than one particle we simply need to add another loop to the code ($ipmax$ represents the number of particles).

```

figure(1);hold on;
ipmax=10;

for ip=1:ipmax
    --
    script précédent
    --

    line(x,y,'color',[ip/ipmax 0 1-ip/ipmax])

    text(20,30-ip*4,num2str(ip),
        'color',[ip/ipmax 0 1-ip/ipmax])
end

axis([-40 40 -40 40])

hold off;
    
```

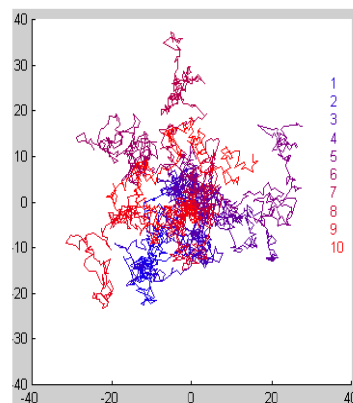


Figure 3 : Marche aléatoire de 10 particules indépendantes

Calculating the spatial concentration

We have plotted the tracks of several particles over time. However, we wish to focus our attention to the problem of diffusion. For this purpose, let us imagine a small arbitrarily shaped domain in which particles are allowed to diffuse.

We can choose a square domain with sides of length 100 (arbitrary units) (the matrix called CONC in the code). Now we want to show the concentration at each point and each instant "it". This can be achieved by reversing the time loop ("it" in the code) with the loop over the number of particles ("ip" in the code). We then place all particles at the initial location (50,50) (for it=1) and make them move (using displacements depx and depy).

```

devat=1; ipmax=4; itmax=10;
xold(1:ipmax)=50;
yold(1:ipmax)=50;

for it=1:itmax
  CONC=zeros(100,100);

  for ip=1:ipmax
    g=0;
    for i=1:12
      r=rand(1);
      g=g+(r-0.5);
    end
    depx=g.*devat;

    g=0;
    for i=1:12
      r=rand(1);
      g=g+(r-0.5);
    end
    depy=g.*devat;

    xnew(ip)=xold(ip)+depx;
    ynew(ip)=yold(ip)+depy;

    if xnew(ip)<1 | xnew(ip)>100 | ynew(ip)<1 |
      ynew(ip)>100

      xnew(ip)=xold(ip);
      ynew(ip)=yold(ip);
    end

    ii=fix(xnew(ip));
    jj=fix(ynew(ip));
    CONC(jj,ii)=CONC(jj,ii)+1;

    xmem(ip)=xnew(ip);
    ymem(ip)=ynew(ip);

    xold(ip)=xnew(ip);
    yold(ip)=ynew(ip);
  end %pour ip

  figure(1);hold on;
  grid;
  contour(CONC)

  plot(xmem,ymem,'k+')
  waitforbuttonpress
  clf;
end %pour it

```

A chaque instant it, on compte combien il y a de particules dans chaque maille de grilles (CONC dans le code).

On remarque sur la figure un léger décalage des iso lignes de concentration, par rapport aux positions réelles des particules (croix noire). Ceci parce que l'on rapporte toutes les particules d'une maille de grille (de i à i+1, et de j à j+1) à un point de coordonnée (i,j). Mais avec un très grand nombre de particule, ceci n'a plus d'importance

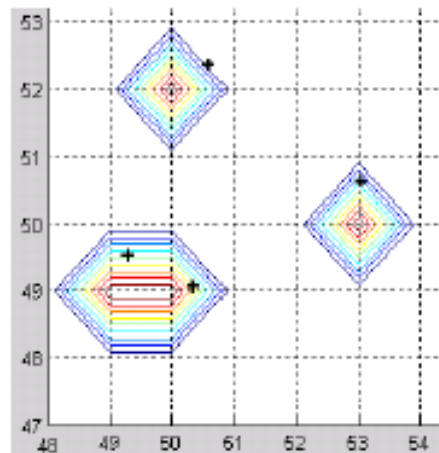


Figure 4 : Calcul de la concentration dans notre espace à l'instant $t=1$

Il ne nous reste maintenant plus qu'à augmenter le nombre de particules représentant la goutte d'encre.

La figure 5 montre 9 étapes de la diffusion d'une goutte d'encre au cours du temps. La goutte d'encre est d'abord centrée en (50,50), puis diffuse dans la boîte.

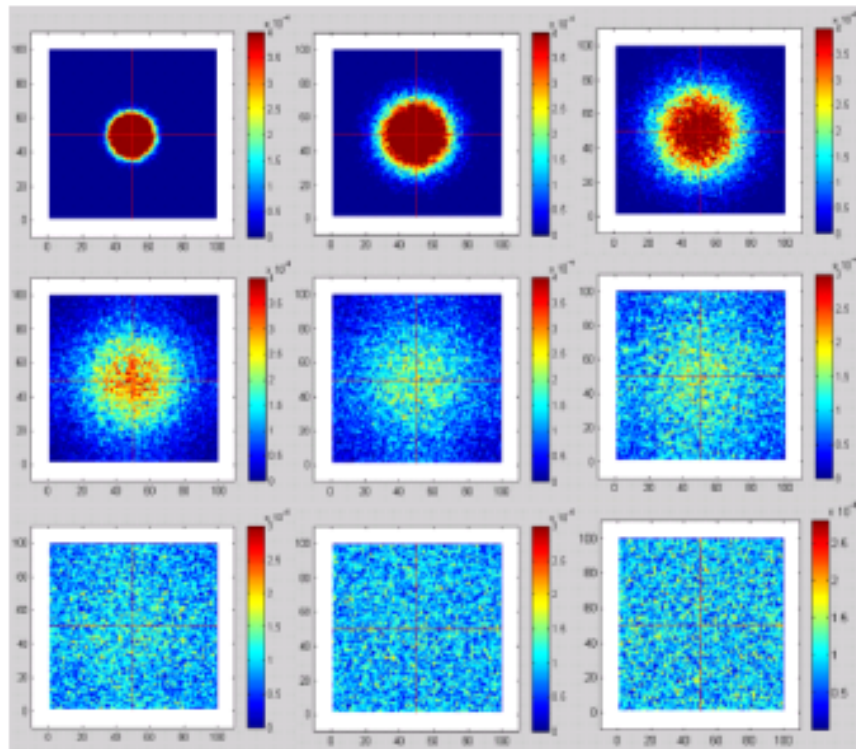


Figure 5 : Diffusion d'une goutte d'encre dans de l'eau

En suivant la concentration le long de l'axe horizontal et vertical (croix rouge sur la figure 5), et en la comparant avec la gaussienne théorique, on obtient la figure 6.

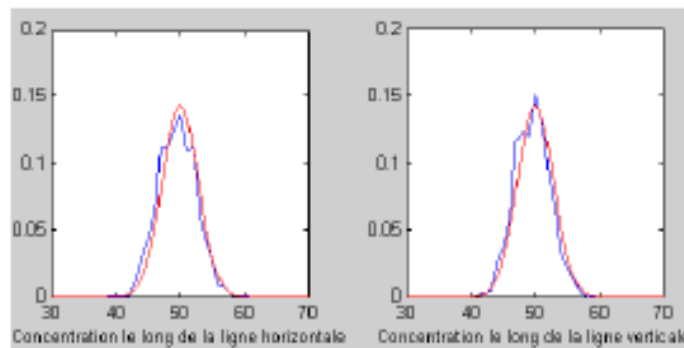


Figure 6 : Concentration (courbe en bleu) le long d'un axe horizontal (à gauche) et vertical (à droite) comparée à la gaussienne théorique (en rouge) à l'instant $t=300$

Figure 2 shows us the random walk of a particle subject to Brownian motion. Although all directions are equiprobable, the random walk is not isotropic. In fact, the random walk is only statistically isotropic, i.e., isotropy only appears after a very large number of steps. This is what Figure 5 shows us, the diffusion of a drop of ink in a fluid. We can easily see that this drop of ink diffuses over time, i.e., it spreads, propagates, until reaching a near homogeneous distribution in space. Here, we clearly see that the spreading is isotropic, i.e., it occurs in all directions equally. Hence, isotropy only appears from a macroscopic point of view as it is a statistical property. Figure 5 also shows that the spreading of the ink drop slows with time. The diffusion equation proposed by A. Fick is:

$$\frac{\partial S}{\partial t} = k_s \cdot \nabla^2 S + \xi$$

Avec k_s coefficient de diffusion, ∇^2 opérateur Laplacien, ξ la source et le puit.

Lorsqu'il n'y a pas de source ni de puit, $\xi=0$, une solution possible de l'équation de diffusion est :

$$K(x,t) = \frac{1}{(4\pi k_s t)^{1/2}} \exp^{-r^2 / (4k_s t)} \quad (1)$$

Où $r^2=x^2$ (pour un espace à 1 dimensions)

Cette solution représente une gaussienne tridimensionnelle de variance

$$\sigma^2 = 2 \cdot k_s \cdot t$$

The standard deviation, σ , is proportional to the square root of time, i.e., it is high at first and decreases with time to near zero. Initially, σ will increase quickly commensurate with the diffusion of our ink drop but this increase will slow down indicating a slowing diffusion. By replacing the term $2 k_s t$ by σ^2 in Eq.(1), we obtain a Gaussian:

$$f_x = \frac{1}{\sqrt{2 \cdot \pi \cdot \sigma^2}} \cdot \exp\left(-\frac{r^2}{2 \cdot \sigma^2}\right) \quad (2)$$

Figure 6 shows a comparison of the particle distribution along the horizontal and vertical axes and the theoretical distribution predicted by Eq.(2) (using $r^2=(x-50)^2$ to centre the Gaussian at 50).

Let us now focus on advection.

The equation that needs to be solved numerically for a single Lagrangian particle is

$$\frac{dX}{dt} = V_a(X, t) + V_d(X, t)$$

with X the particle position, Va the advection velocity and Vd the random velocity linked to turbulence.

Using V=Va+Vd and by integrating we obtain

$$X(t^{n+1}) = X(t^n) + \int_{t^n}^{t^{n+1}} V(X, t) dt \quad (1)$$

Several methods are available to solve this equation.

Here Δt is the time step with $\Delta t = t^{n+1} - t^n$ and n is the time index such that $t^n = n \Delta t$

The Euler method

This method is widely used as it is easy to code. In general, the numerical scheme is written as

$$X^{n+1} = X^n + V(X^n, t^{n+1}) \Delta t$$

One advantage of this method is that it only requires a single velocity field (a snapshot taken at a single instant in time), i.e., $V(X, t^{n+1})$.

In practice, we need to interpolate the velocities from the four nearest grid points to obtain the velocity at the exact location of the particle.

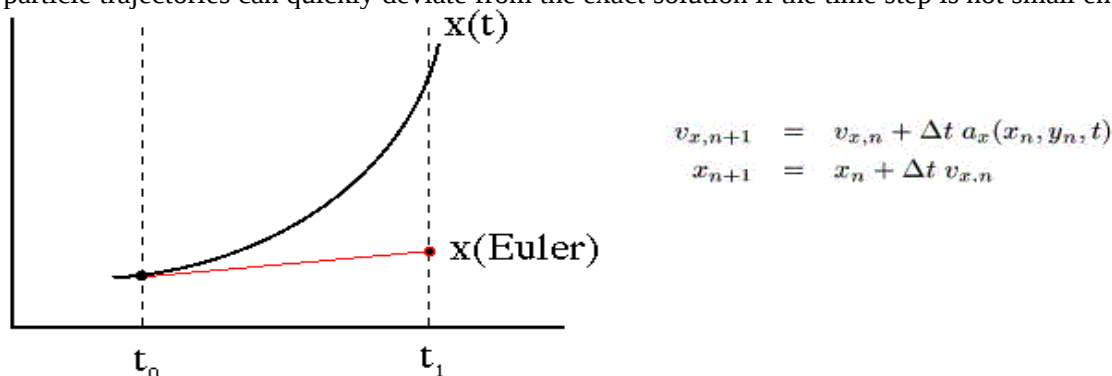
One method is to take a weighed average based on the distance between the particle and the grid points. The coefficients, or weights, are inversely proportional to the distance between the particle and each grid point and can be calculated from

$$v_{det} = w_1 v_{i,j}^{mike} + w_2 v_{i+1,j}^{mike} + w_3 v_{i+1,j+1}^{mike} + w_4 v_{i,j+1}^{mike}$$

I pesi w_k ($k = 1, 2, 3, 4$), inversamente proporzionali alla distanza d_k dai corrispondenti punti di griglia, vengono calcolati mediante la formula numerica

$$w_k = \frac{d_1 d_2 d_3 d_4}{d_k (d_1 d_2 d_3 + d_1 d_3 d_4 + d_1 d_2 d_4 + d_2 d_3 d_4)} \quad \text{con } k = 1, 2, 3, 4.$$

The main disadvantage of the Euler method is its low precision (order 1) which means that the particle trajectories can quickly deviate from the exact solution if the time step is not small enough.



<http://rainman.astro.uiuc.edu/ddr/ddr-galaxy/parameters.html>

Runge-Kutta methods

Runge-Kutta methods can be used to find approximate solutions to differential equations. They have been named in honour of the mathematicians Carl Runge and Martin Wilhelm Kutta who developed the method in 1901.

These methods are based on the principle of iteration, that is, a first estimate of the solution is used to calculate a second, more precise estimate, and so on. Depending on the number of iterations we speak of a different order. The first-order Runge-Kutta method (RK1) is equivalent to the Euler method. The classical Fourth-Order Runge-Kutta method is a special case that is used very frequently. Denoted RK4, it can be written as follows:

$$X^{n+1} = X^n + \frac{1}{6}(a + 2b + 2c + d)$$

with

$$a = \Delta t \left[V(X^n, t^n) \right]$$

$$b = \Delta t \left[V \left(X^n + \frac{1}{2}a, t^{\frac{n+1}{2}} \right) \right]$$

$$c = \Delta t \left[V \left(X^n + \frac{1}{2}b, t^{\frac{n+1}{2}} \right) \right]$$

$$d = \Delta t \left[V(X^n + c, t^{n+1}) \right]$$

The idea is that the next value (X_{n+1}) is approximated by the sum of the current value (X_n) and the product of the time step Δt with the estimated slope (i.e., the velocity or rate of change of the location). The slope is obtained by creating a weighted average of different slopes:

a is the displacement based on the slope at the beginning of the time interval;

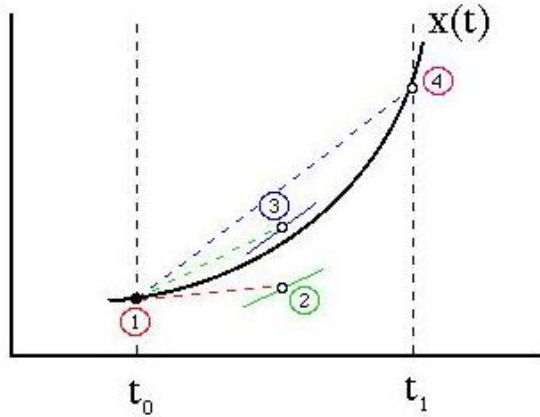
b is the displacement based on the slope at the midpoint of the time interval and at the midpoint of the displacement a calculated by Euler's method;

c is again the displacement based on the slope at the midpoint of the time interval, but at the location obtained from the displacement b ;

d is the displacement based on the slope at the midpoint of the time interval and at the midpoint of the displacement given by c .

In the average of the four slopes, a greater weight is assigned to the slopes at midpoint:

$$\text{slope} = (a + 2b + 2c + d)/6.$$



$$\begin{aligned}
 dx1 &= \Delta t v_{x,n} \\
 dv_{x1} &= \Delta t a_x(x_n, y_n, t) \\
 dx2 &= \Delta t (v_{x,n} + \frac{dv_{x1}}{2}) \\
 dv_{x2} &= \Delta t a_x(x_n + \frac{dx1}{2}, y_n + \frac{dy1}{2}, t + \frac{\Delta t}{2}) \\
 dx3 &= \Delta t (v_{x,n} + \frac{dv_{x2}}{2}) \\
 dv_{x3} &= \Delta t a_x(x_n + \frac{dx2}{2}, y_n + \frac{dy2}{2}, t + \frac{\Delta t}{2}) \\
 dx4 &= \Delta t (v_{x,n} + dv_{x3}) \\
 dv_{x4} &= \Delta t a_x(x_n + dx3, y_n + dy3, t + \Delta t) \\
 x_{n+1} &= y_n + \frac{dx1}{6} + \frac{dx2}{3} + \frac{dx3}{3} + \frac{dx4}{6} \\
 v_{x,n+1} &= v_{x,n} + \frac{dv_{x1}}{6} + \frac{dv_{x2}}{3} + \frac{dv_{x3}}{3} + \frac{dv_{x4}}{4}
 \end{aligned}$$

<http://rainman.astro.uiuc.edu/ddr/ddr-galaxy/parameters.html>

The RK4 is a forth-order method, which means that the error committed at each step is of the order of h^5 , while the total accumulated error is of the order of h^4 .

The problem with this method is that it requires the velocities between two time steps. We therefore need to interpolate not only in space but also in time. The interpolation in time must have the same precision as the method of integration. So a forth-order interpolation is

$$V^{\frac{n+1}{2}}(X) = \frac{5}{16} V^{n+1}(X) + \frac{5}{16} V^n(X) - \frac{5}{16} V^{n-1}(X) + \frac{1}{16} V^{n-2}(X)$$

From a programming point of view, this means that we need to store more information in memory, essentially all four velocity fields for the entire length of the simulation as we cannot know beforehand where the particle will go; this requires more RAM.

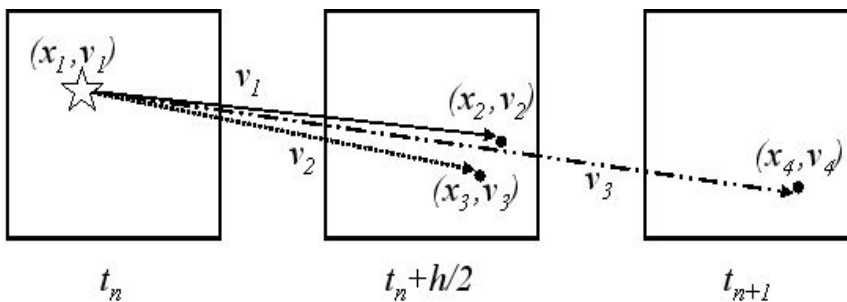


Figure by M.Berta

The Adams-Bashford-Multon (ABM) method

This method is divided into two steps: a predictive part (Adams-Bashford method) and a corrective part (Adams-Multon method).

The predictive part employs a polynomial interpolation of the variable $V(X,t)$ through the points X_n, X_{n-1}, X_{n-2} , and X_{n-3} followed by integrating Eq.(1) between X_n and X_{n+1}

$$\tilde{X}^{n+1} = X^n + \frac{\Delta t}{24} (55V^n - 59V^{n-1} + 37V^{n-2} - 9V^{n-3}) \tag{6}$$

The corrective part uses a polynomial interpolation of the variable $V(X,t)$ through the points \tilde{X}_{n+1} (which we just calculated in the predictive step), X_n, X_{n-1} , and X_{n-2} and by integrating Eq.(1) between X_n and X_{n+1}

$$X^{n+1} = X^n + \frac{\Delta t}{24} (9\tilde{V}^{n+1} + 19V^n - 5V^{n-1} + V^{n-2}) \quad (7)$$

where $\tilde{V}^{n+1} = V(\tilde{X}^{n+1}, t^{n+1})$.

The ABM method is also a fourth-order method with an error of order 5.

Using a Taylor series expansion we can estimate the errors of the predictive part

$$X(t^{n+1}) - \tilde{X}^{n+1} \approx \frac{251}{720} X^{(5)n} (\Delta t)^5 \quad (8)$$

and of the corrective part

$$X(t^{n+1}) - X^{n+1} \approx -\frac{19}{720} X^{(5)n} (\Delta t)^5 \quad (9)$$

where $X(t^{n+1})$ indicates the “true” value.

By combining Eqs.(8) and (9)

$$X(t^{n+1}) = \frac{251}{270} X^{n+1} + \frac{19}{720} \tilde{X}^{n+1} \quad (10)$$

Combine Eq. (6), (7) and (10), we can finally derive the advanced ABM scheme.

$$X^{n+1} = \frac{1}{270} \left[19\tilde{X}^{n+1} + 251 \left[X^n + \frac{\Delta t}{24} (9\tilde{V}^{n+1} + 19V^n - 5V^{n-1} + V^{n-2}) \right] \right] \quad (11)$$

Here \tilde{X}^{n+1} is computed using Eq. (6). Special attention should be concerned that the scheme is not self starting. Therefore the RK method is needed to initiate the scheme, i.e. the locations in the first four time step are computed using the RK method.

One velocity field $V(X, t^{n+1})$, the previous particle position X^n and four previous particle velocities ($V(X^n, t^n)$, $V(X^{n-1}, t^{n-1})$, $V(X^{n-2}, t^{n-2})$ and $V(X^{n-3}, t^{n-3})$) are needed to calculate the new particle position. In a 3D flow field, the total internal memory usage for the advanced ABM scheme is as (memory $\leq N_x + 15N_p$ words).

In general, the storage for the field information is much greater than the number of particles. Therefore, on memory considerations alone, the Euler scheme and the advanced ABM scheme are much less required than the RK scheme.

During one timestep particle integration, the Euler scheme only need to evaluate one new function, however, the RK scheme involves four velocity evaluations, and the advanced ABM scheme adds one velocity evaluation. Therefore, on numerical computation considerations alone, the Euler scheme is the most efficient scheme. And the advanced ABM scheme is efficiently faster than the RK scheme.

5.6 Coupled physical-biogeochemical modelling

Coupling Lagrangian particle tracking models with general circulation models can yield valuable insights when studying the role of different physical processes and their interactions on transport over a wide range of scales. In fact, the Lagrangian technique allows us to simulate a rather wide range of different processes. Apart from simple advection, we can add the grid-based diffusion or biological behaviour employing varying degrees of complexity.

As pointed out by Miller (2007) in a review paper on using Individual Based Models (IBMs) to study fish recruitment, these models, although defined as coupled physical-biological models, are typically used in an offline-coupled mode to reduce computational cost, apart from a few exceptions (e.g., Hinckley96, Mullon03, Guizen06).

In this scheme, runs of the hydrodynamic model are completed and output is stored at set intervals. Then the IBM uses stored velocity data to move and track individual eggs and larvae throughout the model domain.

Adopting this approach it becomes crucial to provide subgrid-scale resolution of fluid flows. Indeed the horizontal and vertical spatial resolution of the hydrodynamic models are several orders of magnitude larger than the length scales of larvae.

Early models used a simple scheme that updates the position of tracked particles based on spatially interpolated model velocities with small random components.

As the field has developed, the particle tracking algorithms have become more sophisticated, with increasing attention being paid to the statistical aspects of the subgrid-scale motion. The stochasticity at subgrid scales creates an ensemble of trajectories for each starting location depending on the small-scale features of the flow critical for eggs and larva.

Then, individual particle movements are tracked offline with Lagrangian Statistical Models (LSM), assuming that the evolution of particle velocity and position in non-homogeneous, non-stationary turbulence can be represented as a Markovian process (e.g. Griffa 1996).

Generally a zero order Markovian process is adopted, also if recently some authors choose higher order (e.g. Paris et al. 07), to take into account the rotation of trajectories driven by submesoscale coherent vortices.

The Lagrangian single-particle tracking algorithms for a zero order Markovian process, are based on the following equation:

$$\frac{d\vec{x}}{dt} = \vec{u} + \vec{u}' + \vec{u}_{larva} \quad (1)$$

where $\vec{x} \equiv (x, y, z)$ is the 3D location, t is the time, $\vec{u} \equiv \vec{u}(\vec{x}, t)$ is the flow velocity at the resolved scale, $\vec{u}' \equiv \vec{u}'(\vec{x}, t)$ is the subgrid-scale fluctuating turbulent component of the velocity field and $\vec{u}_{larva} \equiv \vec{u}_{larva}(\vec{x}, t)$ is the individual larva's velocity.

In the following we present a review of several papers to compare the different approaches to solve (1), as schematically presented in Table 4.1

Markovian process order

| | |
|-----------------------|------------------|
| > 0 <i>Paris07</i> | = 0 other all |
|-----------------------|------------------|

U from ADCP data & linear interpolation

| |
|---------------|
| <i>Heat94</i> |
|---------------|

U from eulerian model

| Horizontal interpolation linear <i>Miller98 finite elements</i> <i>Cianelli07</i> | Vertical interpolation linear <i>Lett07 SIGMA</i> <i>Cianelli07</i> | Temporal interpolation | |
|--|--|---|--|
| | | None <i>Speirs06</i> <i>Lett07</i> <i>Cianelli07</i> <i>Paris07</i> | linear <i>Miller98</i> <i>Lett08</i> |

U' horizontal

| | | |
|--|--------------------------------|---|
| nodiffusion <i>Lett07</i> <i>Allain03</i> <i>Cianelli07</i> | white noise <i>Speirs06</i> | randow walk <i>Guizen06 gaussianeulerian</i> <i>s proportionale eulerian TKE</i> <i>Lett08, Peliz07</i> <i>disrate+unresolvescale</i> |
|--|--------------------------------|---|

U' vertical

| | | | |
|--|--|--|-------------------------------------|
| nodiffusion <i>Lett07</i> <i>Allain03</i> <i>Cianelli07</i> | randow walk <i>Guizen06 from a gaussian with sigma proportional to eulerian TKE</i> | no-naif random walk <i>Peliz07</i> <i>Lett08 following Visser07 con cubic spline interp of diffusivity</i> | inertial eddies??? <i>Heat94</i> |
|--|--|--|-------------------------------------|

ULARVA

| |
|--|
| <i>ontogenic changes+sensitivity to the light+interindividual varaibility (Guizen)</i> |
|--|

schemes

| | | |
|--|---|-----------------------------|
| Euler <i>Guizen06</i> <i>Lett07</i> <i>Lett08</i> | Adams-Bashford-Multon <i>Carr06</i> <i>Lett07</i> <i>Peliz07</i> | RungeKutta <i>Lett08</i> |
|--|---|-----------------------------|

coupling with thermohydrodynamics

| |
|---|
| <i>Lett07, Lett08, Hinckley96, Mullon03</i> |
|---|

AGRIF

| |
|----------------|
| <i>Peliz07</i> |
|----------------|

The deterministic resolved-scale velocity $\vec{u} \equiv \vec{u}(\vec{x}, t)$ is generally provided by an Eulerian model also if some authors obtained it directly from in situ data (Heat et al., 94). In both case, an interpolation of these data is necessary to obtain a value in each particle position from gridded data at each Lagrangian timestep.

Regarding horizontal interpolation, generally a linear one is done.

For example, Miller (98) interpolated from a finite triangular elements grid, while more frequently is performed an interpolation from a orthogonal curvilinear grid such as the one of ROMS model (e.g. Carr et al., Lett et al.) or SYMPHONIE model (Cianelli et al.). Moreover, Peliz et al (04) adapted AGRIF package (<http://www-lmc.imag.fr/MOISE/AGRIF/>) to manage the communication of floats

through the different nested model domains.

In the vertical an interpolation is necessary too, in particular from terrain-following coordinate Eulerian models. Again a linear interpolation is generally adopted (e.g. Lett07, Cianelli07) .

In temporal dimension, some author proposed a linear interpolation when the time interval of the Lagrangian module is shorter than Eulerian model one (Miller98) but frequently the interpolation is not performed (Speirs, Lett, Cianelli, Paris) .

In this case, as pointed out by Guizen, the Lagrangian-model integration timestep is constrained by 2 factors.

Table 4.1

First, it depends on the Stokes number, i.e., the ratio of the particle to fluid response times.

Second, fluctuating velocities should be updated every time a larva encounters a new eddy. This particle-eddy interaction time can be defined as the minimum between the eddy life time and the eddy transit time through a cell. The authors estimate that the particle-eddy interaction time is the transit time of fast moving surface waves through a cell, i.e. close to the barotropic mode timestep of the 3D eulerian model. Then, theoretically the integration timestep for Eq. (1) should be lower than this particle-eddy interaction time. At the same time, several studies in physical oceanography suggest methods to evaluate error and sensitivity to time sampling for off line lagrangian particles, using for example

| | | |
|------------|----------|-----------|
| Finite | Liapunov | Exponents |
| position | from | a |
| deviations | a | reference |
| from | a | case |

or the ensemble-averaged position deviations from a reference case

or the ensemble-averaged position deviations from a reference case (Iudicone_etal_OceanModel02_SensitivityNumericalTracerTrajectories.pdf) or the ensemble-averaged position deviations from a reference case (Valdivieso_Blanke_OceanModel04_lagrangianmethodsClimatologyTrajectoryError.pdf).

In practice, Guizen06 integrated Eq.(1) over the baroclinic timestep, considering that however i) the circulation flow velocity and the larva's own velocity vary slowly and ii) the turbulent velocities provided by the Eulerian model are averaged over the baroclinic timestep.

The subgrid-scale fluctuating turbulent component of the velocity field $\vec{u}' \equiv \vec{u}'(\vec{x}, t)$ is sometime completely neglected in zooplankton studies and Lagrangian particles treated as purely passive particles (Lett07, Allain03, Cianelli07). Other authors simulate the horizontal subgrid turbulence as a white noise (Speirs06). In Guizen06 the turbulent velocity both in horizontal and vertical is obtained by randomly sampling a Gaussian distribution with standard deviation $\sqrt{2k/3}$ where k is the Turbulent Kinetic Energy provided by the Eulerian model (in this specific case by the Gaspar et al, 1990, turbulence closure submodel).

A more sophisticated model is developed by Peliz04, and successively adopted by Lett08, as regarding the horizontal diffusion. Indeed, horizontal diffusion is based on a random component introduced to the horizontal velocity vector using

$$|\vec{u}'| = \delta \sqrt{2 K_h / \Delta t}$$

where $\delta \in [-1, 1]$ is a real uniform random number and K_h is the imposed explicit Lagrangian horizontal diffusion of the form $K_h = \epsilon^{1/3} l^{4/3}$ where l is the unresolved subgrid scale (taken as the cell size) and $\epsilon = 10^{-9} \text{ m}^2 \text{ s}^{-3}$ is the turbulent dissipation rate (e.g., Monin and Ozmidov, 1981).

In the vertical Peliz04 compute the random fluctuation associated with unresolved vertical turbulent fluxes:

$$w' = \delta \sqrt{\frac{2K}{1/3 \Delta t} + \frac{dK}{dz}}$$

where K is the vertical heat turbulent diffusivity taken from the KPP (Large et al., 1991) turbulent closure submodel. According to Ross and Sharples (2004) a correct implementation of this equation

requires a timestep constraint $\Delta t \ll \min \left(1 / \left| \frac{d^2 K}{dz^2} \right| \right)$. This implies that the Lagrangian model has

to be implemented in a sub-timestep relative to the main baroclinic model timestep.

In the vertical, Lett08 implemented a so-called “non-naive” random walk (Visser97) where, with respect to classical random walk models, a correction term is used to make the random walk consistent with the physical description of non-uniform diffusivity.

$$z_{n+1} = z_n + K'(z_n) \delta t + R \{ 2r^{-1} K [z_n + 1/2 K'(z_n) \delta t] \delta t \}^{1/2}$$

where $K' = \delta K / \delta z$ represent the gradient of diffusivity.

Concerning the individual larva's velocity $\vec{u}_{larva} \equiv \vec{u}_{larva}(\vec{x}, t)$, the reader is referred to the previous paragraph?????

In order to solve Eq. 1 numerically, several numerical schemes can be employed. The three most widely used schemes are the Euler method (Parada et al, Guizien et al., 2006; Lett et al., 2007), the Runge-Kutta (RK) method (Batchelder et al., 2002; Oliveira et al., 2002; Tittensor et al., 2003), and the Adams-Bashfold-Moulton (ABM) method (Peliz et al., 2007; Carr et al., 2008; Qiu et al., 2008).

An advantage of the Euler scheme is that only one velocity field is needed to calculate the particle velocity at the new particle position, which conserves computer memory.

$$x^{n+1} = x^n + \vec{V}(x^n, t^n) \Delta t \quad (3)$$

The main drawback of this method is that it is accurate to a first order only and therefore particle trajectories may diverge from the real ones as the time advances unless the timestep is very small

(Bennett and Clites, 1987).

The Runge-Kutta scheme is based on an iterative method of estimating the solution. Generally, the order 4 scheme is adopted which requires more calculations and delivers a fourth order accuracy.

$$X^{n+1} = X^n + \frac{\Delta t}{6} (a + 2b + 2c + d) \quad (4)$$

where

$$\begin{aligned} a &= \vec{V}(X^n, t^n) \\ b &= \vec{V}\left(X^n + \frac{\Delta t}{2} a, t^n + \frac{\Delta t}{2}\right) \\ c &= \vec{V}\left(X^n + \frac{\Delta t}{2} b, t^n + \frac{\Delta t}{2}\right) \\ d &= \vec{V}(X^n + c \Delta t, t^{n+1}) \end{aligned}$$

The advanced ABM method is a predictor-corrector method, combining the Adams-Bashford method (the predictor step) and the advanced Adams-Moulton method (the corrector step).

$$\tilde{X}^{n+1} = X^n + \frac{\Delta t}{24} (55\vec{V}^n - 59\vec{V}^{n-1} + 37\vec{V}^{n-2} - 9\vec{V}^{n-3}) \quad (6)$$

$$X^{n+1} = \frac{1}{270} \left\{ 19\tilde{X}^{n+1} + 251 \left[X^n + \frac{\Delta t}{24} (9\vec{V}^{n+1} + 19\vec{V}^n - 5\vec{V}^{n-1} + \vec{V}^{n-2}) \right] \right\} \quad (7)$$

where $\vec{V}^{n+1} = \vec{V}(\tilde{X}^{n+1}, t^{n+1})$.

Different numerical schemes have different impacts on the accuracy, efficiency, and memory requirements of the particle integration. Darmofal and Haines (1996) found that multistage schemes required at least three times more internal data storage than multistep schemes of equal order and for timesteps within the stability bounds; however, multistage schemes were generally more accurate. Garcia et al. (1999) compared the Euler and RK methods by using simple numerical experiments.

Finally, in a more advanced IBM where larval behaviour depends on thermodynamics, a coupling between the Lagrangian and Eulerian model components is put in place for temperature and salinity fields, with generally trilinear interpolation at the particle position (Lett07, Lett08, Hinckley96, Mullon03).

REFERENCES

Miller_etal_FishOceanogr98_CouplingIBMCirculationModelGeorgesBank.pdf
 Heath_etal_FishOceanogr98_DispersalLarvalJapaneseSardine.pdf
 Guizen_etal_MarEcolProgSer06_DispersalOweniaWinddrivenCurrents.pdf
 Speirs_etal_MarEcolProgSer06_OceanScaleModellingCalanus.pdf
 Lett_etal_MarEcolProgSer07_AssessmentBarrierIchthyoPlanktonBenguela.pdf
 Lett_etal_EnvironModellSoftw08_Ichthyop.pdf

Peliz_etal_JMarineSyst07_CrabLarvaeDispersalWesternIberianShelf.pdf
Hinckley_etal96_DevelopmentSpatiallyExplicitIBM.pdf
Mullon_etal_FishOceanogr03_FromParticlesToIndividualsAnchovy.pdf
Carr_Capet_et_al_FishOc06_VerticalMigrationZooplanktonTransportRecruitmentCoupledBehavioral
PhysicalModel.pdf
Allain_etal_FishOceanogr03_AnchovyBiscayLagrangianSimulations.pdf
Paris_etal_MarEcolProgSer07_SurfingSpinningDivingPopulationConnectivity.pdf
Iudicone_etal_OceanModel02_SensitivityNumericalTracerTrajectories.pdf
Valdivieso_Blanke_OceanModel04_lagrangianmethodsClimatologyTrajectoryError.pdf.

5.7 Example : Dispersion of copepods and medusae in the NW Mediterranean

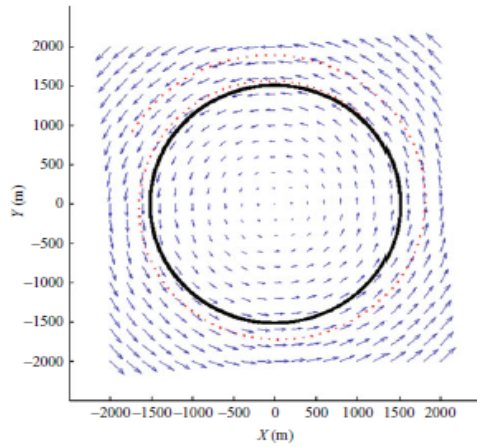


Fig.1 Circular flow field given by Eq.8 for $(a=0, b=0.001)$ and the trajectories of the 1000 particles starting in a 10 m diameter circular cluster centered at the point (1500, 0)

The simulations with $dt=60$ s of the Euler method and the advanced Adams-Bashfold-Moulton scheme are marked in red and black, respectively

We performed a convergence test where all 1000 particles were tracked for 5 h using the three schemes, with different time steps. The errors were computed using Eq.10 and are presented in Fig.3. The RK scheme and the advanced ABM scheme can attain very high precision. For example the errors were $3.6E-06$ and $5.0E-05$ with $dt=100$ s, respectively. Note that to reach an error of 0.025,

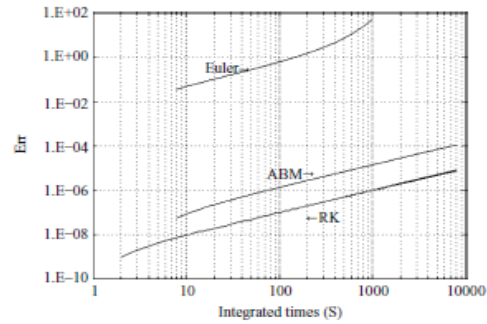


Fig.2 Error evaluations for the Euler method, the Runge-Kutta scheme and the advanced Adams-Bashfold-Moulton scheme simulated with the time step $dt=60$ s

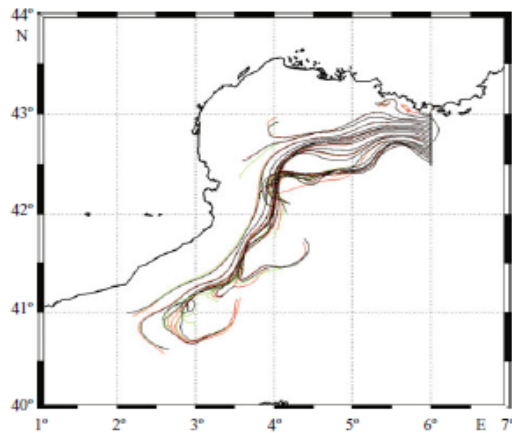


Fig.4 Trajectories of the 21 particles tracked 15 days with three different time steps

The initial locations are marked in black circulations and lines in black, green and red represent the trajectories of particles simulated with time steps $dt=60$ s, $dt=300$ s and $dt=900$ s, respectively

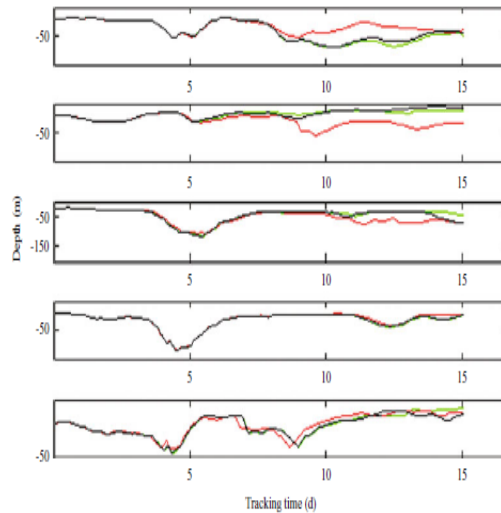
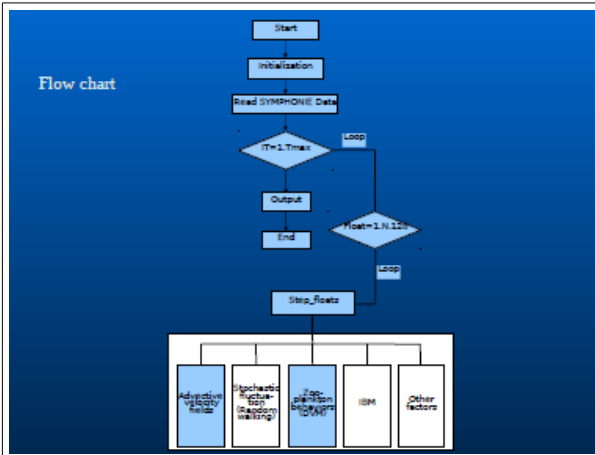


Fig.5 Depth variations of the 5 particles (of total 21) simulated with three different time steps

The lines in black, green and red represent the depth variations of the particles simulated with time steps $dt=60$ s, $dt=300$ s and $dt=900$ s, respectively



Lagrangian Model

We use a Lagrangian particle-tracking code based on the ROMS Offline Floats (ROFF, introduced in details by Carr et al. 2007)

- an advanced fourth-order accurate Adams-Bashford-Moulton predictor-corrector scheme is used for the tracking algorithm

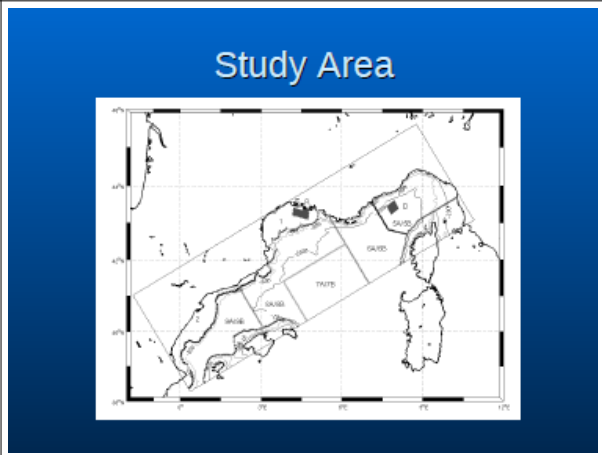
$$\frac{d\vec{x}}{dt} = \vec{u}(\vec{x}, t)$$

$$\vec{u}(\vec{x}, t) = \vec{u}_{sym} + \vec{u}_{DVM}$$

- \vec{u}_{sym} are linearly interpolated from the velocity values of the 8 nearest grid cells, which are daily averaged simulations of the SYMPHONIE model, provided every 24 hours.

DVM scheme

- if upper than -50m on 06:00, swim down with the velocity 50 m/h from 06:00 to 08:00
- otherwise the zooplankton transport processes are only determined by the velocity fields of the model circulation
- from 18:00 to 20:00, swim up from deeper depth to near-surface depth with the velocity 50 m/h.



Model Approach

- Time step: 300s
- SYMPHONIE data: spatial resolution of 3KM
- Starting time: March 1 ~ August 31, 2001, every 3 days
- Simulating time: 40 days
- Particles release information:
 - Location: R(Rhone river plume), D(Dyfamed station)
 - Number: 200 particles each location
 - Depth: -5m and -20m (R) -5m and -100m(D)
- Zooplankton behaviour: passive drift and with DVM

Particles release at D

- After being transported for 40 days, the particles could launch almost anywhere in the NWMS.
- With the influence of the vertical variability of the currents, the final distributions are different with the particles released at different depths.

Blue square: release locations
Red circles: final positions of particles released at -5m
Green points: final positions of particles released at -100m.

- Strong seasonal patterns appear in the final distributions of the particles, which dues to the seasonal variability of the circulations, especially the North Current.
- Very few particles can enter into the GoL. The North Current is a barrier for particles entering the continental shelf in the GoL from the offshore seas.

Particles release at R

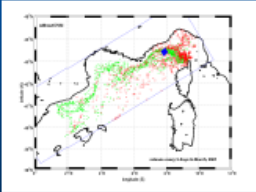
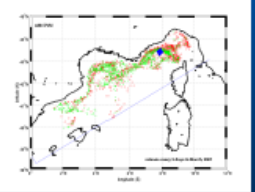
- Final distributions are separated into two parts: one remains in the GoL and the other goes out to scatter in the path of the North Current and in the Catalan Sea.

| | | | | |
|-------|----|---|---|--|
| | 1 | 2 | 3 | |
| March | 24 | 3 | 5 | |
| April | 47 | 1 | 1 | |

- After 40 days, 1/4~1/2 particles remain in the GoL. The GoL could be considered as a retention area for the zooplankton transport and distributions.
- Weak seasonal patterns appear in the final distributions of the particles. No one particle enters into the Ligurian Sea during the simulations.

With DVM

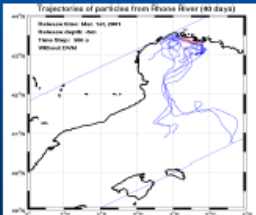
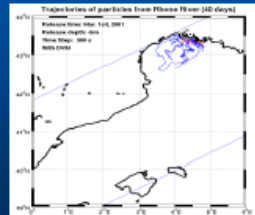
- Final distributions of the particles released at D are mainly similar as the particles simulated without DVM, however more concentrated at the path of the main currents

without DVM
with DVM

DVM discuss

In an upwelling region, there are often offshore currents at the surface and onshore currents at deeper depths. Consequently DVM reduces the transport of the particles away from the region, compared to the particles transport passively at the surface.

without DVM
with DVM

Conclusion

- A Lagrangian module has been developed to simulate the transport and distributions of zooplankton individuals coupling with SYMPHONIE
- Strong seasonal patterns appear in the distributions of the individuals released at DYFAMED sampling station. Individuals could be spread all over the NWMS basin after 40 days but different patterns occurs following the season, the depth of release of the individuals, and the capacity of DVM or not.

- An offshore-shelf transport only occur in April to June. In the other months, the North Current can be properly considered as a barrier for particles entering into the GoL from the offshore sea.
- At the end of the 40 days, passive individuals released in the plume of the Rhone River are spread on the GoL shelf or in the Catalan sea. Following the season between a quarter to a half of the initial released individuals stay in the Gulf. Simple DVM behavior does not increase the retention on the shelf.

Next Step

- Random Walk Scheme
- Nest codes
- Individual Based Model
- ...

LOPB Jérôme Bouffard (LOPB-MIO, Marseille) Séminaire M2

Partie 1: Préambule

Apport de l'altimétrie pour l'observation de surface de la dynamique méso-échelle et sub méso-échelle régionale

2

Définitions

Méso-échelle: échelle caractéristique des processus hydrodynamiques contrôlés par la quasi-géostrophie (eg Gill, 1982).

Tourbillon méso-échelle (campagne LATEX 2008, crédit: LOPB-MIO)
Equilibre rotation/stratification - Premier rayon interne de Rossby (10-100 km, Chelton et al., 1998)

Sub-méso-échelle: échelles < méso-échelle (~1-10 km)

Filaments sub-méso-échelles (campagne ELISA, crédit: LOPB-MIO)

Dans cette exposé: « (sub)méso-échelle » = méso-échelle + sub-méso-échelle

Enjeux scientifiques et sociétaux

Au niveau global

- La (sub)méso-échelle influe sur le système climatique terrestre et les budgets de productivité primaire (Loy, 2008)
- Essentiel des études dans l'océan ouvert à partir de simulations numériques (Klein et al., 2008)

Aux échelles régionales et côtières ?

- Peu d'études pourtant 95% des enjeux socio-économiques localisés dans les régions côtières (Cohern et al., 1997)
- Moitié des côtes méditerranéennes urbanisées d'ici 2025 (Bergametti et Vaudin, 2008).
- Scénario en Méditerranée (GIEC, 2007): Oligotrophisation de l'océan ouvert et Eutrophisation en zone côtière

Etudier les facteurs physiques qui contrôlent les réponses des écosystèmes côtiers

Questions ouvertes

Quelles sont les échelles de variabilité temporelle de l'activité (sub)méso-échelle côtière ?

Quel est son rôle dans le mélange des masses d'eaux et de matières aux interfaces côte-large ?

Quelle théorie décrit le mieux les processus (sub)méso-échelles en zone côtière?

Défi
Observer à long terme la circulation régionale

Moyen
S'appuyer sur des observations multi-sources complémentaires

Approches classiques et limitations

- Modélisation régionale + in-situ (Hu et al., 2009; 2011; Alou et al., 2010)
- Campagnes en Mer (LOPB/MIO: LATEX, IMEDA: SINOCOP ...)
- « Cible les processus » mais périodes courtes et/ou région limitée
- Courants verticaux inaccessibles
- Les mouillages permanents - marégraphes - radars HF (observatoires marins MOOSE - radar ECCOP du LSEET/MIO, SOCIB)
Séries temporelles longues mais couverture spatiale restreinte

Capter un spectre large de variabilité océanique
→ Augmenter l'échantillonnage → Recours aux observations satellites

Principe général de l'altimétrie satellite

■ Mesure de la topographie de surface des océan

Corrections environnementales

- Troposphérique sèche
- Troposphérique humide
- Ionosphérique

Corrections de biais d'état de mer

- Biais électromagnétique
- Biais d'obliquité

Topographie dynamique absolue:
 $h_d = SSH / E - corrections - Géolde / E$

Principe général de l'altimétrie satellite

■ Vocabulaire

-Topographie dynamique absolue (1):
 $h_d = SSH / E - corrections - Géolde / E$
Mesures altimétriques
Comment ? Sat. qui mesurent la gravité (GOCE, GRACE)
Problème: Erreur

-Anomalie de hauteur de Mer (2):
 $SLA = SSH / E - cor - moy(SSM) / E + cor$
Mesures altimétriques
Comment ? Répétitivité du sat. Alti.
Problème: pas hauteur relative

$Géolde / E + MDT / E$ **Comment ?** Cf. Rio et al. 2007

D'où $h_d = SLA + MDT / E$
hd - Zeta (modeles numériques, cf Greatbatch et al., 1994; Bouffard et al., 2008)
hd - Hauteur Dynamique (niveau ref ou courant = 0) (cf Pascual et al., 2003, Ruiz et al., 2008)

Principe général de l'altimétrie satellite

L'altimétrie satellite adaptée pour l'étude de la dynamique hauturière (El Nino, La Nina, Gulf Stream ...)

... mais inadaptée pour les études aux échelles régionales et côtières

Principe général de l'altimétrie satellite

- **Altimétrie côtière de nouvelle génération**
- Nouvelles méthodologies développées afin d'améliorer les **mesures côtières** (Vignudelli et al., 2005; Bouffard, 2007; Roblou et al., 2011; Cipolini et al., 2010)
- Leur exploitation scientifique a permis de caractériser des structures fine (R~20km) jusque là inaccessible (courant ouest Corse: Bouffard et al., 2008b; CN: Bouffard, 2007; Birol et al., 2010; Bouffard et al., 2011)
- L'utilisation conjointe avec la modélisation et les mesures in-situ a permis de mieux appréhender l'origine, les mécanismes et les structures verticales associées (Bouffard et al., 2008a; Hermann et al., 2009; Bouffard et al., 2012)

14

Principe général de l'altimétrie satellite

- **Altimétrie côtière de nouvelle génération**
- Amélioration des données
 - CLASSIQUE
 - AMELIORE
- Caractérisation de courants côtiers
 - Aux échelles (sub)saisonnnières, saisonnières
 - Courantomètres virtuels
 - et inter-annuelles

15

Principe général de l'altimétrie satellite

- De la mesure de hd au calcul du courant...
- The slope of the sea surface relative to the geoid ($\partial z / \partial x$) is directly related to surface geostrophic currents. The two components (u_s, v_s) of the surface geostrophic current

$$u_s = -\frac{g}{f} \frac{\partial \zeta}{\partial y}$$

$$v_s = \frac{g}{f} \frac{\partial \zeta}{\partial x}$$
 where g is gravity, f is the Coriolis parameter, and ζ is the height of the sea surface above a level surface.
- Across-track currents

From Birol et al., 2010

Principe général de l'altimétrie satellite

Très bien ...

...MAIS ...

... Données le long des traces difficilement exploitables pour étudier la turbulence mésoéchelle

Nécessité de générer des champs 2D à haute résolution partir de l'Interpolation Optimale multi-satellite

Principe général de l'altimétrie satellite

- Qu'est ce que l'Interpolation Optimale

Champs de courants 2D pouvant être utilisés pour étudier le mélange et le transport lagrangien de particules (cf. présentation de Francesco)

LOPB

Partie 2: Une application

On the influence of coastal mesoscale dynamics on the jellyfish trajectories and distributions

JELLYWATCH project
Modelling of jellyfish transport and stranding in the NWMed

Main characteristics of *Pelagia Noctiluca*

- Sparse information on the Jellyfish repartition and the associated forcing (Temperature ? Currents ? Wind ? Food ? Predators ?)
- Numerous all along the year, in the NW-MED (Morand et al., 1992)
- At the surface during the night | migration at depth during the day (Dial vertical motion (DVM): down to 400 m, Gorsley personal communication)

Main issues

- What are the impacts of mesoscale and coastal dynamics on the jellyfish trajectories/distribution ?
- In which way coastal-altimetry could be a powerful tool ?

Strategy and data used

- **Strategy** : Using altimetry to simulate the advection of Jellyfish at the surface and at depth
- **Motivation** : altimetry provides almost synoptic currents that should allow a long-term monitoring of Jellyfish transport

Limitation in coastal zone

- Sub-sampling of coastal dynamics
- Significant error

Develop / use alti. products dedicated to coastal zone*

NO subsurface information

- Dial vertical motion of jellyfish !!!!
- Rely SSH to sub-surface geostrophic currents**

Use of statistics from a realistic regional model

Pascual et al 2003 (Vertical EQE de mesure in situ + SSH altimétrique)

23

Strategy and data used

- The symphonie model (POC-SIROCO, Toulouse) and study area characteristics

Model: SYMPHONIE (GoL config., Hu et al., 2009)

- Boussinesq model
- One way Nesting: 3km -> 1km
- Period 2001-2010

Study area :NWMed

- Northern Current (NC): seasonal variability (Gostan, 1967)
- Intense mesoscale variability: eddies, meanders (Mittor, 1991)
- NC intrusion over the GoL continental shelf (Goi et al., 2006)
- Winter deep water formation characterized by a high interannual variability (Martens and d'schott, 1998; Hamman, 2008)

Current intensity at 20m (in m/s)

Current (mb) at 50 m

Strategy and data used

- Altimetry: products used

CLASSIQUE (AVISO + MDT Rio)

AMELIORE (HR + MDT Dob)

- 2 kinds of (M)SLA: From regional AVISO and Higher Resolution (HR) product (correlation scales: 5 days/30km) from IMEDEA (Escudier et al., 2011)
- Validations with *in-situ* measurements from the LATEX08 experiment *

* Influence of submesoscale coupled physics - biogeochemistry on cross-shelf exchanges: <http://www.com-oceri.fr/LOB/LOB4/TEX>

Strategy and data used

- Methodology

- Step 1: Build daily Dynamic Height (DH) from T,S of SYMPHONIE model (period 2001-2010)
- Step 2: Compute a database of daily vertical EOF from the model DH
- Step 3: Create an EOF climatology from 10 years of simulation
- Step 4: If 1st mode highly dominant, reconstruct DH at a given depth by projecting altimetric ADT with the EOF climatology of the model

Advection with geostrophic currents by considering Jellyfish as passive particules with dial vertical migations

Is the 1st EOFmode highly dominant ?
Is the climatology representative of daily EOF ?

Reconstruction of sub-surface currents

- What is an EOF ?

Décomposition d'un champs Phi en somme de N mode propre *i* (~ diagonalisation de matrice)

$$DH(P) = \sum_{i=1}^N A_i(x, y) EOF_i(p)$$

Profil vertical fonction de la profondeur *p*

Amplitude (independante de *p*)

Si Mode 1 dominant: variance(Mode1) >> variance(Mode*i*)

$$\Phi_{x,y}(p) = A_1(x, y) EOF_1(p)$$

$$DH(P) = A1(x,y) EOF1(P)$$

Reconstruction of sub-surface currents

- Create an EOF climatology from 10 years of simulation

Weights of mode 1 / month

Climatology vertical EOF (mode 1)

1st mode : 70 % < weights < 84 %

Representativity of the climatology 8% < error < 14 %

Reconstruction of sub-surface currents

- Create an climatology of EOF from 10 years of simulation:
 - If the first mode is highly dominant (as noted in Pascual et al., 2003) :

$$DH(t, 250m) = DH(t, 0m) \cdot EOF1(t, 250m) / EOF1(t, 0m)$$

DH rebuilt at 250 m

Altimetric ADT (AVISO and HR products)

EOF Climatology (from SYMPHONIE)

Geostrophic current at 250m

Are model and altimetric currents sufficiently consistents ?

Validations / comparisons

- Altimetry vs SYMPHONIE model currents (April - october 2008)

At the surface (m/s):

MEAN

STD

Good agreement between model and altimetry (NC intensity/position ...)

Validations / comparisons

- Altimetry vs LATEX08 drifters comparisons (U & V components)

Method

- Altimetry: current space/time interpolation at 3 drifter locations
- Drifters: current calculated by finite differences (5 days filtered)
- Eikman current removed

Comparisons (with HR Dob)

- Drifter 1 and 2: Good agreement for both (U,V) (absolute mean difference < mean absolute, correlations > 0.5)
- Drifter 3: Strong Disagreement (lag between the coastal structures)
- Statistics slightly better with AVISO than with the HR product

What about the trajectories ?

Validations / comparisons

- Altimetry vs LATEX08 drifters comparisons (lagrangian)

Method

- Virtual particles launched around the LATEX drifters initial positions.
- Particles advected 47 days using RK4 and surface altimetric currents

Results (with HR-Dobricic)

- The particles follow the main temperature fronts
- Very good agreement between the drifters 1 and 2 and the advected particles
- No particle follows the drifter 3 which is advected by a coastal eddy (cf. Hu et al., 2009)

Particles advection from altimetry (HR (M)SLA + MDT Dob) and drifters trajectories

Validations / comparisons

- Altimetry vs LATEX08 drifters comparisons (lagrangian)
- Sensitivity to altimetric product used

« AMELIORE » allows a better agreement with drifter 2
No product allows advection by the coastal eddy (observed with drifters3) Why?

Validations / comparisons

- Altimetry vs LATEX08 drifters comparisons (lagrangian)
- Particles advection with a 10 day delay

In that case, altimetric currents capture the coastal Eddy (2 coastal tracks intercept the structure) → Importance of track availability

Jellyfish trajectories (preliminary results)

- Simple 40 day forward advection with altimetric surface currents
- Virtual Jellyfish launched each month from 3 different locations

- North GOL: Most of the particles remain on the GOL
- West/East GOL: Advection southern by the NC in direction of the Balearic Sea.

Jellyfish trajectories (preliminary results)

- 40 day forward advection by taking into account the DVM
- Virtual Jellyfish launched each month from 3 different locations

- North GOL: Much more particles advected to the south (3 times more)
- West/East GOL: Differences, but patterns also depending on the NC dynamics

Jellyfish trajectories (preliminary results)

- Statistics: differences due to DVM and altimetric products used
- % of particles shored (/ total particles launched) over 4 areas

Spatial repartition

- Much more particles over the GoL (- 50%...)
- Significant differences (e.g. West GOL > 10%)

Influence of the DVM

Also significant (e.g. AVISO RIO)

Conclusions and perspectives

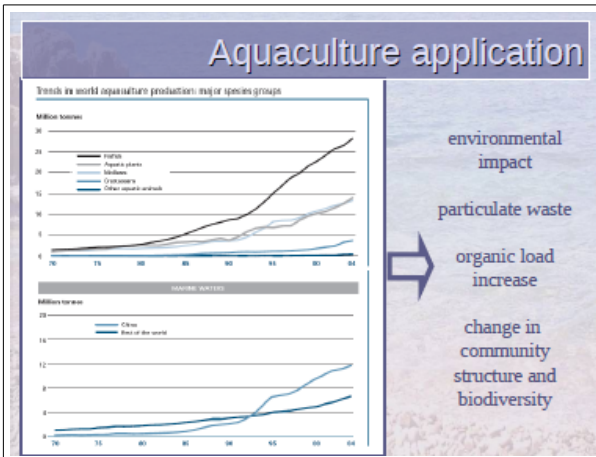
- Conclusions
 - Lagrangian approach is a powerful tool to evaluate coastal altimetry
 - Our simple approach to simulate jellyfish trajectories shows:
 - The influence of the NC (results in agreement with Qiu et al., 2008)
 - The importance of the DVM
- Perspectives (on-going work)
 - The landfall of Jellyfish needs to be validated with independent data (observations of life guard: number of bite per season etc...)
 - The effect of the wind has to be considered
 - Complexity in the Jellyfish behavior by coupling coastal altimetric current with an ecological model (LAGOO, Qiu et al., 2008)
 - Study the interannual variability of jellyfish distribution and better understand its potential relation with climatological indexes

5.8 Example : Dispersion of waste products from aquaculture farms

A new numerical benthic degradative module FOAM (Finite Organic Accumulation Module) has been coupled with the advection-dispersion model POM-LAMP3D in order to improve the prediction of the potential impact of marine fish farms. Moreover, real historic current-meter data are employed to force the hydrodynamic and as are dispersion simulations and recent measurements of settling velocity values specifically targeting Mediterranean fish species.

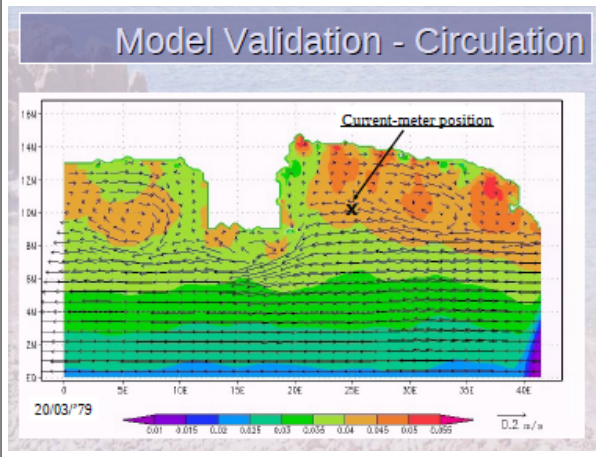
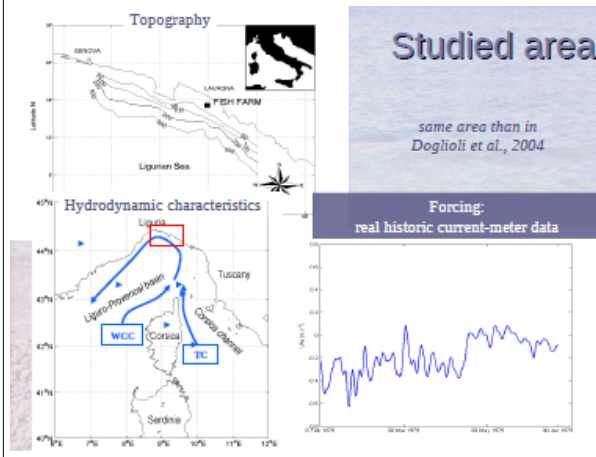
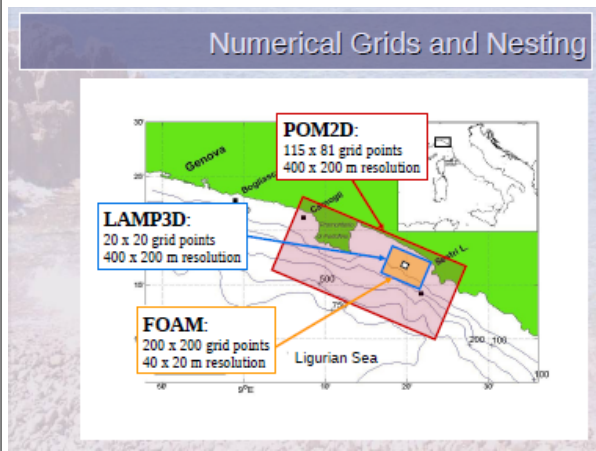
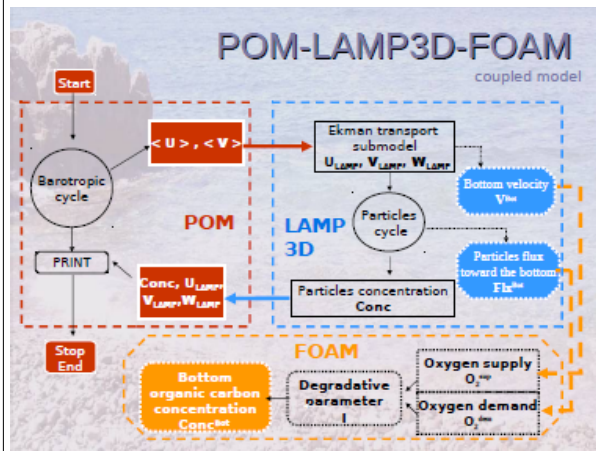
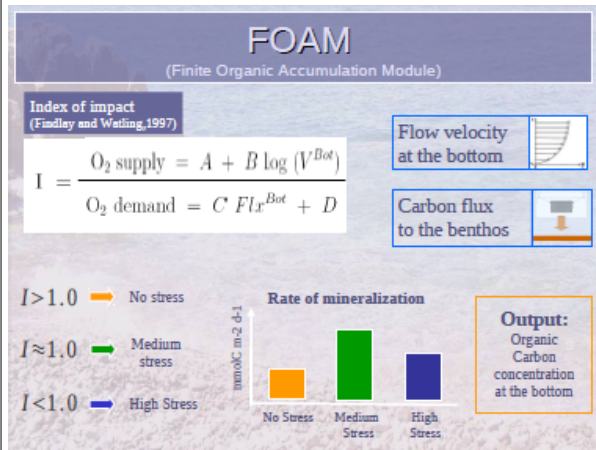
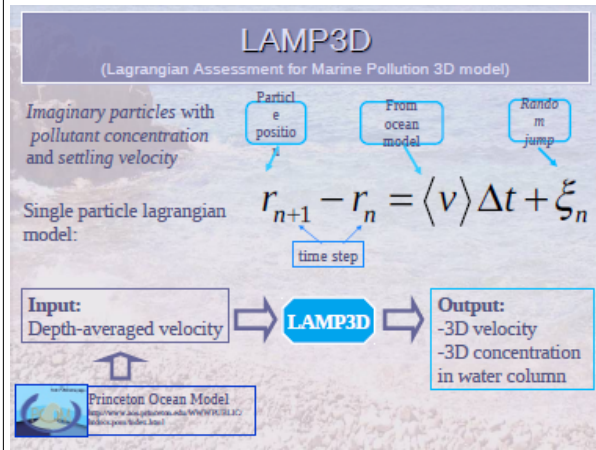
FOAM uses the output of the other functional units of the modelling framework to calculate the organic load on the seabed. It considers the natural capability of the seafloor to absorb part of the organic load. Different remineralization rates reflect the sediment stress levels and are used to compute the organic carbon concentration remaining on the seabed after degradation. Two sampling campaigns have been performed in a typical Mediterranean fish farm in the warm and cold season in 2006 in order to measure the benthic response to the organic load and the mineralization rates under Mediterranean conditions. Organic degradation for both uneaten feed and faeces is evaluated by changing release modality (continuous and periodical) and by varying the settling velocities. The results show that under Mediterranean conditions, the benthic response to the organic enrichment of the bottom depends on water temperature.

We find that the introduced modelling framework successfully improves our predictive capability. It can therefore represent an important tool in the decision making processes, for planning and monitoring purposes.



MAIN QUESTION:
potential impact on surrounding environment

METHOD:
implementation of advection-dispersion model POM-LAMP3D and add a new coupled benthic module FOAM.
evaluation and assess the environmental impact from marine fish farm



Model Validation - Circulation

Current measurements

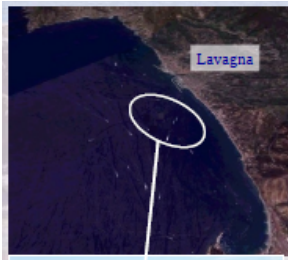
| Winter | Spring | Summer | Autumn | Annual |
|------------------|------------------|------------------|------------------|------------------|
| average | average | average | average | average |
| (std) | (std) | (std) | (std) | (std) |
| 0.066 (0.057) | 0.076 (0.065) | 0.063 (0.052) | 0.070 (0.062) | 0.069 (0.057) |

Model output

| | Winter | Spring | Summer | Autumn | Overall |
|------------------|------------------|------------------|---------|---------|------------------|
| | average | average | average | average | average |
| | (std) | (std) | (std) | (std) | (std) |
| 1st cycle | 0.076 (0.061) | 0.103 (0.084) | - | - | 0.088 (0.047) |
| 5th cycle | 0.059 (0.034) | 0.082 (0.066) | - | - | 0.057 (0.034) |
| 3th - 5th cycles | 0.064 (0.042) | 0.078 (0.050) | - | - | 0.061 (0.034) |



neglect the first 2 cycles to reduce the sensitivity to initial conditions

AQUA fish farm



Productive target:
200 ton year⁻¹

Reared species:
Sparus aurata and *Dicentrarchus labrax*

Wastes Particles

620000 Numerical particle released

| | Uneaten feed | Faecal matter |
|----------|---|---|
| | Feed conversion factor = 1.3 kg pellet/kg fish % of feed supplied = 5% | Faecal production = 1.9 g/kg fish |
| C | % in feed = 45% 1 particles = 308.6 mmol C | % organic carbon = 28% 1 particles = 5.8 mmol C |
| N | % in feed = 6.6% 1 particles = 167.8 mmol N | % particulated = 22% 1 particles = 66.4 mmol N |

Settling velocity

uneaten feed and faeces values specifically targeting Mediterranean fish

| Vassallo et al, 2006 | | Magill et al, 2006 | |
|----------------------|---------------------------------------|-------------------------|---------------------------------------|
| Food pellets | | Faecal pellets | |
| Diameter (mm) | V _{sed} (m s ⁻¹) | Fish species size (g) | V _{sed} (m s ⁻¹) |
| 3 | 0.087 | <i>S. Aurata</i> [380] | 0.004 |
| 3.5 | 0.118 | <i>S. Aurata</i> [60] | 0.005 |
| 4.5 | 0.103 | <i>D. Labrax</i> [280] | 0.006 |
| 5 | 0.144 | <i>D. Labrax</i> [80] | 0.007 |
| 6 | 0.088 | | |

Model Set Up

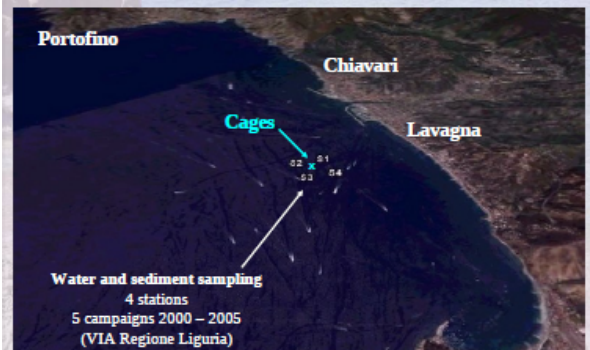
Different scenarios

- waste typology { feed, faeces
- settling velocity { slowly sinking, quickly sinking
- release conditions { continuous, periodical

Indicators

- Impacted area extension
- Barycenter positions
- I parameter
- Organic Carbon concentration

Model Validation - Dispersion



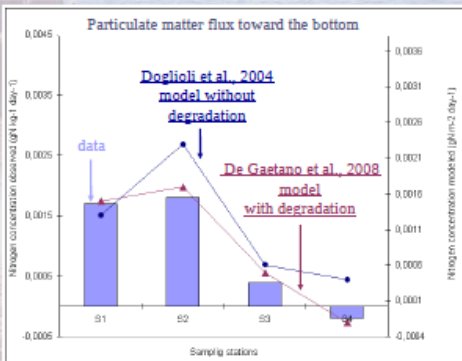
Portofino, **Chiavari**, **Lavagna**

Cages

Water and sediment sampling
4 stations
5 campaigns 2000 – 2005
(VIA Regione Liguria)

Model Validation - Dispersion

Particulate matter flux toward the bottom



Observed data (blue bars)

Doglioli et al., 2004 model without degradation (blue line)

De Gasiano et al., 2008 model with degradation (red line)

Sampling stations: S1, S2, S3, S4

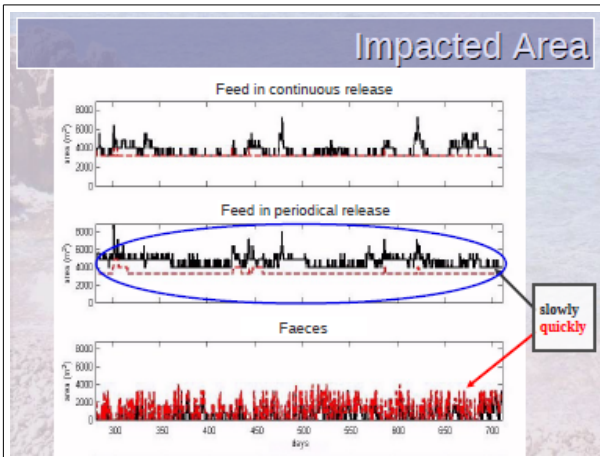
Impacted Area

Impacted Area
sum of the grid meshed areas where particles are still present after the degradation.

$$Area = \sum_{j=1}^N \sum_{i=1}^M \phi(Conc_{i,j}^{Bot}) \Delta x_i \Delta y_j$$

$$\phi(\xi) = \begin{cases} 1 & \text{if } \xi > 0 \\ 0 & \text{if } \xi = 0 \end{cases}$$

M = mesh number in x direction
N = mesh number in y direction
Δx = mesh grid length in x direction (m)
Δy = mesh grid length in y direction (m)
Conc^{Bot} = organic carbon concentration remaining of the bottom after degradation



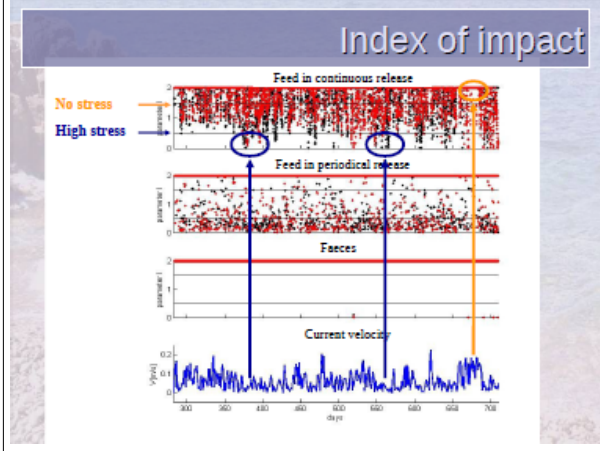
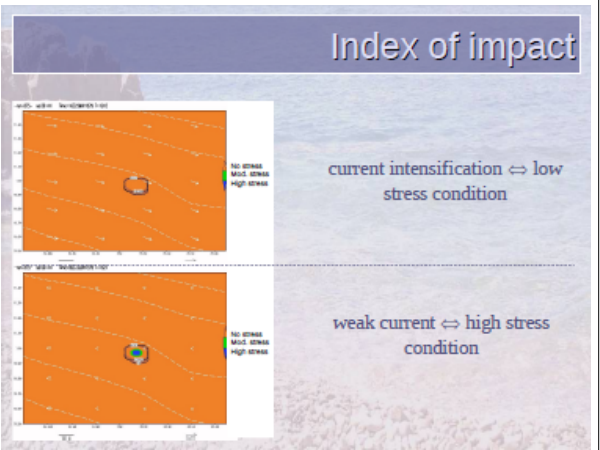
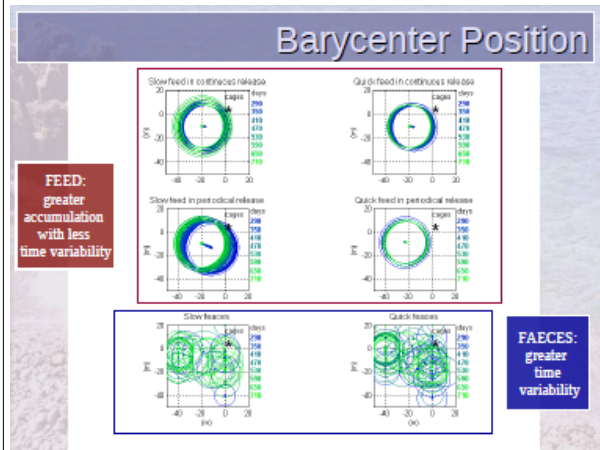
Barycenter Position

*Barycenter position:
position weighted by particles number left in each cell*

$$x_b = \frac{\sum_{j=1}^N \sum_{i=1}^M i \cdot n_{i,j}^{left}}{n_{Tot}^{left}}$$

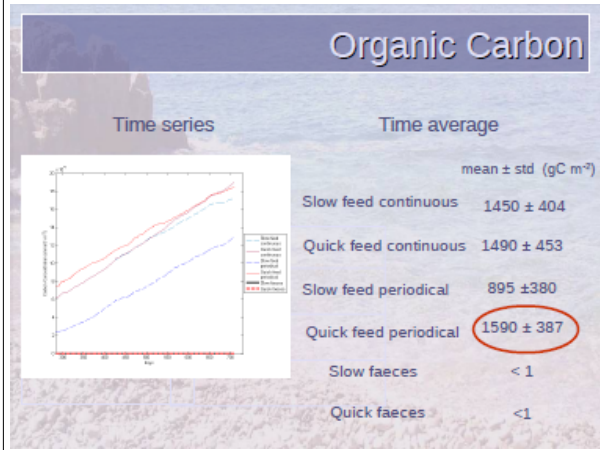
$$y_b = \frac{\sum_{j=1}^N \sum_{i=1}^M j \cdot n_{i,j}^{left}}{n_{Tot}^{left}}$$

M = number of meshes in x direction
 N = number of meshes in y direction
 $n_{i,j}^{left}$ = particle number left on the bottom in mesh i,j
 n_{Tot}^{left} = total number of particles left on the bottom after degradation



Index of impact

| | Occurrence | | |
|--------------------------|----------------------|------------------------|------------------------|
| | No stress I > 1.5 | Medium Stress I = 1 | High Stress I < 0.5 |
| Feed periodical released | 87 % | 4 % | 9 % |
| Feed continuous released | 71 % | 27 % | 2 % |
| faeces | 98 % | 1 % | 1 % |



Summary

Aquaculture Research

FOAM, a new simple benthic degradative module for the LAMP3D model: an application to a Mediterranean fish farm

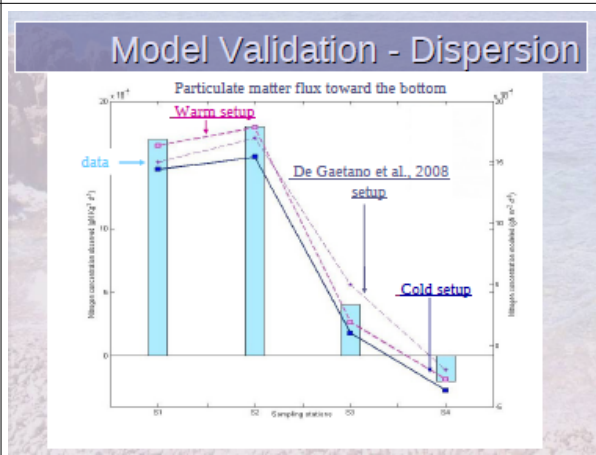
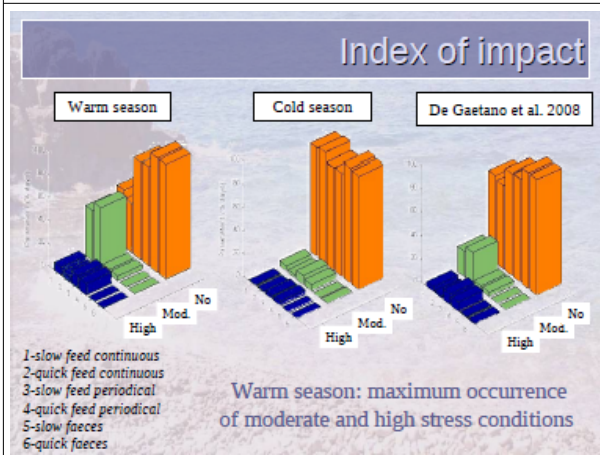
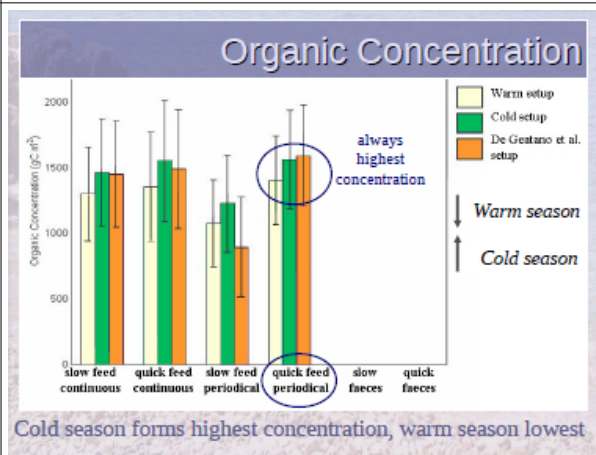
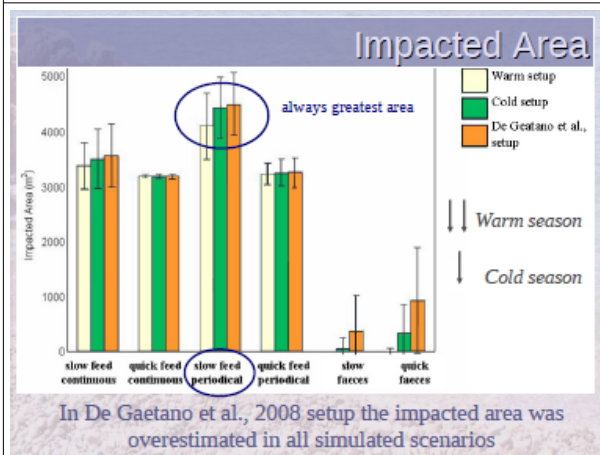
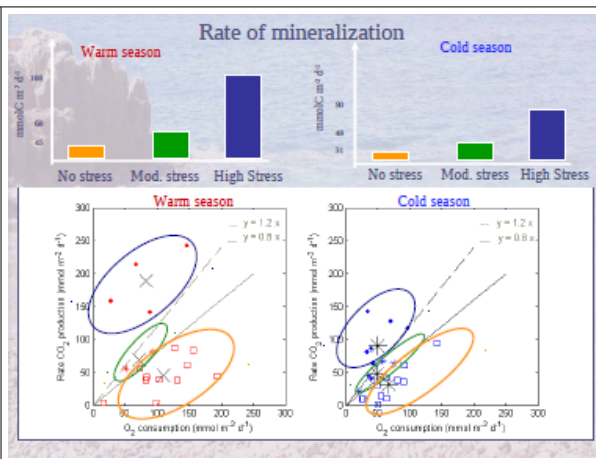
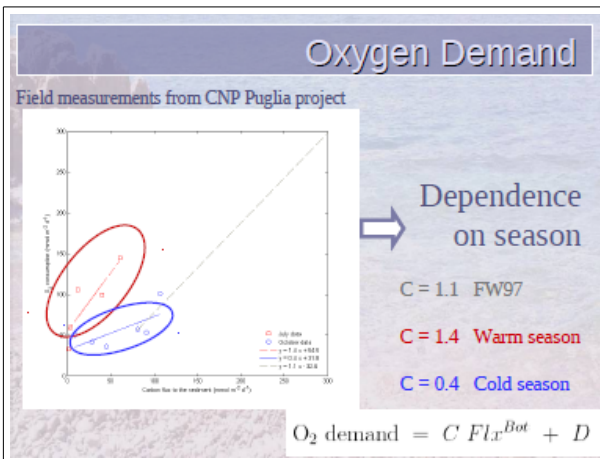
Parrella De Gennaro¹, Andrich H. Deglioli², Marrella G. Magaldi³, Parola Yamallo⁴ & Manno Faldutini⁵

¹VSB (Università di Pisa, Università di Genova, Genova, Italy)
²Università di Pisa (Università di Pisa, Università di Genova, Genova, Italy)
³Università di Pisa (Università di Pisa, Università di Genova, Genova, Italy)
⁴Università di Pisa (Università di Pisa, Università di Genova, Genova, Italy)
⁵Università di Pisa (Università di Pisa, Università di Genova, Genova, Italy)

Uneaten feed primary cause of impact

Periodical release worst condition of sediment stress and carbon concentration

Open question: Mineralization rates in Mediterranean conditions improve modelling reliability ?



Conclusion and Outlook

A new calibration of FOAM based on experimentally measured Mediterranean mineralization rates in cold and warm seasons

Patricia De Gaetano¹, Paolo Vassallo¹, Marco Bartoli¹, Donatella Nizzoli², Andrea M. Doglioli³, Marcello G. Manzoli⁴, Mauro Fabiano⁵

¹ IORIS, Dipartimento di Pesca, Università di Genova, Genova, Italy
² DIPPEDES, Dipartimento per lo Studio del Territorio e delle sue Risorse, Università di Genova, Genova, Italy
³ DSA, Dipartimento di Scienze Ambientali, Università di Pavia, Pavia, Italy
⁴ Laboratorio di Oceanografia, Dipartimento di Scienze e Tecnologie (DSTN), Università di Genova, Genova, Italy
⁵ Division of Microbiology and Physical Oceanography (DMPO), Memorial School of Marine and Atmospheric Sciences (MOSAS), University of Miami, FL, USA

Benthic metabolism depends on season

Results depend on simulated season:
 warm setup
 maximum impact while minimum area and concentration

Better prediction capability

OUTLOOKS:

- sampling campaign for benthic metabolism dependence on water temperature
- improve reliability of hydrodynamic model

5.9 Example : Lagrangian connectivity study in the Mediterranean

Contexte & Objectif

Étude du réseau des AMP

« Effet réserve » & Connectivité

Dispersion du plankton

FP-7

Régionalisation de la Mer Méditerranée à partir de la Chl de la surface

Quelles sont les régions interconnectées dans la Mer Méditerranée?

Régionalisation basée sur la circulation

Méthodologie

Champ Eulérien

Module lagrangien

Diagnostic de connectivité

Classification Hiérarchique

Régionalisation

Méthodologie

Champ Eulérien

MERCATOR

Courants

Données journalières

4 ans de données de champ de vitesse

Méthodologie

Module lagrangien

ARIANE

Advection horizontale à la surface

Pas de vitesse verticale

Temps d'advection 1 an

Méthodologie

Diagnostic de connectivité

Matrice de connectivité

$$C(i, j) = \frac{N_{t,q} \cdot x(t) = i \ \& \ x(t + t_{adv}) = j}{N_{tot}}$$

Mitarai et al. 2003

Méthodologie

Diagnostic de connectivité

Temps de connexion moyen

$$MCT(i, j) = \frac{1}{M} \sum_{n=1}^n T_n(i, j)$$

Mitarai et al. 2003

Méthodologie

Diagnostic de connectivité

Distance océanographique

$$DO(i,j) = \text{sym}(\min(MCT(i,j), MCT(j,i)))$$

Alberto et al. 2011

Méthodologie

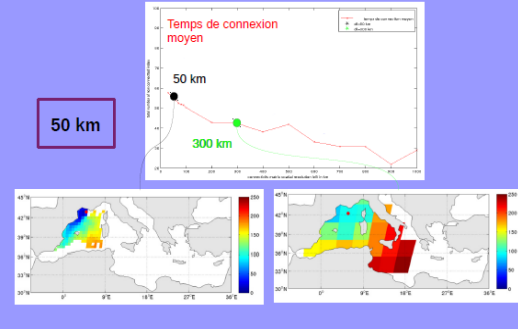
Influence du nombre de particules

| l | Nmax | lâchers/ mois | augment ion p.r. l-1 |
|---|---------|---------------|----------------------|
| a | 25.646 | 1 | - |
| b | 51.292 | 2 | 100 |
| c | 76.938 | 3 | 50 |
| d | 102.584 | 4 | 33 |
| e | 128.230 | 5 | 25 |
| f | 153.876 | 6 | 17 |
| g | 179.522 | 7 | 14 |
| h | 205.168 | 8 | 12 |
| i | 230.814 | 9 | 11 |

Lâcher 9 particules par mois

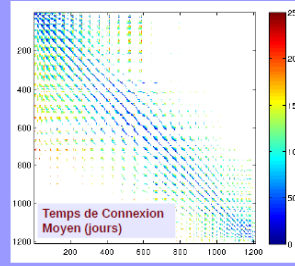
Méthodologie

Influence de la résolution de la grille de connectivité



Méthodologie

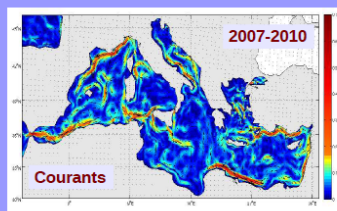
N=8.309.304 dl=50 km



Classification Hiérarchique

Méthodologie

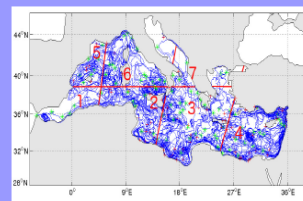
Champ Eulérien MERCATOR



Données journalières
4 ans de données de champ de vitesse

Méthodologie

Module lagrangien ARIANE

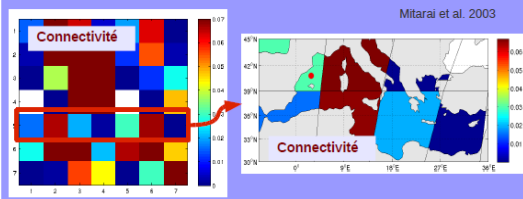


Advection horizontale à la surface
Pas de vitesse verticale
Temps d'advection 1 an

Méthodologie

Diagnostic de connectivité
Matrice de connectivité

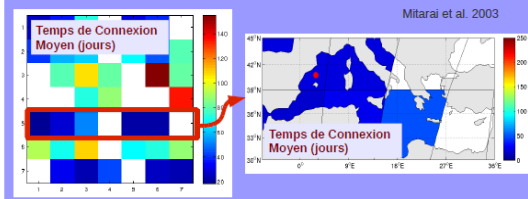
$$C(i, j) = \frac{N t.q. \mathbf{x}(t) = i \ \& \ \mathbf{x}(t + t_{adv}) = j}{N_{rot}}$$



Méthodologie

Diagnostic de connectivité
Temps de connexion moyen

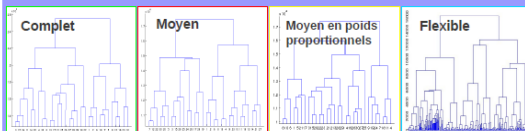
$$MCT(i, j) = \frac{1}{M} \sum_{t=1}^{t=N} T_n(i, j)$$



Méthodologie

Classification hiérarchique et critères d'agrégations

$$D(m, g) = \alpha_x D(k, g) + \beta_y D(l, g) + \beta D(k, l) + \gamma |D(k, g) - D(l, g)|$$



$D(m, g) = \max(\text{dist}(x_k, x_l))$

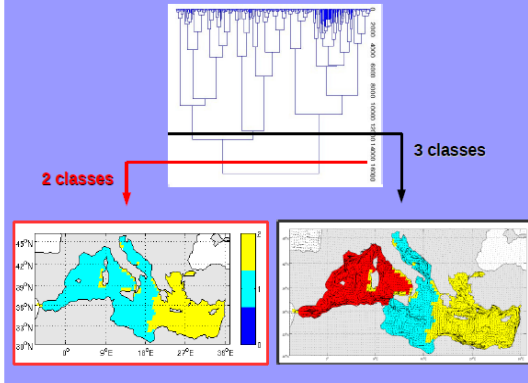
$D(m, g) = \frac{1}{w_m * w_g} \sum_{x_k \in m} \sum_{x_l \in g} \text{dist}(x_k, x_l)$

$D(m, g) = \frac{D(k, g) + D(l, g)}{2}$

$D(m, g) = 0,625 D(k, g) + 0,625 D(l, g) - 0,25 D(k, l)$

Lance & Williams 1967

Résultats



Résultats

22 classes

Circulation de surface (eau atlantique)

2007-2010

Berline et al. In prep.

Perspectives

Analyse avec les graphes

Andrello et al. 2013

Focus plus petites-échelles

Étude de la variabilité saisonnière

Introduire du comportement : taux de mortalité, durée de la phase planctonique, migration verticale

Comparaison avec d'autres méthodes lagrangiennes, données de campagne, études de génétique des populations

Méthodologie

Classification hiérarchique et critères d'agrégations

$$D(m, g) = \alpha_x D(k, g) + \beta_l D(l, g) + \beta_l D(k, l) + \gamma |D(k, g) - D(l, g)|$$

Complet

$$D(m, g) = \max(\text{dist}(x_k, x_l))$$

Moyen

$$D(m, g) = \frac{1}{w_m * w_g} \sum_{x_i \in m} \sum_{x_j \in g} \text{dist}(x_i, x_j)$$

Moyen en poids proportionnels

Flexible

$$D(m, g) = \frac{D(k, g) + D(l, g)}{2}$$

Lance & Williams 1967

$$D(m, g) = 0,625 D(k, g) + 0,625 D(l, g) - 0,25 D(k, l)$$

Résultats

2 classes

3 classes

5.10 Coherent Lagrangian structures and the Lyapunov exponents

From http://en.wikipedia.org/wiki/Lyapunov_exponent

In mathematics the Lyapunov exponent or Lyapunov characteristic exponent of a dynamical system is a quantity that characterizes the rate of separation of infinitesimally close trajectories. Quantitatively, two trajectories in phase space with initial separation vector $\delta Z \equiv \delta Z(t)$ diverge (provided that the divergence can be treated within the linearised approximation) at a rate given by

$$|\delta Z(t)| = e^{\lambda t} |\delta Z_o(t)| \quad \text{with} \quad \delta Z_o = \delta Z(t=0)$$

and λ the Lyapunov exponent.

While this is typically studied in phase space, we can also think of two particle trajectories in a turbulent ocean, which is a dynamical system.

The **phase space** is an abstract space where the dynamic variables, the degrees of freedom, or the system parameters constitute the coordinate system.

A **dynamical system** is a classical system whose evolution over time is:

causal, i.e., its future evolution only depends on the systems past and present;

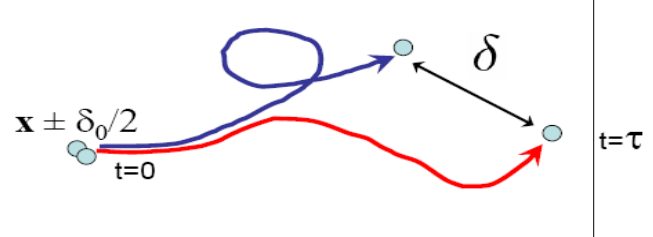
deterministic, i.e., once the initial condition is known, we can know all future states of the system.

We thus exclude any systems that are intrinsically “noisy” as they are described by **probability theory**

E.g., pendulum <http://www.mcasco.com/pend1.html>

The rate of separation can be different for different orientations of the initial separation vector. Hence there is an entire spectrum of Lyapunov exponents, the number of which equals the number of dimensions n of the entire spectrum of λ_n . Usually, we refer to the largest λ_n as the **Maximal Lyapunov exponent (MLE)**, because it provides some information about the predictability of the dynamical system under investigation.

In particular, having $MLE > 0$ suggests that the system is chaotic. It should be noted that any initial separation vector will contain a component in the direction of the MLE. However, due to the exponential growth only the MLE component will be important while the other, smaller components are quickly “forgotten”.



Definition of the MLE

$$\lambda = \lim_{t \rightarrow \infty} \frac{1}{t} \ln \frac{|\delta Z(t)|}{|\delta Z_0|} \quad \text{or} \quad \lambda = \lim_{t \rightarrow \infty} \lambda(t) \quad \text{Lyapunov exponent}$$

with

$$\lambda(t) = \lim_{\|\delta(0)\| \rightarrow 0} \frac{1}{t} \ln \frac{\|\delta(t)\|}{\|\delta(0)\|} \quad \text{Finite-time Lyapunov exponent}$$

while

$$\lambda(\delta_0, \delta_f) \equiv \frac{1}{\tau} \log \frac{\delta_f}{\delta_0} \quad \text{Finite-size Lyapunov exponent FSLE}$$

All the quantities are also functions of the initial position and time:

$$\lambda(\mathbf{x}, t, \delta_0, \delta_f)$$

FSLEs are inversely proportional to the time required by 2 tracers to reach a certain separation.

$\lambda(\mathbf{x}, t, \delta_0, \delta_f)$, the FSLE at position \mathbf{x} and time t , is computed from the time τ it takes for a trajectory starting at time t at a distance δ_0 from \mathbf{x} to reach a separation δ_f from the reference trajectory that started at \mathbf{x} :

$$\lambda(\mathbf{x}, t, \delta_0, \delta_f) \equiv \frac{1}{\tau} \log \frac{\delta_f}{\delta_0} \quad (1)$$

5.10 Example : *In situ* observation of a hyperbolic point in the Gulf of Lion (LATEX10)

| | |
|--|---|
| <p style="text-align: center;">Lagrangian Coherent Structures and transport analysis in the oceans: theory and applications</p> <p style="text-align: center;">F. Nencioli ¹, F. d'Ovidio ², A.M. Doglioli ¹ and A.A. Petrenko ¹</p> <p><small>(1) Aix-Marseille Université, CNRS, IRD, LOPB-UMR 6635, Laboratoire d'Océanographie Physique et Biogéochimique, OSU-Centre d'Océanologie de Marseille, France (2) Laboratoire d'Océanographie et du Climat: Expérimentation et Approches Numériques, IPSL, Paris, France</small></p> <p style="text-align: right;"><i>Student Seminar</i> November 13, 2011, Marseille</p> | <p>1. Intro Transport in fluids</p> <ul style="list-style-type: none"> • Complex due to chaotic and turbulent nature of flow field • Structures and patterns are present • Mathematical methods to detect those patterns: <ul style="list-style-type: none"> • Finite Size Lyapunov Exponents (FSLE) • Lagrangian Coherent Structures (LCS) • Developed for the analysis of DYNAMICAL SYSTEMS |
| <p>2. Math Basic Definitions</p> <p>Dynamical System</p> <p>Mathematical concept consisting of</p> <ol style="list-style-type: none"> 1) Space state (space where system can evolve) 2) Time (during which the system evolves) 3) Evolution Rule (which describes the temporal evolution of the system in the space state) | <p>2. Math Basic Definitions</p> <p>Evolution Rule $\frac{dx}{dt} = f(x)$ with $x = \begin{pmatrix} x_1 \\ \vdots \\ x_n \end{pmatrix}$ State vector</p> <p>Map/Flow $x(t) = x(0) + \int_0^t f(x) dt$ $f(x) = \begin{pmatrix} f_1 = f_1(x_1, \dots, x_n) \\ \vdots \\ f_n = f_n(x_1, \dots, x_n) \end{pmatrix}$ Velocity field</p> <p>Trajectory (Temporal ordered collection of successive states)</p> <p>Map allows to retrieve system state at t</p> |

2. Math Basic Definitions

• Trajectories in system space highly influenced by spatial distribution of **FIXED or EQUILIBRIUM POINTS** → x^e

Characteristics:

- 1) Constant position in time → $x(t) = x^e$
- 2) Vector field is 0 → $\frac{dx^e}{dt} = f(x^e) = 0$

• Classified depending on **LYAPUNOV STABILITY** :

• Fixed point is a **STABLE EQUILIBRIUM** point if trajectories of any point around it remains close to it with time (**UNSTABLE** if the contrary)

Further characterization:

- **ASYMPTOTIC** stable
- **EXPONENTIALLY** stable

2. Math Basic Definitions

• To define type of equilibrium point **STABILITY ANALYSIS**

System Linearization : $\frac{dx}{dt} = f(x) \rightarrow \frac{d(x^e + \xi)}{dt} = f(x^e + \xi)$

$\frac{dx^e}{dt} + \frac{d\xi}{dt} = f(x^e) + J(x^e)\xi + \mathcal{O}(|\xi|^2)$

$\frac{d\xi}{dt} = J(x^e)\xi$

Jacobian matrix

$$J(x^e) = \left(\frac{\partial f_i}{\partial x_j} \right)_{x=x^e} = \begin{pmatrix} \frac{\partial f_1}{\partial x_1} & \frac{\partial f_1}{\partial x_2} & \dots & \frac{\partial f_1}{\partial x_n} \\ \frac{\partial f_2}{\partial x_1} & \frac{\partial f_2}{\partial x_2} & \dots & \frac{\partial f_2}{\partial x_n} \\ \vdots & \vdots & \ddots & \vdots \\ \frac{\partial f_n}{\partial x_1} & \frac{\partial f_n}{\partial x_2} & \dots & \frac{\partial f_n}{\partial x_n} \end{pmatrix}_{x=x^e}$$

2. Math Basic Definitions

• To define type of equilibrium point **STABILITY ANALYSIS**

System Linearization : $\frac{d\xi}{dt} = J(x^e)\xi$

Solution to ODE

$$\xi(t) = \xi(0) \exp^{Jt}$$

Eigenvalues of J can tell if the fixed point is stable or not

$$\det[J(x^e) - \lambda I] = 0$$

- Real or imaginary
- Positive or negative

2. Math Basic Definitions

• **Types of equilibrium points**

(real positive eigenvalues) **unstable node**

(complex eigenvalues, positive real part) **unstable focus**

(real eigenvalues, different signs) **saddle**

(complex eigenvalues, negative real part) **stable focus**

(real negative eigenvalues) **stable node**

$\tau^2 - 4\Delta = 0$

Andronov-Hopf bifurcation

2. Math Basic Definitions

- Particle dispersion around an hyperbolic point
- Manifolds separate distinct regions of the flow!!!

- Particles move along and spread across converging direction: STABLE MANIFOLD
- Particles align along diverging direction (transport barrier) UNSTABLE MANIFOLD

3. LCS Finite Size Lyapunov Exponents

- Theory for manifold analysis developed by Alexandr Lyapunov (June 6 1857 – November 3 1918)

- Lyapunov exponents introduced at the end of 1800
- Based on the rate of separation of initially close trajectories
- Assumes infinite temporal evolution and permanent equilibrium points

- Problem of applications with measured data:
 - 1) Temporally finite time series
 - 2) Time varying velocity field
 - 3) Only transient Hyperbolic points and Manifolds
- Finite Size/Time Lyapunov Exponent techniques developed in the late '80s to apply Lyapunov analysis to measured (temporally finite) velocity fields.

3. LCS Finite Size Lyapunov Exponents

- Based on local relative dispersion of initially near trajectories (integrate information of evolving velocity field)
- <http://mmae.iit.edu/shadden/LCS-tutorial/examples.html>

Example STEADY FLOW:

- Maximum values at points from where trajectories will diverge
- High Lyapunov Exponent values map the manifolds
- Ridges of Lyapunov Exponents are LAGRANGIAN COHERENT STRUCTURES

3. LCS Finite Size Lyapunov Exponents

- At each grid point deployed an array of four floats

- Advected in time (forward or backward) with a Runge-Kutta 4th order (linear spatial and temporal interpolation)
- Recorded the time (τ) at which one of the distances becomes larger than a fixed spatial threshold (fixed size)

$$\xi(0) = \delta_0$$

$$\xi(\tau) = \delta_\tau$$

- Lyapunov exponent is the inverse of that time

$$\xi(t) = \xi(0) \exp^{\lambda t} \implies \delta_\tau = \delta_0 \exp^{\lambda \tau} \implies \lambda = \frac{1}{\tau} \log \left(\frac{\delta_\tau}{\delta_0} \right)$$

- Quantify separation of trajectories due to presence of hyperbolic point (exponential separation)

3. LCS Finite Size Lyapunov Exponents

- Grid resolution and separation distance (initial and final) all affect FSLE
- They must be accurately defined depending on the application

- FSLE Values:
 - The closer to the hyperbolic point the stronger the FSLE
 - The more intense the divergence/convergence at the hyperbolic point the stronger the FSLE
- IMPORTANT CONDITIONS:
 - Hyperbolic point must be persistent during integration
 - Its translation must be slower than local advection

4. Apps Open ocean LCSs

- Open ocean: LCSs from altimetry velocity fields using Lyapunov Exponents
- Detected structures compared to advected tracers

- Accuracy still relatively untested in coastal areas

4. Apps Coastal ocean LCSs

- Coastal ocean: LCSs from HF Radar velocities (Monterey Bay, CA)

<http://mmae.iit.edu/shadden/LCS-tutorial/oceancurrents.html>

4. Apps Biological impact of LCSs

- Creation of ecological niches
- Structuring of phytoplankton communities

(d'Ovidio et al., 2010)

4. Apps Biological impact of LCSs

- Influences on marine top-predator (e.g. Frigates in Mozambique)

<http://www.migratoryconnectivityproject.org/tracking/satellite>

(Kai et al., 2009)

Real-time in-situ tracking of Lagrangian coherent structures in a coastal region

F. Nencioli ¹, F. d'Ovidio ², A.M. Doglioli ¹ and A.A. Petrenko ¹

(1) Aix-Marseille Université, CNRS, IRD, LOPB-UMR 8535, Laboratoire d'Océanographie Physique et Biogéochimique, OSU Centre d'Océanologie de Marseille, France
 (2) Laboratoire d'Océanographie et du Climat: Expérimentation et Approches Numériques, IPSL, Paris, France

CEM LOPB

EGU General Assembly 2011
 April 8, 2011, Vienna

1. Intro The Gulf of Lion

- Altimetry LCSs compared to *in-situ* LCSs in the Gulf of Lion (GoL)

- Large continental shelf
- Three main forcings:
 - Mistral & Tramontane
 - Delta of Rhone river
 - Northern Current
- NC dynamical barrier to cross-shelf exchanges
- (Sub)mesoscale anticyclones in the western part

Lagrangian Transport Experiment
 Latex10, September 1-24, 2010

Transport and biogeochemistry in the western part of the GoL.

3 of 13

2. Methods Altimetry LCSs

- Altimetry LCSs from AVISO velocities using Finite-size Lyapunov exponents analysis (FSLE; d'Ovidio et al., 2004)
- Geostrophic surface velocity fields derived from SSH
- 1/8 degree, daily

4 of 13

2. Methods In-situ LCSs

Latex10 Adaptive Sampling Strategy for detection of *in-situ* LCSs:

- Position of large scale LCSs estimated from altimetry derived FSLE
- In-situ* deployment of drifters
- Mapping of *in-situ* velocities (hull mounted ADCP)

Deployment of 3 drifter arrays:

- Lyap01 (September 12)
- Lyap02 (September 18)
- Lyap03 (September 21)

5 of 13

3. Results Lyap01 – Sept 12 - 14

September 12, 2010

- Altimetry geostrophic velocity vectors
- Attractive (blue) & Repulsive (red) LCSs
- Initial position of drifter array

September 12-14, 2010

- Drifter trajectories
- In-situ* LCSs
- 15m ADCP velocity vectors

- Repelling LCS on the continental shelf not detected
- Confirmed by ADCP velocities

6 of 13

3. Results Lyap02 – Sept 18 - 20

September 18, 2010

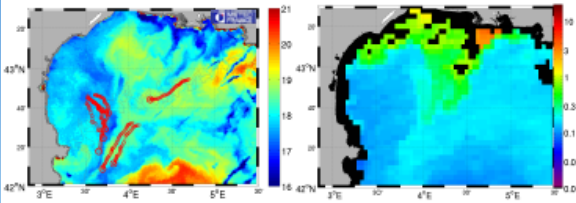
- Altimetry geostrophic velocity vectors
- Attractive (blue) & Repulsive (red) LCSs
- Initial position of drifter array

September 18-20, 2010

- Drifter trajectories
- In-situ* LCSs
- 15m ADCP velocity vectors

- Satellite structures similar to Sept. 12
- Accurate identification of LCSs and hyperbolic point

7 of 13

| | |
|--|--|
| | <div data-bbox="802 152 1396 600"> <p>3. Results LCSs and satellite imagery <small>CENTRE D'Océanologie DE MARSEILLE</small></p> <p>September 14, 2010</p> <ul style="list-style-type: none"> • AVHRR SST field • Lyap01 drifter trajectories  <ul style="list-style-type: none"> • In-situ LCSs associated with a front (NC and coastal waters) • They identify coastal corridor along which water exit the GoL. • Importance of those structures to study cross-shelf exchanges • Importance of those exchanges for biogeochemistry <p style="text-align: right;"><small>10 of 13</small></p> </div> |
| <div data-bbox="196 622 786 1064"> <p>4. Concl. Conclusions <small>CENTRE D'Océanologie DE MARSEILLE</small></p> <ul style="list-style-type: none"> • Adaptive sampling strategy allowed to detect and track <i>in-situ</i> LCSs for two weeks • Translational speed of hyperbolic point satisfies assumption for FSLE analysis • LCSs identified a corridor along which coastal waters left the continental shelf of the GoL • Altimetry LCSs showed some limitations in the coastal region • Corrections are required to improve coastal transport analysis from altimetry velocity fields <p style="text-align: right;"><small>11 of 13</small></p> </div> | <div data-bbox="802 622 1396 1064"> <p>4. Concl. Future Work <small>CENTRE D'Océanologie DE MARSEILLE</small></p> <ul style="list-style-type: none"> • Quantification of transport • Improve satellite velocity field: <ul style="list-style-type: none"> • Different processing schemes for raw data • Add ageostrophic components (Ekman, MIO...) • HF Radar velocities • Numerical models: <ul style="list-style-type: none"> • Extend transport analysis to the whole GoL • Test corrections • Analysis of previous Latex datasets • Further Lyap experiments (???) <p style="text-align: center;">Final goal Method for estimate & predict coastal transport/exchanges (pollutants, oil spill, larval/jellyfish transport, fisheries)</p> <p style="text-align: right;"><small>12 of 13</small></p> </div> |

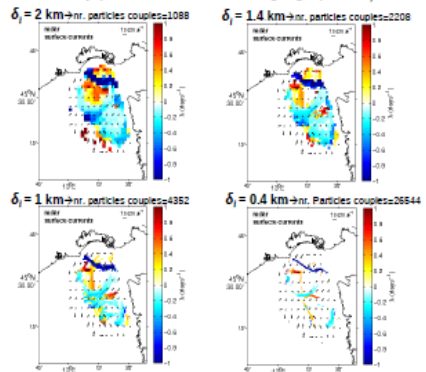
5.11 Example : Studying FSLEs in the Gulf of Trieste using radar measurements

| | |
|---|---|
| <h4>Typical Wind events</h4> <p>BORA</p> <ul style="list-style-type: none"> Siberian katabatic wind (analogous mechanism of Mistral in GoL) blows from E-NE cold, dry and gusty 5 preferential entrances over the Adriatic <p>SIROCCO</p> <ul style="list-style-type: none"> Saharian wind pulled northward by low-pressure cell over Mediterranean Sea blows from S-SE warm, wet and steady <p><i>(after Probst and Raitsch 2003)</i></p> | <h4>Adriatic Sea mean surface circulation</h4> <p>Adriatic cyclonic pattern: WAC / EAC system</p> <p>Mean current field (from radar meas., Aug07-Aug08)</p> <ul style="list-style-type: none"> northward flow along Istria westward jet along Italy <p><i>(after Arregui et al. 2007)</i></p> |
| <h4>Effects of wind on circulation</h4> <p>BORA DRIVES</p> <ul style="list-style-type: none"> upwelling along eastern coast (U) double gyre surface circulation as wind ceases, rapid return mean circulation <p><i>(after Jellison and Liu 2007)</i></p> <p>SIROCCO DRIVES</p> <ul style="list-style-type: none"> sea level rise along northern coast possible WAC reversal (North Adri) as wind ceases, basin-wide barotropic seiches <p><i>(after Ferrante et al. 2005)</i></p> | <p>BORA drives:</p> <ul style="list-style-type: none"> intensification of westward jet along Italy (northern Bora corridor) downwind currents and divergence in front of the Istrian peninsula <p>SIROCCO drives:</p> <ul style="list-style-type: none"> intensification of northward flow along Istria westward veering along Italian coast |
| <h4>AIM AND STRATEGY OVERVIEW</h4> <p>Identification of surface transport patterns in the North Adriatic with Bora and Sirocco winds.</p> <p>combine</p> <p>DATA: High Frequency radar currents measurements</p> <p>METHOD: Finite-Size Lyapunov Exponent (FSLE) technique</p> <p>high resolution information + tracking sub-mesoscale dynamics</p> <p>Investigation:</p> <ul style="list-style-type: none"> Applicability of FSLE on highly variable current field, with small domain Transport structures development under specific wind conditions Implication of spatial organization of transport observed | <h4>Lagrangian methods</h4> <p>single trajectory prediction</p> <p>transport patterns detection</p> <p>Lyapunov Exponent (LE)</p> <p>quantifies relative dispersion between close trajectories</p> <p>transport information integrated over time</p> <p>applied in oceanography to identify attractive and repulsive Lagrangian Coherent Structures (LCSs)</p> |
| <h4>Finite Size LE (FSLE)</h4> <p>Definition: $\lambda(x, \delta_i, \tau, \delta_f) = \frac{1}{\tau} \ln \frac{\delta_f}{\delta_i}$</p> <p>small $\tau \rightarrow$ fast separation \rightarrow large λ</p> <p>Application: particles move with $u(t, x)$</p> <p>VELOCITY GRID</p> <p>FSLE GRID (resolution = initial distance of particles)</p> <p>Num part = f (current field area / FSLE pixel resolution)</p> <p>For each FSLE grid node \rightarrow maximum λ of the 4 nearest couples</p> | <h4>From FSLE to LCS</h4> <p>LCS time scale evolution is very different from temporal variability of the flow field</p> <p>Integration of particles forward in time: look for divergence of particles</p> <p>Integration of particles backward in time: look for convergence of particles</p> <p>positive FSLE: $\lambda_+ = \frac{1}{\tau} \ln \frac{\delta_f}{\delta_i}$ identify repulsive LCS or barriers to transport</p> <p>negative FSLE: $\lambda_- = -\frac{1}{\tau} \ln \frac{\delta_f}{\delta_i}$ identify attractive LCS or direction of transport</p> <p><i>(after Hall and Yuan 2000)</i></p> |

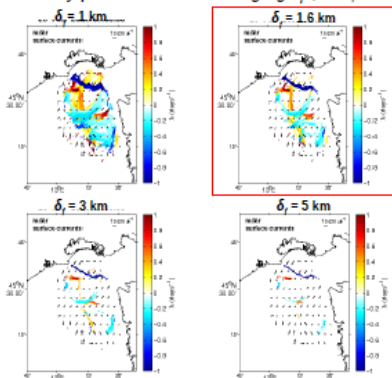
Algorithm and settings

- Trajectories evolution $\rightarrow \frac{dx}{dt} = u(t, x)$ \rightarrow Integration in time: 4th order Runge-Kutta
Interpolation in space: bilinear (4)
- Choice of δ_x and δ_y \rightarrow Depends on current features, length scale of structures and details requirements in structures identification.
- Independent runs \rightarrow Forward FSLE (looking for divergence)
Backward FSLE (looking for convergence)
- Graphical superposition of forward and backward FSLE

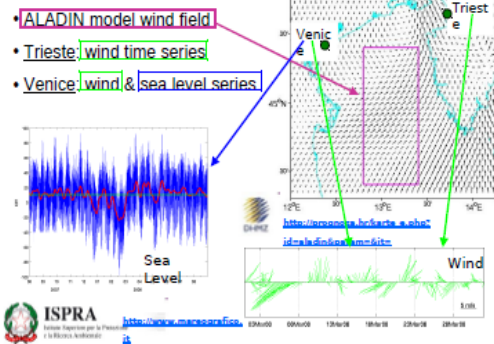
Sensitivity parameters test changing δ_x (with $\delta_y = 3$ km)



Sensitivity parameters test changing δ_y (with $\delta_x = 0.4$ km)



Meteo-mareographic dataset



Wind episodes selection

CRITERIA :

- INTENSITY \rightarrow
- DIRECTION \downarrow



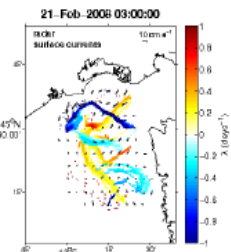
| | ALADIN MODEL | TRIESTE STATION | VENICE STATION |
|-----------|--------------|---|---------------------------------------|
| CALM WIND | | Persistence ≥ 7 days Speed < 3 m/s | |
| BORA | | Persistence ≥ 3 days Speed ≥ 5 m/s | |
| SIROCCO | | | Low pass filtered Sea Level > 20 cm |

- Trieste: ideal for Bora identification
- Venice: ideal for Sirocco identification

FSLE during calm wind (case 1)

17-Feb-2008 29-Feb-2008

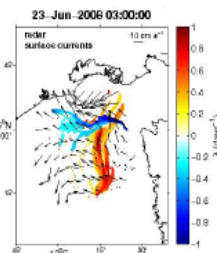
- Current field rich in transport structures
- Evolution of transport structures slower than currents variability
- Attractive transport line detached from the Italian coast



FSLE during calm wind (case 2)

17-Jun-2008 30-Jun-2008

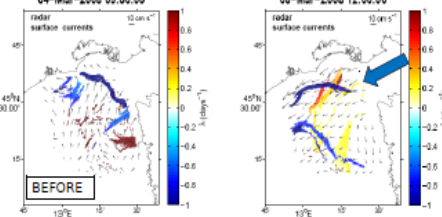
- Current field rich in transport structures
- Evolution of transport structures slower than currents variability
- Attractive transport line detached from the Italian coast



FSLE during Bora (case 1)

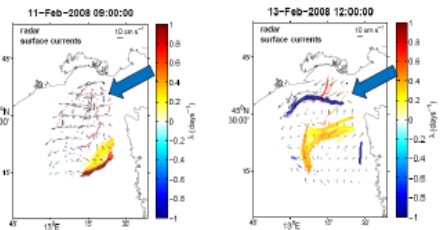
04-Mar-2008 08-Mar-2008

- Bora drives significant spatial variability in surface currents
- new structures develop and pre-existent ones change spatial configuration
- transport structures configuration evolves slower than the current field



FSLE during Bora (case 2)

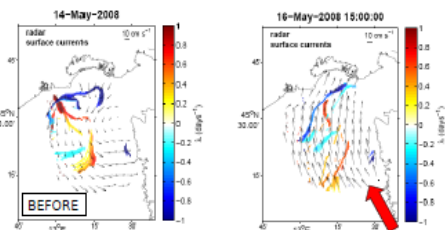
06-Feb-2008 13-Feb-2008



- Reduced coverage does not allow to identify attractive LCS at the beginning
- Development of repulsive LCS in front of the Istrian coast and northward propagation
- At the end of the event appearance of attractive structure

FSLE during Sirocco (case 1)

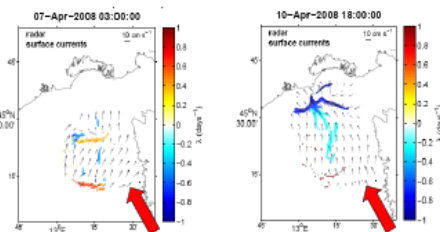
16-May-2008 19-May-2008



- Sirocco drives coherent surface velocities
- lines of transport align perpendicularly to dominant wind direction
- local transport reversed from "mean condition": particles

FSLE during Sirocco (case 2)

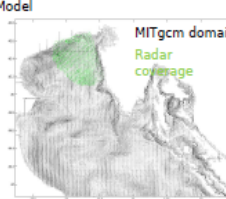
09-Apr-2008 11-Apr-2008



- At the beginning reduced radar coverage to identify any structures
- At the end of the event, the transport line along Italy comes out

Model: MITgcm*

* General Circulation Model



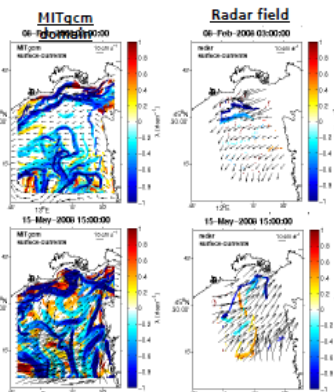
- Simulates physical variables (velocity, temperature and salinity)
- non hydrostatic
- finite volume
- free surface
- 1/64 ° spatial res., 1h temporal res.
- Z-levels (surface - 40m depth)
- forced by ALADIN wind field (also used for wind events identification)

FSLE evaluation:

- Particles: same radar launch grid, but evolution all over MITgcm domain
- $\delta_x = 0.4$ km, $\delta_y = 1.6$ km (same radar parameters)
- Maximum evolution time (forward and backward): 6 days

<http://mitgcm.org> MITgcm

SIMILARITIES AND DIFFERENCES
 Model currents forced by ALADIN wind (more homogeneous and less intense than actual wind)
 Long-lived structures
 Model domain wider
 Particles have higher chance to satisfy the final distance criteria
 Tangle of structures



SUMMING-UP...

- High variability (spatial and temporal) of the velocity field affects structures configuration and persistence
- Line of transport along the Italian coast: different meandering and detachment from coastline according to wind conditions
- Greater variability of transport structures in the southern part of the domain, due to close orographic influence on winds.

COMMENTS

- The "optimum scenario" for FSLE application would be:
 - extended flow field (size >> length scale of the structures to be identified)
 - evolution of flow field slower than advective time scale (frozen field Hp)
- In oceanography FSLE is usually applied over current fields derived from satellite altimetry or model output:
 - Size of the domain larger than radar coverage
 - Slower variability of the velocity field with respect to radar measurements
- One of the first FSLE application on HF radar current field: (see also Mazz et al. 2010 for application on VHF radars)
 - High resolution, but small domain
 - Transport structures evolve faster than their translational velocity

Through an accurate setting of initial and final separation between

PERSPECTIVES...

- Application of FSLE method both on modeled and radar currents: combination of the surface dynamics information from model and radar field
- FSLE transport analysis on deeper layers of modeled currents can give important information on water column dynamics.
- FSLE method in association with advection of clusters of drifters (at the surface and deeper deployments) to compare trajectories with the transport structures identified from radar and model.

Matlab programmes (OLD VERSIONS, for 2018 the web archive)

```

%% program to show that numbers are only pseudo-random and not really random

clear;close;
disp('PROGRAM TEST_RANDOM')
disp('*** without reset ***')

s = rand('state');
u1 = rand(10,1);
%rand('state',s);
u2 = rand(10,1); % contains exactly the same values as u1
[u1';u2']

disp('*** with reset ***')

%Save the current state, generate 10 values, reset the state, and repeat the sequence.
s = rand('state');
u1 = rand(10,1);
rand('state',s);
u2 = rand(10,1); % contains exactly the same values as u1
[u1';u2']

```

```

%% program to extract the pseudo-random numbers
%% 1) between 0 and 1 with uniform pdf
%% 2) between -inf and +inf with Gaussian pdf of zero mean

```

```

disp('PROGRAM HISTOGRAMS')
clear;close all;

imax=10000;

for i=1:imax
    r(i)=rand(1);
end

figure(1)
subplot(2,1,1)
intedge=0.1;
edges=[0:intedge:1];
N=histc(r, edges);
bar(edges,N./imax*100, 'histc')
y(1:size(edges'))=intedge;
line(edges,y*100, 'color', 'r')
ylabel('%')

pause(2)

devst=10;
for i=1:imax
    g=0;
    for ig=1:12
        r=rand(1);
        g=g+(r-0.5);
    end
    gg(i)=g.*devst;
end

subplot(2,1,2)
intedge=0.25;
edges=[-100:intedge:100];
N=histc(gg, edges);
bar(edges,N./imax*100, 'histc')
var=devst^2;
y=1/sqrt(2*pi*var).*exp(-(edges).^2/(2*var));
line(edges,y.*intedge*100, 'color', 'r')
ylabel('%')

```

```

%% program to extract pseudo-random numbers
%% 1) between 0 and 1 with uniform pdf
%% 2) between -inf and +inf with Gaussian pdf of zero mean

```

```

disp('PROGRAM HISTOGRAMS')
clear;close all;

imax=10000;

for i=1:imax
    r(i)=rand(1);
end

figure(1)
subplot(2,1,1)
intedge=0.1;
edges=[0:intedge:1];
N=histc(r,edges);
bar(edges,N./imax*100,'histc')
y(1:size(edges'))=intedge;
line(edges,y*100,'color','r')
ylabel('%')

pause(2)

devst=10;
for i=1:imax
    g=0;
    for ig=1:12
        r=rand(1);
        g=g+(r-0.5);
    end
    gg(i)=g.*devst;
end

subplot(2,1,2)
intedge=0.25;
edges=[-100:intedge:100];
N=histc(gg,edges);
bar(edges,N./imax*100,'histc')
var=devst^2;
y=1/sqrt(2*pi*var).*exp(-(edges).^2/(2*var));
line(edges,y.*intedge*100,'color','r')
ylabel('%')

```

```

%% program to perform the Random Walk of more than one particle
clear;close;

```

```

disp('PROGRAM RANDOM_WALK_NPART');

ipmax=10;%number of particles
itmax=100;%[s]
devst=1;%[m]

figure(1);hold on;
axis([-50 50 -50 50])
text(-1,-1,'*', 'color','red', 'fontSize',20)
grid on;
xlabel('distance en direction x [m]');
ylabel('distance en direction y [m]');

for ip=1:ipmax

x(1)=0;
y(1)=0;

for it=2:itmax
    % displacement in x-direction
    g=0;
    for ig=1:12
        r=rand(1);
        g=g+(r-0.5);
    end

```

```

depx=g.*devst;
% displacement in y-direction
g=0;
for ig=1:12
    r=rand(1);
    g=g+(r-0.5);
end
depy=g.*devst;
% assign new location
x(it)=x(it-1)+depx;
y(it)=y(it-1)+depy;

end%for it

line(x,y,'color',[ip/ipmax 0 1-ip/ipmax])
text(51,51-ip*4,num2str(ip),'color',[ip/ipmax 0 1-ip/ipmax])
end%for ip
hold off;


```

```

%% program to calculate the particle concentration in each grid cell

clear;close all;
Xsource=5; % initial x position of particles
Ysource=5; % initial y position of particles
ipmax=5; % number of particles
itmax=100; % number of time steps per day
imax=10; % size of matrix CONC in m (box containing the particles)
jmax=10; % size of matrix CONC en m
deltatime=50; % tie step (to calculate and trace CONC)
k=1.5*10^(-7); % diffusion coeff [m2/s]
xold(1:ipmax)=Xsource; %initial position
yold(1:ipmax)=Ysource;

scrsz = get(0,'ScreenSize');
figure('Position',[1 scrsz(4) scrsz(3) scrsz(4)]);

for it=1:itmax
devst=sqrt(2*k*3600*24); %standard deviation (in m)
% initial condition using concentrations of zero
CONC=zeros(10,10);
for ip=1:ipmax
    % displacement in x direction
    g=0;
    for ig=1:12
        r=rand(1);
        g=g+(r-0.5);
    end
    depx=g.*devst;
    % displacement in y direction
    g=0;
    for ig=1:12
        r=rand(1);
        g=g+(r-0.5);
    end
    depy=g.*devst;
    % assign new location
    xnew(ip)=xold(ip)+depx;
    ynew(ip)=yold(ip)+depy;
    % boundary condition: closed boundary
    if(xnew(ip)<1 | xnew(ip)>100 | ynew(ip)<1 | ynew(ip)>100)
        xnew(ip)=xold(ip);
        ynew(ip)=yold(ip);
    end%if
    % calculating concentrations
    ii=fix(xnew(ip));
    jj=fix(ynew(ip));
    CONC(jj,ii)=CONC(jj,ii)+1;
    % save the particle positions
    xmem(ip)=xnew(ip);
    ymem(ip)=ynew(ip);
    xold(ip)=xnew(ip);
    yold(ip)=ynew(ip);
end%for ip

subplot(1,2,1);hold on;

```



```

title(['it=',num2str(it)]);
pcolor(CONC);
colorbar;
plot(xmem,ymem,'k+')
axis([1 10 1 10])
axis square
xlabel('mesh index in x-direction');
ylabel('mesh index in y-direction');

subplot(1,2,2);hold on;
axis([0 10 0 10])
plot(xmem,ymem,'k+')
contour(CONC)
colorbar
axis([1 10 1 10])
axis square
xlabel('mesh index in x-direction');
ylabel('mesh index in y-direction');
title([' CLICK ON THE FIGURE TO CONTINUE']);
waitforbuttonpress
hold off; clf;
end %pour it

```



```

%% program to simulate the diffusion of a drop of ink in a glass
%% contribution by G.Ginoux

clear all;close all;scrsz = get(0,'ScreenSize');

disp('PROGRAM DIFFUSION')

Xsource=50; % initial particle positions (x)
Ysource=50; % initial particle positions (y)
ipmax=10000; %nombre of particles
itmax=1000; %number if time steps per day
imax=100; % size of matrix CONC in m (box containing the particles)
jmax=100; % size of matrix CONC en m
deltatime=50; %time step (to calculate and trace CONC)
k=10.5*10^(-7); %m2/s
devst=sqrt(2*k*3600*24); %standard deviation (in m)
xold(1:ipmax)=Xsource; %initial position
yold(1:ipmax)=Ysource;

for it=1:itmax
it
for ip=1:ipmax
g=0;
for i=1:12
r=rand;
g=g+(r-0.5);
end
depX=g*devst;
h=0;
for i=1:12
r=rand;
h=h+(r-0.5);
end
depy=h*devst;
X(ip)=xold(ip)+depX;
Y(ip)=yold(ip)+depy;
% boundary condition
if X(ip)<1 | X(ip)>100 | Y(ip)<1 | Y(ip)>100
% closed boundary
X(ip)=xold(ip);
Y(ip)=yold(ip);
end
xold(ip)=X(ip);
yold(ip)=Y(ip);
end %pour ip

%Afin de n'afficher la figure que tous les 'deltatimes' pas de temps
if rem(it,deltatime)==0
CONC=zeros(jmax,imax);
devst
for ip=1:ipmax
%Calcule le nombre de particules dans chaque maille
ii=fix(X(ip));

```

```

    jj=fix(Y(ip));
    CONC(jj,ii)=CONC(jj,ii)+1;
end

close all
figure('Position',[1 scrsz(4)/2 scrsz(3)/2 scrsz(4)/2]);
hold on;
contourf(CONC(:, :)./ipmax,[0:1:20]./ipmax); shading flat;
axis([-10 imax+10 -10 jmax+10])
box on;
colorbar;
title('concentration specifique de particules par maille de grille');
axis([1 100 1 100])
axis square
xlabel('mesh index in x-direction');
ylabel('mesh index in y-direction');

% Croix rouge (centée en 50,50)
cf= repmat(50,1,100);
cs=1:100;
plot(cf,cs,'r-')
plot(cs,cf,'r-')

CONCf1=CONC(50, :)/sum(CONC(50, :));
CONCf2=CONC(:, 50)/sum(CONC(:, 50));
xx=[1:0.1:100];
moy=50;
yy=1/sqrt(2*pi*devst^2*it).*exp(-1/2*((xx-moy)./(devst.*sqrt(it)).^(2));

figure('Position',[scrsz(3)/2 scrsz(4)/2 scrsz(3)/2 scrsz(4)/2]);
subplot(1,2,1), plot(CONCf1); axis([40 60 0 0.3]); hold off;
%Superposition de la gaussienne
line(xx,yy,'color','r')
xlabel('Concentration le long de la ligne horizontale');
subplot(1,2,2), plot(CONCf2); axis([40 60 0 0.3]); hold off;
%Superposition de la gaussienne
line(xx,yy,'color','r')
xlabel('Concentration le long de la ligne verticale');
hold off;
title([' CLICK ON THE FIGURE TO CONTINUE']);
waitforbuttonpress;

end %pour if
end %pour it

```

```

%% programme pour la advection diffusion d'une goutte d'encre
%% dans un champs de vitesse uniforme

```

```

clear all;close all;
figure(1)
disp('PROGRAM ADVECTION-DIFFUSION')

Xsource=50; %position en x initiale des particules
Ysource=50; %position en y initiale des particules
ipmax=10000; %nombre de particules
itmax=1000; %nombre de pas de temps en jour
imax=100; %taille de la matrice CONC en m (boite où sont enfermée les particules)
jmax=100; %taille de la matrice CONC en m
deltatime=50; %pas de temps (pour calculer et tracer CONC)
k=10.5*10^(-7); %m²/s
devst=sqrt(2*k*3600*24); %ecart type (en m)
xold(1:ipmax)=Xsource; %initial position
yold(1:ipmax)=Ysource;
U=0.1;%[m/s]
V=0;%[m/s]
deltaT=1;%[s]

for it=1:itmax
    it
    for ip=1:ipmax
        g=0;
        for i=1:12
            r=rand;
            g=g+(r-0.5);
        end
        depx=g*devst;
    end
end

```

```

h=0;
for i=1:12
    r=rand;
    h=h+(r-0.5);
end
depy=h*devst;
X(ip)=xold(ip)+depx+U*deltaT;
Y(ip)=yold(ip)+depy+V*deltaT;
% condition à la frontière
if X(ip)<1 | X(ip)>100 | Y(ip)<1 | Y(ip)>100
    %frontière fermée
    X(ip)=xold(ip);
    Y(ip)=yold(ip);
end
xold(ip)=X(ip);
yold(ip)=Y(ip);
end %pour ip

%Afin de n'afficher la figure que tous les 'deltatimes' pas de temps
if rem(it,deltatime)==0
    CONC=zeros(jmax,imax);
    devst
    for ip=1:ipmax
        %Calcule le nombre de particules dans chaque maille
        ii=fix(X(ip));
        jj=fix(Y(ip));
        CONC(jj,ii)=CONC(jj,ii)+1;
    end
    figure(1);hold on;
    contourf(CONC(:, :)./ipmax,[0:1:20]./ipmax);shading flat;
    axis([-10 imax+10 -10 jmax+10])
    box on;
    colorbar;
    title('concentration spécifique de particules par maille de grille');
    % Croix rouge (centée en 50,50)
    cf= repmat(50,1,100);
    cs=1:100;
    plot(cf,cs,'r-')
    plot(cs,cf,'r-')
    pause(1)
    hold off; clf reset
end %pour if

end %pour it

```

```

%% programme pour la advection diffusion avec un source de particules
%% dans un champs de vitesse uniforme
clear all;close all;
figure(1)
disp('PROGRAM ADVECTION-DIFFUSION CONTINUOUS RELEASE')

Xsource=50; %position en x initiale des particules
Ysource=50; %position en y initiale des particules
ipmax=5000000; %nbre de particules
iprelease=100;
itmax=ipmax/iprelease; %nbre de pas de temps en jour
imax=100; %taille de la matrice CONC en m (boite où sont enfermée les particules)
jmax=100; %taille de la matrice CONC en m
deltatime=50; %pas de temps (pour calculer et tracer CONC)
k=1.5*10^(-7); %m²/s
devst=sqrt(2*k*3600*24); %ecart type (en m)
U=0.1;%[m/s]
V=0;%[m/s]
deltaT=1;%[s]
activity(1:ipmax)=0;

for it=1:itmax
    it
    activity(it:it+9)=1;
    xold(it:it+iprelease-1)=Xsource;
    yold(it:it+iprelease-1)=Ysource;
    for ip=1:ipmax
        if activity(ip)==1;
            g=0;
            for i=1:12
                r=rand;
                g=g+(r-0.5);
            end
        end
    end
end

```

```

end
depx=g*devst;
h=0;
for i=1:12
    r=rand;
    h=h+(r-0.5);
end
depy=h*devst;
X(ip)=xold(ip)+depx+U*deltaT;
Y(ip)=yold(ip)+depy+V*deltaT;
% BOUNDARY CONDITION
if X(ip)<1 | X(ip)>100 | Y(ip)<1 | Y(ip)>100
    %closed boundary
    X(ip)=xold(ip);
    Y(ip)=yold(ip);
    % particles that leave (no longer active)
    activity(ip)=0;
end
xold(ip)=X(ip);
yold(ip)=Y(ip);
    end%if activity(ip)=1;

end %pour ip

%Afin de n'afficher la figure que tous les 'deltatimes' pas de temps
if rem(it,deltatime)==0
    CONC=zeros(jmax,imax);
    devst
    for ip=1:ipmax
        if activity(ip)==1;
            %Calculate the number of particles in each grid cell
            ii=fix(X(ip));
            jj=fix(Y(ip));
            CONC(jj,ii)=CONC(jj,ii)+1;
            end%if activity(ip)=1;
        end
    figure(1);hold on;
    contourf(CONC(:, :)./ipmax,[0:1:20]./ipmax);shading flat;
    axis([1 imax 1 jmax])
    box on;
    colorbar;
    title('concentration specifique de particules par maille de grille');
    % Red X (centred on 50,50)
    cf=repmat(50,1,100);
    cs=1:100;
    plot(cf,cs,'r-')
    plot(cs,cf,'r-')
    pause(1)
    hold off; clf reset
    end %pour if

end %pour it

```

Problems from previous exams

Academic year 2018-2019
Single Session

OPB306 – Lagrangian Approach: fundamentals

Duration: 2 hours

Documents : none allowed

Calculator: allowed

Answers must be as concise and precise as possible.

Part A. Doglioli

- 1) What is the difference between an Eulerian and a Lagrangian approach?
- 2) How do vortices form downstream from capes/headlands?
- 3) Explain cyclo-geostrophic balance.
- 4) Describe and explain the different techniques for identifying and tracking oceanic eddies.

Academic Year 2018-2019
Single Session

OPB309 – Lagrangian Approach: sampling strategies

Duration : 2 hours

Documents : none allowed

Calculator : allowed

Answers must be as concise and precise as possible.

Part A. Doglioli

- 1) Explain the different terms in the integral form of the conservation equation for a generic property ψ

$$\frac{d}{dt} \int_V \psi dV + \oint_S \psi \mathbf{u} \cdot d\mathbf{S} + \oint_S \chi \cdot d\mathbf{S} = \int_V \xi dV.$$

- 2) What is a random walk model?

***** ATTENTION ! write the answers on separate sheets *****

Part A. Petrenko

- 3) Describe an inertial oscillation (OI) in a two-layer medium with wind forcing perpendicular to the coast. What is the definition (and unit) of the inertial frequency for a particular latitude? Calculate the inertial frequency and periods of inertial oscillations (in hours) at two latitudes: 20° and 60°; comment.

Indicate two data analysis techniques to detect inertial oscillations.

***** ATTENTION ! write the answers on separate sheets *****

Part F. d'Ovidio

- 4) What are the typical scales (spatial and temporal) of the meso- and submesoscale? How can the dynamics of an eddy affect the dynamics of phytoplankton? (one or two mechanisms to choose from). Can you identify and describe some coupling mechanisms between the mesoscale, the submesoscale, and the pelagic food web?

Academic year 2019-2020
Single Session

OPB306 – Lagrangian Approach: fundamentals

Duration : 2 hours

Documents : none allowed

Calculator : allowed

Answers must be as concise and precise as possible.

Part A. Doglioli

- 1) Explain the process of flow separation near a cape/headland?
- 2) Why do mesoscale anticyclones tend to drift toward the equator?
- 3) What is the difference between an irrotational vortex and a rigid-body vortex?

Part A. Petrenko

- 4) Write down the Omega equation and the vector Q , explaining briefly what each term means. What are the underlying assumptions of this equation?

Academic Year 2019-2020
Single Session

OPB309 – Lagrangian Approach: sampling strategies

Duration : 2 hours


Documents : none allowed

Calculator : allowed

Answers must be as concise and precise as possible.

Part A. Doglioli

1) Explain the functioning of a piece of code to calculate the Finite Size Lyapunov Exponents (FSLE)

2) What is a numerical particle model 

***** ATTENTION ! write the answers on separate sheets *****

Part A. Petrenko

3) Describe an inertial oscillation (OI) in a two-layer medium. Identify three data analysis techniques to detect inertial oscillations.

***** ATTENTION ! write the answers on separate sheets *****

Part F. d'Ovidio

4) Provide some examples of how satellite altimetry data can be used to study mesoscale processes in the ocean. Briefly discuss the limitations of altimetry data.